Non-Uniform SERS Substrates to Three-Dimensional SERS Platforms: Optimizing Raman Spectroscopy for Advanced Applications

Dissertation

der Mathematisch-Naturwissenschaftlichen Fakultät

der Eberhard Karls Universität Tübingen

zur Erlangung des Grades eines

Doktors der Naturwissenschaften

(Dr. rer. nat.)

vorgelegt von

M.Sc. Ashutosh Mukherjee

aus Nashik/Indien

Tübingen

2024

Gedruckt mit Genehmigung der Mathematisch-Naturwissenschaftlichen Fakultät der Eberhard Karls Universität Tübingen.

Tag der mündlichen Qualifikation:	03.02.2025
Dekan:	Prof. Dr. Thilo Stehle
1. Berichterstatter:	Prof. Dr. Marc Brecht
2. Berichterstatter:	Prof. Dr. Andreas Schnepf

I would like to acknowledge the funding partner, the **German Federal Ministry of Education and Research (Bundesministerium für Bildung und Forschung - BMBF)**, for their financial support within the framework of IngenieurNachwuchs 2016,

With specific reference to the "CompeTERS" project and grant number **13FH596IX6.**

Bibliographical Description

Raman spectroscopy is a valuable technique for analyzing materials and their properties. However, due to the small scattering cross-section of many analytes, only weak signals with low signal-to-noise ratios (SNRs) are obtained. Researchers have explored various methodologies to overcome these limitations and enhance the power of this technique. Plasmonics, particularly Surface-Enhanced Raman Spectroscopy (SERS), has garnered global attention as a means to overcome weak Raman intensity. However, SERS has limitations and constraints, such as complex sample preparation and high costs, that must be overcome for broader applicability.

This dissertation demonstrates that gradient two-dimensional (2D) SERS substrates with multiple resonances improve the analysis of numerous samples. Such substrates enable fast screening of various molecules. With conventional 2D substrates, the signal from molecules is only enhanced when they are very close (a few nanometers) to the substrate surface. To overcome this limitation, innovative, stable, and three-dimensional (3D) SERS substrates based on spherical silica microspheres (SMPs) are developed as carriers for metal nanoparticles (NPs). These novel substrates offer the advantage of allowing analyses in all spatial directions, showing multiple resonances, being cost-effectively synthesized, and being used in various solutions. They address some of the limitations of conventional SERS substrates.

Furthermore, this doctoral thesis deals with advanced data analysis in SERS and Raman spectroscopy, which can lead to difficulties interpreting the data. Advanced data analysis is applied to identify subtle spectral differences and improve data interpretation. However, optimizing and maintaining spectrometers' performance and calibration stability over time is essential for reliable data interpretation. For this purpose, a quality factor is introduced, which represents the fit between theoretically calculated and experimentally measured spectral resolution (SR). This is applied to a commercial spectrometer used in the dissertation.

In summary, this work addresses central challenges and weaknesses in Raman spectroscopy, improving its applicability and addressing the associated challenges.

Zusammenfassung

Raman-Spektroskopie ist eine vielversprechende Methode zur Analyse verchiedener Materialien und deren Eigenschaften. Aufgrund des kleinen Streuquerschnitts vieler Analyten werden jedoch nur schwache Signal mit niedrigen Signal zu Rauschen Verhältnis beobachtet. Ein Ansatz diese Herausforderung zu überwinden ist die Plasmonik, insbesondere die oberflächenverstärkte Raman-Spektroskopie (SERS). Für den breiten Einsatz müssen allerdings Limitierungen, wie aufwendige Probenvorbereitung und hohe Kosten, in Kauf genommen werden.

Diese Dissertation zeigt, dass Gradienten-zwei-dimensionale (2D) SERS-Substrate mit mehreren Resonanzen die Analyse zahlreicher Proben verbessert und dass solche Substrate ein schnelles Screening verschiedener Moleküle ermöglichen. Bei herkömmlichen 2D-Substraten wird das Signal von Molekülen nur verstärkt, wenn sich diese sehr Nahe (wenige Nanometer) über der Substratoberfläche befinden. Um dies zu überwinden, werden innovative, stabile dreidimensionale (3D) SERS-Substrate auf Basis kugelförmiger Silicamikrosphären (SMPs) als Träger für Metallnanopartikel (NP) entwickelt. Diese neuartigen Substrate bieten den Vorteil, dass Sie Analysen in allen Raumrichtungen ermöglichen, mehrere Resonanzen zeigen, kostengünstig synthetisiert werden können und in verschiedenen Lösungen verwendet werden können. Sie adressieren somit einige der Einschränkungen herkömmlicher SERS-Substrate.

Darüber hinaus beschäftigt sich diese Doktorarbeit mit der erweiterten Datenanalyse in SERS- und Raman Spektroskopie, welche zu Schwierigkeiten bei der Interpretation der Daten führen können. Um subtile spektrale Unterschiede zu identifizieren und damit die Interpretation der Daten zu verbessern wird fortgeschrittene (multivariate) Datenanalyse angewendet. Die Optimierung und Aufrechterhaltung der Leistungsfähigkeit sowie der Kalibrierungsstabilität von Spektrometern im Laufe der Zeit ist jedoch entscheidend für eine zuverlässige Dateninterpretation. Dafür wird ein Qualitätsfaktor eingeführt, der die Anpassung zwischen theoretisch berechneter und experimentell gemessener spektraler Auflösung repräsentiert. Dieser wird auf ein, im Rahmen der Dissertation verwendetes, kommerzielles Spektrometer angewendet.

Zusammenfassend befasst sich diese Arbeit mit zentralen Herausforderungen in der Raman-Spektroskopie und verbessert letztendlich deren Anwendbarkeit und Praktikabilität.

Table of Contents

Publication list

1 **Ashutosh Mukherjee**, Anita Lorenz, Marc Brecht, *Determination and monitoring of quality parameters: a detailed study of optical elements of a lens-based Raman spectrometer*, Applied spectroscopy, 76, 2, **2021**.
DOI: 10.1177/00037028211055148

2 Miriam C. Bassler, Mona Stefanakis, Elena Gerhard Hartmann, **Ashutosh Mukherjee**, Almoatazbellah Youssef, Rudolf Hagen, Agmal Scherzad, Manuel Stöth, Edwin Ostertag, Maria Steinke, Marc Brecht, Stephan Hackenberg, Till Jasper Meyer, *Differentiation of salivary gland and salivary gland tumor tissue by Raman imaging combined with multivariate data analysis*, Diagnostics, 14, 1, 92, **2024**.
DOI: 10.3390/diagnostics14010092

3 **Ashutosh Mukherjee**, Quan Liu, Frank Wackenhut, Fang Dai, Monika Fleischer, Pierre-Michel Adam, Alfred J. Meixner, Marc Brecht, *Gradient SERS substrate with multiple resonances for analyte screening: Fabrication and SERS applications,* Molecules, 27, 16, 5097, **2022**.
DOI: 10.3390/molecules27165097

4 Akanksha Dohare, Swathi Sudhakar, Björn Brodbeck, **Ashutosh Mukherjee**, Marc Brecht, Andreas Kandelbauer, Erik Schäffer, Hermann A- Mayer, *Anisotropic and Amphiphilic Mesoporous Core–Shell Silica Microparticles Provide Chemically Selective Environments for Simultaneous Delivery of Curcumin and Quercetin*, Langmuir, 37, 45, 13460–13470, **2021**.
DOI: 10.1021/acs.langmuir.1c02210

5 Alexandra Wagner, Stefanie Wagner, Jan-Erik Bredfeldt, Julia Steinbach, **Ashutosh Mukherjee**, Sandra Kronenberger, Kai Braun, Andreas Kandelbauer, Hermann A. Mayer, Marc Brecht, *Chemical imaging of single anisotropic polystyrene/poly (methacrylate) microspheres with complex hierarchical architecture,* Polymers, 13, 9, 1438, **2021.**
DOI: 10.3390/polym13091438

6 **Ashutosh Mukherjee**, Frank Wackenhut, Akanksha Dohare, Anke Horneber, Anita Lorenz, Hendrik Müchler, Alfred J. Meixner, Hermann A. Mayer, and Marc Brecht, *Three-Dimensional (3D) Surface-enhanced Raman Spectroscopy (SERS) substrates Fabrication and SERS Application*, The Journal of Physical Chemistry C, 127, 28, 13689–13698, **2023**.
DOI: 10.1021/acs.jpcc.3c02410

7 **Ashutosh Mukherjee**, Frank Wackenhut, Alfred J. Meixner, Hermann A. Mayer, and Marc Brecht, *Three-Dimensional (3D) Surface-Enhanced Raman Spectroscopy (SERS) Substrates for Sensing Low Concentration Molecules in Solutions*, MDPI Nanomaterials, 14, 21, 1728, **2024**.
DOI: 10.3390/nano14211728

Declaration of Contribution

Erklärung nach § 5 Abs. 2 Nr. 8 der Promotionsordnung der Math.-Nat. Fakultät

-Anteil an gemeinschaftlichen Veröffentlichungen

Declaration according to § 5 Abs. 2 No. 8 of the PhD regulations of the Faculty of Science

-Collaborative Publications-

Nr.	**Accepted Publications YES or NO**	List of Authors	Position of candidate in the list of authors	Scientific ideas by the candidate (%)	Data generation by the candidate (%)	Analysis and Interpretation by the candidate (%)	Paper writing done by the candidate (%)
1	**YES**	**Ashutosh Mukherjee**, Anita Lorenz, Marc Brecht	1	90	100	70	90
2	**YES**	Miriam C. Bassler, Mona Stefanakis, Elena Gerhard Hartmann, **Ashutosh Mukherjee**, Almoatazbellah Youssef, Rudolf Hagen, Agmal Scherzad, Manuel Stöth, Edwin Ostertag, Maria Steinke, Marc Brecht, Stephan Hackenberg, Till Jasper Meyer	4	15	10	15	10

3	**YES**	**Ashutosh Mukherjee**, Quan Liu, Frank Wackenhut, Fang Dai, Monika Fleischer, Pierre-Michel Adam, Alfred J. Meixner, Marc Brecht	1	60	50	80	80
4	**YES**	Akanksha Dohare, Swathi Sudhakar, Björn Brodbeck, **Ashutosh Mukherjee**, Marc Brecht, Andreas Kandelbauer, Erik Schäffer, Hermann A- Mayer	4	20	20	30	20
5	**YES**	Alexandra Wagner, Stefanie Wagner, Jan-Erik Bredfeldt, Julia Steinbach, **Ashutosh Mukherjee**, Sandra Kronenberger, Kai Braun, Andreas Kandelbauer, Hermann A. Mayer, Marc Brecht	5	10	10	10	30
6	**YES**	**Ashutosh Mukherjee**, Frank Wackenhut, Akanksha Dohare, Anke Horneber, Anita Lorenz, Hendrik Müchler, Alfred J. Meixner, Hermann A. Mayer, and Marc Brecht	1	80	90	80	80
7	**YES**	**Ashutosh Mukherjee**, Frank Wackenhut, Alfred J. Meixner, Hermann A. Mayer, and Marc Brecht	1	80	90	80	80

Nomenclature

2D	Two-dimensional
3D	Three-dimensional
ACS	Ammonium carbonate
AFM	Atomic force microscopy
Ag	Silver
Au	Gold
BG	Background
BG acc	Background accumulated
BPE	1,2-bi-(4-pyridyl) ethylene
BLZ	Blaze wavelength
BPO	Benzoyl peroxide
CARS	Coherent anti-Stokes Raman spectroscopy
CCD	Charge-coupled device
CRM	Confocal Raman microscopy
CS	Core-sell silica particle
CTAB	Cetyltrimethylammonium bromide
Cur	Curcumin
CVD	Chemical vapor deposition
DA	Discrimination analysis
DACF	Diffraction and aberration correction factor
DCS	Dumbbell silica-core-shell particle
DMSO	Dimethyl sulfoxide
DNA	Deoxyribonucleic acid

DRIFT	Diffuse reflectance infrared Fourier transform
EDMA	Ethylene di-methacrylate
EDX	Energy dispersive X-ray
EF	Enhancement factor
EM	Electromagnetic
EMCCD	Electron-multiplying charge-coupled device
FIB	Focused ion beam
FISH	Fluorescence in-situ hybridization
FWHM	Full width at half maximum
FN	Facet normal
Gly	Glycerin/Glycerol
GMA	Glycidyl methacrylate
GN	Grating normal
HE	Haematoxylin and eosin
IR	Infrared
LO	Longitudnal Optical
LSP(R)	Localized surface plasmon (Resonance)
MB	Methylene blue
MerTMS	Mercapto-trimethoxysilane
MTT	3-(4, 5-dimethyl thiazolyl-2)-2, 5-diphenyltetrazolium bromide
MVA	Multivariate data
N.A.	Numerical aperture
NMR	Nuclear magnetic resonance
NP(s)	Nanoparticle(s)
PBS	Phosphate-buffered saline

PC(s)	Principal component(s)
PCA	Principal component analysis
PL	Photoluminescence
PS	Polystyrene
PSF	Point spread function
PVA	Poly (vinyl alcohol)
Q	Quality factor of Raman spectrometer
QT	Quercetin
RI	Raman imaging
RR	Resonance Raman
RT	Room temperature
RNA	Ribonucleic acid
mRNA	Messenger ribonucleic acid
SD	Spectrometer design
SDS	Sodium dodecyl sulfate
SEM	Scanning electron microscopy
SERS	Surface-enhanced Raman spectroscopy
SGT	Salivary gland tumor
SIM	Structured illumination microscopy
SMP(s)	Silica microsphere(s)
SMP@Ag	Silica microspheres with silver nanoparticles
SNR	Signal-to-noise ratio
SPM	Scanning probe microscopy
SP(R)	Surface plasmon (Resonance)
SR	Spectral resolution

STED	Stimulated emission depletion
STEM	Scanning transmission electron microscopy
STM	Scanning tunneling microscopy
TEOS	Tetraethyl orthosilicate
mTEOS	Mercapto modified tetraethyl orthosilicate
TERS	Tip-enhanced Raman spectroscopy
UHTS	Ultra-high throughput screening
UVA	Univariate data analysis
VCA	Vector component analysis
WHO	World Health Organization

List of Symbols

$2d$	Second-order overtone of graphene/graphite D peak
a	Angle between incidence and GN
α	Include angle
b	Angle between reflection and FN
$\vec{B}$	Magnetic induction or Flux density
b_{img}	FWHM of the entrance slit or pinole
b_{limit}	Smallest value of FWHM at pinhole/slit width
b_{ent}	Slit/Pinhole width
c	Radius of spherical NP
$\mathrm{C}^{13}/\mathrm{C}^{15}$	Carbon isotopes
CH_2	Raman peaks of hydrocarbon groups
$\mathrm{C}-\mathrm{O}$	Raman peaks of carbon-oxygen
d	Grating Groove Density
D	Dielectric displacement
ε	Dielectric function of a medium or dielectric constant
ε_m	Dielectric Constant of the surrounding medium
$\varepsilon(s)$	Dielectric Constant of spherical NP
ε_0	electric permitivity
σ_{RS}	Cross-section of Raman
σ_{SERS}	Cross-section of SERS
ϵ	Relative permeability
ϵ_0	magnetic permeability
$E, \overrightarrow{E_i}$	Electric field (vector)

E_0	Electric field Amplitude
E_{loc}	local field amplitude at the active Raman site
E_F	Fermi level of metal
E_M	Energy level of material
ΔE	Energy difference
EF_{max}	Maximum enhancement factor
EF_{min}	Minimum enhancement factor
EF_{avg}	Average enhancement factor
f	Focal length of the spectrometer $(\mathrm{f}_1\ or\ \mathrm{f}_2)$
G	Grating grooves(/lines)
G'/G^*	Raman peak of Graphene/Graphite
ħ	Planck's Constant
H	Magnetic field
$I(\omega_\mathrm{i})$	intensity of excitation source (laser)
$I_{HOTSPOT}$	Spectral intensity of a certain peak at the bright regions (hotspots)
$I_{SUBSTRATE}$	Spectral intensity of a certain peak on the substrate
J_f	External current density
k	Wave vector
$L(\omega)$	Electromagnetic Enhancement Factor
$L(\omega_\mathrm{i})$	Electromagnetic Enhancement Factor of the incident field
$L(\omega_\mathrm{v})$	Electromagnetic Enhancement Factor of scattered field
L_{SP}	Electromagnetic Enhancement Factor of surface plasmon
L_{LR}	Electromagnetic Enhancement Factor of LSPR
λ	Wavelength of incident field (laser)

λ_B	Blaze wavelength
m	Diffraction order
m_e	Mass of free electrons
M	System Magnification (f_2/f_1)
η	Refractive index
n_e	density of free electrons
N	Number of stokes active scatterers
$\vec{p}$	induced electric dipole vector
P_s	Power of scattered beam
Q	Quality Factor
r_{airy}	Laser spot size
rpm	Rotations per minute
ρ_f	External charge density
S_0	Ground electronic state
$Si-O$	Raman peaks corresponding to silicon-oxygen
SiO_2	Silicon-di-oxide
SH	Characteristic Raman peak of mercapto sulphur-hydrogen
t	Time
T_i	Signal intensity of SMPs
T_0	Scattered light intensity through a bare glass slide
T_L	Intensity of the halogen lamp
T_D	Dark intensity of the spectrometer
θ_B	Blaze Angle
θ_0	Angle between dipole moment and direction $(\hat{x}, \hat{y}, \hat{z})$

μ, μ_s	Molecular polarizability
v, v_0, V	Equilibrium of the vibrational molecule
ω	Frequency
ω_a	Angular frequency
ω_i	Frequency of incident field (laser)
ω_v	Frequency of scattered field
$\Delta\omega$	Spectral resolution (SR)
ω_L	Absolute wavelength of excitation source (laser)
ω_p	Plasma frequency
ω_R	Raman wavenumber shift
$\Delta\omega_D$	Frequency difference between incident and scattered field
Δx	Spatial Resolution
$\Delta x_{confocal}$	Spatial Resoultion in confocal confocal microscope
$\hat{x}$	Spatial dimension/direction in x
$\hat{y}$	Spatial dimension/direction in y
Δz	Depth Resolution
$\Delta z_{\mathrm{confocal}}$	Depth Resolution iin confocal microscope
$\hat{z}$	Spatial dimension/direction in z

List of Equations

List of Figures

List of Tables

Introduction

Raman spectroscopy is a highly valuable analytical technique with multiple applications across various scientific domains. It uses inelastic light scattering to provide information about a sample's chemical composition without damaging it.[1] It is unique because it generates data without sample preparation or labeling. This is particularly beneficial for samples whose original composition may be altered during preparation.[2–5] This quantitative technique correlates the intensity of the signal directly with the concentration of the material and is versatile enough to evaluate solids,[6, 7] liquids,[8–10] and gases,[10, 11] making it an essential analytical tool for researchers in diverse study domains.

However, Raman spectroscopy has some limitations that need to be considered. Analytes with a small cross-section can be challenging to obtain inelastic light scattering, making the technique less effective. Additionally, it can be challenging to detect and analyze samples with low analyte concentrations due to the technique's reduced sensitivity and low SNR. The spatial resolution in Raman spectroscopy is also limited by Abbe's diffraction limit, which is approximately half the wavelength of the incident light.

A growing demand for enhanced sensitivity and resolution in Raman spectroscopy prompts the development of various methodologies.[11–16] One approach is plasmonics, which is responsible for advancing the sensitivity of Raman signal detection.[16–18] Plasmonics are the electron oscillations in metal nanostructures due to electromagnetic (EM) wave excitation. On plasmonic active NPs, strong electric fields are produced by localized surface plasmons (LSPs), which are the primary cause of this signal enhancement. Based on plasmonics, SERS increases the Raman signal strength by 10^5–10^{10} times, making it possible to surpass the detection limit.[19–21] SERS can detect concentrations as low as a single molecule, overcoming a significant drawback of Raman spectroscopy.[22–26]

Sample preparation represents a considerable worry and effort for a successful SERS acquisition. A specific arrangement of plasmonic metal NPs, known as a SERS sample or SERS substrate, is required to achieve maximum enhancement of the Raman signal. Several SERS substrates are available in the market, including surface-

roughened films,[27, 28] colloidal NPs,[29, 30] metal/metal island films,[31–34] and uniform SERS substrates.[35–37]

However, SERS has some drawbacks, including substrate reproducibility, surface fouling, background interference signals, restricted analyte selectivity, small detection volume, and cost-effectiveness. Addressing these issues is essential to improving SERS's applicability and making it more widely usable in different sample types like solids, liquids, and gases.

Adaptable, reproducible, cost-effective substrates must be designed and developed to improve SERS's applicability. This thesis addresses the challenges faced in improving SERS application and eventually demonstrates the fabrication of suitable SERS substrates to overcome them. Furthermore, the research explores methods to enhance spectrometer performance and advanced data interpretation techniques.

1. Theoretical and Scientific Principles

This chapter explores the theoretical and scientific principles that form the basis of research in this thesis. These principles offer a robust framework for comprehending and analyzing the experimental results. They help clarify the core ideas behind the study and contribute to the broader knowledge in the field.

1.1. Applications of Raman Spectroscopy

Raman spectroscopy has significantly contributed to various fields, revolutionizing scientific research and industry applications. This analytical technique, based on the inelastic scattering of photons, has profoundly impacted the world in several ways. The goal of this section and the following list is to examine the diverse uses of Raman spectroscopy in different scientific fields:

1. Materials Science:

Raman spectroscopy has revolutionized materials science by providing valuable insights into the composition,[38–40] structure,[41, 42] characterization of polymers,[43–46] nanomaterials,[47–49] semiconductors,[50–53] catalysts,[54–56] composite materials,[57–59] identification of phases,[60–62] monitoring of crystallographic changes,[63–66] detection of impurities,[67–70] and defect analysis.[71–73] It also allows for the investigation of stress/strain effects,[74, 75] and the determination of vibrational modes and phonon dispersion.[76–78]

2. Biology and Biomedical Research:

Due to its non-destructive nature and ability to provide label-free molecular information, it is widely employed for studying cells, tissues, biomolecules, and biofluids.[79–83] Raman spectroscopy enables the identification and characterization of biomolecules such as proteins,[74, 84, 85] nucleic acids,[75, 86, 87] lipids,[88–90] and carbohydrates.[91, 92] It facilitates the detection of disease biomarkers, analysis of cellular processes, and monitoring drug interactions with cells and tissues.[93, 94] It also plays a crucial role in cancer research, aiding in identifying tumor margins, understanding cellular transformations, and assessing drug efficacy.[95–97]

3. Chemistry:

Raman spectroscopy plays a vital role in chemical analysis and identification. It is used for the qualitative and quantitative analysis of chemical compounds, even in complex mixtures.[98, 99] Raman spectroscopy monitors chemical reactions in real-time, molecular dynamics,[100–104] and intermolecular interactions.[105, 106]

4. Pharmaceutical Analysis:

Raman spectroscopy has found extensive applications in the pharmaceutical industry. It is used for drug discovery,[107–110] formulation analysis,[111] and quality control.[112–114] Raman spectroscopy enables the identification and quantification of active pharmaceutical ingredients and excipients,[115, 116] analysis of polymorphism,[117] investigation of drug-polymer interactions,[118–120] and monitoring of drug release profiles.[121, 122] It offers rapid and non-destructive analysis, making it an attractive pharmaceutical research and development tool.

5. Environmental Analysis:

Raman spectroscopy plays a crucial role in environmental monitoring and analysis. It allows identifying and quantifying pollutants,[123–126] analysis of aerosols and particulate matter.[127–129] Raman spectroscopy can detect and analyze complex mixtures of organic and inorganic compounds, providing insights into environmental contamination, chemical transformations, and pollutant sources. It is also employed for the analysis of minerals,[130–132] rocks,[133–135] and geological samples,[136, 137] aiding in the understanding of Earth's processes.

6. Geology and Planetary Science:

Raman spectroscopy plays a crucial role in geology and planetary science by providing valuable insights into the composition and mineralogy of geological samples. It is employed in the analysis of meteorites,[138–140] lunar samples,[141, 142] and other extraterrestrial materials,[143, 144] providing insights into the geological processes and conditions on other planets and moons. In planetary science, Raman spectroscopy has been employed in space missions to analyze the composition of extraterrestrial surfaces, such as Mars and the Moon, contributing to understanding planetary geology and the potential presence of critical minerals essential for assessing habitability.[145–151]

7. Forensic Science:

Raman spectroscopy finds applications in forensic science for analyzing and identifying trace evidence,[152–154] illicit drugs,[155, 156] and counterfeit detection,[157, 158] moreover, legally questioned documents. It helps characterize fibers, paints, inks, and other materials encountered in forensic investigations.[159–162] Raman spectroscopy's ability to provide rapid and non-destructive analysis assists in examining crime scene samples, identifying unknown substances, and differentiating genuine and counterfeit products.

8. Art and Cultural Heritage:

Raman spectroscopy's non-destructive nature makes it particularly valuable for analyzing precious and fragile artworks. It has become essential in studying and preserving art and cultural heritage artifacts.[163, 164] It aids in the identification of pigments,[165–167] dyes,[168, 169] binders and varnishes,[170] and other materials used in the artwork. Raman spectroscopy enables the characterization of layers.[166] It also identifies degradation products and assesses the effects of environmental factors on cultural artifacts.

9. Nanotechnology:

Nanotechnology extensively uses Raman spectroscopy to characterize and analyze nanomaterials and nanostructures. It enables the investigation of size-dependent properties,[171–173] SERS,[174–176] and plasmonic effects in NPs.[177, 178] Raman spectroscopy is used to study nanomaterials such as carbon nanotubes,[179, 180] 2D materials,[181–183] 0D materials,[184, 185] nanowires.[186–188] It provides valuable information on their structural properties, chemical composition, and functionalization.

10. Food and Agriculture:

Raman spectroscopy is used in the food and agriculture industries for quality control, authentication, and analysis of food products.[189–191] It can detect pollutants, contaminants, and the presence of allergens in food.[192–194] It also aids in studying the molecular changes occurring during food processing, ripening, and storage.

These applications showcase the versatility of Raman spectroscopy, making it a valuable tool for researchers and professionals across diverse scientific and industrial disciplines. Despite its numerous applications, Raman spectroscopy still faces

challenges regarding sensitivity, SR, and sample requirements, which are discussed in later sections. Continued advancements in instrumentation and techniques further enhance its capabilities and broaden its potential applications in the future.

1.2. Basic Principles of Raman Spectroscopy

Raman spectroscopy, named after its discoverer, C.V. Raman, was first observed in 1928. Raman spectroscopy is a type of vibrational spectroscopy used to investigate a system's vibrational, rotational, low- and high-frequency modes. It is based on monochromatic light's inelastic also called Raman scattering, typically scattered by a laser in the visible, near-infrared, or near-ultraviolet ranges. When laser light interacts with molecular vibrations, phonons, or other system excitations, the energy of the laser photons is shifted up or down. The energy shift reveals information about the system's vibrational modes. There are two ways to explain Raman spectroscopy: quantum theory and classical theory.

1.2.1. Quantum Theory

The quantum theory of Raman spectroscopy provides a profound understanding of the underlying principles governing the interaction of light with matter. At its core, Raman spectroscopy relies on the scattering of photons when they interact with various materials, including crystalline and amorphous solids, liquids, and gases. Consider photons with energy $\hbar\omega_i$ is incident on a material, and the molecules are excited from the ground to a virtual energy state (green arrow, as shown in Figure 1.1). The molecule can relax elastically, known as Rayleigh scattering (Figure 1.1(a)), and inelastically, known as Raman scattering. Raman scattering results in photons being scattered by the molecules with different energies than the incident photons, either $\hbar(\omega_i - \omega_v)$ (Stokes scattering, red arrow as shown in Figure 1.1(b)) or $\hbar(\omega_i + \omega_v)$ (anti-Stokes scattering, blue arrow as shown in Figure 1.1(c)). Here, ω_v corresponds to a molecule's vibrational frequency or a crystal's phonon frequency.

This energy shift ($\hbar(\omega_i \pm \omega_v)$) is the basis of Raman spectroscopy; the amount of energy transferred from the incident photons to the molecules is determined by the transition probability, a function of the energy difference between the molecule's initial and final states. Thus, the frequency of the scattered photons is determined by the energy difference between the molecule's initial and final states, also called the Raman shift.

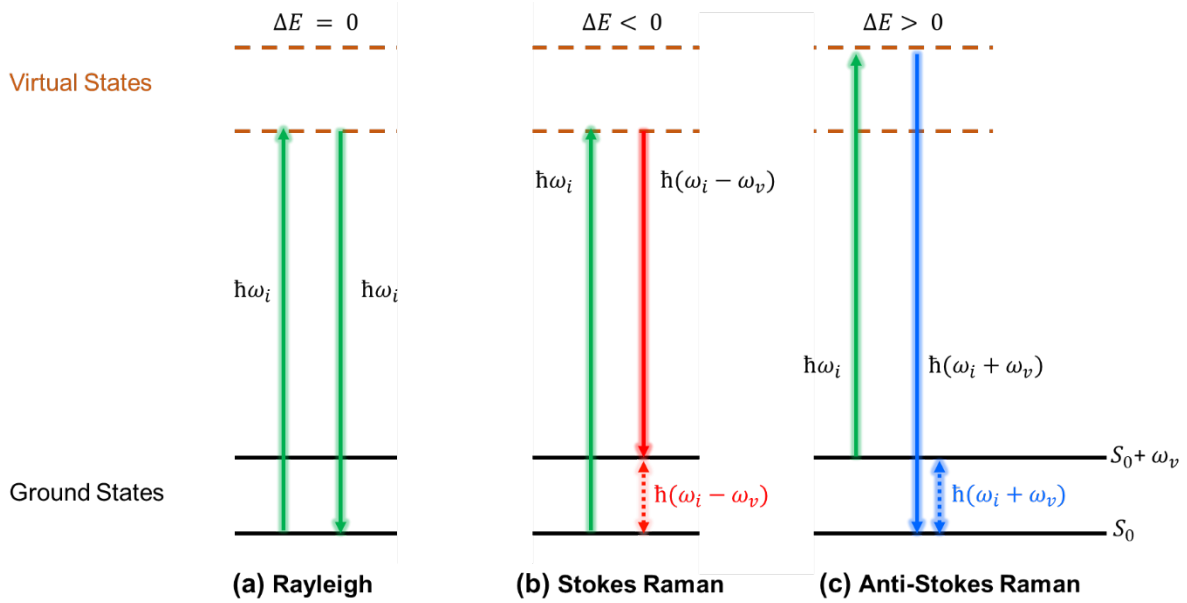

Figure 1.1: The energy diagram for (a) Rayleigh, (b) Stokes Raman, and (c) anti-Stokes Raman scattering processes. The energy disparity between the incident and dispersed light is shown by the symbol ΔE. The incident photon's energy is indicated by the green arrow heading upward. In contrast, the downward arrow indicates a photon's energy gain or loss.

Quantum mechanics, as described in the quantum theory of Raman spectroscopy, provides a more comprehensive and precise explanation of the observed spectral shifts and intensities. While the classical theory of Raman spectroscopy offers a valuable qualitative framework for understanding the phenomenon, it does not delve into the quantum mechanical details of the scattering process.

However, classical theory is still a valuable tool for understanding the basics of Raman spectroscopy. It provides straightforward concepts that help explain the basic working principle of Raman spectroscopy, which will be discussed in the next section.

1.2.2. Classical Theory

Central to the classical theory of Raman spectroscopy is the concept of polarizability. Polarizability is a measure of how easily the electron cloud of an atom or molecule can be distorted in response to an external electric field.

In Raman spectroscopy, the vibrational modes of molecules, which involve the periodic motion of atoms within the molecule, give rise to changes in polarizability and are responsible for Raman scattering. The incident photons can either lose energy (Stokes scattering) or gain energy (anti-Stokes scattering) during the scattering process. The energy difference is related to the vibrational energy levels of the molecule, resulting in the Raman shift.

The origin of the scattering radiation is an induced electric dipole ($\vec{p}$) in a material. The classical theory of Raman scattering can be described as follows:

$$\vec{p} = \mu\overrightarrow{E_\iota} \qquad \textit{Eqn. 1}$$

Where $\vec{p}$ is an induced electric dipole vector induced by an external electric field $\overrightarrow{E_\iota}$– electric field vector characterized by its vector amplitude E_0 of the incident radiation and oscillation frequency ω_i.

The proportionality factor between the external field and the induced dipole moment in Eqn. 1 is the molecular polarizability μ. The real part of the electric field is expressed as,

$$\overrightarrow{E_\iota}(t) = E_0 \cdot \cos(\omega_i t) \qquad \textit{Eqn. 2}$$

The polarizability (μ) of a molecule changes with its vibrational motion. To mathematically describe this effect, the polarizability is expressed as a Taylor series expansion centered around the equilibrium nuclear geometry denoted by v.

$$\mu = \mu(v) = \mu_0 + \sum_{v=1}^{N}\left[\left(\frac{\partial\mu}{\partial v}\right)_{v_0} \cdot v + \frac{1}{2}\left(\frac{\partial^2\mu}{\partial v \partial v'}\right)_{v_o v_0'} \cdot v \cdot v' + O(v^3)\right]_1^N$$

or,

$$\mu(v) = \mu_0 + \left(\frac{\partial\mu}{\partial v}\right)_0 \cdot v + \frac{1}{2}\left(\frac{\partial^2\mu}{\partial v \partial v'}\right)_0 \cdot v^2 + \cdots \qquad \textit{Eqn. 3}$$

Where v is the vibrational normal coordinate of the molecule, μ_0 is the polarizability at equilibrium and $\left(\frac{\partial \mu}{\partial v}\right)_0$ is the first derivative of the polarizability for v at equilibrium.

For simplicity, only the first-order term in the expansion is considered by assuming small displacements,

$$\mu(t) = \mu_0 + \left(\frac{\partial \mu}{\partial v}\right)_0 \cdot v(t) \qquad \textit{Eqn. 4}$$

Consequently, vibrations with a specific vibrational frequency denoted as ω_v can be stimulated along sinusoidal wave function for a simple harmonic oscillator as,

$$v(t) = v_0 \cdot \cos(\omega_v t) \qquad \textit{Eqn. 5}$$

Where v_0 is the amplitude of the vibrational motion, and ω_v is the molecular vibration frequency.

Substituting in polarizability expression that is Eqn. 5 in Eqn. 4,

$$\mu(t) = \mu_0 + \left(\frac{\partial \mu}{\partial v}\right)_0 \cdot v_0 \cdot \cos(\omega_v t) \qquad \textit{Eqn. 6}$$

The time-dependent induced dipole moment $\vec{p}(t)$ from Eqn. 1 is given by

$$p(t) = \mu(t) \cdot E_i(t) \qquad \textit{Eqn. 7}$$

Substituting, $\mu(t)$ from Eqn. 6 and $\overrightarrow{E_i}(t)$ from Eqn. 2 in Eqn. 7,

$$p(t) = \left[\mu_0 + \left(\frac{\partial \mu}{\partial v}\right)_0 \cdot v_o \cdot \cos(\omega_v t)\right] \cdot E_0 \cdot \cos(\omega_i t) \qquad \textit{Eqn. 8}$$

Expanding Eqn. 8 gives,

$$p(t) = \mu_0 \cdot E_0 \cdot \cos(\omega_i t) + \left(\frac{\partial \mu}{\partial v}\right)_0 \cdot v_o \cdot E_0 \cdot \cos(\omega_v t) \cdot \cos(\omega_i t) \qquad \textit{Eqn. 9}$$

Applying trigonometric identity $\cos(A)\cos(B)$ to second summand in Eqn. 9,

$$\cos(A)\cos(B) = \frac{1}{2}[\cos(A+B) + \cos(A-B)] \qquad \textit{Eqn. 10}$$

Therefore, Eqn. 9 can be rewritten using Eqn. 10 as,

$$p(t) = \mu_0 \cdot E_0 \cdot \cos(\omega_i t) + \frac{1}{2}\left(\frac{\partial \mu}{\partial v}\right)_{v_0} \cdot v_o \cdot E_0 \cdot \cos(\omega_i + \omega_v)t + \frac{1}{2}\left(\frac{\partial \mu}{\partial v}\right)_{v_0} \cdot v_o \cdot E_0 \cdot \cos(\omega_i - \omega_v)t \qquad \textit{Eqn. 11}$$

This equation (Eqn. 11) forms the fundamental principle of Raman scattering when viewed as a notable instance of general light scattering. In this context, the time-varying induced dipole moment, serving as a secondary radiation source, comprises three separate components.

In the final form, the first summand of Eqn. 11 corresponds to Rayleigh scattering, oscillating at the same frequency as the incident radiation. The second is anti-Stokes Raman scattering, representing a source of blue-shifted radiation to laser frequency. The third one is Stokes-Raman scattering, as the induced dipole moment oscillates at a frequency lower than the laser frequency.

1.2.3. Classical Selection Rule

The classical theory of Raman spectroscopy provides an understanding of the principles governing Raman scattering selection rules. These rules determine the molecular vibrational modes that exhibit Raman activity by relying on symmetry principles and variations in the polarizability tensor components associated with distinct vibrational modes.[195]

Inelastic scattered light arises from a situation where there is a non-zero derivative of electronic polarizability concerning the equilibrium geometry along the v^{th} normal coordinate, represented as,

$$\left(\frac{\partial \mu}{\partial v}\right)_{v_0} \neq 0 \qquad \textit{Eqn. 12}$$

The present relationship establishes a selection rule for Raman scattering, which is fundamental in distinguishing between molecules active in Raman scattering and those active in infrared (IR), that is,

$$\left(\frac{\partial \mu}{\partial v}\right)_{v_0} = 0 \qquad \textit{Eqn. 13}$$

To initiate the discussion, the focus is on the vibrational behavior of the symmetric stretching of a diatomic molecule, as shown in Figure 1.2(a). This particular molecule lacks a permanent dipole moment when in its equilibrium geometry. Even when subjected to minor variations, the derivative of the dipole moment remains zero. This renders the vibration IR inactive but Raman active, as Figure 1.2(a) depicts.

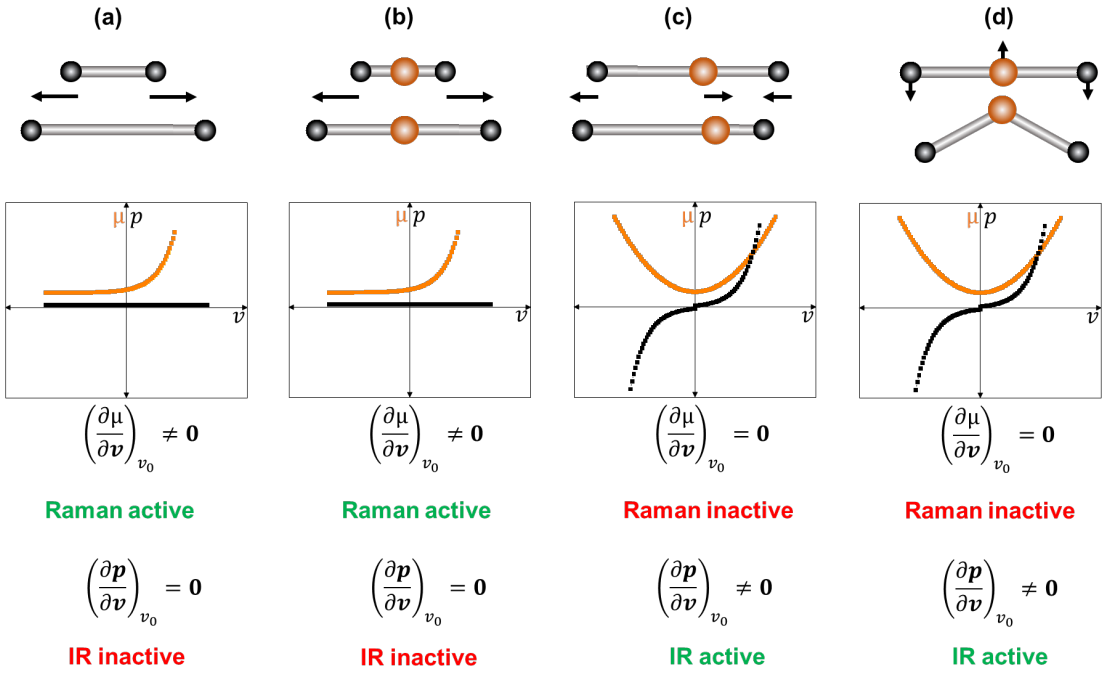

Figure 1.2: Schematics (not to scale) of the derivates of polarizability (black) and dipole moment (orange) are depicted for normal modes of (a) two atomic molecules, (b), (c), and (d) for three nuclear molecules. [Figure adapted and modified from T. Dieing, O. Hollricher, J. Toporski, Confocal Raman Microscopy (Springer, Heidelberg, London, 2011)].[196]

Studying linear triatomic molecules can become intricate, particularly in molecular dipole moment and polarizability. To simplify the analysis, consider these molecules as the sum of bond dipole moments and bond polarizability in a first-order approximation. Figure 1.2(b) demonstrates that the dipole moment remains constant during symmetric stretching vibration due to opposite, identical bonds. This leads to the molecule being IR inactive and Raman active.

However, the situation changes when asymmetric stretching and bending are considered, as depicted in Figure 1.2(c) and Figure 1.2(d). In these cases, the dipole moment changes sign as the system moves through the equilibrium configuration, rendering both vibrations IR active. While non-zero changes in polarizability occur along these modes, they are symmetric when the reaction coordinate sign is inverted.[196]

Hence, for small displacements, the changes in polarizability are harmonic and can be assumed, making both stretching and bending vibrations Raman inactive.

1.3. Instrumentation for Raman spectroscopy

Understanding the instrumentation of Raman spectroscopy is crucial for experimental design, instrument optimization, data interpretation, troubleshooting, method development, and collaboration. Several factors must be considered to ensure optimal results when setting up a Raman spectroscopy experiment. These include laser power and wavelength selection, SR, SNR, and integration time. The choice of these parameters depends on the sample's nature, the desired sensitivity level, and the spectral features of interest.

Knowledge of the instrumentation improves the quality of measurements and advances understanding of Raman spectroscopy. In the subsequent section, an extensive exploration of the instrumentation employed in Raman spectroscopy is presented. With a focus on the working principle of a Raman spectrometer and confocal Raman microscopy (CRM)/spectroscopy, hyperspectral Raman imaging is discussed.

1.3.1. Working principle of Raman setup

The Raman signal is often weak; therefore, optimizing the Raman spectrometer to achieve the best results is essential. An optimized Raman setup is necessary for improved sensitivity, SR, accurate analysis, reduced interference and artifacts, reproducibility, comparability, and expanded application capabilities. This allows researchers to get reliable results, explore various scientific applications, and gain insights into molecular structures and chemical compositions. This section explores the working principle of a Raman setup designed to illuminate, collect, and detect Raman-scattered light. Figure 1.3 illustrates the schematics of the working principle of the Raman setup.

The Raman setup is divided into different compartments: the excitation, microscope, and spectrometer, as shown in Figure 1.3.

(a) Excitation

Figure 1.3(a) shows schematics of an excitation compartment that consists of a laser as an illumination source and a laser-line filter that allows only a narrow band of

wavelength to pass through it. This laser line filter also suppresses sidebands that might overlap with and interfere with Raman lines, ensuring accurate detection.

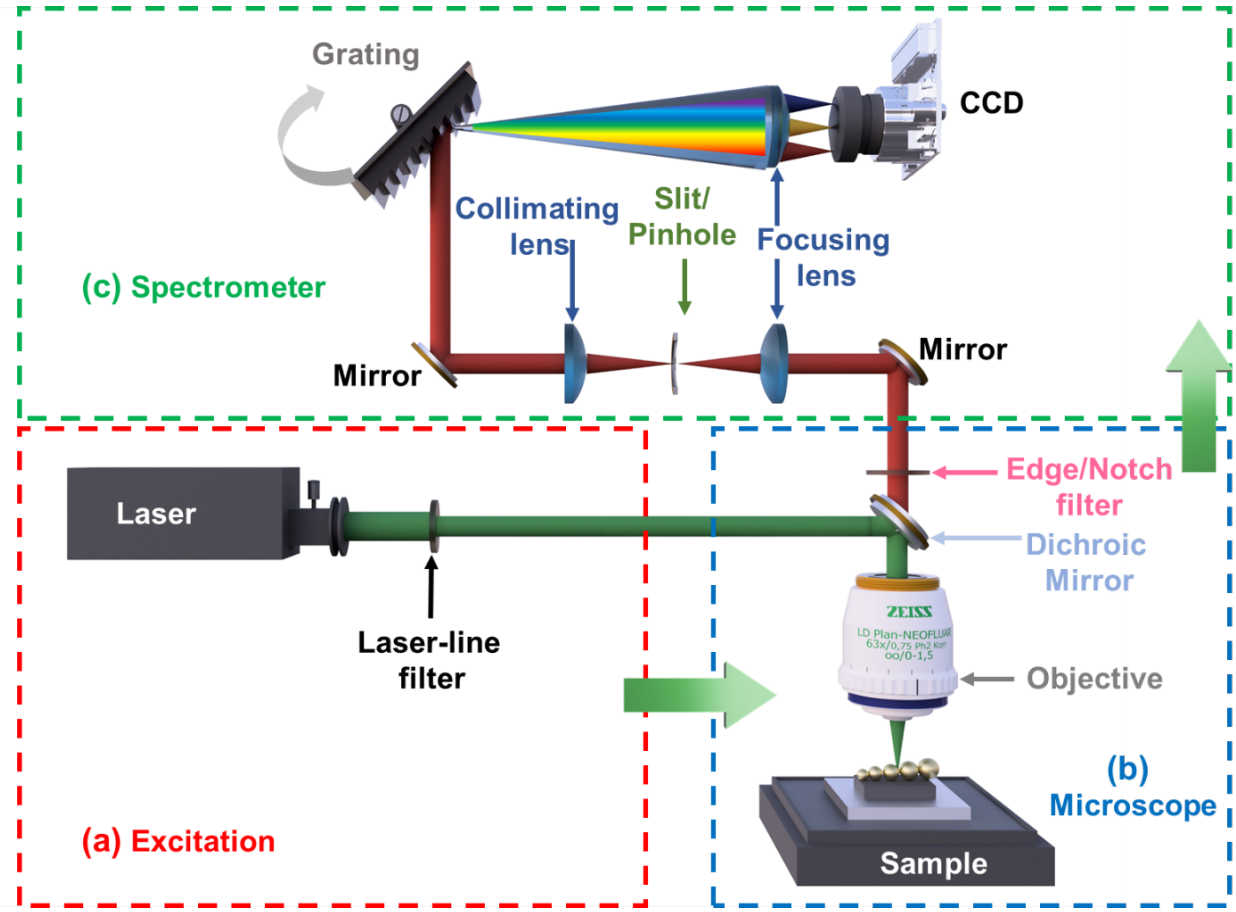

Figure 1.3: Depicts schematics (not to scale) outlining the operational concept of a standard Raman spectrometer, (a) the excitation compartment comprising a laser source and a laser-line filter, selectively permitting a particular wavelength to pass (b) presents the microscope compartment, featuring an edge/notch filter, an objective lens, and a sample holder/sample stage and, (c) illustrates the spectrometer compartment, tracing the optical path of the scattered Raman signal from the pinhole, through the grating, and to the CCD detector.

The Raman signal's intensity is directly proportional to the laser frequency, which is related to ω_v^4. Consequently, shorter laser wavelengths result in a stronger Raman signal than longer ones. Moreover, the use of shorter excitation wavelengths enhances the spatial resolution by Abbe's diffraction limit given by,

$$\Delta x = 0.61 \cdot \frac{\lambda}{N.A.} \qquad \textit{Eqn. 14}$$

Where Δx represents the shortest distinguishable distance between two points, λ is the laser's wavelength, and N.A. is the numerical aperture of the objective used. Spatial resolution is distinguishing two separated point-like objects from a single object. The point spread function (PSF) measures an optical system's resolving power, mainly determined by the objective lens. The narrower the PSF, the better the resolution. In practical Raman spectroscopy applications, it is crucial to use a laser with specific properties that can provide optimal results. The laser should have a Gaussian beam shape, a narrow spectral bandwidth of less than 1 cm^{-1}, and a stable frequency of less than 0.01 cm^{-1} variation. Additionally, it is essential to ensure that the laser has stable intensity, and the excitation power should be carefully selected to avoid thermal decomposition caused by absorption.

After the laser is emitted from its source, it passes through a laser line filter, which can be placed in the excitation compartment. A laser line filter is an optically engineered, dielectric, thin-film interference device with a carefully designed multilayer coating on a transparent substrate. The filter efficiently suppresses transmission across other spectral regions through selective interference, allowing only the targeted laser emission to pass with minimal dispersion and negligible spectral distortion.

(b) Microscope

This section, as shown in Figure 1.3(b), consists of optical elements that efficiently coupling the laser to the microscope, such as a dichroic mirror or beam-splitter, an objective that focuses the light onto a particular spot on the sample, and a sample stage to position the sample. The components are further discussed below.

- Microscope coupling

The critical coupling of the excitation(Figure 1.3(a)) compartment with the microscope (Figure 1.3(b)) is a cornerstone in advanced microscopy applications. Figure 1.3(b) demonstrates the laser beam's precise coupling to the microscope through a dichroic mirror or beam splitter. A crucial feature of this mirror or splitter is its reflective capability, which is finely tuned to maximize the excitation laser wavelength while ensuring high transmission for Raman scattered light.

- Objective lens

The microscope objective lens, a crucial optical component, is essential to microscopes. It focuses light on the specimen and collects the detected signal. Designed to

provide high-resolution and magnified images of microscopic objects, the quality and N.A. of the objective lens determine the microscope's resolving power (given by the Abbes diffraction limit as shown in equation Eqn. 14) and the ability to distinguish fine details within the specimen.

- Interaction with the Sample

The interaction of laser light with a sample results in various processes, including transmission, absorption, scattering, and reflection. In Raman spectroscopy, most of the incident light undergoes elastic scattering, known as Rayleigh scattering. However, only a tiny fraction of the light interacts with the molecules in the sample and undergoes inelastic scattering or Raman scattering. The objective lens then collects the Raman and Rayleigh scattered light for detection.

To effectively suppress the Rayleigh scattering and enhance the detection of Raman scattering, detection filters such as notch filters or edge filters are employed, as shown in Figure 1.3(c). Edge filters, also known as long-pass or short-pass filters, use specialized coatings or interference effects to transmit light above or below a cutoff wavelength while blocking the other side. In contrast, notch filters selectively suppress specific laser lines by creating destructive interference with specialized coatings or structures, drastically reducing transmission in the stopband. These filters can reduce the laser line intensity by up to six orders of magnitude.

(c) Spectrometer

The optical coupling between the microscope (Figure 1.3(b)) and spectrometer (Figure 1.3(c)) compartments is again critical since it has to serve several functions. The scattered light from the microscope must be coupled into the entrance slit of the spectrometer. This is achieved by implementing a focusing lens that focuses the collimated Raman scattered light from the microscope into the entrance slit, as shown in Figure 1.3(c). The light must be efficiently coupled into the entrance slit; a higher divergence than the acceptance angle of the entrance slit results in massive losses, and a smaller divergence results in a reduced resolution because the grating will be only partially illuminated. Efficient coupling can be achieved by selecting a pinhole or slit size that matches the diameter of the PSF on the image side of the objective lens. The correct pinhole size in spectroscopy depends on the trade-off between SR and SNR, with

smaller pinholes offering higher SR but potentially lower signal intensity and larger pinholes allowing more signal intensity but lower SR.[196]

Figure 1.3(c) shows the grating is another crucial spectrometer component. It disperses the signal onto the charge-coupled device (CCD) detector by directing each wavelength at distinct angles. The number of grooves or lines per millimeter determines the dispersion characteristics. The higher the number of lines, the higher the SR, and vice versa. Gratings are typically “blazed” to optimize the efficiency for a particular wavelength. The gratings are angled to reach 80% of the efficiency for the first diffraction order.

The CCD is a fundamental component in the Raman spectrometer; the working principle involves the conversion of incoming photons into electrical charge, which is then digitized to produce Raman spectra. The CCD consists of a grid of pixels, each capable of storing an electrical charge proportional to the number of photons it receives. As photons impact the CCD's surface, they generate electron-hole pairs within the silicon lattice of the pixels. The electrons are collected in potential wells beneath each pixel, creating an electrical charge proportional to the incident light intensity at that wavelength. After a predetermined integration time, the CCD undergoes readout, during which the accumulated charge in each pixel is sequentially measured and converted into digital values. These values are then used to construct the Raman spectrum.[196]

The significance of CCDs in Raman spectroscopy lies in their high sensitivity, enabling the detection of weak Raman scattered photons. This sensitivity is crucial for studying low-concentration analytes or samples with low cross-sections. It also contributes to the SR, allowing for the precise identification and characterization of molecular vibrations in materials. CCDs are indispensable for real-time, high-quality Raman measurements, facilitating applications in numerous fields of science. Optimizing an instrument is crucial for achieving consistent, reproducible, and optimal results, and this performance should be upheld over an extended period.

Further details on this topic are outlined in Chapter 4, which describes this method in detail.[1]

[1] Explained in Chapter 4

1.3.2. Raman Imaging

Raman imaging is an advanced analytical microscopy technique that visualizes the distribution of molecular components in a sample. It combines Raman spectroscopy and microscopy to create a single instrument. Adding a Raman setup to a microscope allows for chemical analysis. It is called Raman imaging, which is when spectral data is combined with spatial information across two or three dimensions. One effective method is systematically moving a sample underneath a laser-focused measuring area. This results in collecting spectral data across the sample surface, effectively creating a Raman data cube.

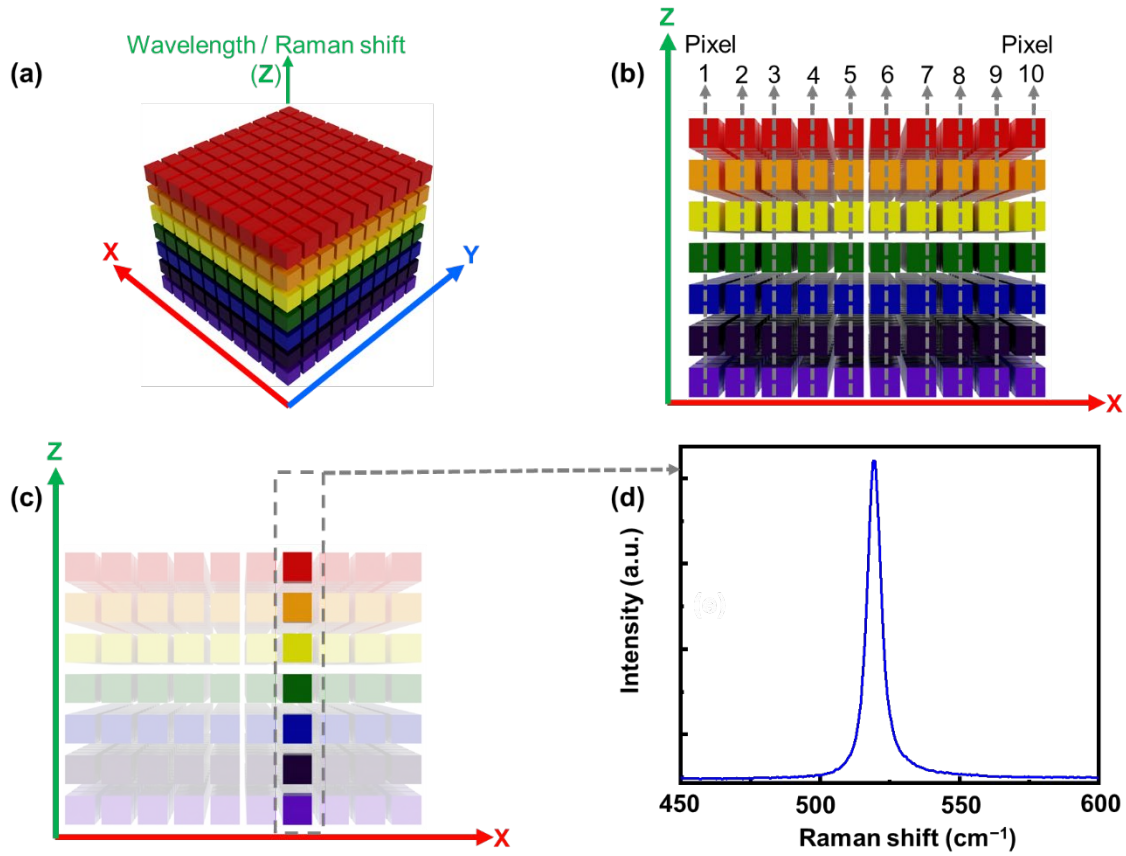

Figure 1.4: (a) Schematics (not to scale) showing the orthographic view of a Raman data cube (also known as a data hypercube) of a 3D dataset, (b) Schematics (not to scale) showing a side view of the Raman data cube with several pixels marked. (c) Schematics (not to scale) the same Raman data cube as in (b) with a specific pixel highlighted. (d)Example of a Raman spectrum of silicon (Si) from the pixel marked in (c).

A Raman data cube, a data hypercube, is a 3D dataset. In this dataset, the X and Y axes represent the spatial coordinates of the sample, while the Z axis contains the spectral information (wavelength or Raman shift), as shown in Figure 1.4(a). When a sample is scanned, several pixels are acquired along a defined spatial grid. Each "pixel" in the XY plane corresponds to a specific spatial location on the sample, as depicted in Figure 1.4(b). For example, the highlighted pixel in Figure 1.4(c) contains chemical information combining all the wavelengths at that specific spatial position. This setup allows for the visualization of chemical composition across the sample's surface and provides insight into its chemical structure at each point; an example is shown in Figure 1.4(d), resulting in a volumetric dataset.

For instance, Figure 1.5 shows schematics of an excitation laser focused through an objective lens onto a lithographically designed silica (SiO_2)-silicon (Si) sample. This sample possesses a well-defined structure and exhibits straightforward Raman characteristic peaks, making it an ideal specimen for a comprehensive understanding of Raman imaging. It is highlighted by marked spots and arrows (illustrated in red). Each marked spot represents a ‘pixel,’ the spectral acquisition at each point as the sample stage moves. The laser precisely targets pre-defined sample locations while incrementally scanning the entire region of interest, creating a 3D Raman hypercube.

Figure 1.5(b) is an optical image of a SiO_2-Si sample, as shown in Figure 1.5(a) schematic. The image focuses on a specific area of interest where multiple pixels are arranged across a grid measuring 10 x 10 µm. This process generates a 3D Raman hypercube, each pixel representing the chemical composition at that position across all Raman shifts or wavelengths. A Raman spectrum acquired from a pixel covering the complete wavelength range from the hypercube is displayed in Figure 1.5(c). It shows a typical spectrum of a longitudinal optical (LO) phonon Si peak (with varying intensities) at 520.5 cm^{-1}. If a specific wavelength (Raman shift) or a range of wavelengths (Raman shifts) is chosen from the spectrum as indicated in Figure 1.5(c) (light green box), an intensity distribution map can be derived from that particular wavelength or wavelength range. Such an intensity distribution map is presented in Figure 1.5(d). Since the wavelength range is marked for the LO Si phonon peak at 520.5 cm^{-1}, the image obtained in Figure 1.5(d) is an intensity distribution image of Si present across the measured sample grid. In other words, it allows the visualization of chemical distribution with their intensity variations to be visually represented using grayscale or false

colors, as shown in Figure 1.5(d). This means that areas with higher Si intensity are visually represented with a false color indicating "high".

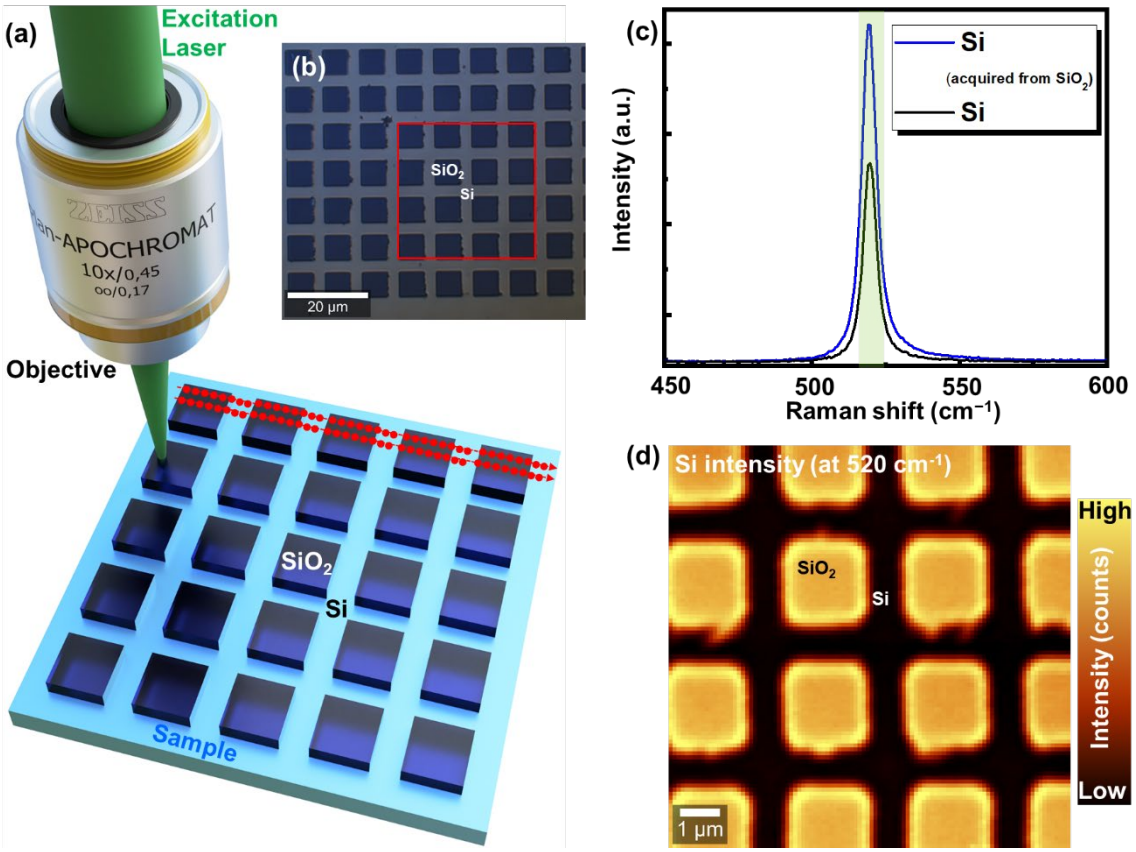

Figure 1.5: (a) Schematic (not to scale) representation of Raman imaging conducted on a lithographically designed sample with alternating silica (SiO_2) and silicon (Si) pitches. Highlighted by red indicators denoting the areas where Raman acquisition occurs as the sample stage moves beneath the laser beam focused through an objective lens. (b) Optical depiction of the SiO_2-Si sample, as indicated in (a), outlining the region subjected to Raman imaging, as demonstrated in (c), (c) Raman image of the SiO_2-Si sample as marked in (b) at the silicon peak (520.5 cm^{-1}), with (d) corresponding spectra of SiO_2 and Si derived from the specified regions in (c).

Meanwhile, regions with lower Si intensity are rendered with a false color denoting "low." Figure 1.5(d) depicts regions containing SiO_2 exhibiting a stronger Si signal. In contrast, areas devoid of SiO_2 display a lower Si intensity. This is also confirmed by their corresponding Raman spectra at their respective pixels from different regions in Figure 1.5(c). The diffraction of light ultimately limits the spatial resolution of the image, as stated in Eqn. 14. This visualization depicts the chemical distribution within the

sample with its intensity variations. Various parameters, including intensities of multiple peaks, peak shifts, ratios, and widths, generate Raman images.[2]

Acquiring an image necessitates capturing numerous pixels, potentially extending the overall measurement time, especially when dealing with spectra in thousands or millions. Sensitivity plays a pivotal role in expediting the acquisition of Raman images, allowing for shorter spectrum acquisition times. Therefore, optimizing the selection of the target sample, laser power, and optical efficiency is crucial for more rapid imaging acquisition. Additionally, carefully processing such massive data sets is a challenge, and advanced processing techniques should be used for such data sets.[3]

1.3.3. Confocal Raman Microscopy (CRM)

Confocal microscopy is an advanced optical imaging technique that enhances the ability to visualize specimens with exceptional clarity and resolution. Unlike traditional wide-field microscopy, which collects light from all sample depths and can result in blurred images due to out-of-focus light, confocal microscopy uses a spatial pinhole to focus on a single, defined plane within the specimen. This technique allows for precise imaging of thin optical sections by aligning the illumination and detection pathways, ensuring that only light from the focal plane reaches the detector. As a result, confocal microscopy produces high-resolution, high-contrast images with minimal background noise, making it ideal for detailed examination of fine structures and dynamic processes.

Figure 1.6 illustrates the optical path of a confocal microscope, emphasizing the confocal principle. A laser beam is directed through an objective lens and focused onto a specific point within the sample. The emitted or reflected light from this focal point is then collected by the same objective lens and passes through a pinhole. This pinhole selectively permits only in-focus light from the targeted focal plane to reach the detector, effectively blocking out-of-focus light from areas above or below the focal plane. This configuration enhances the microscope's optical sectioning capabilities, allowing

[2] Further explained in section 1.4
[3] Detailed explanation in 1.4.2

for high-resolution and high-contrast images by minimizing background noise and improving depth resolution.

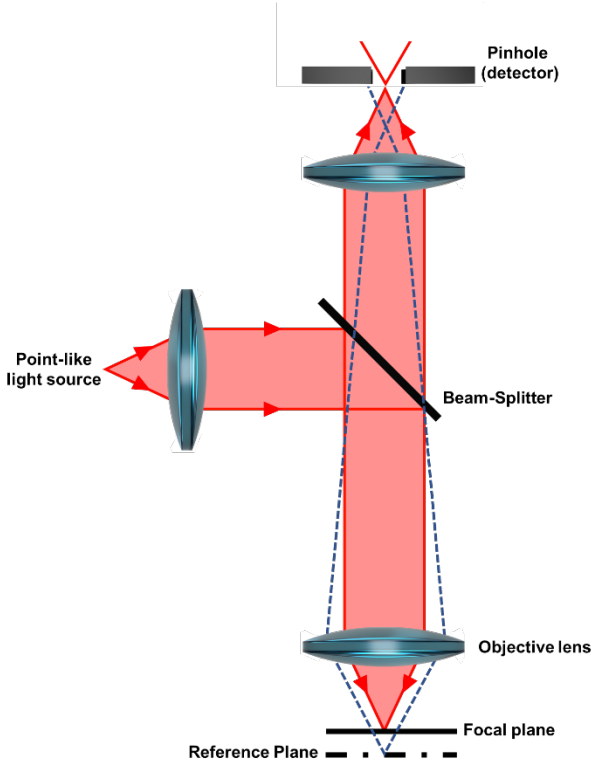

Figure 1.6: Schematics (not to scale) for principle setup of a confocal microscope [Adapted and modified from Figure adapted and modified from T. Dieing, O. Hollricher, J. Toporski, Confocal Raman Microscopy (Springer, Heidelberg, London, 2011)].[196]

Confocal volume is crucial in defining the specific region within the sample from which light is collected to form an image. This volume is typically shaped like an ellipsoid or toroid around the focal point of the objective lens, determined by the intersection of the focal planes of the illuminating laser and the detection pinhole. The confocal volume creates a well-defined 3D space where excitation and detection of light occur. Several factors influence the size and shape of the confocal volume, including the N.A. of the objective lens, the wavelength of the excitation light (λ), and the size of the confocal aperture.

Confocal microscopy is used in varied fields of science, including, in cell biology, precise confocal volume adjustment with a high N.A. lens and a small pinhole allows for the detailed imaging of fluorescently labeled proteins, such as GFP-tagged molecules.[197–200] Similarly, confocal microscopy in neuroscience enables the study of

calcium signals within dendritic spines, facilitating the analysis of synaptic activity.[201–205] In cell membrane research, confocal microscopy aids in imaging lipid molecules at specific depths, which is crucial for studying membrane dynamics.[206–209] In molecular biology, fluorescence in situ hybridization (FISH) benefits from confocal microscopy to enhance the detection of specific messenger ribonucleic acid (mRNA) molecules.[210, 211] In pharmacology, confocal microscopy allows for detailed analysis of receptor-ligand interactions.[212–214]

Conversely, confocal imaging, the combination of confocal microscopy and Raman imaging, is a powerful technique used in microscopy to obtain high-resolution and high-contrast images of samples by selectively imaging specific planes within the specimen, as shown in the example in Figure 1.7, and one that sets CRM apart in the field of microscopy.

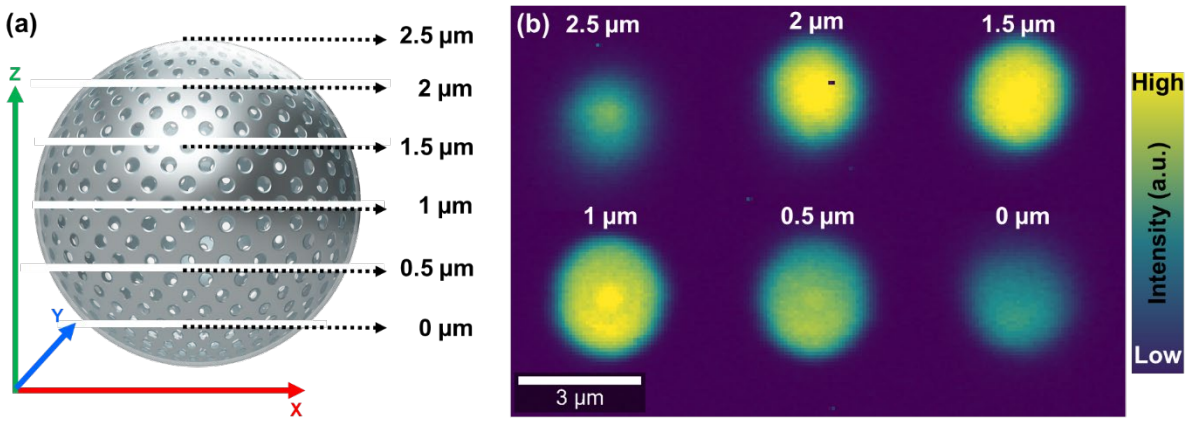

Figure 1.7: (a) Schematics (not to scale) illustrating a spherical silica particle with a diameter of 2.5 µm, functionalized with mercapto groups, positioned in a 3D space. It is segmented at 500 nm intervals, outlining the individual sections for confocal Raman imaging, as depicted in (b) and (b) Confocal Raman images captured from each of the sections indicated in (a) at the Raman shift of 2566 cm^{-1}, demonstrating the capabilities of 3D imaging.

Figure 1.7(a) provides a practical application of CRM in studying spherical particles. The schematic representations of a spherical mercapto-functionalized silica particle, segmented into six distinct planes, each separated by 500 nm, demonstrate the use of CRM for 3D imaging purposes. In Figure 1.7(b), corresponding Raman images captured at various depths, ranging from 2.5 µm to 0 µm, are displayed using CRM, with a focus on the intensity of the sulphur-hydron (SH) band of the mercapto group at 2566 cm^{-1}. Figure 1.7(b) illustrates that each section possesses a unique geometry

and shape attributable to the particle's spherical geometry. The particle's size varies at each section due to its spherical structure. As demonstrated in this study, CRM overcomes a fundamental limitation of conventional microscopy. It allows for sectioning and imaging at different depths without interference from neighboring sections, a feat impossible with conventional microscopy due to the detection of out-of-focus light and light from neighboring sections. This empirical evidence confirms the feasibility of comprehensive 3D imaging and underscores the superiority of CRM in this context.

Objective, N.A.	Δx	$\Delta x_{confocal}$	Δz	$\Delta z_{confocal}$
10x, 0.3air	1.10 µm	0.70 µm	11.8 µm	8.2 µm
20x, 0.4air	0.81 µm	0.53 µm	6.6 µm	4.6 µm
50x, 0.7 air	0.40 µm	0.30 µm	2.1 µm	1.5 µm
100x, 0.9 air	0.36 µm	0.23 µm	1.3 µm	0.9 µm
100x, 1.25 oil	0.25 µm	0.17 µm	1.0 µm	0.7 µm

Table 1: The data are based on Eqn. 14, Eqn. 15, Eqn. 16, and Eqn. 17 using wavelength 532 nm and η = 1 for air objectives and η =1.5 for oil objectives.

The spot size in CRM is defined by Abbe's diffraction limit shown in Eqn. 14, also denoted as the Airy disk radius or r_{airy}. Eqn. 14 represents spatial resolutions for a wide-field microscope (non-confocal system). For a confocal system, the pinhole/slit radius is smaller than r_{airy}, and hence the spatial resolution is given by,

$$\Delta x_{confocal} = 0.4 \cdot \frac{\lambda}{N.A.} \qquad \textit{Eqn. 15}$$

For depth resolution, the refractive index (η) between the lens and the specimen has to be considered apart from the N.A. and λ. The depth resolution (Δz) for a wide field microscope (non-confocal system) is given by,

$$\Delta z = 2\eta \cdot \frac{\lambda}{(N.A.)^2} \qquad \textit{Eqn. 16}$$

For a confocal system, the pinhole allows light only from the focal plane to pass to the detector; thus, the depth resolution (Δz) is given by,

$$\Delta z_{confocal} = 1.4\eta \cdot \frac{\lambda}{(N.A.)^2} \qquad \textit{Eqn. 17}$$

Table 1 compares wide-field microscope and confocal microscope resolutions (spatial/depth) for commonly used objectives in this work.

As mentioned earlier, in CRM, the pinhole (or aperture) plays a crucial role in improving spatial resolution and enhancing the quality of Raman spectra by suppressing background fluorescence. Figure 1.7 demonstrates how different pinhole widths affect Raman spectra. Figure 1.7(a)/(b) displays a Raman spectrum of diamond, which has a peak at 1334.4 cm^{-1} obtained using various pinhole widths: 100 µm, 50 µm, 25 µm, and 10 µm. When viewing the non-normalized graph in Figure 1.7(a), a larger pinhole allows more light to enter the spectrometer, which increases signal intensity. This comes at the cost of a reduced SNR and broader peaks.

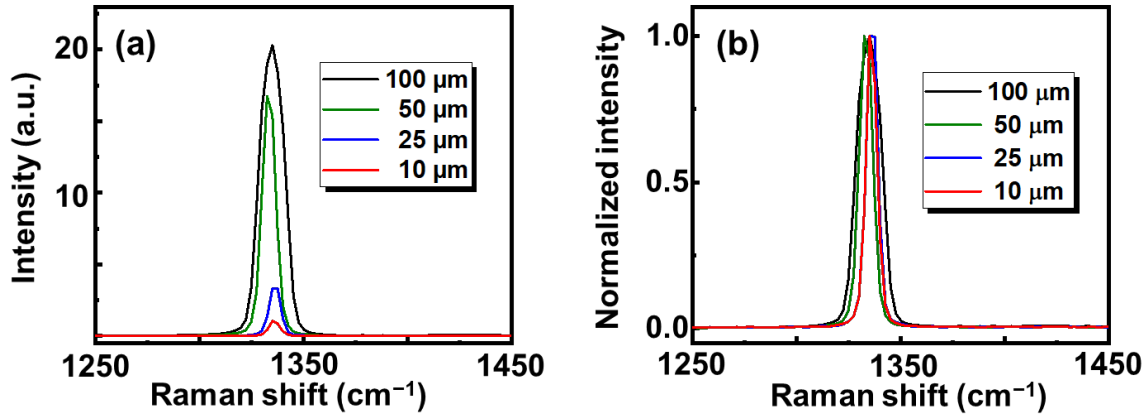

Figure 1.8: (a) Raman spectra of diamond obtained using various pinhole widths of 100 µm, 50 µm, 25 µm, and 10 µm, and (b) Raman spectra (normalized for intensity) of diamond acquired with different pinhole widths of 100 µm, 50 µm, 25 µm, and 10 µm.

Conversely, Figure 1.7(b) presents the normalized Raman spectra, showing that smaller pinholes, due to less light divergence, provide better SR with a narrower full width at half maximum (FWHM). This reduction in light divergence enhances the clarity and sharpness of the spectral peaks, which is crucial for distinguishing closely spaced Raman signals. Therefore, optimal pinhole alignment is essential for achieving high spatial and depth resolution in confocal microscopy. It ensures that only in-focus light from a precise volume is collected, minimizing background noise and enhancing the detection of fine structural details.[4]

[4] Elaborated in Chapter 4

1.4. Data Processing and Analysis

Confocal Raman imaging produces multidimensional datasets, encompassing aspects like spatial coordinates in 3D. To effectively visualize and interpret this multi-faceted data, dimensionality must often be reduced. For instance, when examining a single Raman image captured within a plane, the dataset can be simplified to two spatial dimensions: Raman shift and intensity. Image data analysis typically employs two primary approaches: univariate and multivariate data analysis (MVA). The univariate analysis (UVA) focuses on individual variables or factors independently. In contrast, MVA considers multiple variables, exploring their interrelationships, interactions, and dependencies. This section delves into understanding and describing UVA and MVA.

1.4.1. Univariate Data Analysis (UVA)

In UVA, each spectrum determines one value corresponding to each pixel in the image or images. UVA's primary objective is to describe and summarise the characteristics and distribution of the chosen variable. Filters or fitting procedures can determine the value of these pixels.

- **Filters**

UVA filters evaluate specific parts of the spectrum, such as integrated intensity, peak positions, widths, and intensity ratios. Each filter serves a particular purpose in characterizing and understanding the properties of the materials under investigation.[5]

Figure 1.9 and Figure 1.10 illustrate the filters used, with a graphene flake as the sample. This graphene flake, synthesized using chemical vapor deposition (CVD) with C^{13} and C^{15} carbon isotopes, exhibits two G peaks: G' for C^{13} and G* for C^{15}. The G peak is a unique graphene feature from C-C vibrations, as shown in Figure 1.9(a). Additionally, graphene's characteristic 2d peak, a double resonance peak, is depicted in the exact figure as '2d'. While another 2d peak exists for a different carbon isotope, it is omitted here for simplicity. It is essential to clarify that this example aims to

[5] Examples are shown in Chapter 7, 8, 9, and 10

demonstrate the applied filters and data processing without delving into detailed explanations of peak origins. The commonly used UVA filters are :

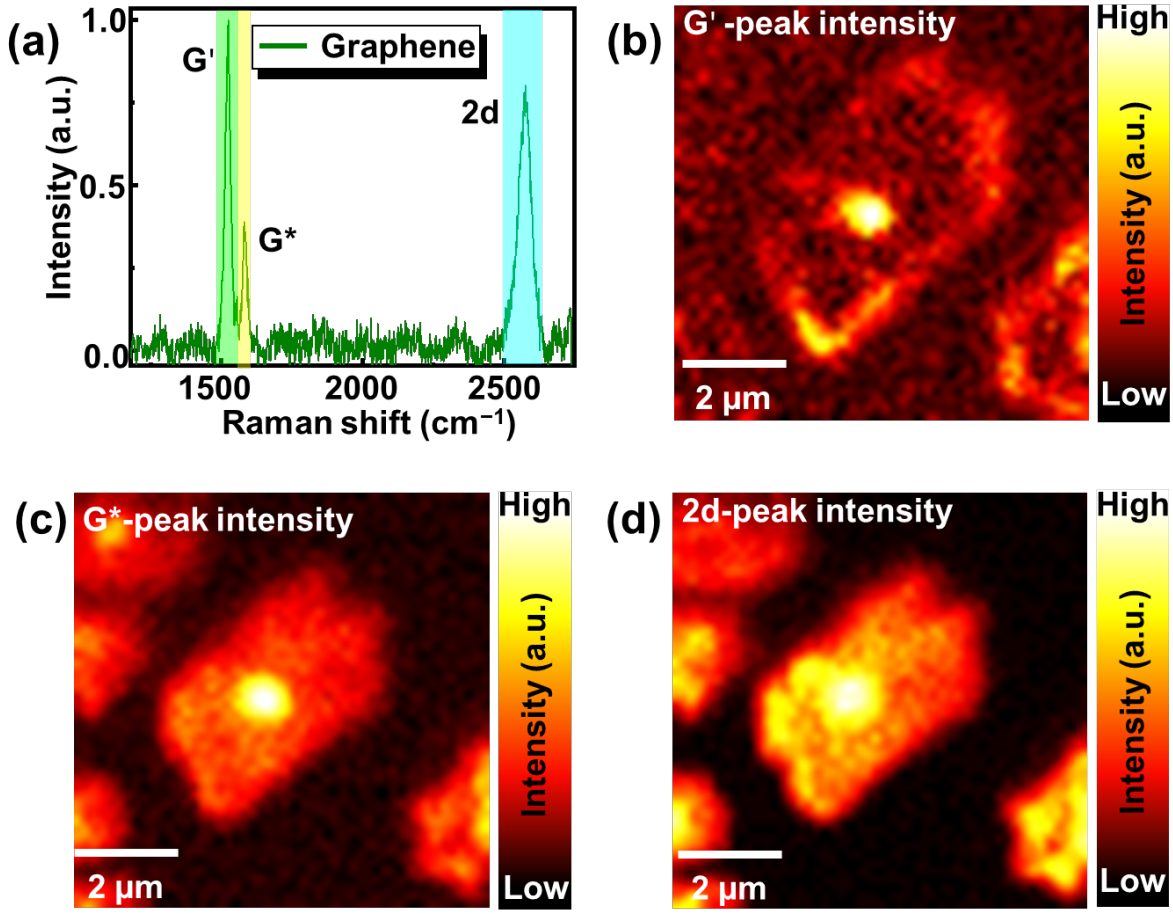

Figure 1.9: (a) Confocal Raman spectrum of graphene flake synthesized using CVD using two carbon isotopes C^{13} and C^{15}, (b) Confocal 2D Raman image showing the integrated peak intensity of G'-peak (at 1525 cm^{-1}) for the graphene flake, (c) Confocal 2D Raman image showing the integrated peak intensity of G-peak (at 1583 cm^{-1}) for the graphene flake, and (d) Confocal 2D Raman image showing the integrated peak intensity of 2d-peak (at 2580 cm^{-1}) for the graphene flake.*

1. Integrated intensity filter:[6]

An integrated intensity filter, a precise tool, measures the total area of a spectral peak as marked for each graphene peak G', G*, and 2d peaks. It calculates the sum of all intensity values within a specified spectral region. Integrated intensity filters, with their

[6] Examples are shown in Chapters 7, 8, 9, and 10

high level of precision, help quantify the amount of a particular chemical species or compound in a sample. By applying an integrated intensity filter, one can derive corresponding images for these specific peaks, as illustrated in Figure 1.9(b) for G', Figure 1.9(c) for G*, and Figure 1.9(d) for 2d. These images reveal the chemical distribution of distinct peaks with their intensity variations in different regions of the same graphene flake.

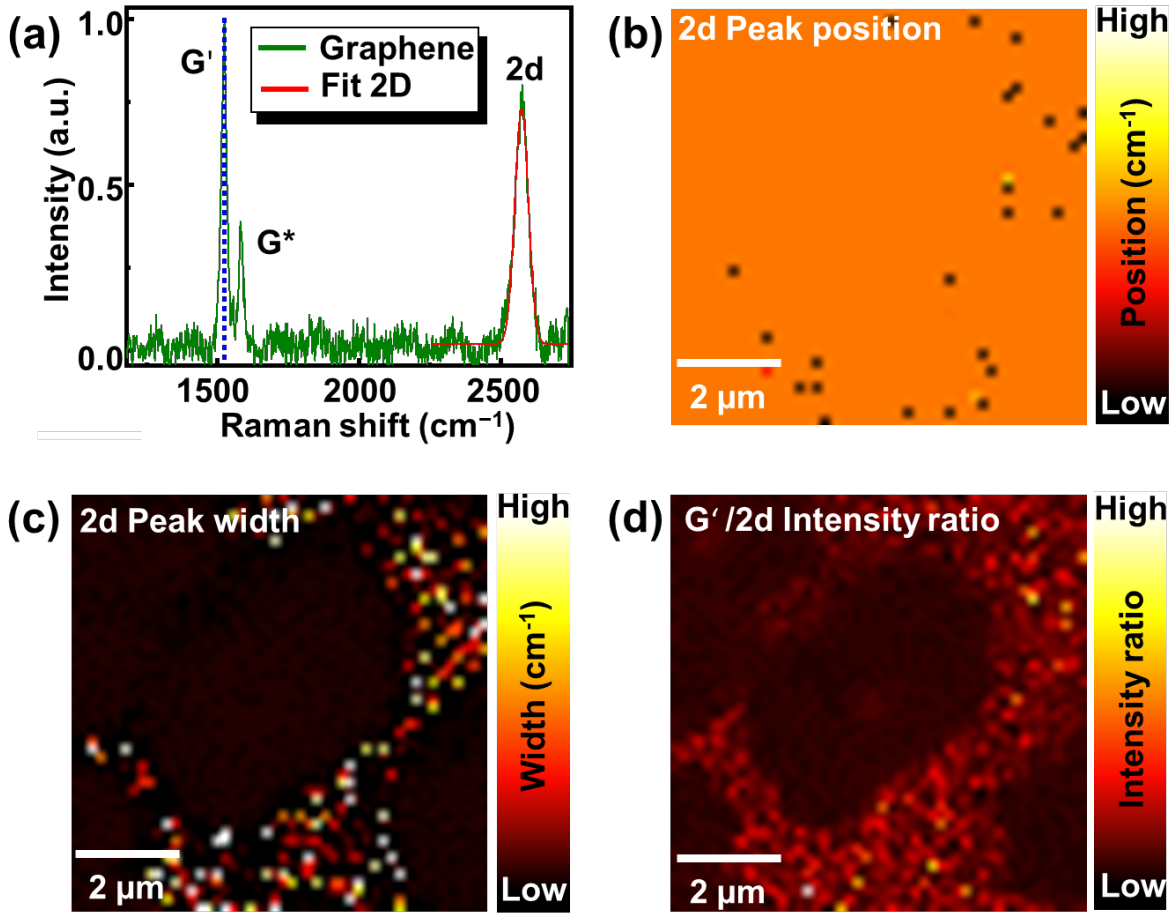

Figure 1.10: All figures are on the same graphene flake and spectra as shown in Figure 1.9, (a) Confocal Raman spectrum of graphene flake synthesized using CVD using two carbon isotopes C^{13} and C^{15}, (b) Confocal 2D Raman image showing the peak position of the 2d peak at 2580 cm^{-1}, (c) Confocal 2D Raman image showing the peak width of the 2d peak at 2580 cm^{-1} and (d) Confocal 2D Raman image showing the intensity ratio of G' to 2d.

2. Peak position filter:

Peak position filters are essential for identifying and characterizing chemical compounds based on their characteristic Raman shifts. It also signifies the stress/strain

within a material due to neighboring molecules or doping by identifying the peak position shifts.[215–218] The outcome of the peak position filter is obtained by fitting the peak under investigation, as shown in Figure 1.10(a)-Fit 2d-red curve. After fitting the curve, the resultant image is shown in Figure 1.10(b), suggesting that the peak position is uniform throughout the image except for minute shifts on the substrate.

3. Peak width filter:

A peak width filter characterizes the width of a spectral peak, often expressed as FWHM. FWHM measures the width of the peak at its half-maximum intensity point. Peak width filters play a pivotal role in assessing a material's degree of crystallinity and structural alignment, for example.[219] Materials subjected to stress or strain may exhibit non-uniform peak broadening. For instance, the fitted 2d peak and its corresponding image in Figure 1.10(c) are shown when examining the same graphene flake. The results indicate that the peaks are broader at the flake's edges. This phenomenon could be attributed to defects present at the edges, potentially experiencing stress from the underlying substrate or contamination from impurities in the environment, leading to the observed peak broadening.

4. Intensity ratio filter:[7]

An intensity ratio filter compares the relative intensities of two or more peaks within a spectrum. It calculates the ratio of peak heights or areas to assess the composition or changes in a sample. Intensity ratio filters are valuable for qualitative analysis and identifying specific chemical interactions or changes in a sample.[220, 221] For instance, in the graphene flake illustrated in Figure 1.10(d), the intensity ratio of G' to 2d is most pronounced at the substrate due to varying noise. The substrate has no peak but only noise, giving the variation pixels on the substrate, as shown in Figure 1.10(d).

- **Fitting filters**

Different filters, such as Gaussian, Lorentzian, and pseudo-Voigt functions, are commonly used in mathematical models. Gaussian functions analyze inhomogeneous broadening of peaks, while Lorentzian functions are for homogeneous broadening. The pseudo-Voigt[8] function combines Gaussian and Lorentzian functions to approximate

[7] Example shown in Figure 1.11
[8] Example shown in Figure 1.10(a)

the Raman peak line shape, which is typically Voigt-shaped. These filters are applied to experimental spectra to extract essential data such as peak position, width, intensity, and area.

1.4.2. Multivariate Data Analysis (MVA)

UVA might not suffice for intricate datasets. For example, the dataset in Figure 1.11 features a spherical silica particle functionalized with mercapto groups and secondary particles adhering to its surface. These modified silica particles are created by combining water and aqueous ammonium hydroxide (NH_4OH) in specific proportions and stirring continuously. Next, a syringe pump adds a mixture of tetraethoxysilane (TEOS) and mercapto-trimethoxysilane (MerTMS) in controlled ratios.

The composition and quantity of this mixture help control the particles' shape, size, and structure. After adding the silane mixture, the solution is stirred at room temperature for several hours. The solvent is then removed by washing with water and ethanol, and the spherical modified particles are dried in an oven. The resulting particles are non-porous, approximately 3 µm, and have mercapto functionalization. However, if the stirring time is prolonged, secondary particles may grow on the primary particles.[222, 223] These secondary particles may have the same functionalization as the primary particle or a different functionalization from one of the solution's components. Figure 1.11 shows such particles.

Figure 1.11(a)-shows the most prominent mercapto peak, SH peak intensity at 2566 cm^{-1}. A typical mercapto spectrum is shown in Figure 1.11(b). The SH peak's chemical distribution across the particle, as demonstrated in Figure 1.11(a), reveals uniform SH group distribution.

However, additional peaks resembling TEOS peaks were detected (at 167 cm^{-1}, 814 cm^{-1}, 1007 cm^{-1}, and 1263 cm^{-1}) as shown in Figure 1.11(c) marked as mercapto-modified TEOS or mTEOS. It is purposely named mercapto-modified TEOS or mTEOS because the prominent peaks of mercapto are still visible, for example, SH peak at 2566 cm^{-1} and CH_2 stretch peak at 2912 cm^{-1}. The possible explanation for the detection of TEOS is reaction by-products due to TEOS being used as a surfactant during particle synthesis. mTEOS peak is shown in Figure 1.11(c) and its corresponding

spectral image at CH_2 (ring) peak intensity at 1263 cm^{-1} is shown in Figure 1.11(e). It can be seen that the TEOS is mainly deposited on the secondary particles and only a few traces of it on the primary sphere. Understanding the spatial relationship between TEOS and mercapto distribution is essential, where UVA may prove less effective.

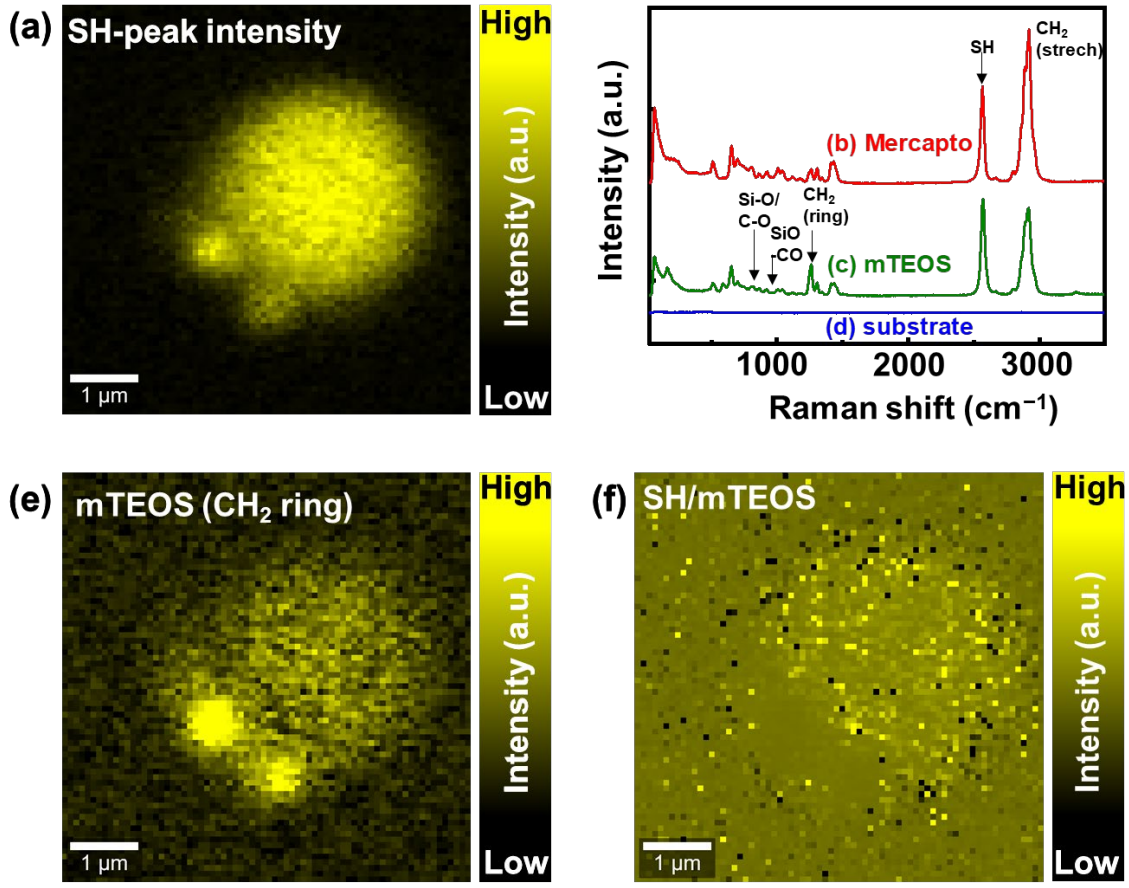

Figure 1.11: (a)Confocal 2D Raman image of mercapto functionalized spherical silica particle showing mercapto characteristic peak SH (at 2566 cm^{-1}), (b) Characteristic Raman spectrum of mercapto, (c) Characteristic mercapto Raman spectra modified with TEOS (d) spectrum of the glass substrate, (e) Confocal 2D Raman image of mercapto functionalized spherical silica particle showing another mercapto characteristic peak CH_2 ring (at 2912 cm^{-1}), and (f) Confocal 2D Raman image of mercapto functionalized spherical silica particle showing intensity ratio of SH and mTEOS.

Figure 1.11(f) shows a preliminary example of this understanding as the ratio of SH and mTEOS. MVA becomes crucial for complex datasets, simplifying high-dimensional data while retaining critical information.

MVA encompasses data collection, pre-processing, dimension reduction (principal component analysis (PCA)), statistical modeling, interpretation, visualization, decision-making, and validation. Techniques in MVA include PCA,[224] factor analysis, cluster analysis, multiple regression, discriminant analysis (DA), and vertex component analysis (VCA). Given the scope of the research, this thesis primarily focuses on explaining PCA principles.

- **Fundamentals of PCA**

Section 1.3.2 explained Raman imaging and the generation of a large hypercube with thousands of spectra.[9] This leads to the production of a massive amount of data. For example, consider the confocal 2D image of the mercapto-functionalized silica spheres shown in Figure 1.11. This image has a pixel resolution of 100 x 100 pixels, generating a 3D Raman datacube or hypercube containing 10,000 pixels. Consequently, there are 10,000 spectra in the hypercube, making it a vast dataset to analyze.

In Raman spectroscopy, each recorded spectrum can be represented as a single point within a high-dimensional space, where the number of dimensions corresponds to the number of CCD detector pixels (for example, 1600 pixels in this case). Each pixel along the detector represents an intensity value for a particular Raman shift, forming a vector that defines the spectrum in this high-dimensional space. When the spectrum contains a single Raman peak, it occupies a relatively small region of this space. However, when multiple Raman peaks are present, the complexity of the spectrum increases, and it spreads across more dimensions within the space.

PCA is a mathematical tool used to identify the fundamental directions in this high-dimensional space that capture the most significant variations in the data. These directions, referred to as principal components (PCs), describe the variance within the spectra and are orthogonal to one another.[10] The first few components typically account for the most essential features in the spectra, such as prominent Raman peaks, by ranking these components by the amount of variance they explain. Subsequent components describe progressively smaller variations, with the final components representing noise in the data. Thus, PCA effectively reduces the dimensionality of Raman spectral data while retaining the essential chemical information, allowing for more efficient data interpretation and noise reduction. This is particularly useful when analyzing

[9] Explained in 1.3.2
[10] Explained with examples in Chapter 5

complex mixtures, where the goal is to identify pure spectral components and minimize the influence of noise and less significant variations. It should be noted that PCA can only work if the data set is not dominated by noise. Otherwise, even the PCs with the highest Eigenvalues only describe the noise.[196]

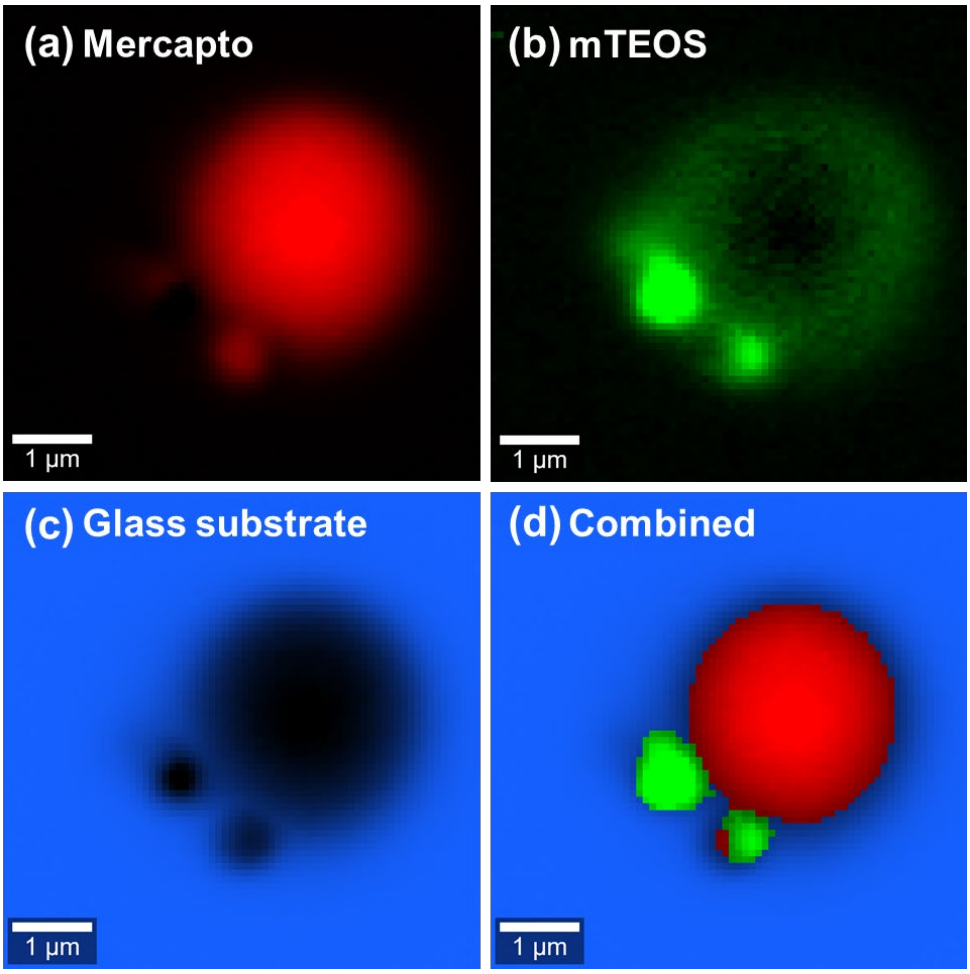

Figure 1.12: A recreated image of the data set shown in Figure 1.11 after performing PCA and reducing it to three main components explains 95% of the data set: (a) the Mercapto component, (b) the Mercapto component modified with TEOS, and (c) the Glass substrate component.

Following the PCA, one can extract a variety of results, such as:

1. **Reduced data set:** This study's PCA method represents 10,000 spectra. It is well-established that a relatively small number of PCs is sufficient to describe the complete dataset. In this case, only three PCs are required to capture 95% of the dataset's information. This implies that the dataset's dimensionality is reduced from 1600 to just three dimensions. This reduced dataset, comprised of only a few pixels, is then extracted for further analysis.

2. **Images of PCs:** Each of the spectra included in the analysis can be represented as a weighted combination of spectral components. Focusing on just one component would yield a single value for each image pixel, allowing the generation of a Raman image depicting the chemical distribution of that specific component within the dataset (if it is not correlated). The dataset presented in Figure 1.11 is reduced to only three components. When assigned a false color to each component and reconstructed the Raman image using these false colors. An illustration of this process is shown in Figure 1.12. Figure 1.12(a) represents the mercapto component, (b) shows the mTEOS component, and (c) depicts the glass substrate component.[11]

These separate component distributions enable the representation of the chemical distribution of each component within the image. It is also feasible to merge these false colors into a single image that accurately illustrates the relative abundance of a specific component compared to the others, as demonstrated in Figure 1.12(d). Figure 1.12(d) shows that the mercapto component is predominantly distributed throughout the microsphere, especially in the primary sphere. Some peaks of mTEOS are concentrated on the secondary particles. At the same time, the glass substrate dominates only on the substrate without the microspheres.

Performing such measurements on a confocal Raman microscope allows for sectioning, as demonstrated in Figure 1.7. Applying PCA to each section enables the creation of a 3D image that highlights the dominant components in a 3D volume, as depicted in Figure 1.13.

Figure 1.13(a) provides a practical application of CRM in studying spherical particles. The schematic representations of a spherical mercapto-functionalized silica particle, segmented into six distinct planes, each separated by 500 nm, demonstrate the use of CRM for 3D imaging purposes. Figure 1.13(b) reveals that at a depth of 1 µm, the secondary particle is minuscule and goes undetected, as does TEOS at 0 µm, which has entirely disappeared at 0 µm depth. At a depth of 0 µm, only the mercapto component dominates.

[11] Examples are shown in Chapters 5, 7 and 8

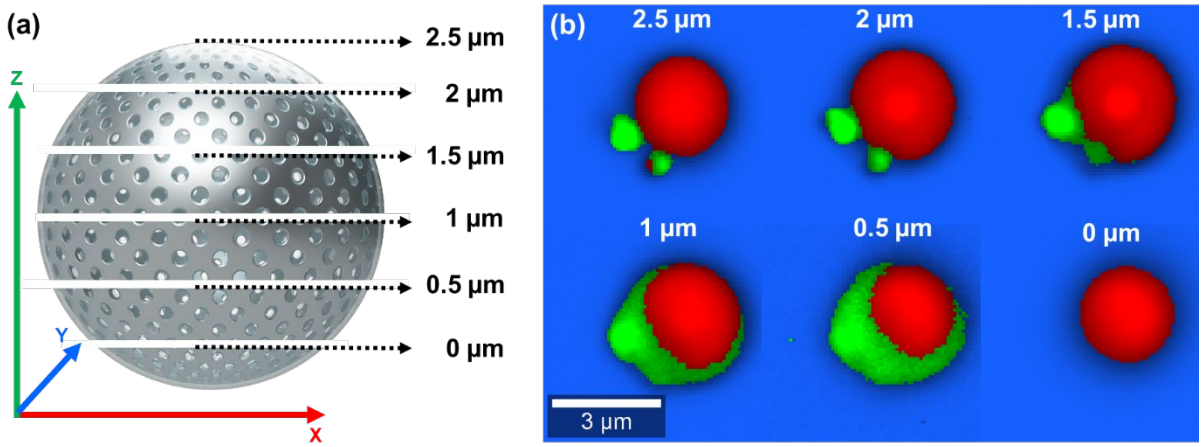

Figure 1.13: Confocal Raman images of the sectioning as demonstrated in Figure 1.7 to visualize each CRM section as a combined component of the silica particle in 3D space.

Combining CRM and PCA offers enhanced capabilities for visualizing dominant components' distribution in a 3D representation. This combination is precious for future scientific research, particularly in medicine and biology, as it provides new data analysis and interpretation perspectives. It emphasizes the need to move beyond UVA in research endeavors.

1.5. Key Factors of Raman Spectroscopy

Raman spectroscopy is a powerful analytical technique that offers numerous advantages for investigating molecular structures and chemical compositions. However, it has limitations, particularly concerning the challenge of weak signals. This sub-section explores Raman spectroscopy's key advantages, disadvantages, and limitations.

1.5.1. Advantages of Raman Spectroscopy

Chemical Specificity: It can differentiate between chemical compounds, including isomers and polymorphs, without complex sample preparation or labeling.

Non-Destructive: It allows for the analysis of samples without altering their integrity. This is particularly valuable when working with precious or irreplaceable materials.

Minimal Sample Requirements: Only a tiny sample makes it suitable for analyzing limited or precious materials. This is crucial in art conservation, forensics, and pharmaceutical research.

Versatility: application to various sample types, including solids, liquids, gases, and biological tissues.

1.5.2. Limitations of Raman Spectroscopy

Solution Sensitivity: In a solution, several challenges persist, including intensity fluctuations, aggregation, background interference, low SNR, molecular adsorption competition, signal averaging complexity, and reproducibility issues.[225] Techniques like SERS with careful sample preparation for SERS substrates are required to address this limitation.

Fluorescence Background: Fluorescence from the sample can overshadow Raman signals, making obtaining accurate results in the presence of fluorescence is challenging. Typical Raman scattering cross sections are usually more than ten orders of magnitude weaker than the fluorescent process:10^{-31} cm^2/molecule ≤ Raman cross section(σ_{RS}) ≤ 10^{-29} cm^2/molecule depending on whether the scattering is non-resonant or resonant.

SNR: Achieving a favorable SNR is crucial; noise can easily obscure weak signals, limiting the ability to detect and quantify analytes accurately.

1.5.3. Disadvantages of Raman Spectroscopy

Two main disadvantages of Raman spectroscopy are,

Raman spectroscopy struggles with **weak signals** from molecules with low Raman scattering efficiency, especially when analyzing trace amounts or dilute solutions. Extended acquisition times and advanced signal processing are advised to enhance the SNR. However, fluorescence interference complicates weak signal detection and quantification.

Additionally, Raman spectroscopy faces **spatial resolution** limitations due to the diffraction limit of light, which constrains the minimum spot size for sample focus. This limits its suitability for applications demanding ultra-high spatial resolution, such as specific nanomaterial characterization and sub-cellular imaging tasks.

Specific techniques exist to address the challenge of weak signals and the desire for high spatial resolution. Achieving this requires meticulous sample preparation or enhancing instrumentation capabilities.

1.6. Methods to Overcome Disadvantages

The primary drawback of this method is the limited strength of the Raman signal despite its potential to provide valuable and essential information about the material and its properties. Weak signals can lead to unreliable results, necessitating the development of techniques for enhancing these weak Raman signals. This need arises because Raman spectroscopy alone may prove insufficient for low-concentration analytes, solutions, or biological samples. Such intricate samples demand more advanced Raman spectroscopy methodologies for comprehensive and critical analysis. Over time, numerous approaches have been developed and discovered to address the issue of weak signals, with plasmonic activities garnering significant attention since the 1970s due to their intriguing optical properties, which ultimately serve to amplify the Raman signal. Here are some of the most commonly employed methodologies:

SERS:

When molecules are close to metal NPs, the EM field around the NPs enhances their Raman scattering. This method can provide signal enhancements of several orders of magnitude, making it highly effective for detecting even trace amounts of analytes.[12]

Coherent Anti-Stokes Raman Scattering (CARS):

CARS is a nonlinear Raman spectroscopy technique that generates a strong anti-Stokes signal, significantly enhancing the Raman signal intensity. It relies on the

[12] Explained in section 1.7

interaction of three laser beams, including a pump and a Stokes beam, to create a coherent vibrational response in the sample.[226–229]

Tip-enhanced Raman spectroscopy (TERS):

TERS combines Raman spectroscopy with AFM/STM/tuning fork to achieve nanoscale spatial resolution. A metal-coated AFM tip focuses the laser on a tiny sample area, allowing Raman measurements with sub-nanometer spatial resolution. TERS is particularly valuable for studying nanomaterials and surface structures.[230–232]

Super-Resolution Raman Imaging:

Super-resolution techniques, such as stimulated emission depletion (STED) and structured illumination microscopy (SIM), can enhance spatial resolution in Raman imaging.[233–237] These methods use advanced optical setups to achieve spatial resolutions well beyond the diffraction limit of light, enabling the visualization of fine details within a sample.

Resonance Raman (RR) Spectroscopy:

Resonance Raman spectroscopy takes advantage of the natural resonance of specific molecules with the laser excitation wavelength. It involves tuning the excitation wavelength of the incident light to coincide with an electronic transition of the target molecule. The Raman scattering efficiency is significantly increased by resonantly exciting the molecule, leading to more pronounced and easily detectable spectral features. This technique is particularly valuable for studying complex molecular systems, such as biological molecules and transition metal complexes, where traditional Raman spectroscopy might have limited sensitivity.[238–241] However, it is essential to note fluorescence's drawbacks. Fluorescence poses a challenge for Resonance Raman techniques, especially when employing visible-range sources.

Deconvolution and Advanced Data Processing:

Advanced data processing techniques like MVA can efficiently filter the noise and extract essential data, such as complex spectral data and improved data resolution.[13]

[13] Explained in section 1.4

1.7. Principles of SERS

The Raman scattering discussed in section 1.2 is a spontaneous scattering event representing a linear process. The total power of the inelastically scattered beam increases linearly with the intensity of the incoming excitation beam. In the following section, the Stokes process is explained, where the power of the scattered beam can be expressed as follows:

$$P_s(\omega_v) = N\sigma_{RS}I(\omega_i) \qquad \textit{Eqn. 18}$$

Here, N represents the number of Stokes-active scatters within the excitation spot, σ_{RS} denotes the Raman scattering cross section, and $I(\omega_i)$ is the intensity of the excitation beam.

SERS refers to the enhancement of this process, achieved by situating the Raman-active molecules close to a metallic nanostructure. This nanostructure can take the form of metal colloids, designed NP assemblies, or the topography of a metal roughened surface. The enhancement of $P_s(\omega_v)$ (scattered power) is attributed to two main factors. Firstly, σ_{RS} is altered due to a change in the molecule's environment. This alteration to $\sigma_{SERS} > \sigma_{RS}$, is referred to as the chemical or EM contribution to the Raman enhancement.

1.7.1. Electromagnetic (EM) enhancement

The interaction of metals with EM fields can be explained using the framework based on Maxwell's equations. The starting point of Maxwell's equations of macroscopic electromagnetism is in the following form:

$$\nabla \cdot D = \rho_f \qquad \text{Eqn. 19} \qquad \nabla \cdot B = 0 \qquad \text{Eqn. 20}$$

$$\nabla \times E = -\frac{\partial B}{\partial t} \qquad \text{Eqn. 21} \qquad \nabla \cdot H = J_f \mp \frac{\partial D}{\partial t} \qquad \text{Eqn. 22}$$

These equations link the four macroscopic fields E (electric field), H (magnetic field), $\vec{B}$ (magnetic induction of flux density), and D (dielectric displacement) with ρ_f and J_f as external charge and current densities respectively.

The constitutive relations for linear, isotropic, and nonmagnetic media are defined by,

$$D = \varepsilon_0 \varepsilon E \qquad \textit{Eqn. 23}$$

$$B = \in_0 \in E \qquad \textit{Eqn. 24}$$

where ε_0 and $\in_0$ are electric permittivity and magnetic permeability of vacuum, ε is dielectric function of medium (complex number $\varepsilon = \varepsilon_1 + i\varepsilon_2$) and $\in$ is relative permeability. For non-magnetic materials ($\in = 1$), isotropic and without external stimulation ($\rho_f = J_f = 0$) Maxwell's equation for genralized wave equation yields,

$$\in_0 \frac{\partial^2 D}{\partial t^2} = \nabla^2 E \qquad \textit{Eqn. 25}$$

Solving this wave equation depends on D and E, that is, the material's behavior with the frequency of dielectric function $\varepsilon(\omega)$, which, in the case of metals, is influenced by both conduction electrons and bound electrons contributing due to interband excitations. The contribution of electrons to the $\varepsilon(\omega)$ can be obtained using the Drude model as

$$\varepsilon(\omega) = 1 - \frac{\omega_p^2}{{\omega_a}^2} \qquad \textit{Eqn. 26}$$

The parameter $\omega_p = n_e e^2/\varepsilon_0 m_e$ is called plasma frequency, n_e is density of free electrons, m_e is free electron mass and ω_a here is the angular frequency. For $\omega_a < \omega_p$, the dielectric constant is negative, yielding a complex refractive index, and limiting EM wave penetration to a finite depth. Conversely, for $\omega_a > \omega_p$, the dielectric constant is positive, resulting in an accurate refractive index; here, metals behave like dielectric material. Now, returning to Eqn. 25, two cases can be distinguished depending on the polarization of E concerning wave vector K. For transverse waves (not relevant for this work) and for longitudinal waves which denote $\varepsilon(\omega) = 0$ signifying longitudinal oscillations can only occur this frequency. In a material medium, longitudinal solutions of Maxwell equations are called *Plasmons*, quantized wave-like excitations in a plasma.

1.7.1.1. Light Scattering by a Sphere

Consider the most convenient geometry for analytical treatment: a uniform, isotropic sphere with a radius of '*c*' positioned at the origin within a uniform, static electric field, depicted in Figure 1.14 as,

$$\vec{E} = E_0\hat{z} \qquad \text{Eqn. 27}$$

The surrounding medium is isotropic and non-absorbing, with a dielectric constant ε_m, and the electric field lines are aligned parallel to the z-direction. The dielectric response of the sphere is characterized by the dielectric function $\varepsilon(\omega)$.

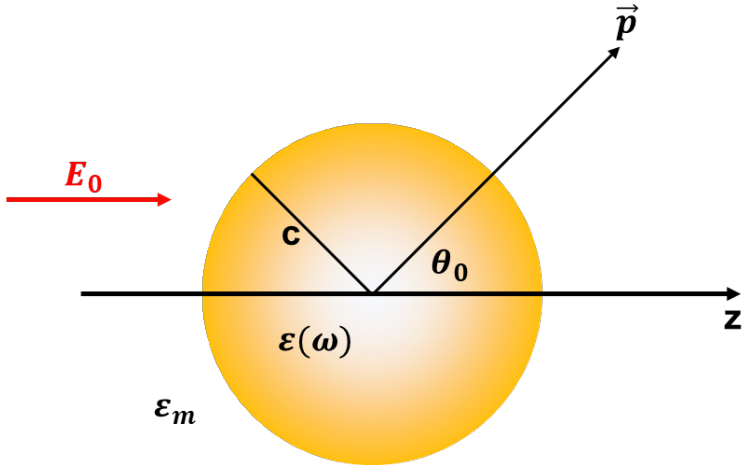

Figure 1.14: Schematics (not to scale) of a homogeneous sphere placed into an electrostatic field. [Figure adapted and modified from Stefan A. Maier, Plasmonics: Fundamentals and Applications (Springer New York, NY)].[242]

The applied electric field induces a dipole moment within the sphere, and its magnitude is directly proportional to $|E_0|$, The polarizability μ_s defined as,

$$\vec{p} = \varepsilon_0\varepsilon_m\mu_s E_0 \qquad \text{Eqn. 28}$$

Upon consideration, the following expression is derived:

$$\mu_s = 4\pi c^3 \frac{\varepsilon-\varepsilon_m}{\varepsilon+2\varepsilon_m} \qquad \text{Eqn. 29}$$

This equation is the central result in this section. It depicts the polarizability of a small sphere with a sub-wavelength diameter under the electrostatic approximation.[243] It becomes evident that the polarizability experiences a resonant enhancement when the condition $\varepsilon+2\varepsilon_m$ is a minimum or in the case of a slowly varying $Im[\varepsilon]$, particularly around resonance, this simplifies to

$$Re[\varepsilon(s)] = -2\varepsilon_m \qquad \text{Eqn. 30}$$

This relationship is referred to as the Fröhlich condition, and the corresponding mode in an oscillating field is denoted as the dipole surface plasmon for the metallic NP. Significant enhancement is observed when $\varepsilon = -2$. This enhancement results from the denominator in Eqn. 27 approaching zero, thus inducing a resonance phenomenon,

scientifically termed LSPR. LSPs are non-propagating excitations involving the conduction electrons within metallic nanostructures coupled to the EM field. The materials with values approaching $\varepsilon = -2$, would provide maximum enhancement. Gold (Au), silver (Ag), copper, and even aluminum fulfill those conditions in the visible spectral range.[242]

This equation (Eqn. 30) highlights the pronounced dependency of the resonance frequency on the dielectric environment: the resonance shifts towards longer wavelengths (a red shift) as ε_m increases. The resonance shift for materials like Au and Ag NPs places it within the visible region of the EM spectrum, with applications in the expanding field of SERS. The concept of dipole particle plasmon resonance applies to smaller particles (<100 nm) under visible or near-infrared radiation. At the same time, a more comprehensive electrodynamic methodology, called Mie theory, is necessary for larger particles.

1.7.1.2. Field Enhancement in SERS

A significantly important factor contributing to the overall enhancement of P_s is the increased EM field resulting from the excitation of LSPs and the convergence of electric field lines, often referred to as the 'lightning rod effect' at the metal interface.[13, 242, 244–246] This results in an enhancement of both the incoming and scattered light fields, as depicted by the equation:

$$L(\omega) = \left|\frac{E_{loc}(\omega)}{E_0}\right| \qquad \textit{Eqn. 31}$$

Here, E_{loc} represents the local field amplitude at the Raman-active site, and $L(\omega)$ is called the *EM* enhancement factor (*EF)*. The total power of the Stokes beam in the context of SERS conditions is defined as:

$$P_s(\omega_v) = N\sigma_{RS}L(\omega_i)^2L(\omega_s)^2I(\omega_i) \qquad \textit{Eqn. 32}$$

As the frequency difference $\Delta\omega_D$ is,

$$\Delta\omega_D = \omega_i - \omega_v \qquad \textit{Eqn. 33}$$

between the incoming and scattered photons is generally much smaller than the line width of the LSP mode,

$$L(\omega_i) \approx L(\omega_v) \qquad \text{Eqn. 34}$$

leading to equation Eqn. 31 to be rewritten for the Stokes beam in SERS as follows,

$$L(\omega) = \left|\frac{E_{loc}(\omega)}{E_0}\right|^4 \qquad \text{Eqn. 35}$$

Thus, the significant conclusion is that the EM contribution to the total SERS enhancement is directly proportional to the fourth power of the electric field.[13, 242, 247, 248]

The fundamental basis of the EM enhancement encompasses two primary contributions: enhancement due to the resonant excitation of LSPs in metallic nanostructures and the lightning rod effect, as mentioned earlier.[13, 244, 246] LSP resonance or LSPR exhibits strong frequency dependence among these two factors. In contrast, the lightning rod effect arises from the purely geometrical phenomenon of electric field crowding near the sharp edges of metallic features. Thus, it can expressed as:

$$L(\omega) = L_{SP}(\omega) L_{LR} \qquad \text{Eqn. 36}$$

The functional form of L_{SP} essentially resembles the polarizability of metallic nanostructures with specific geometrical shapes. For spherical NPs of sub-wavelength diameter, it is expressed as:

$$L(\omega) \propto \frac{\varepsilon(\omega) - 1}{\varepsilon(\omega) + 2} \qquad \text{Eqn. 37}$$

Similarly, the appropriate form of polarizability must be employed for ellipsoids, nanorods, and other nanostructures with distinct shapes. LSP describes the field enhancement averaged over the particle's surface.[242]

1.7.2. Chemical Enhancement

The EM enhancement mechanism alone cannot explain many phenomena observed in SERS systems. Evidence indicates that the chemical interaction is a prerequisite for SERS enhancement, although insufficient. This complicates the differentiation of the two enhancement mechanisms in natural surfaces, leading to ongoing disagreement in the literature.[249]

Chemical enhancement results from alterations in the Raman polarizability upon the adsorption of a molecule onto the metal surface.[250] These mechanisms can be

summarized in three cases: first, the metal disrupts the material's electronic structure, altering Raman polarizability through physisorption; second, molecules form covalent bonds with the metal, modifying energy states, potentially resonating with incident laser light; and third, photo-driven charge transfer occurs when metal states provide intermediate energy levels for material transitions (Figure 1.15), leading to resonance enhancement when laser energy aligns with the energy difference between the Fermi level of the metal (E_F) and the material's energy level (E_M).[251]

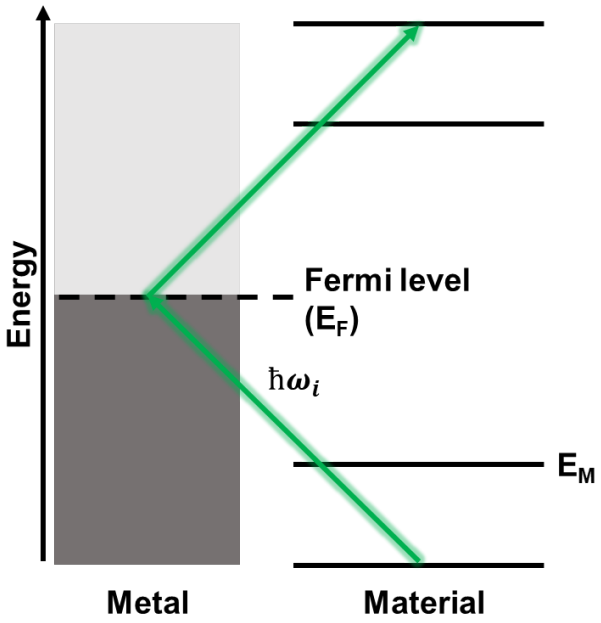

Figure 1.15: Illustration of charge transfer mechanism in SERS

The charge transfer mechanism has been extensively studied, as resonance conditions can be experimentally tuned by creating a potential step on the metal surface and adjusting an external voltage.

Plasmon resonance imaging, as an advanced technique, relies on the interaction between surface plasmon resonances and incident light to visualize plasmons. When NPs are placed near target molecules, their resonance frequency undergoes a detectable shift, offering high sensitivity and specificity for identification and visualization. Among various methods, dark-field optical microscopy[14] is commonly employed, using a far-field approach to collect only the scattered light from NPs with the assistance of a dark-field condenser.

[14] Example shown in Chapter 9

1.8. Applications of SERS

SERS is a powerful analytical technique that has found various applications across various scientific fields and industries due to its remarkable sensitivity and specificity. Here are some notable applications of SERS:

1. **Chemical Analysis:** SERS is extensively used for chemical analysis, allowing for the identification and quantification of molecules even at deficient concentrations. It has applications in environmental monitoring, forensic science, and pharmaceutical research.[252–255]
2. **Biosensing:** SERS is invaluable in biosensing. It can detect and characterize biological molecules, such as deoxyribonucleic acid (DNA), proteins, and pathogens, with high sensitivity. This makes it useful in medical diagnostics, disease detection, and drug development.[256–260]
3. **Food Safety:** SERS can rapidly and sensitively detect contaminants and pollutants in food products. It helps ensure food safety by identifying harmful substances at trace levels.[261–265]
4. **Materials Science:** In materials science, SERS is used to study the properties of nanomaterials and NPs. It aids in the characterization of material surfaces and interfaces, contributing to the development of advanced materials,[266–268]
5. **Pharmaceuticals:** SERS is crucial in pharmaceutical research. It analyzes drug formulations and delivery systems and detects counterfeit drugs. It also plays a role in quality control and drug development.[269–271]
6. **Environmental Monitoring:** SERS is used in environmental studies to detect and quantify pollutants, heavy metals, and other contaminants in soil, water, and air. It helps monitor ecological quality and compliance with regulations.[272–277]
7. **Cancer Research:** SERS can detect cancer biomarkers and study cellular processes at the molecular level. It has the potential to improve early cancer diagnosis and treatment monitoring.[278–281]
8. **Nanotechnology:** SERS is instrumental in nanotechnology research, enabling the precise characterization of NPs and nanostructures. It aids in the development of nanomaterials for various applications.[282–284]

9. **Art and Cultural Heritage Conservation:** SERS has been employed to analyze pigments, dyes, and materials in artworks and historical artifacts. It assists in preservation efforts by providing insights into their composition and degradation.[285–288]
10. **Security and Forensics:** SERS is utilized in security applications, including detecting explosives and illicit drugs. It also plays a role in forensic science by identifying trace evidence at crime scenes.[289–292]
11. **Gas Sensing:** SERS-based gas sensors are being developed to detect highly sensitive gases like hydrogen, methane, and carbon dioxide. These sensors have applications in industrial and environmental monitoring.[293–296]
12. **Energy Materials:** SERS helps characterize materials used in energy storage and conversion devices, such as batteries, fuel cells, and solar cells. It contributes to the improvement of energy-efficient technologies.[297–299]

These diverse applications showcase the versatility and potential of SERS as a valuable analytical tool in various scientific, industrial, and research endeavors. Its ability to provide detailed molecular information at the nanoscale drives innovation and advances knowledge in numerous fields.

1.9. Key Factors of SERS

The advantages of SERS are evident in its remarkable sensitivity; however, like any analytical technique, SERS comes with challenges and limitations. Understanding the advantages and disadvantages of SERS is crucial for researchers and practitioners aiming to leverage its capabilities effectively in diverse fields ranging from chemistry and biology to environmental monitoring and material science.

1.9.1. Advantages of SERS

The advantages of SERS are as follows:

1. **Enhanced Sensitivity:** SERS substrates significantly amplify Raman signals, making them highly sensitive to trace amounts of analytes. This sensitivity is invaluable for detecting molecules at low concentrations.

2. **Chemical Specificity:** SERS provides specific chemical information, allowing for the differentiation of molecules based on their Raman spectra. This specificity is crucial for accurate identification and characterization.
3. **Label-Free Detection:** SERS is a label-free technique, eliminating the need for chemical labels or tags. This simplifies sample preparation and reduces the risk of interference.
4. **Multiplexing Capability:** SERS substrates can detect multiple analytes simultaneously, enabling the study of complex mixtures and high-throughput analysis.
5. **Versatility:** SERS substrates can be customized and applied to various sample types, including solids, liquids, and gases. They have broad applications in chemistry, biology, materials science, and environmental monitoring.

1.9.2. Disadvantages of SERS

The disadvantages of SERS are as follows:

1. **Intimate Contact Requirement:** SERS necessitates intimate contact between the enhancing surface and the analyte, making it challenging to analyze samples that do not readily adhere to or interact with the substrate. This limits its applicability to certain sample types.
2. **Substrate Degradation:** SERS substrates can degrade with time, decreasing signal intensity and reliability. This degradation affects the long-term stability and reproducibility of SERS measurements.
3. **Limited Selectivity:** SERS substrates may have limited selectivity for a specific analyte. This means they may not effectively differentiate between different molecules, potentially leading to interference or cross-reactivity issues.
4. **Limited Reusability:** SERS substrates typically have limited reusability. After multiple uses, their enhancing capabilities may diminish, requiring frequent replacement. This can increase the overall cost of SERS analysis.
5. **Homogeneity and Reproducibility Issues:** Achieving homogeneity and reproducibility of the SERS signal within a substrate can be challenging. Variations in the distribution of enhancing sites and analyte coverage can result in

inconsistent and non-reproducible measurements, affecting the reliability of SERS data.

1.9.3. Challenges of SERS and SERS Substrates

SERS has both advantages and drawbacks that depend on the quality of the SERS substrate, which is essential for achieving reliable outcomes. The design of the substrate impacts reproducibility and cost, requiring a balance between complexity and simplicity. Traditional 2D SERS substrates have limitations in detecting molecules a few hundred nanometers above the surface, restricting their use in complex environments like solutions or biological samples. Therefore, enhancing substrate engineering and expanding applicability is a key challenge for researchers in the field.

1.9.4. Methods to Improve SERS Applicability

Improving the quality of SERS substrates is vital to make SERS more applicable in different research and industrial settings. This can be achieved through various strategies such as precise manufacturing techniques, creating substrates with multiple functions, tuning the plasmon resonances,[15] improving stability, making 3D and flexible substrates,[16] using scalable production methods, integrating with microfluidics, enabling real-time monitoring, customizing for specific applications, and ensuring strict quality control. Together, these approaches aim to enhance SERS substrates' performance, accessibility, and reliability, thus expanding the applicability of SERS in different research and industrial contexts.

[15] Further explained in Chapter 6
[16] Further explained in Chapters 9 and 10

2. Objectives

The primary aim of this study is to improve the practicality of instrumentation in Raman spectroscopy. Additionally, it aims to enhance the practicality and effectiveness of chemical imaging by incorporating advanced data processing techniques, while also improving the applicability of SERS.

Raman spectroscopy/imaging and SERS analysis accuracy relies on robust data acquisition. Accurate spectrometer calibration and continuous optimization for lens-based Raman spectrometers are necessary to ensure robust data acquisition. This thesis addresses a method achieved by carefully monitoring the difference between theoretically obtained and experimentally measured SR, which is critical to maintaining and optimizing the spectrometer over a more extended period. Furthermore, it addresses improving the practicality of Raman imaging by combining it with advanced processing techniques such as MVA, which are employed to detect subtle spectral differences in large data sets. Thus enhancing the sensitivity, specificity, practicality, and applicability of the analysis.

On the other hand, to improve the applicability of SERS, commercially available SERS substrates still face several limitations. These include short shelf life, high cost, challenges in process optimization, substrate variability, reproducibility issues, and a limited range of applicable analytes. To address some of these limitations, gradient SERS substrates have been developed, consisting of plasmonic metal NPs arranged in gradients of different sizes to produce multiple resonances. These substrates are cost-effective, reproducible, and easy to fabricate, making them ideal for rapid and effective analyte screening. However, limitations such as using a variety of analytes, sample compatibility, scalability, and substrate consistency persist.

To overcome the limitations of 2D SERS substrates, a sensitive 3D substrate has been developed to detect molecules in all directions, regardless of their location. This 3D substrate expands the range of analyte applications and enables the detection of samples containing low quantities of analytes in cells, tissues, or fluids. Furthermore, these 3D substrates have been tested in static and dynamic scenarios in low-concentration fluids to assess their SERS properties and stability in complex environments.

3. Summary

This thesis explores the capabilities of Raman spectroscopy and develops and investigates novel SERS substrates. It aims to enhance the theoretical understanding of Raman spectrometers and utilize advances in data processing technology for large data sets used in Raman imaging. The thesis also presents a synthesis of 3D SERS substrates and compares different preparation methods for 3D SERS substrates, including finding the suitable base material. Additionally, it produces 2D gradient SERS substrates for rapid multi-analyte screening.

Chapter 1 provides a clear explanation of the theoretical and scientific principles behind Raman spectroscopy. It covers the classical and quantum theories of Raman scattering and explains the optical components of a CRM. It delves into the spectrometer and optical path details, enabling a better understanding of the system's functioning. Additionally, it discusses Raman spectroscopy's benefits, limitations, and drawbacks and provides fundamental information on overcoming its limitations. The chapter explains data analysis and its sophisticated analysis tools. Furthermore, it describes the basic concepts behind SERS and the contributing mechanisms. It covers the EM and chemical enhancement mechanisms and the benefits, drawbacks, restrictions, and requirements for sample preparations. Chapter 2 provides an overview of the objectives and goals of this thesis, while Chapter 3 summarizes the explanation of key results and discussions in this thesis.

Chapter 4 explores the optimization of a lens-based spectrometer used in commercial applications. It highlights the importance of SR and quality factor (Q) in determining the performance of a spectrometer. It establishes protocols to determine SR and Q to ensure the accuracy and reliability of experimental results. The study quantifies the optimal match between the experimentally measured SR and the theoretically calculated SR of a spectrometer setup as the Q factor. The importance of these findings is illustrated through two distinct cases. In the first case, the study used a neon lamp as the emission source to reveal that the best achievable SR is obtained with the highest available grating and the smallest pinhole width. This yielded SR values below 1 cm^{-1}. In the second case, the study employed a diamond sample and studied three excitation wavelengths. The results showed that the highest SR is achieved at 633 nm with a pinhole width of 10 µm, resulting in an SR of 2 cm^{-1}, which is in close agreement

with the natural linewidth of the diamond (1.2 cm^{-1}). In this case, the Q values exceeded those from the neon lamp experiment, emphasizing the significance of natural linewidth in spectrometer performance assessment. By maintaining a high Q factor over time, the SR of the spectrometer can be sustained, resulting in reliable data acquisition over an extended period.

Chapter 5 explores the optimization of Raman experiments and the use of advanced data analysis tools such as PCA and DA to investigate materials with subtle spectral variations. The research focuses on human tissue samples, specifically salivary gland tumors (SGT) such as warthin tumors, pleomorphic adenomas, and non-tumor SGTs. Although visual differences between tissue types were limited in the Raman spectroscopy data obtained, PCA revealed significant differences, highlighting the crucial role of sophisticated data analysis tools in interpreting vital samples effectively. This demonstrates the potential of combining Raman imaging with MVA as a valuable tool in medical diagnostics.

Chapter 6 presents a method for fabricating non-uniform SERS substrates using annealed thin Au films. These substrates offer multiple resonances within a single sample, are chemically stable, and exhibit consistent geometry and plasmonic properties. Scanning electron microscopy (SEM) revealed different particle-like and island-like morphologies with varying gap sizes at different lateral positions of the substrates. The extinction spectrum helps to characterize the morphology of the Au film, with sharp spectra indicating NPs and broad spectra indicating connected islands. The substrates demonstrated a wide range of resonances from 560 nm to 680 nm. Notably, the SERS enhancement was observed at different lateral positions, which correlated with the surface morphology for the analytes 1,2-bis(4-pyridyl) ethylene (BPE) and methylene blue (MB). Non-uniform SERS substrates like these provide a practical solution for rapid analyte screening, with reproducible characteristics and ease of fabrication. These substrates offer tunable resonances and surface morphologies, making them valuable tools for optimizing SERS efficiency and finding optimal surface structures. They demonstrate the substrates' versatility in providing cost-effective, reproducible, and fast analyte screening.

Chapter 7 focuses on the search for suitable base particles for 3D SERS substrates. Among the different particles explored, the core-shell silica particles stood out due to their drug-carrying capabilities. An exciting variation of this type of particle was

fabricated as a core-shell with a lobe, offering a larger surface area. It was found to be highly effective as a micro-drug carrier that can carry multiple drugs simultaneously. The synthesis, characterization, and potential applications for revolutionizing drug delivery systems were thoroughly examined.

Chapter 8 focuses on a type of particle with distinct surface properties. The study investigates polystyrene particles, including variations with different proportions of porogen, which result in diverse morphologies. Advanced analytical techniques were used to analyze the chemical composition of these particles and track their development during each synthesis step. A marker-free approach utilizing 3D-CRM was used to characterize the chemical composition of these spherical polymer particles. This method eliminated the need for additional labeling, making it a streamlined and non-invasive procedure.

Chapter 9 presents a method for fabricating and using 3D SERS substrates. The ideal base particles were found to be spherical-shaped silica particles with mercapto groups on their surface. These allowed for the successful trapping of Au and Ag NPs. Confocal Raman imaging showed uniform mercapto group distribution, with stability up to 220°C. Two deposition methods (Tollens' reagent and sputtering) yielded Ag and Au NPs. The resulting substrates exhibited inter- and intra-particle heterogeneity and enhanced Raman signals for MB up to 25-fold. The optical properties of such 3D SERS substrates revealed multiple resonances in the visible range. The spherical 3D-SERS substrates offer versatility in sample orientation and application, particularly in biological and medical contexts. They provide improved depth resolution in SERS, overcoming the limitations of 2D surfaces. Investigating 3D SERS substrates has resulted in a significant breakthrough in SERS. These innovative substrates offer unique advantages, particularly their ability to operate effectively in diverse 3D environments.

Chapter 10 delves deeper into the potential of 3D SERS substrates by testing them in solutions with low-concentration analytes. Two different types of solvents were used to demonstrate the potential of these substrates in both static and dynamic scenarios. In the static scenario, SMPs were immobilized in solutions using glycerin, allowing SERS imaging within the solution and mimicking situations where SMPs are trapped in cellular compartments or tissue structures. 3D SERS substrates exhibited excellent enhancement capabilities for multiple analytes in this context, with both

glycerin and the model analyte MB displaying significant SERS enhancements, with EFs reaching impressive levels of up to 15 for glycerin and approx. 370 for MB.

In the dynamic scenario, the mobility of SMPs functionalized with Ag NPs in a solution of MB in water was explored. The SMPs were free to move and randomly floating, allowing time-dependent experiments where the SERS signal of MB was detected as an SMP passed through the laser focus. Observations revealed that single and clustered SMPs could pass through the laser focus, providing consistent and significant SERS enhancements with EFs reaching up to 200. This dynamic approach to 3D SERS holds immense promise for real-time, in-situ analysis of complex samples.

These findings have significant implications for varied fields of science, including biomedicine, environmental science, and analytical chemistry.

4. Determination and Monitoring of Quality Parameters: A Detailed Study of Optical Elements of a Lens-Based Raman Spectrometer

Ashutosh Mukherjee[1,2,3], Anita Lorenz[1,2], and Marc Brecht[1,2,3]

[1]Center for Process Analysis & Technology (PA&T), School of Applied Chemistry, Reutlingen University, Alteburgstrasse 150, 72762 Reutlingen, Germany.

[2]Reutlingen Research Institute (RRI), Reutlingen University, Alteburgstrasse 150, 72762 Reutlingen, Germany.

[3]Institute of Physical and Theoretical Chemistry, University of Tübingen, Auf der Morgenstelle 18, 72076 Tübingen, Germany.

This chapter was originally published in the Journal of Applied Spectroscopy as

Mukherjee A, Lorenz A, Brecht M. Determination and Monitoring of Quality Parameters: A Detailed Study of Optical Elements of a Lens-Based Raman Spectrometer. Applied Spectroscopy, 2022, 76, 2,199-206.

DOI: 10.1177/00037028211055148

Supplementary Material/Supporting Information shown in Appendix 1

Submitted Paper

Applied Spectroscopy

Applied Spectroscopy
2022, Vol. 76(2) 199–206

DOI: 10.1177/00037028211055148
journals.sagepub.com/home/asp
SAGE

Determination and Monitoring of Quality Parameters: A Detailed Study of Optical Elements of a Lens-Based Raman Spectrometer

Ashutosh Mukherjee[1,2,3], Anita Lorenz[1,2], and Marc Brecht[1,2,3]

Abstract

A lens-based Raman spectrometer is characterized by studying the optical elements in the optical path and we study the measure of aberration–diffraction effects. This is achieved by measuring the spectral resolution (SR) thus encompassing almost all optical elements of a spectrometer that are mostly responsible for such effects. An equation for SR is used to determine the quality factor *Q* which measures aberration/diffraction effects occurring in a spectrometer. We show how the quality factor changes with different spectrometer parameters such as grating groove density, the wavelength of excitation, pinhole width, charge-coupled device (CCD) pixel density, etc. This work provides an insight into the quality of a spectrometer and helps to monitor the performance of the spectrometer over a certain period. Commercially available spectrometers or home-built spectrometers are prone to misalignment in optical elements and can benefit from this work that allows maintaining the overall quality of the setup. Performing such experiments over a period helps to minimize the aberration/diffraction effects occurring as a result of time and maintaining the quality of measurements.

Keywords

Raman spectroscopy, principle of Raman spectrometer, spectral resolution, full width half-maximum, FWHM

Date received: 12 August 2021; accepted: 29 September 2021

Introduction

Raman spectroscopy is one of the most powerful techniques in identifying chemical compositions of a sample through designated peak positions also known as the chemical signature/fingerprint of a material.[1] Apart from material identification, typical Raman spectra contain rich information about specific properties such as crystallinity, doping, stresses, etc. For example, the width of a peak may indicate the crystallinity of a material,[2,3] intensity and intensity ratios determine the concentration (per unit area exposed to the laser) and relative quantities of materials present,[4] a peak shift from its signature position may determine whether the material is stressed/strained,[5–9] doped,[10–13] or in an excited state, e.g., at elevated temperature.[13–16] However, not always are these cases prevalent and often there are peak shifts or broadened peaks irrespective of their origin, and generally such details are ignored as long as they do not fit the aim of the experiment. If the shift of the peak of interest is within the permissible limits of the spectral resolution (SR), then it is critical to commemorate the origin of the shift to the factors concerning the strain, doping, crystallinity, temperatures, etc. Therefore, it is of utmost importance to study the spectrometer properties before concluding any critical analysis of any material under investigation.

A good spectrometer design (SD) for Raman instruments in general, and Raman microscopes in particular, can solve the problem and the SD is one of the most important factors in assessing the quality of a spectrometer

[1]Center for Process Analysis and Technology (PA&T), School of Applied Chemistry, Reutlingen University, Reutlingen, Germany
[2]Reutlingen Research Institute (RRI), Reutlingen University, Reutlingen, Germany
[3]Institute of Physical and Theoretical Chemistry, University of Tübingen, Tübingen, Germany

Corresponding author:
Marc Brecht, Hochschule Reutlingen, Alteburgstr. 150 Reutlingen, Baden-Württemberg 72762, Germany.
Email: marc.brecht@reutlingen-university.de

or measurement. The basis of good SD in a Raman instrument (or spectrometer) lies in the effectiveness of the optical elements in the optical path to form an image of the entrance slit at the exit plane with the wavelengths involved in the excitation source. This can be seen in its optimum signal-to-noise ratio and in the spectral resolution of the measured Raman spectra, in the depth resolution of the microscope, etc. The elements on which the aforesaid qualities of spectrometer depend are the excitation source, objective (magnification/numerical aperture), grating groove density, slit width/pinhole size, focal length, system magnification, pixels of the charge-coupled device (CCD), and other aberration/diffraction effects occurring due to optical elements in the setup like lenses and mirrors. For a good spectrometer, an optimum combination of all the aforementioned factors and their interaction must be considered and optimized.

However, the challenge to deal and consecutively compensate for aberrations/diffractions is persistent. In some of the commercial Raman microscopes, the optical path usually is handled with mechanical interfaces such as beam steering motors, motors for grating rotation, lens adjustments, slit opening, beam splitters, mirrors, etc. Such interfaces undergo creep or hysteresis, and over a certain period the motors are not in the same position as they should have been during the manufacturing and calibration of the machine.

This leads to discrepancies in the experimental data, which must be tracked and investigated to maintain the optimal quality of the spectrometer. These discrepancies can be eliminated if the optical path is thoroughly calibrated each time, which can be a challenge for commercial spectrometers. An optical beam is very sensitive to any changes of optical elements in the beam path. These changes can lead to spherical, chromatic aberrations, diffractions, beam deflections, reflections, etc. Therefore, the elimination of such effects is an important challenge in optical spectroscopy. A typical SD used in a Raman instrument is an uncrossed Czerny–Turner configuration, consisting of two concave mirrors and one planar diffraction grating and has proved to be the most suitable configuration for Raman spectrometer.[17–21]

It is important to study the Raman spectrometer without manipulating the elements in the optical path. To study every element in the optical path is time consuming and is a challenge by itself. In this work, we describe how the quality of a spectrometer can be studied in detail in a commercial Raman microscope comprising all elements in an optical path. This work has been inspired by the previous work of Liu and Berg[21] where they analyzed an uncrossed Czerny–Turner spectrometer by measuring its SR. Further, they determined the aberration/diffraction correction factor for their setup.[21] Conducting the described procedure over a certain period will help to maintain the quality of a setup and, in case of problems, to be able to identify their origin and solve them accordingly.

Mathematical Background

Studying the SR of the spectrometer will include a major portion of the elements in a Raman instrument such as the grating groove density, focal length, lenses/mirrors, CCD pixels, and pixel size.

Spectral Resolution

To determine the SR with the available options, Liu and Berg[21] combined all the factors that influence SR into one expression, the derivation of this equation is explained in detail in previous studies.[20,21] The advantage of this equation is that it shows the dependence of SR under different optical configurations. The factors affecting SR can be summarized in Eq. 1:

$$\begin{aligned}\Delta\omega[\omega_L, \omega_R, G, f_2, \alpha, b_{img}] &= (\omega_L - \omega_R)^2 \cdot \frac{b_{img}}{G \cdot f_2} \\ &\cdot \cos\left\{\arcsin\left(\frac{G}{2 \cdot (\omega_L - \omega_R) \cdot \cos\left(\frac{\alpha}{2}\right)}\right) + \frac{\alpha}{2}\right\}\end{aligned} \quad (1)$$

in which $\Delta\omega$ is SR, ω_L is the absolute wavelength of the excitation source, ω_R is the Raman wavenumber shift of the desired peak under investigation, G is the grating groove density per μm, the groove's distance can be calculated as $d = 1/G$ (μm), f_2 is the focal length of the system (distance from a second Czerny–Turner lens to the CCD), α is the angle between the incident and diffracted beam on the grating, also known as "include angle". The calculation for this angle is shown in detail in the Supplemental Material, b_{img} is the full width half-maximum (FWHM) of the entrance slit or pinole. FWHM of the entrance pinhole/slit is limited by aberration/diffraction effects. To take this into account, an empirical relationship[21] between b_{img} and the entrance pinhole/slit width b_{ent} is given by Eq. 2:

$$b_{img} = M \cdot \sqrt{(b_{ent})^2 + (b_{limit})^2} \quad (2)$$

where M is the system magnification and b_{limit} is the smallest value possible of FWHM of the pinhole/slit width.

When $M = 1$, b_{limit} is given by

$$b_{limit} = \frac{Q}{(\omega_L - \omega_R)} \quad (3)$$

Here, Q, the so-called quality factor is approximated as a constant for a spectrometer with a specific design.[21] It is calculated by best fitting the experimental results to the

theoretically derived values using Eq. 1. The resulting curve for SR as a function of pinhole/slit width is a hyperbolic curve which will be discussed later in the results section.

Liu and Berg[21] used an uncrossed Czerny–Turner monochromator (Renishaw) where they compared spectral resolutions of two different lasers and different gratings and measured the correction factor of their setup.[21] They have attributed "quality factor *Q*" as diffraction and aberration correction factor (DACF) or A. In this paper, we deal in detail with the quality factor *Q* and with the parameters that influence *Q*. It is important to study how it variates if different parameters in Eq. 1 change, e.g., the excitation wavelength, the grating, etc.

Materials and Methods

A single crystalline diamond was used as a sample with a characteristic Raman peak at 1332.4 cm^{-1} and a true Raman FWHM of 1.2 cm^{-1}.[22] For atomic emission spectra, a calibration neon lamp from Kaiser Electronics was used. A commercial Raman microscope from WITec (Alpha300 RAandS) was used and a detailed optical path is sketched in Fig. 1. Raman spectra were obtained using an air objective (Carl Zeiss; EC Epiplan-Neofluar DIC M27, 100×, NA = 0.90). This system is equipped with a lens-based UHTS 300 spectrometer connected using a multimode optical fiber and thermoelectric cooled CCD and electron multiplying CCD (EMCCD, Andor DU970N-BV). The CCD and EMCCD is a back-illuminated CCD with 1600 × 200 pixels and each pixel is 16 μm × 16 μm. The used multimode fibers had different diameters that transported the scattered signal to the spectrometer. Thus, the diameter of these fibers determines the size of the pinhole. They were 10 μm, 25 μm, 50 μm, and 100 μm all with a NA = 0.12. For excitation, a diode laser (532 nm) with a nominal output power of 40 mW, a helium–neon laser (633 nm) with an output power of 25 mW, and a helium–cadmium laser (442 nm) with an output power of 25 mW were used. Data processing was done using Control Project Plus 5.0 software provided by WITec and all experiments were carried out at ambient conditions.

Results and Discussion

Equation 1 shows that SR ($\Delta\omega$) depends on factors that can be classified into three types: (i) instrument-specific, (ii) experiment-specific, and (iii) sample-specific parameters. The instrument-specific parameters are those parameters that are fixed during manufacturing like system magnification, incident/diffraction angle, aberration/diffraction effects, focal length, and CCD pixels. For a commercially available Raman microscope, instrument-specific parameters cannot easily be changed since the complete optical path is calibrated and fixed precisely. Experiment-specific parameters are specific to a certain experiment/measurement that can sometimes be changed depending upon the available options. These include the grating groove density (*G*), excitation source wavelength (ω_L), pinhole/slit widths. Sample-specific parameters are those parameters that completely depend on the sample under an investigation like the Raman peak positions of the sample (ω_R). Out of all these experiment-specific parameters, only pinhole widths can be changed to reliably determine the SR.

We first studied the case where $\omega_R = 0$, by using atomic emission lines consisting of a single wavelength that is measured as a function of pinhole width. This reveals the true

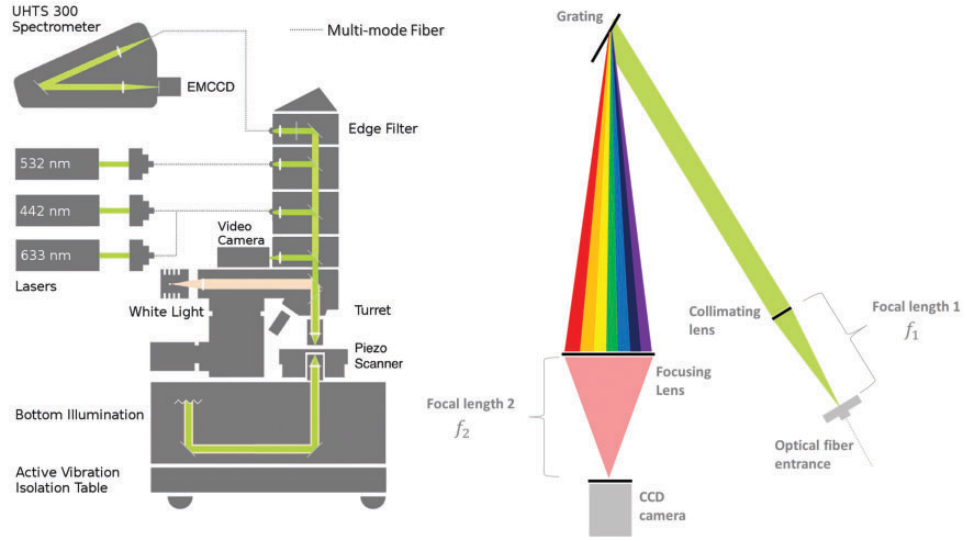

Figure 1. Schematic of the optical path of WITec alpha 300RAandS. Left: Beam path of the confocal Raman microscope. Right: Beam path inside the spectrometer.

potential and the limit of determining the SR. For this reason, these lamps that are emitting a single frequency are generally used for calibration of the setups.[23,24] Here, a neon lamp is used. The lamp is placed directly under the 100× (NA = 0.9) objective so that the light follows the optical path like from any other sample. For the experiment, the emission line at 640.2 nm with a natural line width of 0.0001 nm was chosen and the results are shown in Fig. 2.[25,26]

Figures 2a and 2c show the emission line of the neon lamp at 640.2 nm depending on available pinhole widths for both the gratings. At smaller pinhole widths (10 μm, 25 μm) the emission line is sharper compared to the emission lines at larger widths (50 μm, 100 μm). This can be explained by the fact that with larger pinhole diameters the point source becomes broader resulting in a broadened line width. It can be observed that there is a gradual shift observed in the emission line position starting from pinhole width 100 μm to 10 μm. Although the line under investigation has a very narrow linewidth, it is significantly broadened when measured with 100 μm pinhole width (broad top-hat function). The emission lines positions observed in the Figs. 2a and 2c range from 640.17 nm to 640.2 nm. If calculated, the Raman shift would be $\Delta\omega_L \sim 2$–$3\ \mathrm{cm}^{-1}$, all other measurements with smaller pinhole widths lie in this range. This small value does not affect our calculated results later on and hence can be neglected. Each of the spectra in both Figs. 2a and 2c looks edged and does not have a typical Lorentzian line shape. This is because of the CCD pixel widths in which the density of CCD pixels is not enough to give a perfect line shape to the spectra. Figures 2b and 2d show the experimentally measured FWHM plotted along with the theoretically calculated SR using Eq. 1. Substituting $\omega_L = 640.2$ nm and $\omega_R = 0$ in Eq. 1, yields for the 1800 l/mm grating, a fitting value of Q that is 10 ± 5 and for the 600 l/mm grating, the value of Q that fits best is 50 ± 5. These values of Q give the best fit with experimentally measured results.

For both gratings, experimentally measured data fit very well to the theoretically calculated values and deviates only for the smallest pinhole widths (10 μm). This disagreement is because of two reasons: first, at smaller pinhole widths the effects of aberration/diffraction become more prominent, and second, the width of the CCD pixels yielding an artificial broadening. For samples containing almost single frequencies (in this case a neon lamp), the constituent dispersion does not cause as many aberration/diffraction effects. Thus, this disagreement can arise due to the width of the CCD pixels and this agrees with previously published literature for smaller slit widths.[21]

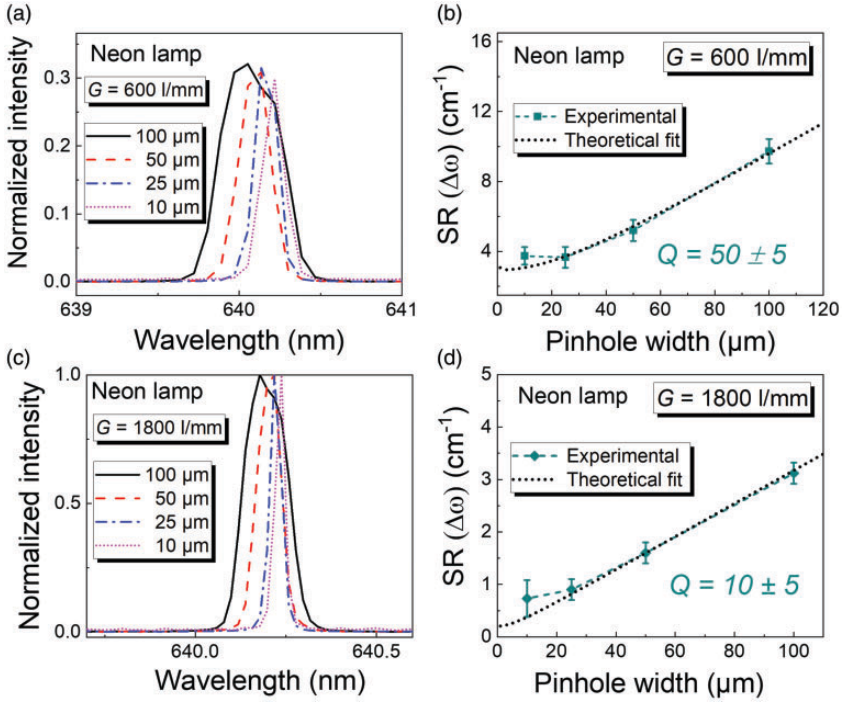

Figure 2. (a) Neon lamp spectra at 640.2 nm measured with different pinhole widths and a grating of 600 lines/mm, (b) experimentally measured and theoretically calculated FWHM plotted as a function of pinhole width and a grating of 600 lines/mm using Eq. 1, (c) neon lamp spectra measured with different pinhole widths and a grating of 1800 lines/mm, and (d) experimentally measured and theoretically calculated FWHM plotted as a function of pinhole width and a grating of 1800 lines/mm using Eq. 1.

To interpret these results, it is important to better understand *Q*. If the value of *Q* is changed then the agreements between the experimentally measured values and theoretically calculated values also change. An example of this is shown in Fig. 3.

Figure 3 shows the various values of *Q* ranging from 10 to 100 fitted to the experimentally measured data shown in Fig. 2b. It can be seen that for $Q = 50$, it gives the best theoretical fit for the experimentally measured data using Eq. 1. It can be observed that at higher values of *Q* the SR gets worse, and the effect of the pinhole size becomes smaller. Therefore, the quality factor *Q* can be directly related and defined by aberrations–diffraction effects occurring in the setup due to misalignment in the optical path. The higher the *Q* value, the higher the aberration/diffractions leading to a lower SR and vice versa. However, SR also depends on the excitation wavelength, thus a larger wavelength chosen would give a better SR. Such a relation is plotted in the Fig. S2a, (Supplemental Material) for both the gratings and is also known from the literature.[21]

Now, in the case of $\omega_R \neq 0$, by using a Raman scatterer (diamond, in this case) for three different lasers, values of ω_L (442 nm, 532 nm, 633 nm) are investigated. Diamond has a peak position at 1332.4 cm^{-1} corresponding to the triply degenerated vibration of the two Bravais lattices of the carbon atoms and with a natural bandwidth of 1.2 cm^{-1}.[22,27,28] The neon lamp used before has a natural line width that is much narrower than the natural linewidth of diamond and this difference must be considered. An analysis of the Raman spectrum of diamond with the same methodology is shown in Fig. 4.

Figures 4a and 4c show the spectra of a diamond measured at different pinhole widths for both the gratings and three excitation sources. The spectra do not have a typical Voigt line shape due to the limitation in the CCD pixel width as discussed earlier. However, it can be seen that the SR improves with larger wavelengths. It can also be observed that with different wavelengths of excitation, the peak position of the diamond (at 1332.4 cm^{-1}) also shifts. However, this peak position shift does not affect our results later and hence can be ignored but must be considered where wavenumber accuracy plays a role. Figure 4b shows the results of the experiment with a 600 l/mm grating for three different values of ω_L. The natural linewidth of a diamond is 1.2 cm^{-1} and is within the CCD resolution, so it is much larger than the natural linewidth of the neon lamp.

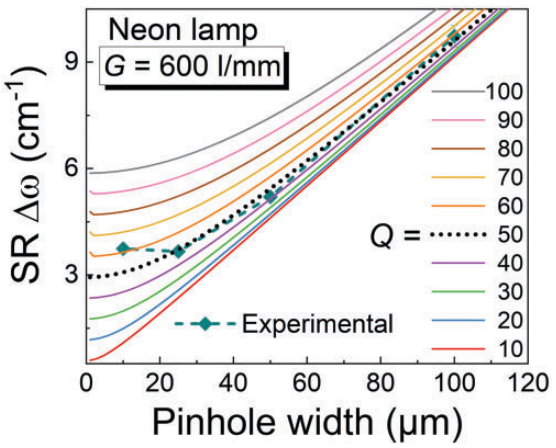

Figure 3. Different values of Q simulated to the experimentally measured results from Fig. 2.

As a consequence, there is almost no deviation between the experimental value and the theoretical fit as can be seen in Figs. 4b and 4d for a pinhole width of 10 μm. The *Q* value for the 633 nm excitation source (red curve) obtained is 100 ± 10, for 532 nm (green curve) and 442 nm (blue curve) are 80 ± 10. Figure 4d shows the results of the experiment with an 1800 l/mm grating, for three different values of ω_L. It is found that the experimentally measured values agree with the theoretically calculated values, and *Q* is 110 ± 10 for all three excitation sources.

According to Eq. 1, SR is inversely proportional to ω_L and ω_R, these are the two main reasons why the numeric value of SR varies here. The experiments are shown in Figs. 2 and 4 differ only in ω_L and ω_R. The experiments shown in Fig. 2 have only an excitation emission line $\omega_L = 640.2$ nm and $\omega_R = 0$. The natural linewidth is narrow and, hence, the SR is low. This results in the *Q* value of 10 ± 5 (for 600 l/mm grating) and 50 ± 5 (for 1800 l/mm grating). The diamond experiments as shown in Fig. 4 have three different excitation sources $\omega_L = 442$ nm, 532 nm, and 633 nm, and $\omega_R = 1332$ cm^{-1}. Here, the natural linewidth of the sample depends also on ω_R resulting in broader line. This results in SR being higher than for neon emission lines and hence the value of *Q* is higher.

The value of *Q* depends on ω_L and ω_R and will change if any one of them varies. For example, if ω_R is further increased to 3000 cm^{-1}, this would result in a lower natural line width of the peak resulting in a different value of SR and, hence, a different value of *Q*. Such a dependence of SR as a function of ω_R is shown in the Fig. S2b (Supplemental Material) for three excitation wavelengths and two gratings.

The value of *Q* can be manipulated to find the best fit between experimental and theoretical results. In Fig. 4b, it can be observed the SR are approximately similar with a grating 600 l/mm at smaller pinhole widths (10 μm/25 μm), for excitation sources 532 nm (green curve) and 633 nm (red curve). The deviation occurs only from a pinhole width of 50 μm. This is because with ω_L values being so close to each other (532 nm and 633 nm) the SR cannot be properly differentiated due to the lack of CCD pixel resolution for this grating. With 1800 l/mm grating as shown in Fig. 4c, it is worthwhile to note that at 10 μm pinhole width using a 633 nm excitation source the SR

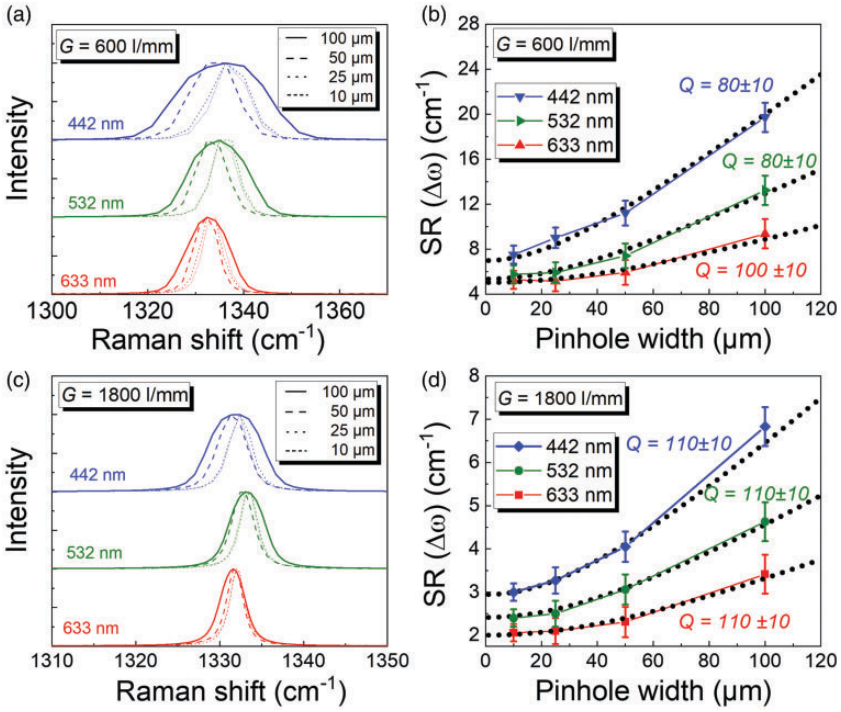

Figure 4. (a) Diamond spectra measured with 600 lines/mm grating with three excitation wavelengths, (b) measured FWHM of diamond spectra at 1332.4 cm^{-1} for 600 lines/mm measured with pinhole widths 10 µm, 25 µm, 50 µm, and 100 µm and different excitation wavelengths 442 nm (blue symbols), 532 nm (green symbols), and 633 nm (red symbols compared to theoretical calculations as per Eq. 1; black dashed lines), (c) diamond spectra measured with 1800 lines/mm grating with three excitation wavelengths, and (d) measured FWHM of diamond spectra at 1332.4 cm^{-1} for 1800 lines/mm measured with pinhole widths 10 µm, 25 µm, 50 µm, and 100 µm and different excitation wavelengths 442 nm (blue symbols), 532 nm (green symbols), and 633 nm (red symbols) compared to theoretical calculations per Eq. 1 (black dashed lines).

obtained is approximately 2 cm^{-1}. This FWHM of the measured peak is very close to the true bandwidth of the diamond that is 1.2 cm^{-1}. For a real-life sample if the combination of larger ω_L and smaller pinhole width, the SR can be close to the natural bandwidth of the sample. Overall, the experiments shown prove that the quality of the spectrometer used is good.

Our results differ slightly from the previously published literature by Liu and Berg.[21] We believe the principal reason for this is the different designs of the spectrometer. They characterized the SR of an uncrossed Czerny–Turner spectrometer (designed by Renishaw) and obtained a correction factor *A* (in their paper) to be 100. In their work *A* remains the same for the diamond sample as well as for a mercury lamp and does not change with a change in grating or excitation source. Nevertheless, the SR of the mercury lamp was comparable to the SR of our diamond sample at the 532 nm excitation source.

Spectral resolution as per Eq. 1 should also depend on the pixel density of the CCD camera and this can also change with the readout mode of the CCD camera. Experiments were performed keeping this in mind and changing the binning of the CCD camera resulting in no change in the SR. This is because the multimode fiber and its core diameter act as the entrance aperture of the spectrometer, eliminating the necessity of an additional slit system at the exit of the spectrograph. An additional slit system would cause the dispersed light to fall only on certain defined pixels of the CCD which might affect SR. In our case, the dispersed light covers the entire CCD chip thus the effect of SR only depends on the core diameter size of the multimode fiber.

Conclusion

The spectral resolution (SR) of a lens-based Raman spectrometer (WITec alpha300 RAandS) is influenced by instrument-specific, experiment-specific, and sample-specific parameters. To determine the SR, two cases were considered from Eq. 1, first $\omega_L \neq 0$: $\omega_R = 0$, and second $\omega_L \neq 0$: $\omega_R \neq 0$. For the first case ($\omega_L \neq 0$; $\omega_R = 0$), a neon lamp was used, and the SR of an emission line at $\omega_L = 640.2$ nm was characterized. The narrow natural line width of an atomic emission line depicts the best possible SR attainable by a spectrometer. It was found that with the best possible SR was with 1800 l/mm grating and 10 µm pinhole width the attainable SR can approach values near or below 1 cm^{-1}. The *Q* value or the quality factor depends

on the agreement between the experimentally obtained and theoretically calculated results. The best-simulated agreement between them gives the value of *Q*. It was found out that for 600 l/mm grating, the *Q* value obtained was 50 ± 5 and for 1800 l/mm the *Q* value obtained was 10 ± 5.

For the second case ($\omega_L \neq 0 : \omega_R \neq 0$), a diamond sample was used ($\omega_R = 1332.4\,cm^{-1}$) and three excitation wavelengths ω_L (442 nm, 532 nm, and 633 nm). It was found that the best obtained SR was for $\omega_L = 633$ nm and a pinhole width of 10 μm resulting in a value of $\Delta\omega_R = 2\,cm^{-1}$. This value of SR is very close to the natural FWHM of diamond ($\Delta\omega_R = 1.2\,cm^{-1}$), and hence proves the quality of the spectrometer. The *Q* value obtained for 600 l/mm grating is 80 ± 10 (for 442 nm and 532 nm) and 100 ± 10 (for 633 nm). Whereas for 1800 l/mm, the *Q* value obtained is 110 ± 10 for all excitation wavelengths. In these experiments the value of *Q* is higher than for neon lamp experiments since the natural linewidth of a diamond is considerably higher than the neon lamp emission line.

Determining the quality factor *Q* and the SR of a spectrometer is straightforward with standard samples as shown here. It is therefore advisable to routinely perform the described protocol to monitor the quality of the setup and thus ensure the quality of the results in the long run.

Acknowledgments

The authors would like to thank WITec GmbH (Ulm, Germany) for their kind support and fruitful discussions.

Declaration of Conflicting Interests

The author(s) declared no potential conflicts of interest with respect to the research, authorship, and/or publication of this article.

Funding

The author(s) disclosed receipt of the following financial support for the research, authorship, and publication of this article: The authors would like to acknowledge the financial support within the framework IngenieurNachwuchs 2016 (project: CompeTERS) by the German Federal Ministry of Education and Research (BMBF; Grant no.: 13FH596IX6).

ORCID iDs

Ashutosh Mukherjee https://orcid.org/0000-0002-8162-598X
Anita Lorenz https://orcid.org/0000-0003-4658-9036

Supplemental Material

All supplemental material mentioned in the text is available in the online version of the journal.

References

1. C.V. Raman, K.S. Krishnan. "A New Type of Secondary Radiation". Nature. 1928. 121(3048): 501–502. doi: 10.1038/121501c0.
2. A.S. Nielsen, D.N. Batchelder, R. Pyrz. "Estimation of Crystallinity of Isotactic Polypropylene Using Raman Spectroscopy". Polymer. 2002. 43(9): 2671–2676. doi: 10.1016/S0032-3861(02)00053-8.
3. G.R. Strobl, W. Hagedorn. "Raman Spectroscopic Method for Determining the Crystallinity of Polyethylene". J. Polym. Sci. Polym. Phys. Ed. 1978. 16(7): 1181–1193. doi: 10.1002/Pol.1978.180160704.
4. C. Casiraghi. "Raman Intensity of Graphene". Phys. Status Solidi B. 2011. 248(11): 2593–2597. doi: 10.1002/Pssb.201100040.
5. J.F. Digregorio, T.E. Furtak. "Analysis of Residual Stress in 6H-SiC Particles Within Al_2O_3/SiC Composites Through Raman Spectroscopy". J. Am. Ceramic Soc. 1992. 75(7): 1854–1857. doi: 10.1111/J.1151-2916.1992.Tb07207.X.
6. J.F. Digregorio, T.E. Furtak, J.J. Petrovic. "A Technique for Measuring Residual Stress in Sic Whiskers Within an Alumina Matrix Through Raman Spectroscopy". J. Appl. Phys. 1992. 71(7): 3524–3531. doi: 10.1063/1.350907.
7. I.-H. Lee, I.-H. Choi, C.-R. Lee, E.-J. Shin, et al. "Stress Relaxation in Si-Doped GaN Studied by Raman Spectroscopy". J. Appl. Phys. 1998. 83(11): 5787–5791. doi: 10.1063/1.367501.
8. V.K. Mitra, W.M. Risen, R.H. Baughman. "A Laser Raman Study of the Stress Dependence of Vibrational Frequencies of a Monocrystalline Polydiacetylene". J. Polym. Sci. Polym. Phys. Ed. 1977. 66(6): 2731–2736. doi: 10.1063/1.434219.
9. I. De Wolf, H.E. Maes, S.K. Jones. "Stress Measurements in Silicon Devices Through Raman Spectroscopy: Bridging the Gap Between Theory and Experiment". J. Appl. Phys. 1996. 79(9): 7148–7156. doi: 10.1063/1.361485.
10. A.C. Ferrari. "Raman Spectroscopy of Graphene and Graphite: Disorder, Electron–Phonon Coupling, Doping, and Nonadiabatic Effects". Solid State Commun. 2007. 143(1–2): 47–57. doi: 10.1016/J.Ssc.2007.03.052.
11. H. Liu, Y. Liu, D. Zhu. "Chemical Doping of Graphene". J. Mater. Chem. 2011. 21(10): 3335–3345. doi: 10.1039/C0JM02922J.
12. C. Stampfer, F. Molitor, D. Graf, K. Ensslin, et al. "Raman Imaging of Doping Domains in Graphene On SiO_2". Appl. Phys. Lett. 2007. 91(24): 241907. doi: 10.1063/1.2816262.
13. L. Zhang, T. Fujita, F. Chen, D.L. Feng, et al. "Doping and Temperature Dependence of Raman Scattering From NdFeAsO1−xFx(x=0–0.2) Superconductor". Phys. Rev. B. 2009. 79(5). doi: 10.1103/Physrevb.79.052507.
14. I. Calizo, A.A. Balandin, W. Bao, F. Miao, et al. "Temperature Dependence of the Raman Spectra of Graphene and Graphene Multilayers". Nano Lett. 2007. 7(9): 2645–2649. doi: 10.1021/Nl071033g.
15. T.R. Hart, R.L. Aggarwal, B. Lax. "Temperature Dependence of Raman Scattering in Silicon". Phys. Rev. B. 1970. 1(2): 638–642. doi: 10.1103/Physrevb.1.638.
16. R. Cuscó, E. Alarcón-Lladó, J. Ibáñez, L. Artús, et al. "Temperature Dependence of Raman Scattering in ZnO". Phys. Rev. B. 2007. 75(16): G3. doi: 10.1103/Physrevb.75.165202.
17. K.M. Rosfjord, R.A. Villalaz, T.K. Gaylord. "Constant-Bandwidth Scanning of the Czerny–Turner Monochromator". Appl. Opt. 2000. 39(4): 568–572. doi: 10.1364/AO.39.000568.
18. A.B. Shafer, L.R. Megill, L. Droppleman. "Optimization of the Czerny–Turner Spectrometer". J. Opt. Soc. Am. 1964. 54(7): 879. doi: 10.1364/JOSA.54.000879.
19. J.M. Simon, M.A. Gil, A.N. Fantino. "Czerny–Turner Monochromator: Astigmatism in the Classical and in the Crossed Beam Dispositions". Appl. Opt. 1986. 25(20): 3715. doi: 10.1364/AO.25.003715.
20. G. Tondello, F. Zanini. "High-Resolution Czerny–Turner Monochromator for Application to Undulators". Rev. Sci. Instrum. 1989. 60(7): 2116–2119. doi: 10.1063/1.1140840.
21. C. Liu, R.W. Berg. "Determining the Spectral Resolution of a Charge-Coupled Device (CCD) Raman Instrument". Appl Spectrosc. 2012. 66(9): 1034–1043. doi: 10.1366/11-06508.

22. S. Prawer, R.J. Nemanich. "Raman Spectroscopy of Diamond and Doped Diamond". Philos. Trans. R. Soc., A. 2004. 362(1824): 2537–2565. doi: 10.1098/Rsta.2004.1451.
23. W.J. Orville-Thomas. "Basic Laser Raman Spectroscopy". J. Mol. Struct. 1971. 9(4): 490. doi: 10.1016/0022-2860(71)87045-X.
24. S.B. Kim, R.M. Hammaker, W.G. Fateley. "Calibrating Raman Spectrometers Using a Neon Lamp". Appl Spectrosc. 1986. 40(3): 412–415. doi: 10.1366/0003702864509231.
25. S.A. Kandela, H. Schmoranzer. "Precision Lifetime Measurement of Fine Structure States in the NeI 2p53p Configuration". Phys. Lett. A. 1981. 86(2): 101–104. doi: 10.1016/0375-9601(81)90176-6.
26. M.J. Seaton. "Oscillator Strengths in NeI". J. Opt. Soc. Am. 1998. 31(24): 5315–5336. doi: 10.1088/0953-4075/31/24/013.
27. R.S. Krishnan. "Raman Spectrum of Diamond". Nature. 1945. 155(3928): 171. doi: 10.1038/155171a0.
28. S. Bhagavantam. "Normal Oscillations of the Diamond Structure". Proc. Indian Acad. Sci. (Math. Sci.). 1943. 18(5): 251–256. doi: 10.1007/BF03046532.

5. Differentiation of salivary gland and Salivary gland tumor tissue by Raman imaging combined with multivariate data Analysis

Miriam C. Bassler[1,2], Mona Stefanakis[1,2], Elena Gerhard-Hartmann[3], Ashutosh Mukherjee[1,2], Almoatazbellah Youssef[3], Rudolf Hagen[4], Agmal Scherzad[4], Manuel Stöth[4], Edwin Ostertag[1], Maria Steinke[5], Marc Brecht[1,2], Stephan Hackenberg[6], and Till Jasper Meyer[4]*

[1]Process Analysis and Technology (PA&T) Reutlingen University, Alteburgstr. 150, 72762 Reutlingen, Germany

[2]Institute of Physical and Theoretical Chemistry University of Tübingen, Auf der Morgenstelle 18, 72076 Tübingen, Germany

[3]University of Würzburg, Institute of Pathology, Josef-Schneider-Str. 2, 97080 Würzburg, Germany

[4]University Hospital Würzburg, Department of Oto-Rhino-Laryngology, Plastic, Aesthetic & Reconstructive Head and Neck Surgery, Josef-Schneider-Str. 11, 97080 Würzburg, Germany

[5]University Hospital Würzburg, Chair of Tissue Engineering and Regenerative Medicine, Röntgenring 11, 97070 Würzburg, Germany

[6]RWTH Aachen University Hospital, Department of Otorhinolaryngology – Head and Neck Surgery, Pauwelsstr. 30, 52074 Aachen, Germany

This chapter was originally published in MDPI-Diagnostics as,

Bassler, M.C.; Knoblich, M.; Gerhard-Hartmann, E.; Mukherjee, A.; Youssef, A.; Hagen, R.; Haug, L.; Goncalves, M.; Scherzad, A.; Stöth, M.; et al. Differentiation of Salivary Gland and Salivary Gland Tumor Tissue via Raman Imaging Combined with Multivariate Data Analysis. Diagnostics 2024, 14, 1, 92.

DOI: https://doi.org/10.3390/diagnostics14010092

Supplementary Material/Supporting Information shown in Appendix 2

diagnostics

MDPI

Article

Differentiation of Salivary Gland and Salivary Gland Tumor Tissue via Raman Imaging Combined with Multivariate Data Analysis

Miriam C. Bassler [1,2], Mona Knoblich [1,2], Elena Gerhard-Hartmann [3], Ashutosh Mukherjee [1,2], Almoatazbellah Youssef [3], Rudolf Hagen [4], Lukas Haug [3], Miguel Goncalves [4], Agmal Scherzad [4], Manuel Stöth [4], Edwin Ostertag [1], Maria Steinke [5,6], Marc Brecht [1,2,*], Stephan Hackenberg [4] and Till Jasper Meyer [4,*]

1 Process Analysis and Technology (PA&T), School of Life Science, Reutlingen University, Alteburgstr. 150, 72762 Reutlingen, Germany; miriam.bassler@reutlingen-university.de (M.C.B.); mona.knoblich@reutlingen-university.de (M.K.); ashutosh.mukherjee@reutlingen-university.de (A.M.); edwin.ostertag@rpt.bwl.de (E.O.)
2 Institute of Physical and Theoretical Chemistry, Faculty of Science, University of Tübingen, Auf der Morgenstelle 18, 72076 Tübingen, Germany
3 Institute of Pathology, University of Würzburg, Josef-Schneider-Str. 2, 97080 Würzburg, Germany; elena.hartmann@uni-wuerzburg.de (E.G.-H.); almoatazbellah.youssef@uni-wuerzburg.de (A.Y.); lukas.haug@uni-wuerzburg.de (L.H.)
4 Department of Oto-Rhino-Laryngology, Plastic, Aesthetic & Reconstructive Head and Neck Surgery, University Hospital Würzburg, Josef-Schneider-Str. 11, 97080 Würzburg, Germany; hagen_r@ukw.de (R.H.); goncalves_m@ukw.de (M.G.); scherzad_a@ukw.de (A.S.); stoeth_m@ukw.de (M.S.); hackenberg_s@ukw.de (S.H.)
5 Chair of Tissue Engineering and Regenerative Medicine, University Hospital Würzburg, Röntgenring 11, 97070 Würzburg, Germany; maria.steinke@isc.fraunhofer.de
6 Fraunhofer Institute for Silicate Research ISC, Röntgenring 11, 97070 Würzburg, Germany
* Correspondence: marc.brecht@reutlingen-university.de (M.B.); meyer_t2@ukw.de (T.J.M.); Tel.: +49-7121-271-2065 (ext. 2032) (M.B.); +49-931-201-21323 (T.J.M.)

Citation: Bassler, M.C.; Knoblich, M.; Gerhard-Hartmann, E.; Mukherjee, A.; Youssef, A.; Hagen, R.; Haug, L.; Goncalves, M.; Scherzad, A.; Stöth, M.; et al. Differentiation of Salivary Gland and Salivary Gland Tumor Tissue via Raman Imaging Combined with Multivariate Data Analysis. *Diagnostics* **2024**, *14*, 92. https://doi.org/10.3390/diagnostics14010092

Academic Editor: Qiwei Tian

Received: 6 November 2023
Revised: 10 December 2023
Accepted: 29 December 2023
Published: 30 December 2023

Abstract: Salivary gland tumors (SGTs) are a relevant, highly diverse subgroup of head and neck tumors whose entity determination can be difficult. Confocal Raman imaging in combination with multivariate data analysis may possibly support their correct classification. For the analysis of the translational potential of Raman imaging in SGT determination, a multi-stage evaluation process is necessary. By measuring a sample set of Warthin tumor, pleomorphic adenoma and non-tumor salivary gland tissue, Raman data were obtained and a thorough Raman band analysis was performed. This evaluation revealed highly overlapping Raman patterns with only minor spectral differences. Consequently, a principal component analysis (PCA) was calculated and further combined with a discriminant analysis (DA) to enable the best possible distinction. The PCA-DA model was characterized by accuracy, sensitivity, selectivity and precision values above 90% and validated by predicting model-unknown Raman spectra, of which 93% were classified correctly. Thus, we state our PCA-DA to be suitable for parotid tumor and non-salivary salivary gland tissue discrimination and prediction. For evaluation of the translational potential, further validation steps are necessary.

Keywords: salivary gland tumor; confocal Raman imaging; principal component analysis; discriminant analysis; multivariate data analysis; molecular diagnostics

1. Introduction

Salivary gland tumors (SGTs) are a sub-group of head and neck tumors and account for 3% to 6% of all head and neck neoplasms [1,2]. Most SGTs are of benign nature, representing approx. 80% of all incidences [3,4]. More than thirty different malignant and benign SGTs are known according to the 2017 WHO classification, of which the two main benign tumors are the cystadenolymphoma (Warthin tumor) and pleomorphic adenoma [5]. Due to the

high variety in tumor entities, a reliable diagnosis only based on histo- or cytomorphological criteria is difficult and sometimes impossible [6]. As a result, pre- and intraoperative malignancy assessment based on fine-needle aspiration cytology, core needle biopsy and open biopsy is sometimes unreliable [7–9]. However, reliable malignancy assignment is necessary to avoid revision surgery [10]. The cytological methods frequently used preoperatively and also intraoperative histopathological diagnostics highly depend on the experience of the pathologist and may occasionally be subject to uncertainties, even in the case of experienced diagnosticians [6].

In addition to standard cyto- and histopathologic approaches, spectroscopic methods in combination with multivariate data analysis (MVA) are finding increasing acceptance to support tumor diagnostic methodologies [11–17]. By applying different spectroscopy principles, either chemical or morphological signatures are obtained, which reveal tissue-related features and are thus highly tissue-specific. Due to improvements in spatial resolution and scanning speed, spectroscopic imaging became increasingly popular for data acquisition [18–20]. Consequently, large imaging data sets with a high spatial and spectral resolution are obtained [21,22]. The linkage with MVA techniques, such as principal component analysis (PCA), allows the extraction of the most relevant spectral characteristics from the imaging data and to distinguish the samples based on the previously extracted attributes [23,24]. A combination of PCA with discriminant analysis (DA) additionally describes the distinction in a quantitative manner and enables a prediction of non-included spectra or samples. Typical imaging methods applied for tumor diagnosis are Fourier-transform infrared spectroscopy [25], fluorescence [26] and Raman imaging [27], which are mainly associated with statistical tools, such as PCA, DA, support vector machine, the k-nearest neighbor algorithm or artificial neural network analysis [25,28–30]. The spectroscopy-based models are used for the identification or distinction of brain [31], colon [32], breast [33] or head and neck tumors [34,35].

First spectroscopic attempts of parotid tumor identification were performed using Raman spectroscopy coupled with support vector machine [36,37]. Further studies focused on identifying differences in lipid composition and changes in secondary protein structure between cancerous and non-cancerous salivary gland tissue using Raman imaging [38]. Our group just recently published a study employing Raman spectroscopy and PCA analysis to enable a differentiation between benign pleomorphic adenoma and low-malignant adenoid cystic carcinomas [39]. Although primary efforts in differentiating SGTs were achieved, no study on deploying spectral differences has been published yet to implement a Raman-MVA model as diagnostic adjunct and review its functionality.

To evaluate the translational potential of Raman imaging (RI) for the overarching objective to use RI for supporting SGT entity and malignancy determination, probably a multi-stage data analysis process will be necessary. Due to the high number of tumor entities of SGTs, a multi-stage process with identification of the spectra that were acquired in the tumor tissue and exclusion of all spectra that were acquired in the non-tumor salivary gland tissue could help to enhance the statistical accuracy. Therefore, our study deals with the implementation of a PCA-DA model using Raman imaging data of normal salivary gland tissue, Warthin tumor and pleomorphic adenoma to differentiate between the tissue types and predict unknown parotid samples. Relevant tissue regions of unstained parotid cross-sections are chosen based on a hematoxylin and eosin (HE) assessment and measured using Raman imaging. The obtained imaging data are initially analyzed via a detailed Raman band evaluation. Afterwards, a PCA is computed to achieve the best possible tissue type separation due to tissue-specific information and combined with a DA to enable the classification of model-unknown Raman spectra. By applying the final PCA-DA, new tissue areas of interest are tested and classified in a proof-of-principle concept. The assignments are validated by a corresponding HE diagnosis to confirm whether the PCA-DA predictions are correct. Final model classification abilities are expressed by the overall accuracy, sensitivity, specificity and precision. As a result of a successful PCA-DA implementation, its utilization as diagnostic assistance in the clinical routine might be possible.

2. Materials and Methods

2.1. Patient Selection and Parotid Tissue Sample Preparation

This study was approved by the institutional ethics committee on human research of the Julius-Maximilians-University Würzburg (vote 224/18). All experiments were performed according to the Declaration of Helsinki. All patients agreed to participate in this study through informed consent.

Patients with a salivary gland tumor (parotid tumor) were preoperatively screened, and respective tissue specimens were selected. Suitable tissue samples had to consist of either Warthin tumor (n = 5) or pleomorphic adenoma (n = 4) and non-tumor salivary gland tissue (n = 9) in order to be included in the final sample set. All tissues were identified by a trained pathologist.

Tissue specimens were initially cut into smaller tissue pieces, which were arranged to display tumor and non-tumor salivary gland tissue. Afterwards, the tissue pieces were frozen in this arrangement and a series of 10 µm thick consecutive cryosections was prepared. Parotid cryosections were placed onto quartz objective slides (Suprasil® 1, Aachener Quarzglas-Technologie Heinrich GmbH & Co. KG, Aachen, Germany) and subsequently fixed with a 4% paraformaldehyde solution (ROTI®Histofix 4%, Carl Roth, Karlsruhe, Germany) for 30 min. Following cross-section fixation, three washing steps with phosphate buffered saline were performed, and the samples were dried overnight at ambient temperature. These unstained sections were used for Raman imaging.

A detailed histopathological evaluation was applied based on corresponding 3 µm thick HE-stained cross-sections. The HE staining was performed according to a standardized protocol. HE cross-sections were analyzed and imaged using the BZ-9000 BIOREVO System (Keyence, Neu-Isenburg, Germany). Whole slide images were scanned at 40× using a slide scanner, Panoramic SCAN II (3DHISTECH, Budapest, Hungary).

2.2. Confocal Raman Imaging

Raman data acquisition was performed with a confocal microscopic setup (Alpha 300 RA&S, WITec, Ulm, Germany) according to the summarized measurement and data extraction workflow illustrated in Figure 1.

A confocal microscope system, equipped with a lens-based spectrometer (UHTS 300, WITec, Ulm, Germany) and a CCD camera (DU970, Andor Technology, Belfast, UK), was used for Raman imaging [40]. Excitation was performed with a 532 nm frequency-doubled Nd:YAG laser transmitted via a single-mode fiber onto the tissue cross-sections. The inelastically scattered light was collected with a 20× objective (EC Epiplan, 20×/0.4, Carl Zeiss AG, Oberkochen, Germany) and transferred to the spectrometer and CCD camera (EMCCD, 16 Bit, 1600 × 200 pixel, 16 µm × 16 µm, thermoelectrically cooled: −60 °C) via a 100 µm core diameter multimode fiber. Each Raman image encompassed a size of 20 µm × 20 µm and was acquired with a scan step size of 1 µm and a scan speed of 30 s/line. Thus, 20 × 20 spectra within the image were recorded with an integration time of 1.5 s per spectrum, resulting in a total number of 400 Raman spectra per tissue area. The Raman shift was recorded from 50 cm^{-1} to 3670 cm^{-1} with a 600 g/mm (blaze wavelength (BLZ) = 500 nm) grating and centering the spectrometer at 2000 cm^{-1}. The spectral resolution of the optical system was 2 cm^{-1} [41]. Overall, three tumorous areas (Warthin tumor or pleomorphic adenoma) and three salivary gland areas per tissue sample and patient were selected for Raman imaging. Following image acquisition, Raman spectra were subtracted from the quartz background and treated with a baseline fluorescence correction (shape: 100) and a cosmic ray correction (filter size: 2, dynamic factor: 8).

2.3. Data Pre-Treatment and Multivariate Data Analysis

MVA was performed with The Unscrambler X 10.5 (Camo Analytics AS, Oslo, Norway). All model-included Raman mean spectra were preprocessed equally by applying a standard normal variate transformation followed by a Savitzky–Golay smoothed 1st order derivative (2nd polynomial order, symmetrical 41 points). The spectral area of

900–1750 cm^{-1} was used for MVA calculations, while additional spectrum ranges (50 cm^{-1} to 900 cm^{-1}, 1750 cm^{-1} to 3670 cm^{-1}) without relevant information were excluded for variable reduction. The PCA was calculated with mean centering, a full cross-validation and the singular value decomposition algorithm to distinguish between the different parotid tissue types. Model outliers were identified in the influence plot hotelling's T^2 versus F-residuals (outlier limits 5% each) and excluded from the model if proven to be true.

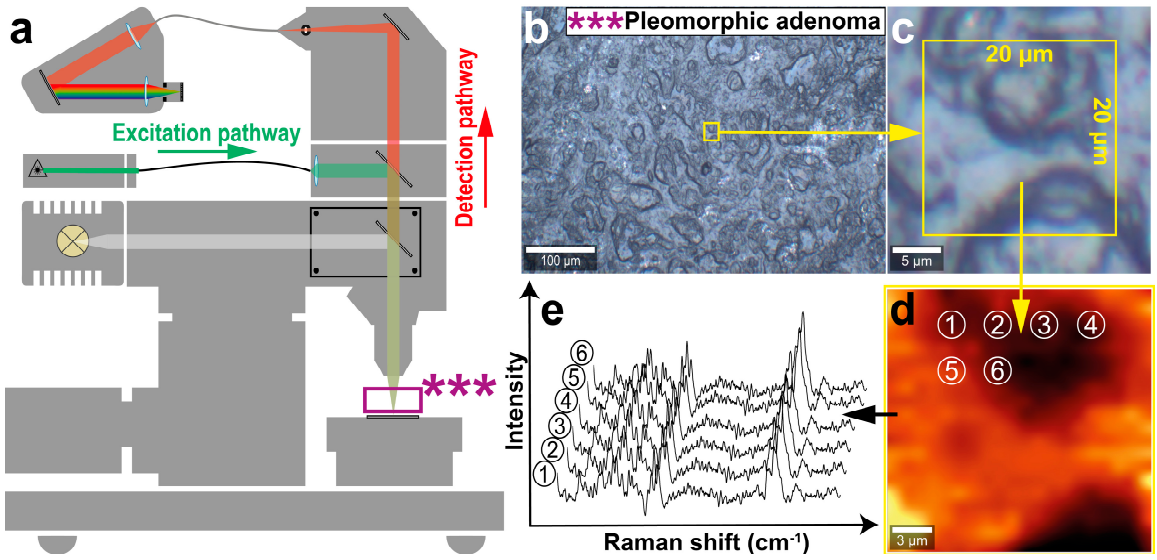

Figure 1. Schematic acquisition workflow for Raman imaging of parotid tissue cross-sections and data extraction. Raman images were recorded with the WITec Alpha 300 RA&S using a 532 nm frequency-doubled Nd:YAG laser for excitation purposes (**a**). Initially, a suitable tissue region was chosen in an overview brightfield image, which was in accordance with the corresponding HE evaluation ((**b**), *** marks the sample). In this overview image, a 20 µm × 20 µm tissue area of interest ((**b**,**c**), yellow box) was determined and Raman imaged in a stepwise manner. The obtained Raman image (**d**) is composed of single Raman spectra (1–6) located at distinct x,y-positions. Raman spectra were extracted individually for PCA-DA model formation (**e**).

PCA was combined with DA by using the Mahalanobis distance algorithm and PCA score values. The number of deployed principal components (PCs) for the DA was similar to the shown PCA model. In total, 5 PCs were applied for calculating the DA. The overall accuracy, sensitivity, specificity and precision of the PCA-DA model were additionally calculated based on the confusion matrix terminology [42,43].

3. Results

3.1. Raman Mean Spectra Analysis

To reveal significant spectral differences, Raman mean spectra for normal salivary gland, Warthin tumor and pleomorphic adenoma tissues were compared and calculated by averaging all respective Raman spectra to one overall mean spectrum including the corresponding 95% confidence interval, illustrated in Figure 2. Potential differences between the spectra can be a varying number of Raman bands, a changing relation between bands or different intensities or variations in shape. From 500 cm^{-1} to 3500 cm^{-1} (Figure 2a), no clear spectral variations are distinguishable. Two major bands at 746 cm^{-1} and 2927 cm^{-1} correspond to a ring breathing of DNA/RNA bases and to CH/CH_3 vibrations of lipids and proteins, respectively, and are identical in each spectrum. A detailed band analysis in the range of 900–1700 cm^{-1} was performed, and main spectral differences were highlighted (Figure 2b, (1)–(14)). A superimposed illustration of this range is shown in Figure S1, Supplementary information and a summary of all Raman signal assignments is presented in Table 1.

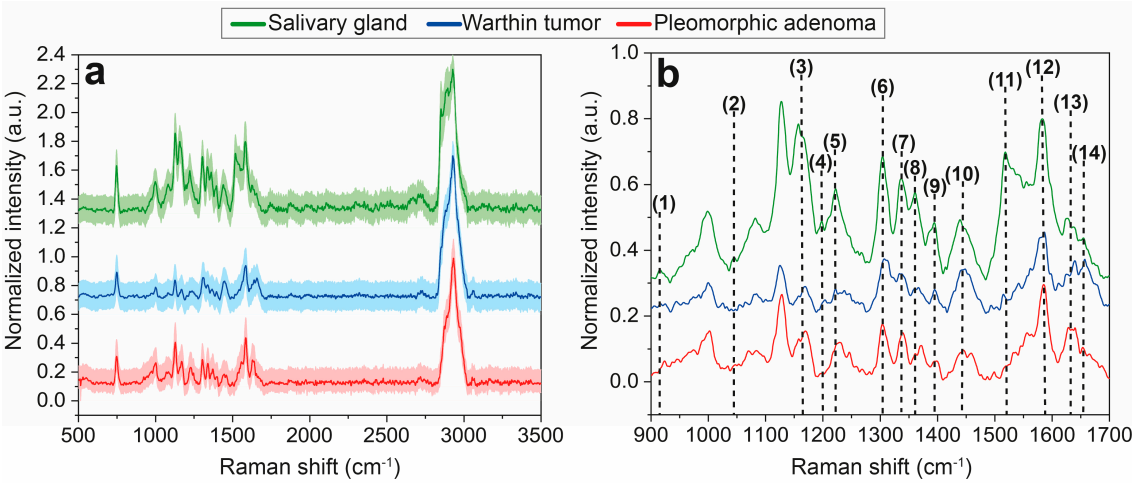

Figure 2. Overall Raman mean spectra with corresponding 95% confidence intervals (light colors) of normal salivary gland tissue (green), Warthin tumor (blue) and pleomorphic adenoma (red), illustrated in a Raman shift region of 500–3500 cm^{-1} (**a**). Main spectral differences were noticed between 900 and 1700 cm^{-1}, which was analyzed in more detail (**b**). In this region, distinct Raman band assignments were performed (1–14). The spectra are vertically displayed. Corresponding molecular vibrations and causes are comprehensively listed in Table 1.

Table 1. Raman band assignments for non-tumor salivary gland tissue, Warthin tumor, pleomorphic adenoma. Column 1 indicates the number assigned to the corresponding Raman band in the overall mean spectra (Figure 2b). Column 2 reveals the distinct relative shift (cm^{-1}) of each Raman band identified in the mean spectra. The molecular vibration (column 3) resulting from specific molecules (column 4) within the tissues are listed. In column 5, all references of the Raman band assignments are summarized.

Number	Raman Shift/cm^{-1}	Assignment	Cause	Reference [44]
(1)	915; 920	-; C-C stretch	Ribose RNA; collagen	[45,46]
(2)	1043	ring stretching	Collagen proline	[46]
(3)	1158; 1168	C-N stretching; ν(C=C); ν(C-C)	Proteins/lipids	[47,48]
(4)	1197; 1204	Antisymmetric phosphate vibrations; amide III, CH_2 wagging vibrations	Glycine backbone or proline side chains	[48,49]
(5)	1222; 1228	C-N stretching and N-H bending, thymine, adenine stretch	Amide III, proteins, DNA/RNA	[47,50]
(6)	1304	CH_2/CH_3 deformation, twisting or bending	Lipids, collagen	[46,51]
(7)	1337	CH_2/CH_3 wagging, twisting and/or bending mode	Collagens, lipids, amide III (proteins)	[45,48,52]
(8)	1360	-	Tryptophan	[44]
(9)	1396	-	β-carotene	[44]
(10)	1443; 1454	CH_2 deformation; CH_2 stretching/CH_3 asymmetric deformation	Lipids, proteins, triglycerides (fatty acids); elastin, collagen, phospholipids	[51,53–55]
(11)	1517	C-C stretch mode	β-Carotene accumulation	[53]
(12)	1585	C=C olefinic stretch	Proteins	[54,56]
(13)	1628; 1640	C_α=C_α stretch; -	Proteins; amide I (proteins)	[44,57]
(14)	1654	C-C stretch, C=O stretching mode	Amide I (proteins), collagen, lipids	[46,48,51]

At 915 cm^{-1}, one distinct weak Raman band (1) occurs for normal salivary gland tissue, which is less pronounced or even absent for both parotid tumors (Figure 2b), and can be assigned to vibrations of ribose RNA (Table 1). Instead, pleomorphic adenoma tissue reveals a band at 920 cm^{-1} that can be ascribed to a C-C stretching of collagen proline,

which is also visible in the Warthin tumor, but far less distinctive. A further spectral band at 1043 cm^{-1} (2) is clearly illustrated for the salivary gland tissue, but missing for both tumors that can also be assigned to collagen proline (Figure 2b, Table 1). Varying intensity relations can be observed for two bands at 1158 cm^{-1} and 1168 cm^{-1} (3). In case of salivary gland tissue, the band at 1158 cm^{-1} is more highlighted than the second band at 1168 cm^{-1}, which is opposite for the Warthin tumor and pleomorphic adenoma tissues. Both Raman bands can mainly be deduced from C-N and C-C stretching vibrations of proteins and C-C/C=C lipid oscillations (Table 1). While salivary gland and pleomorphic adenoma tissues exhibit a Raman band at 1197 cm^{-1} (4), the Warthin tumor exposes a slightly shifted band maximum at 1204 cm^{-1} (4, Figure 2b). The bands can either be allocated to antisymmetric phosphate (1197 cm^{-1}) or amide III and CH_2 wagging vibrations (1204 cm^{-1}) of glycine backbone or proline side chains (Table 1). Changes in band intensity, shape and position between the tissue types are indicated for the 1222 cm^{-1} band (5). It is most intense for salivary gland tissue, but varies in intensity and shape for Warthin tumor tissue and is even slightly shifted for pleomorphic adenoma tissue (1228 cm^{-1}) (Figure 2b). The two signals (1222 cm^{-1} and 1228 cm^{-1}) are mainly assignable to amide III vibrations of proteins and thymine/adenine stretching of DNA/RNA (Table 1). Between 1300 and 1400 cm^{-1}, a series of distinct Raman bands (6–9) occurs in all three Raman mean spectra with pronounced shoulders or double maxima mainly for Warthin tumor tissue (6–8), but also for salivary gland (9) and pleomorphic adenoma (8) tissues, respectively. Reasons for the occurrence of these Raman bands are oscillations of lipids, collagens, proteins, tryptophan and β-carotene within the respective tissues (Table 1). Additional differences in intensity relations emerge between two Raman band maxima at 1443 cm^{-1} and 1454 cm^{-1} (10), which reveal a slightly more emphasized first maximum at 1443 cm^{-1} in the salivary gland and Warthin tumor spectra compared to the second band at 1454 cm^{-1}. In contrast, pleomorphic adenoma tissue shows equally dominant Raman bands for both (Figure 2b). The two bands are mainly caused by the CH_2/CH_3 stretching of proteins, lipids, triglycerides and collagen (Table 1). A Raman band at 1517 cm^{-1} (11) is observed for salivary gland tissue with the highest intensity, followed by Warthin tumor and pleomorphic adenoma tissues with a decreasing peak appearance. This band is ascribable to the C-C stretching mode of β-carotene (Table 1). The Raman band at 1585 cm^{-1} (12) solely exhibits an additional shoulder in the Warthin tumor spectrum, which is missing in the salivary gland and pleomorphic adenoma spectra and corresponds to a C=C olefinic stretching of proteins (Table 1). Signature differences between the parotid tissues can further be attributed to Raman bands at 1628 cm^{-1}/1640 cm^{-1} (13) and 1654 cm^{-1} (14), which mainly result from the C_α=C_α, C-C and C=O stretching modes of proteins, collagen and lipids (Table 1). Aside from these few spectral differences (1)–(14), the Raman patterns are highly similar and overlapping, with small signatures that can hardly be assigned to distinct vibrational modes. Therefore, a PCA evaluation is inevitable to extract minor pattern variations as a result of the high spectral similarity.

3.2. Raman Data Analysis via PCA-DA

Due to there being only minor Raman band differences in the overall mean spectra, an improved discrimination of all three tissue types is needed. This was accomplished by a PCA calculation. As a PCA allows the extraction of the most relevant and differing chemical information of the Raman spectra, a precise distinction of the tissue types is enabled. For this purpose, three tumorous areas (Warthin tumor or pleomorphic adenoma) and three non-tumor salivary gland tissue areas were selected for Raman image acquisition, which resulted in 6 × 400 Raman spectra (2400 spectra) for each patient. Consequently, 9 × 6 × 400 Raman spectra (21,600 spectra) were measured overall. Mean spectra were formed by averaging 100 adjacent, processed spectra, which yielded four spectra per tissue area. Therefore, a total number of 216 Raman mean spectra (48 pleomorphic adenoma, 60 Warthin tumor and 108 salivary gland tissue) were used to generate the PCA model. The final PCA is illustrated in Figure 3. Different perspectives of the 3D PCA scores plot are shown in Figure S2, Supplementary information. Since the most dominant changes

were previously identified within 900–1750 cm^{-1}, PCA was performed only on the basis of this region.

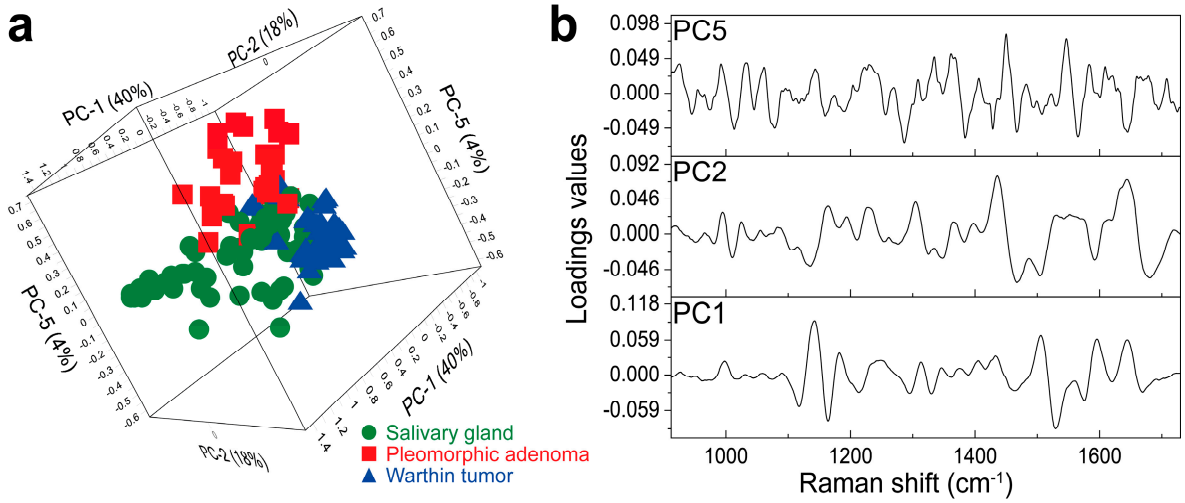

Figure 3. PCA model for the differentiation of salivary gland, Warthin tumor and pleomorphic adenoma. The 3D scores plot is illustrated in (**a**), displaying PC1 (40%), PC2 (18%) and PC5 (4%). A successful separation of salivary gland (green circles), Warthin tumor (blue triangles) and pleomorphic adenoma (red squares) clusters is achieved with only minor group overlaps in the center. The corresponding loading plots are shown in (**b**), revealing the main influencing Raman shift of PC1, PC2 and PC5 for the group segregation. To demonstrate the clear differentiation between parotid tissue clusters by the PCA model, various perspectives on the 3D scores plot are shown in Figure S2. Additional 2D scores and respective loading plots of all model-included PCs are summarized in Figure S3, Supplementary information.

The PCA model encompasses a total number of five PCs to distinguish between the different parotid gland tumors and the parotid gland tissues and reaches a total explained variance of 77%, considering PC1–PC5. The number of PCs was chosen based on the explained variance and the interpretable information on loadings [58–60]. The aim was to create a PCA-DA model with as few PCs as possible for a reliable prediction of the parotid tissue types. Information about the relation of the calibration and validation PCA is given in Figure S4, Supplementary information. Within the 3D scores plot (Figure 3a), PC1, PC2 and PC5 are presented, explaining 40%, 18% and 4% of the explained variance, respectively. The separation of the Warthin tumor cluster (blue triangles) has already been realized by PC1 and PC2. Here, the Warthin cluster is arranged almost completely below-average for PC1 and above-average for PC2. Additionally, PC1 and PC2 cause a group splitting of the salivary gland (green circles) and pleomorphic adenoma (red squares) cluster into mixed tissue type groups, respectively. Here, salivary gland and pleomorphic adenoma are randomly organized into above and below the average of PC1 and PC2, with no apparent cluster formation. This is more clearly shown in the 2D scores plot illustration in Figure S2, Supplementary information. Therefore, PC5 is required to clearly demarcate between salivary gland and pleomorphic adenoma spectra. Within the PC2/PC5 plane, the salivary gland cluster is completely structured below-average, whereas the pleomorphic adenoma group is organized above-average in terms of PC5 (Figure 3a). The Warthin group, however, is arranged above-average for PC2 and almost completely below-average for PC5 within this setting. As a result, a clear group separation between Warthin tumor, pleomorphic adenoma and salivary gland spectra is achieved, with only minor cluster overlaps at the center (Figure 3a). Although PC3 and PC4 explain 15% of the model variance, this represented information does not contribute to the tissue type differentiation. An overview of the complete PCA model including all PCs (PC1–PC5), as well as related 2D scores and loading plots, is represented in Figure S3, Supplementary information.

In Figure 3b, the corresponding loading plots of PC1, PC2 and PC5 are illustrated. The loadings plots display the highest spectral influence on the tissue type separation in the 3D scores plot. Some of the main influencing maxima can even be referred to Raman bands assigned in Figure 2. Negative maxima at 1164 cm^{-1} (3, Figure 2, Table 1) and 1530 cm^{-1} in the PC1 loadings have a major impact on the tissue separation (Figure 3b). Further influencing maxima can be defined at 1596 cm^{-1} and 1643 cm^{-1} (13, Figure 2, Table 1) according to the PC1 loadings. The PC2 loadings plot shows the most dominating impact between 1440 and 1680 cm^{-1} with main positive maxima at 1440 cm^{-1} (10, Figure 2, Table 1) and 1643 cm^{-1} (13, Figure 2, Table 1) and negative maxima at 1467 cm^{-1} and 1680 cm^{-1} (Figure 3b). Within the PC5 loadings, a few pronounced positive maxima can be determined at 1450 cm^{-1} (10, Figure 2, Table 1) and 1546 cm^{-1} as well as negative ones at 1285 cm^{-1} and 1384 cm^{-1}.

Based on the formed PCA model, a DA was subsequently calculated by using the PCA score values of PC1 to PC5 and the Mahalanobis distance algorithm. The PCA-DA's performance is evaluated using an internal validation process. For this purpose, each model-included spectrum was allocated to one tissue cluster as if it was not contained in the model. As a result, a confusion matrix is obtained (Table S1, Supplementary information), which describes the accordance of the model's assignments and the pathologist's diagnosis and is used to compute the model's accuracy, sensitivity, specificity and precision (Table 2). Salivary gland model spectra were most accurately assigned with 97% accuracy, whereas Warthin tumor spectra resulted in 91% correctly matched spectra. Pleomorphic adenoma is still allocated correctly with 89% accuracy. Due to the excellent group assignment of the model spectra, high performance parameters of 94% accuracy, 94% sensitivity, 95% specificity and 94% precision were accomplished (Table 2).

Table 2. Model performance parameters for the tissue entity distinction. All model-included Raman mean spectra (column 2) were ascribed to one tissue group in order to validate the PCA-DA. The total and relative (%) number of correctly assigned model spectra are listed in columns 3 and 4. Overall accuracy, sensitivity, specificity and precision of the model are summarized in columns 5–8.

Entity	Total Spectra	Correctly Assigned	Correctly Assigned/%	Accuracy /%	Sensitivity /%	Specificity /%	Precision /%
Salivary gland tissue	94	91	97	94	94	95	94
Pleomorphic adenoma	35	31	89				
Warthin tumor	47	43	91				

The PCA-DA was finally used to predict model-unknown Raman mean spectra of all investigated parotid tissues in order to verify the model's classification abilities. For this purpose, histopathologically distinct regions of non-tumor salivary gland tissue (Figure 4, 1–5, light blue squares) and tumor tissue (Figure 4, 1–5, black squares) were previously defined as suitable prediction regions on HE sections (Figure 4, 1). These HE regions were afterwards identified on the consecutive, unstained cross-section used for Raman imaging (Figure 4, 2; 1–5, light blue and black squares). After Raman image acquisition, mean spectra of the tissues were again calculated by processing and averaging 100 adjacent Raman spectra (Figure 4, 3 and 4). This second group of 15 Raman mean spectra (5 per entity; 1500 spectra) was predicted by the final PCA-DA model and evaluated whether they were classified falsely (red cross) or correctly (green check mark) (Figure 4, 5). This corresponded to an external model validation. The model prediction outcome was finally corroborated by the initial HE diagnosis, which allowed a final assessment of the PCA-DA. Typical HE sections of a pleomorphic adenoma (Figure 4f) and a Warthin tumor (Figure 4g) with a magnification of 4× are shown in detail to compare the different morphological features.

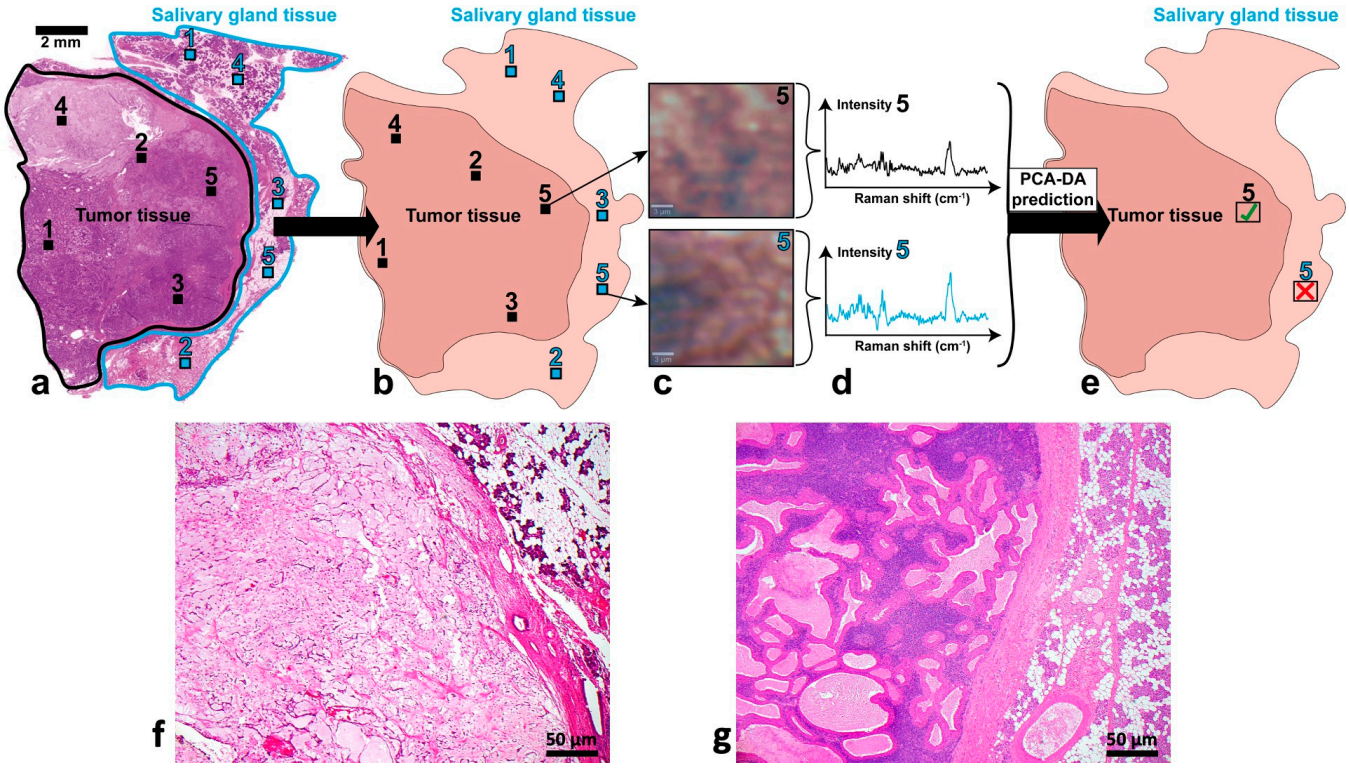

Figure 4. Schematic description of the external PCA-DA validation. At first, histopathologically appropriate tissue regions were defined on the HE-stained cross-sections (1–5 tumor tissue, 1–5 salivary gland tissue in (**a**)). Afterwards, these regions were identified on the corresponding unstained cross-sections used for Raman imaging (1–5 tumor tissue, 1–5 salivary gland tissue in (**b**)). Raman images (**c**) and resulting Raman mean spectra (**d**) were acquired and calculated to be predicted by the PCA-DA model. The tested Raman mean spectra are either correctly (✓) or falsely (✕) classified by the model (**e**), which is evaluated by the initial HE diagnosis in step (**a**). Examples for the typical histomorphology of (**f**) a pleomorphic adenoma and (**g**) a Warthin tumor with adjacent healthy salivary gland tissue.

The classification results of unknown Raman mean spectra by the PCA-DA model are summarized in Table 3. Almost all Raman mean spectra were assigned to the correct tissue type, except for one pleomorphic adenoma spectrum, which was classified as salivary gland tissue.

Table 3. Prediction outcome of model-unknown Raman mean spectra. Five Raman mean spectra for salivary gland, Warthin tumor and pleomorphic adenoma (column 1 and 2) tissues were classified, respectively, by the PCA-DA model (column 3) and compared with the initial HE diagnosis (column 4). Correctly predicted Raman mean spectra are indicated in green and bold, whereas wrong classifications are depicted in red and regular font.

Entity	Prediction Spectra	Model Classified as	HE Diagnosed as
Salivary gland tissue	1	**Salivary gland tissue**	**Salivary gland tissue**
	2	**Salivary gland tissue**	**Salivary gland tissue**
	3	**Salivary gland tissue**	**Salivary gland tissue**
	4	**Salivary gland tissue**	**Salivary gland tissue**
	5	**Salivary gland tissue**	**Salivary gland tissue**

Table 3. *Cont.*

Entity	Prediction Spectra	Model Classified as	HE Diagnosed as
Pleomorphic adenoma	1	Pleomorphic adenoma	Pleomorphic adenoma
	2	Pleomorphic adenoma	Pleomorphic adenoma
	3	Pleomorphic adenoma	Salivary gland tissue
	4	Pleomorphic adenoma	Pleomorphic adenoma
	5	Pleomorphic adenoma	Pleomorphic adenoma
Warthin tumor	1	Warthin tumor	Warthin tumor
	2	Warthin tumor	Warthin tumor
	3	Warthin tumor	Warthin tumor
	4	Warthin tumor	Warthin tumor
	5	Warthin tumor	Warthin tumor

4. Discussion

Accurate classification of salivary gland tumors can be difficult but is clinically very important. Therefore, new approaches that can support a correct diagnosis are of great interest. Thus, we focused on Raman spectroscopic imaging combined with MVA to create a valid and robust PCA-DA model for the differentiation of salivary gland, Warthin tumor and pleomorphic adenoma tissues.

A comparison of Raman mean spectra in the range of 900–1700 cm^{-1} enabled us to reveal individual spectral patterns and thus spectral changes between the different tissue types (Figure 2b, Table 1). Throughout the investigated Raman shift, most of the identified Raman bands match between the tissue types with only a few distinct band differences (1)–(14), (Figure 2b). Most of these differences allow the discrimination of non-tumor salivary gland tissue from parotid gland tumors. This is expressed by several bands or band relations, which are different for normal salivary gland tissue than for both tumors. A distinctly appearing band (1) for the salivary gland tissue, which is less pronounced or shifted within the tumor spectra, indicates variations in RNA. Comparably, band (5) also implies changes in DNA/RNA between the tissue types. DNA/RNA differences can be correlated to the abundance of DNA/RNA in tumors due to an intensified proliferation and metabolic activity of cancer cells [61,62]. Aside from DNA/RNA related differences, mainly protein and lipid associated vibrations (3)–(5) allow a demarcation of non-tumor salivary gland tissue from Warthin tumor and pleomorphic adenoma (Figure 2b). This can be attributed to a dysregulated synthesis of certain lipids and proteins, often enhanced in tumors [63,64]. Additionally, characteristic tumor signal relations are observed at (3), (10), (13) for Warthin tumor and pleomorphic adenoma that are also related to triglyceride, lipid and protein variations and help to discriminate between tumor and non-tumor tissue. These band relations additionally enable distinguishing between the tumor entities themselves, as shown, e.g., for (13). This is assumed to result from the individual protein or lipid expression levels of both tumors [65]. Furthermore, the triglyceride indication can be ascribed to a high endogenous synthesis of fatty acids, which is estimated to be linked to the high degree of tumor cell proliferation [66]. Further bands, e.g., (1; 920 cm^{-1}), (2), (10), (14), enable differentiating salivary gland tissue from parotid tumors (Figure 2b), which are expected to correlate with collagen vibrations of the tumor's extracellular matrix. Collagen was proven to be increasingly accumulated and expressed in tumorous tissue and thus contribute to tumor progression, invasion and metastasis [67,68]. As a result, the abundance, type and composition of collagen might be different in the three tissue types, which also allows the distinction of the parotid tumors.

Although spectral differences are already indicated by the band allocations, the smallest changes that contribute to a clear parotid differentiation might not be assignable or might even be missed. To identify these, a PCA analysis between 900 and 1750 cm^{-1} was

performed (Figure 3). The final tissue type separation was achieved by PC1, PC2 and PC5 and can be deduced from the corresponding loading plots (Figure 3b). The main loading maxima allow spectral regions or bands with the highest impact on the tissue demarcation to be identified. As the Warthin tumor is almost fully separated by PC1 and PC2, the main influences in both loadings are assumed to affect this segregation. Within the PC1 loadings, maxima at 1164 cm^{-1} (3, Figure 2, Table 1), 1530 cm^{-1}, 1596 cm^{-1} and 1643 cm^{-1} (13, Figure 2, Table 1) are identified to have a major impact on the Warthin cluster position. The impact at 1164 cm^{-1} is associated with a tyrosine variation in the tissues that mainly causes a separation of Warthin tumor tissue from pleomorphic adenoma. Tyrosine was found to be accumulated as crystals in pleomorphic adenoma, assumed to result from a disordered protein synthesis [69]. This seems not to be the case for other parotid tumors, such as the Warthin tumor, which explains the discrimination of both tumor entities at 1164 cm^{-1} (3, Figure 2, Table 1) and also the differentiation from salivary gland tissue. Another PC1 loading maximum corresponds to 1530 cm^{-1}, which can be correlated to a carotenoid vibration. Carotenoids were mainly shown to suppress tumor metastasis or progression, but were also suggested to promote tumor invasion by actively interfering into various signal pathways [70]. Variations in carotenoids in Warthin tumor tissue might thus result in a differently up- or downregulated gene expression, which affects changes in molecular mechanisms and tissue composition. As a consequence, the Warthin tumor group is more distinguishable from salivary gland and pleomorphic adenoma tissues on PC1. Furthermore, the influence of PC1 loadings at 1596 cm^{-1} and 1643 cm^{-1} (13, Figure 2, Table 1) are mostly ascribable to amide III oscillations of proteins and lipids that were previously discussed to be highly abundant in tumors as a result of protein and lipid dysregulation [63,64]. Consequently, this contributes to a segregation of the tumors from non-tumor salivary gland tissue. A high concentration of unsaturated triacylglycerol in healthy salivary gland tissue and a high protein concentration in SGT tissue were observed by Paluszkiewicz et al. [6].

PC2 is additionally needed to achieve a complete separation of the Warthin tumor group. Here, the loading at 1440 cm^{-1} (10, Figure 2, Table 1) enables a separation of Warthin tumor and pleomorphic adenoma from salivary gland tissue and is tentatively assigned to a cholesterol vibration. This can be explained by an increased cholesterol concentration in tumors, especially in proliferating cancer cells [71], which was shown for numerous cancers [71,72]. Particularly in Warthin tumors, the cystic structures contain cell debris and cholesterol crystals, which further supports the cholesterol-based explanation. Another explanation for the 1440 cm^{-1} band derives from a varying lipid composition or concentration in Warthin tumor tissue, as it is a characteristic vibration for lipids [73,74]. This might be corroborated by the fact that further cholesterol bands, such as 701 cm^{-1} and 1087 cm^{-1}, are less pronounced in the Raman spectra. Additional PC2 loadings at 1467 cm^{-1}, 1643 cm^{-1} (13, Figure 2, Table 1) and 1680 cm^{-1} again indicate a high impact of proteins and lipids on the separation of the Warthin tumor cluster, which implies a varying protein and lipid composition for Warthin tumors.

PC5, however, was required to enable a complete distinction between pleomorphic adenoma and normal salivary gland tissue. The most influencing PC5 loading maxima are shown at 1285 cm^{-1}, 1384 cm^{-1}, 1450 cm^{-1} (10, Figure 2, Table 1) and 1546 cm^{-1}. The PC5 loading at 1285 cm^{-1} points to the impact of collagen on the distinction between pleomorphic adenoma and salivary gland tissue. This again confirms that tumors differ from normal tissues by their collagen composition, type and abundance, as was already discussed. Another influence is also assigned to cytosine, which is associated with tumorigenesis due to cytosine methylation [75]. Compared to that, pronounced PC5 loadings at 1384 cm^{-1} and 1450 cm^{-1} (10, Figure 2, Table 1) result from CH_2/CH_3 bending modes that are at least partly malignant-specific. A further assignment of these loadings is possible due to the CH_2/CH_3 modes of biomolecules, including proteins and lipids. Both loading allocations can be interpreted as an increase in biomass, typically observed for tumors [76], and are thus highly specific for pleomorphic adenoma. At a PC5 loading value of 1546 cm^{-1},

bound/free nicotinamide adenine dinucleotide hydride (NADH) and tryptophan are expected to additionally trigger the separation of pleomorphic adenoma from salivary gland tissue. This is reasonable since tumors reveal an increased metabolism that correlates with a higher NADH and tryptophan demand [62,77]. Furthermore, the ratio of bound to free NADH differs between normal and tumorous tissue and thus contributes to a better distinction between non-tumor salivary gland tissue and pleomorphic adenoma [78].

The final PCA-DA model was used to predict model-unknown Raman mean spectra of the three tissue types and test its classification suitability. Model performance parameters are all beyond 90% and thus demonstrate the model's applicability for prediction purposes. Except for one misclassification of pleomorphic adenoma, all Raman mean spectra were predicted correctly according to the corresponding HE diagnosis (Table 3). A possible reason for the failed prediction might be the high tissue heterogeneity of pleomorphic adenoma, which could hamper its classification by the model. However, all other pleomorphic adenoma spectra were distinctly identified by the model and thus suggest that the PCA-DA covers the variations in tissue heterogeneity. This indicates the high potential of the PCA-DA model to be a supporting diagnostic tool. Our findings support, that Raman spectroscopy (RS)-based imaging systems are able to separate non-tumor salivary gland tissue and salivary gland tumor tissue based on spectroscopic information with a high accuracy. However, further validation steps are necessary to evaluate whether RS-based spectroscopy approaches are suitable for salivary gland tumor entity determination. In the next step, the investigation of a data set with more different tumor entities is planned. Although a good classification accuracy is achieved, the time-consuming Raman imaging prevents the measurement of a large number of patient samples. Consequently, an automatization is required to enable a high imaging throughput in the future.

5. Conclusions

This study focused on the identification and differentiation of non-tumor salivary gland tissue, Warthin tumor and pleomorphic adenoma via Raman imaging combined with MVA. Representative regions of all three tissue types were Raman-imaged in a point-scanning manner with an adequate spatial and high spectral resolution. This allowed us to conduct a thorough Raman band analysis in order to identify differences in the spectra and understand the biological background. Spectral variations were mainly observed for RNA/DNA-, lipid-, protein- and collagen-related bands or band relations that primarily contribute to a discrimination of tumorous and non-tumorous tissues. Due to the high spectral similarity between the tissues, a subsequent PCA calculation with the Raman data was necessary to uncover the tissue-specific impact responsible for a distinct differentiation. This revealed major influences of tyrosine, carotenoids, cholesterol, cytosine, NADH and tryptophan, aside from proteins and lipids, that allowed for a clear parotid tissue separation via PCA. These results emphasized the necessity of PCA to extract the hidden information, not determinable to this extent by a Raman band analysis. By combining the PCA with a subsequent DA, a reliable PCA-DA model was formed, which achieved an accuracy of 94%, sensitivity of 94%, specificity of 95% and precision of 94%. To verify the model's prediction capability, an external proof-of-principle validation of model-unknown Raman mean spectra was performed. The results revealed an almost completely correct prediction outcome, except for one false pleomorphic adenoma classification. Possible reasons for that were ascribed to its pronounced heterogeneity. All prediction results were additionally confirmed by corresponding HE diagnoses. Consequently, we consider our PCA-DA model to be a useful supportive means in identifying salivary gland tumor tissue. However further evaluation steps are necessary for a more in-depth assessment of the translational potential. In detail, an evaluation of the PCA-DA model with a big dataset containing a higher number of different salivary gland tumor entities is necessary.

Supplementary Materials: The following supporting information can be downloaded at: https://www.mdpi.com/article/10.3390/diagnostics14010092/s1, Figure S1: Superimposed Raman mean spectra of normal salivary gland, Warthin tumor and pleomorphic adenoma within 900–1700 cm^{-1}; Figure S2: Different perspectives of the 3D PCA scores plot for distinguishing salivary gland, Warthin tumor and pleomorphic adenoma; Figure S3: 2D score plots and corresponding loading plots of the PCA model; Figure S4: 2D score plots of the calibration and validation model and explained variance / residual variance of the PCA model; Table S1: Confusion matrix of the final PCA-DA model.

Author Contributions: Conceptualization, M.C.B., M.K., E.G.-H., E.O., M.B., S.H. and T.J.M.; methodology, M.C.B., M.K., E.G.-H. and A.M.; software, M.C.B. and M.K.; validation, M.C.B., M.K., L.H., M.G. and E.O.; formal analysis, M.C.B. and M.K.; investigation, M.C.B., M.K., E.G.-H. and A.Y.; resources, M.C.B., M.K., A.M. and E.O.; data curation, M.C.B., M.K., E.G.-H., A.Y., A.S., M.S. (Manuel Stöth), M.S. (Maria Steinke) and T.J.M.; writing—original draft preparation, M.C.B., M.K. and T.J.M.; writing—review and editing, M.C.B., M.K., E.G.-H., L.H., M.G., A.M., A.Y., R.H., A.S., M.S. (Manuel Stöth), E.O., M.S. (Maria Steinke), M.B., S.H. and T.J.M.; visualization, M.C.B.; supervision, E.O., A.S., R.H., M.B. and T.J.M.; project administration, M.C.B., M.K., E.O., A.S., R.H., S.H., M.B. and T.J.M.; funding acquisition, E.O., M.B. and T.J.M. All authors have read and agreed to the published version of the manuscript.

Funding: This research was funded by the Interdisciplinary Centre for Clinical Science (IZKF) at the University of Würzburg, Grant Number Z-2/78 to TJM. This publication was supported by the Open Access Publication Fund of the University of Würzburg. Additional financial support was provided by the doctoral program of the University of Tübingen and Reutlingen University "Intelligente Prozess- und Materialentwicklung in der Biomateriomics (IPMB)", which is aided by the MWK Baden-Württemberg PhD student fellowship to M.C.B. and M.K. Additionally, this work was supported by a MINT-funded project from Vector Stiftung Stuttgart and the framework Ingenieur Nachwuchs 2016 (project: CompeTERS) by the German Federal Ministry of Education and Research (BMBF; Grant no.: 13FH596IX6).

Institutional Review Board Statement: This study was approved and conducted in accordance with the Declaration of Helsinki and approved by the Institutional Ethics Committee on human research of the Julius-Maximilians-University Würzburg (vote No. 224-18, first approval 18 January 2019).

Informed Consent Statement: Informed consent was obtained from all subjects involved in the study.

Data Availability Statement: The datasets used and/or analyzed during the current study are available from the corresponding author on reasonable request.

Acknowledgments: We especially thank Max Eberle (Reutlingen University) for the valuable discussion about principal component analysis.

Conflicts of Interest: The authors declare no conflicts of interest. The funders had no role in the design of the study; in the collection, analyses, or interpretation of data; in the writing of the manuscript, or in the decision to publish the results.

References

1. Israel, Y.; Rachmiel, A.; Ziv, G.; Nagler, R. Benign and Malignant Salivary Gland Tumors—Clinical and Demographic Characteristics. *Anticancer Res.* **2016**, *36*, 4151–4154. [PubMed]
2. Fu, J.-Y.; Wu, C.-X.; Shen, S.-K.; Zheng, Y.; Zhang, C.-P.; Zhang, Z.-Y. Salivary gland carcinoma in Shanghai (2003–2012): An epidemiological study of incidence, site and pathology. *BMC Cancer* **2019**, *19*, 350. [CrossRef] [PubMed]
3. Franzen, A.; Buchali, A.; Lieder, A. The rising incidence of parotid metastases: Our experience from four decades of parotid gland surgery. *Acta Otorhinolaryngol. Ital.* **2017**, *37*, 264–269. [CrossRef] [PubMed]
4. Zhan, K.Y.; Khaja, S.F.; Flack, A.B.; Day, T.A. Benign Parotid Tumors. *Otolaryngol. Clin. N. Am.* **2016**, *49*, 327–342. [CrossRef] [PubMed]
5. El-Naggar, A.K.; Chan, J.K.C.; Grandis, J.R.; Takata, T.; Slootweg, P.J. *WHO Classification of Head and Neck Tumours*, 4th ed.; El-Naggar, A.K., Chan, J.K.C., Grandis, J.R., Takata, T., Slootweg, P.J., Eds.; International Agency for Research on Cancer: Lyon, France, 2017; Volume 9, p. 347.
6. Paluszkiewicz, C.; Roman, M.; Piergies, N.; Pięta, E.; Woźniak, M.; Guidi, M.C.; Miśkiewicz-Orczyk, K.; Marków, M.; Ścierski, W.; Misiołek, M.; et al. Tracking of the biochemical changes upon pleomorphic adenoma progression using vibrational microspectroscopy. *Sci. Rep.* **2021**, *11*, 18010. [CrossRef] [PubMed]

7. Postema, R.J.; van Velthuysen, M.-L.F.; van den Brekel, M.W.M.; Balm, A.J.M.; Peterse, J.L. Accuracy of fine-needle aspiration cytology of salivary gland lesions in the netherlands cancer institute. *Head Neck* **2004**, *26*, 418–424. [CrossRef]
8. Dostalova, L.; Kalfert, D.; Jechova, A.; Koucky, V.; Novak, S.; Kuchar, M.; Zabrodsky, M.; Novakova Kodetova, D.; Ludvikova, M.; Kholova, I.; et al. The role of fine-needle aspiration biopsy (FNAB) in the diagnostic management of parotid gland masses with emphasis on potential pitfalls. *Eur. Arch. Otorhinolaryngol.* **2020**, *277*, 1763–1769. [CrossRef] [PubMed]
9. Psychogios, G.; Bohr, C.; Constantinidis, J.; Canis, M.; Vander Poorten, V.; Plzak, J.; Knopf, A.; Betz, C.; Guntinas-Lichius, O.; Zenk, J. Review of surgical techniques and guide for decision making in the treatment of benign parotid tumors. *Eur. Arch. Otorhinolaryngol.* **2021**, *278*, 15–29. [CrossRef]
10. Mantsopoulos, K.; Velegrakis, S.; Iro, H. Unexpected Detection of Parotid Gland Malignancy during Primary Extracapsular Dissection. *Otolaryngol.–Head Neck Surg.* **2015**, *152*, 1042–1047. [CrossRef]
11. Auner, G.W.; Koya, S.K.; Huang, C.; Broadbent, B.; Trexler, M.; Auner, Z.; Elias, A.; Mehne, K.C.; Brusatori, M.A. Applications of Raman spectroscopy in cancer diagnosis. *Cancer Metastasis Rev.* **2018**, *37*, 691–717. [CrossRef]
12. Bellisola, G.; Sorio, C. Infrared spectroscopy and microscopy in cancer research and diagnosis. *Am. J. Cancer Res.* **2012**, *2*, 1–21. [PubMed]
13. Kong, K.; Kendall, C.; Stone, N.; Notingher, I. Raman spectroscopy for medical diagnostics—From in-vitro biofluid assays to in-vivo cancer detection. *Adv. Drug Del. Rev.* **2015**, *89*, 121–134. [CrossRef] [PubMed]
14. Kaznowska, E.; Depciuch, J.; Szmuc, K.; Cebulski, J. Use of FTIR spectroscopy and PCA-LDC analysis to identify cancerous lesions within the human colon. *J. Pharm. Biomed. Anal.* **2017**, *134*, 259–268. [CrossRef] [PubMed]
15. Devi, S.; Panigrahi, P.; Pradhan, A. Detecting cervical cancer progression through extracted intrinsic fluorescence and principal component analysis. *J. Biomed. Opt.* **2014**, *19*, 127003. [CrossRef] [PubMed]
16. Francisco, A.L.N.; Correr, W.R.; Azevedo, L.H.; Kern, V.G.; Pinto, C.A.L.; Kowalski, L.P.; Kurachi, C. Fluorescence spectroscopy for the detection of potentially malignant disorders and squamous cell carcinoma of the oral cavity. *Photodiagnosis Photodyn. Ther.* **2014**, *11*, 82–90. [CrossRef] [PubMed]
17. Aaboubout, Y.; Nunes Soares, M.R.; Bakker Schut, T.C.; Barroso, E.M.; van der Wolf, M.; Sokolova, E.; Artyushenko, V.; Bocharnikov, A.; Usenov, I.; van Lanschot, C.G.F.; et al. Intraoperative assessment of resection margins by Raman spectroscopy to guide oral cancer surgery. *Analyst* **2023**, *148*, 4116–4126. [CrossRef] [PubMed]
18. Cheng, J.-X.; Xie, X.S. Vibrational spectroscopic imaging of living systems: An emerging platform for biology and medicine. *Science* **2015**, *350*, aaa8870. [CrossRef]
19. Gao, L.; Smith, R.T. Optical hyperspectral imaging in microscopy and spectroscopy—A review of data acquisition. *J. Biophotonics* **2015**, *8*, 441–456. [CrossRef]
20. Halicek, M.; Fabelo, H.; Ortega, S.; Callico, G.M.; Fei, B. In-Vivo and Ex-Vivo Tissue Analysis through Hyperspectral Imaging Techniques: Revealing the Invisible Features of Cancer. *Cancers* **2019**, *11*, 756. [CrossRef]
21. Anderson, N.G.; Butler, A.P. Clinical applications of spectral molecular imaging: Potential and challenges. *Contrast Media Mol. Imaging* **2014**, *9*, 3–12. [CrossRef]
22. Boldrini, B.; Kessler, W.; Rebner, K.; Kessler, R.W. Hyperspectral Imaging: A Review of Best Practice, Performance and Pitfalls for in-line and on-line Applications. *J. Near Infrared Spectrosc.* **2012**, *20*, 483–508. [CrossRef]
23. Abdi, H.; Williams, L.J. Principal component analysis. *WIREs Comput. Stat.* **2010**, *2*, 433–459. [CrossRef]
24. Wold, S.; Esbensen, K.; Geladi, P. Principal component analysis. *Chemom. Intellig. Lab. Syst.* **1987**, *2*, 37–52. [CrossRef]
25. Gajjar, K.; Heppenstall, L.D.; Pang, W.; Ashton, K.M.; Trevisan, J.; Patel, I.I.; Llabjani, V.; Stringfellow, H.F.; Martin-Hirsch, P.L.; Dawson, T.; et al. Diagnostic segregation of human brain tumours using Fourier-transform infrared and/or Raman spectroscopy coupled with discriminant analysis. *Anal. Methods* **2013**, *5*, 89–102. [CrossRef]
26. Croce, A.C.; Bottiroli, G. Autofluorescence spectroscopy and imaging: A tool for biomedical research and diagnosis. *Eur. J. Histochem.* **2014**, *58*, 2461. [CrossRef] [PubMed]
27. Cui, S.; Zhang, S.; Yue, S. Raman Spectroscopy and Imaging for Cancer Diagnosis. *J. Healthc. Eng.* **2018**, *2018*, 8619342. [CrossRef] [PubMed]
28. Li, Y.; Pan, J.; Chen, G.; Li, C.; Lin, S.; Shao, Y.; Feng, S.; Huang, Z.; Xie, S.; Zeng, H.; et al. Micro-Raman spectroscopy study of cancerous and normal nasopharyngeal tissues. *J. Biomed. Opt.* **2013**, *18*, 027003. [CrossRef]
29. Ghassemi, K.M.; Barzegari, S.; Hajian, P.; Zham, H.; Mirzaei, H.R.; Shirazi, F.H. Diagnosis of normal and malignant human gastric tissue samples by FTIR spectra combined with mathematical models. *J. Mol. Struct.* **2021**, *1229*, 129493. [CrossRef]
30. Argov, S.; Ramesh, J.; Salman, A.; Sinelnikov, I.; Goldstein, J.; Guterman, H.; Mordechai, S. Diagnostic potential of FTIR microspectroscopy and advanced computational methods in colon cancer patients. *J. Biomed. Opt.* **2002**, *7*, 248–254. [CrossRef]
31. Bergner, N.; Romeike, B.F.M.; Reichart, R.; Kalff, R.; Krafft, C.; Popp, J. Tumor margin identification and prediction of the primary tumor from brain metastases using FTIR imaging and support vector machines. *Analyst* **2013**, *138*, 3983–3990. [CrossRef]
32. Dong, L.; Sun, X.; Chao, Z.; Zhang, S.; Zheng, J.; Gurung, R.; Du, J.; Shi, J.; Xu, Y.; Zhang, Y.; et al. Evaluation of FTIR spectroscopy as diagnostic tool for colorectal cancer using spectral analysis. *Spectrochim. Acta Part A Mol. Biomol. Spectrosc.* **2014**, *122*, 288–294. [CrossRef] [PubMed]
33. Surmacki, J.; Musial, J.; Kordek, R.; Abramczyk, H. Raman imaging at biological interfaces: Applications in breast cancer diagnosis. *Mol. Cancer* **2013**, *12*, 48. [CrossRef] [PubMed]

34. Scheer, M.; Fuss, J.; Derman, M.A.; Kreppel, M.; Neugebauer, J.; Rothamel, D.; Drebber, U.; Zoeller, J.E. Autofluorescence imaging in recurrent oral squamous cell carcinoma. *Oral Maxillofac. Surg.* **2016**, *20*, 27–33. [CrossRef] [PubMed]
35. van Lanschot, C.; Schut, T.B.; Barroso, E.; Sewnaik, A.; Hardillo, J.; Monserez, D.; Meeuwis, C.; Keereweer, S.; de Jong, R.B.; Puppels, G.; et al. Raman spectroscopy to discriminate laryngeal squamous cell carcinoma from non-cancerous surrounding tissue. *Lasers Med. Sci.* **2023**, *38*, 193. [CrossRef] [PubMed]
36. Yan, B.; Li, Y.; Yang, G.; Wen, Z.-N.; Li, M.-L.; Li, L.-J. Discrimination of parotid neoplasms from the normal parotid gland by use of Raman spectroscopy and support vector machine. *Oral Oncol.* **2011**, *47*, 430–435. [CrossRef] [PubMed]
37. Czaplicka, M.; Kowalska, A.A.; Nowicka, A.B.; Kurzydłowski, D.; Gronkiewicz, Z.; Machulak, A.; Kukwa, W.; Kamińska, A. Raman spectroscopy and surface-enhanced Raman spectroscopy (SERS) spectra of salivary glands carcinoma, tumor and healthy tissues and their homogenates analyzed by chemometry: Towards development of the novel tool for clinical diagnosis. *Anal. Chim. Acta* **2021**, *1177*, 338784. [CrossRef] [PubMed]
38. Brozek-Pluska, B.; Kopec, M.; Niedzwiecka, I.; Morawiec-Sztandera, A. Label-free determination of lipid composition and secondary protein structure of human salivary noncancerous and cancerous tissues by Raman microspectroscopy. *Analyst* **2015**, *140*, 2107–2113. [CrossRef]
39. Meyer, T.J.; Gerhard-Hartmann, E.; Lodes, N.; Scherzad, A.; Hagen, R.; Steinke, M.; Hackenberg, S. Pilot study on the value of Raman spectroscopy in the entity assignment of salivary gland tumors. *PLoS ONE* **2021**, *16*, e0257470. [CrossRef]
40. Mukherjee, A.; Lorenz, A.; Brecht, M. Determination and Monitoring of Quality Parameters: A Detailed Study of Optical Elements of a Lens-Based Raman Spectrometer. *Appl. Spectrosc.* **2022**, *76*, 199–206. [CrossRef]
41. Ostertag, E.; Stefanakis, M.; Rebner, K.; Kessler, R.W. Elastic and inelastic light scattering spectroscopy and its possible use for label-free brain tumor typing. *Anal. Bioanal. Chem.* **2017**, *409*, 6613–6623. [CrossRef]
42. Stefanakis, M.; Lorenz, A.; Bartsch, J.W.; Bassler, M.C.; Wagner, A.; Brecht, M.; Pagenstecher, A.; Schittenhelm, J.; Boldrini, B.; Hakelberg, S.; et al. Formalin Fixation as Tissue Preprocessing for Multimodal Optical Spectroscopy Using the Example of Human Brain Tumour Cross Sections. *J. Spectrosc.* **2021**, *2021*, 5598309. [CrossRef]
43. Bassler, M.C.; Stefanakis, M.; Sequeira, I.; Ostertag, E.; Wagner, A.; Bartsch, J.W.; Roeßler, M.; Mandic, R.; Reddmann, E.F.; Lorenz, A.; et al. Comparison of Whiskbroom and Pushbroom darkfield elastic light scattering spectroscopic imaging for head and neck cancer identification in a mouse model. *Anal. Bioanal. Chem.* **2021**, *413*, 7363–7383. [CrossRef]
44. Talari, A.C.S.; Movasaghi, Z.; Rehman, S.; Rehman, I.u. Raman Spectroscopy of Biological Tissues. *ApSRv* **2015**, *50*, 46–111. [CrossRef]
45. Chan, J.W.; Taylor, D.S.; Zwerdling, T.; Lane, S.M.; Ihara, K.; Huser, T. Micro-Raman Spectroscopy Detects Individual Neoplastic and Normal Hematopoietic Cells. *Biophys. J.* **2006**, *90*, 648–656. [CrossRef] [PubMed]
46. Bonnier, F.; Byrne, H.J. Understanding the molecular information contained in principal component analysis of vibrational spectra of biological systems. *Analyst* **2012**, *137*, 322–332. [CrossRef] [PubMed]
47. Liu, Z.; Davis, C.; Cai, W.; He, L.; Chen, X.; Dai, H. Circulation and long-term fate of functionalized, biocompatible single-walled carbon nanotubes in mice probed by Raman spectroscopy. *Proc. Natl. Acad. Sci. USA* **2008**, *105*, 1410–1415. [CrossRef] [PubMed]
48. Dukor, R.K. Vibrational Spectroscopy in the Detection of Cancer. In *Handbook of Vibrational Spectroscopy*; John Wiley & Sons, Ltd.: Hoboken, NJ, USA, 2001.
49. Schulz, H.; Baranska, M. Identification and quantification of valuable plant substances by IR and Raman spectroscopy. *Vib. Spectrosc.* **2007**, *43*, 13–25. [CrossRef]
50. Gniadecka, M.; Wulf, H.C.; Nymark Mortensen, N.; Faurskov Nielsen, O.; Christensen, D.H. Diagnosis of Basal Cell Carcinoma by Raman Spectroscopy. *J. Raman Spectrosc.* **1997**, *28*, 125–129. [CrossRef]
51. Stone, N.; Kendall, C.; Smith, J.; Crow, P.; Barr, H. Raman spectroscopy for identification of epithelial cancers. *Faraday Discuss.* **2004**, *126*, 141–157. [CrossRef]
52. Cheng, W.-T.; Liu, M.-T.; Liu, H.-N.; Lin, S.-Y. Micro-Raman spectroscopy used to identify and grade human skin pilomatrixoma. *Microsc. Res. Tech.* **2005**, *68*, 75–79. [CrossRef]
53. Silveira, L., Jr.; Sathaiah, S.; Zângaro, R.A.; Pacheco, M.T.T.; Chavantes, M.C.; Pasqualucci, C.A.G. Correlation between near-infrared Raman spectroscopy and the histopathological analysis of atherosclerosis in human coronary arteries. *Lasers Surg. Med.* **2002**, *30*, 290–297. [CrossRef] [PubMed]
54. Ó Faoláin, E.; Hunter, M.B.; Byrne, J.M.; Kelehan, P.; McNamara, M.; Byrne, H.J.; Lyng, F.M. A study examining the effects of tissue processing on human tissue sections using vibrational spectroscopy. *Vib. Spectrosc.* **2005**, *38*, 121–127. [CrossRef]
55. Lau, D.P.; Huang, Z.; Lui, H.; Man, C.S.; Berean, K.; Morrison, M.D.; Zeng, H. Raman spectroscopy for optical diagnosis in normal and cancerous tissue of the nasopharynx—Preliminary findings. *Lasers Surg. Med.* **2003**, *32*, 210–214. [CrossRef] [PubMed]
56. Sahu, A.; Dalal, K.; Naglot, S.; Aggarwal, P.; Murali Krishna, C. Serum Based Diagnosis of Asthma Using Raman Spectroscopy: An Early Phase Pilot Study. *PLoS ONE* **2013**, *8*, e78921. [CrossRef] [PubMed]
57. Almond, L.M.; Hutchings, J.; Lloyd, G.; Barr, H.; Shepherd, N.; Day, J.; Stevens, O.; Sanders, S.; Wadley, M.; Stone, N.; et al. Endoscopic Raman spectroscopy enables objective diagnosis of dysplasia in Barrett's esophagus. *Gastrointest. Endosc.* **2014**, *79*, 37–45. [CrossRef] [PubMed]
58. Khristoforova, Y.; Bratchenko, L.; Bratchenko, I. Combination of Raman spectroscopy and chemometrics: A review of recent studies published in the Spectrochimica Acta, Part A: Molecular and Biomolecular Spectroscopy Journal. *arXiv* **2022**, arXiv:2210.10051.

59. Boehmke, B.; Greenwell, B.M. *Hands-on Machine Learning with R*; CRC Press: Boca Raton, FL, USA, 2019.
60. Kessler, W. *Multivariate Datenanalyse: Für die Pharma, Bio-und Prozessanalytik*; John Wiley & Sons: Hoboken, NJ, USA, 2007.
61. Calvo, M.B.; Figueroa, A.; Pulido, E.G.; Campelo, R.G.; Aparicio, L.A. Potential Role of Sugar Transporters in Cancer and Their Relationship with Anticancer Therapy. *Int. J. Endocrinol.* **2010**, *2010*, 205357. [CrossRef]
62. Romero-Garcia, S.; Lopez-Gonzalez, J.S.; B'ez-Viveros, J.L.; Aguilar-Cazares, D.; Prado-Garcia, H. Tumor cell metabolism. *Cancer Biol. Ther.* **2011**, *12*, 939–948. [CrossRef]
63. Ackerman, D.; Simon, M.C. Hypoxia, lipids, and cancer: Surviving the harsh tumor microenvironment. *Trends Cell Biol.* **2014**, *24*, 472–478. [CrossRef]
64. Zaidi, N.; Lupien, L.; Kuemmerle, N.B.; Kinlaw, W.B.; Swinnen, J.V.; Smans, K. Lipogenesis and lipolysis: The pathways exploited by the cancer cells to acquire fatty acids. *Prog. Lipid Res.* **2013**, *52*, 585–589. [CrossRef]
65. Donadio, E.; Giusti, L.; Seccia, V.; Ciregia, F.; da Valle, Y.; Dallan, I.; Ventroni, T.; Giannaccini, G.; Sellari-Franceschini, S.; Lucacchini, A. New Insight into Benign Tumours of Major Salivary Glands by Proteomic Approach. *PLoS ONE* **2013**, *8*, e71874. [CrossRef] [PubMed]
66. Kuhajda, F.P. Fatty-acid synthase and human cancer: New perspectives on its role in tumor biology. *Nutrition* **2000**, *16*, 202–208. [CrossRef] [PubMed]
67. Egeblad, M.; Rasch, M.G.; Weaver, V.M. Dynamic interplay between the collagen scaffold and tumor evolution. *Curr. Opin. Cell Biol.* **2010**, *22*, 697–706. [CrossRef] [PubMed]
68. Chen, P.; Cescon, M.; Bonaldo, P. Collagen VI in cancer and its biological mechanisms. *Trends Mol. Med.* **2013**, *19*, 410–417. [CrossRef] [PubMed]
69. Chaplin, A.J.; Darke, P.; Patel, S. Tyrosine-rich crystals in pleomorphic adenomas of parotid glands. *J. Oral Pathol. Med.* **1983**, *12*, 342–346. [CrossRef] [PubMed]
70. Koklesova, L.; Liskova, A.; Samec, M.; Zhai, K.; Abotaleb, M.; Ashrafizadeh, M.; Brockmueller, A.; Shakibaei, M.; Biringer, K.; Bugos, O.; et al. Carotenoids in Cancer Metastasis—Status Quo and Outlook. *Biomolecules* **2020**, *10*, 1653. [CrossRef] [PubMed]
71. Chimento, A.; Casaburi, I.; Avena, P.; Trotta, F.; De Luca, A.; Rago, V.; Pezzi, V.; Sirianni, R. Cholesterol and Its Metabolites in Tumor Growth: Therapeutic Potential of Statins in Cancer Treatment. *Front. Endocrinol.* **2019**, *9*, 807. [CrossRef]
72. Llaverias, G.; Danilo, C.; Mercier, I.; Daumer, K.; Capozza, F.; Williams, T.M.; Sotgia, F.; Lisanti, M.P.; Frank, P.G. Role of Cholesterol in the Development and Progression of Breast Cancer. *Am. J. Pathol.* **2011**, *178*, 402–412. [CrossRef]
73. Yue, S.; Li, J.; Lee, S.Y.; Lee, H.J.; Shao, T.; Song, B.; Cheng, L.; Masterson, T.A.; Liu, X.; Ratliff, T.L.; et al. Cholesteryl Ester Accumulation Induced by PTEN Loss and PI3K/AKT Activation Underlies Human Prostate Cancer Aggressiveness. *Cell Metab.* **2014**, *19*, 393–406. [CrossRef]
74. Czamara, K.; Majzner, K.; Pacia, M.Z.; Kochan, K.; Kaczor, A.; Barańska, M. Raman spectroscopy of lipids: A review. *J. Raman Spectrosc.* **2015**, *46*, 4–20. [CrossRef]
75. Warnecke, P.M.; Bestor, T.H. Cytosine methylation and human cancer. *Curr. Opin. Oncol.* **2000**, *12*, 68–73. [CrossRef] [PubMed]
76. Lunt, S.Y.; Heiden, M.G.V. Aerobic Glycolysis: Meeting the Metabolic Requirements of Cell Proliferation. *Annu. Rev. Cell Dev. Biol.* **2011**, *27*, 441–464. [CrossRef] [PubMed]
77. Badawy, A.A.-B. Targeting tryptophan availability to tumors: The answer to immune escape? *Immunol. Cell Biol.* **2018**, *96*, 1026–1034. [CrossRef] [PubMed]
78. Betz, V.; Schneckenburger, H.; Alleroeder, H.; Sybrecht, G.; Meyer, J.-U. *Evaluation of Changes in the NADH Level between Carcinogenic and Normal Tissue Samples by Use of Fluorescence Spectroscopy*; SPIE: Bellingham, WA, USA, 1995; Volume 2324.

6. Gradient SERS Substrates with Multiple Resonances for Analyte Screening: Fabrication and SERS Applications

Ashutosh Mukherjee[1,2,3], Quan Liu[3,4], Frank Wackenhut[1,2,], Fang Dai[5,6], Monika Fleischer[5,6], Pierre-Michel Adam[4,*], Alfred J. Meixner[3,6] and Marc Brecht [1,2,3,6,*]*

[1]Center for Process Analysis and Technology (PA&T), School of Applied Chemistry, Reutlingen University, 72762 Reutlingen, Germany

[2]Reutlingen Research Institute (RRI), Reutlingen University, 72762 Reutlingen, Germany

[3]Institute of Physical and Theoretical Chemistry, Eberhard Karls University of Tübingen, 72076 Tübingen, Germany

[4]Laboratory Light, Nanomaterials & Nanotechnologies–L2n and CNRS EMR 7004, University of Technology of Troyes, 10000 Troyes, France

[5]Institute for Applied Physics, Eberhard Karls University of Tubingen, 72076 Tübingen, Germany

[6]Center for Light-Matter-Interaction, Sensors and Analytics (LISA+), Eberhard Karls University of Tübingen, 72076 Tübingen, Germany

This chapter was originally published in MDPI-Molecules as

Mukherjee, A.; Liu, Q.; Wackenhut, F.; Dai, F.; Fleischer, M.; Adam, P.-M.; Meixner, A.J.; Brecht, M. Gradient SERS Substrates with Multiple Resonances for Analyte Screening: Fabrication and SERS Applications. Molecules 2022, 27, 5097.

DOI: https://doi.org/10.3390/molecules27165097

Supplementary Material/Supporting Information shown in Appendix 3

molecules

MDPI

Article

Gradient SERS Substrates with Multiple Resonances for Analyte Screening: Fabrication and SERS Applications

Ashutosh Mukherjee [1,2,3], Quan Liu [3,4], Frank Wackenhut [1,2,*], Fang Dai [5,6], Monika Fleischer [5,6], Pierre-Michel Adam [4,*], Alfred J. Meixner [3,6] and Marc Brecht [1,2,3,6,*]

1 Center for Process Analysis and Technology (PA&T), School of Applied Chemistry, Reutlingen University, 72762 Reutlingen, Germany
2 Reutlingen Research Institute (RRI), Reutlingen University, 72762 Reutlingen, Germany
3 Institute of Physical and Theoretical Chemistry, Eberhard Karls University of Tübingen, 72076 Tübingen, Germany
4 Laboratory Light, Nanomaterials & Nanotechnologies–L2n and CNRS EMR 7004, University of Technology of Troyes, 10000 Troyes, France
5 Institute for Applied Physics, Eberhard Karls University of Tubingen, 72076 Tübingen, Germany
6 Center for Light-Matter-Interaction, Sensors and Analytics (LISA+), Eberhard Karls University of Tübingen, 72076 Tübingen, Germany
* Correspondence: frank.wackenhut@reutlingen-university.de (F.W.); pierre_michel.adam@utt.fr (P.-M.A.); marc.brecht@reutlingen-university.de (M.B.)

Abstract: Surface-enhanced Raman spectroscopy (SERS) provides a strong enhancement to an inherently weak Raman signal, which strongly depends on the material, design, and fabrication of the substrate. Here, we present a facile method of fabricating a non-uniform SERS substrate based on an annealed thin gold (Au) film that offers multiple resonances and gap sizes within the same sample. It is not only chemically stable, but also shows reproducible trends in terms of geometry and plasmonic response. Scanning electron microscopy (SEM) reveals particle-like and island-like morphology with different gap sizes at different lateral positions of the substrate. Extinction spectra show that the plasmonic resonance of the nanoparticles/metal islands can be continuously tuned across the substrate. We observed that for the analytes 1,2-bis(4-pyridyl) ethylene (BPE) and methylene blue (MB), the maximum SERS enhancement is achieved at different lateral positions, and the shape of the extinction spectra allows for the correlation of SERS enhancement with surface morphology. Such non-uniform SERS substrates with multiple nanoparticle sizes, shapes, and interparticle distances can be used for fast screening of analytes due to the lateral variation of the resonances within the same sample.

Keywords: surface-enhanced Raman spectroscopy (SERS); SERS substrates; multiple plasmonic resonances; island film

Citation: Mukherjee, A.; Liu, Q.; Wackenhut, F.; Dai, F.; Fleischer, M.; Adam, P.-M.; Meixner, A.J.; Brecht, M. Gradient SERS Substrates with Multiple Resonances for Analyte Screening: Fabrication and SERS Applications. *Molecules* **2022**, *27*, 5097. https://doi.org/10.3390/molecules27165097

Academic Editor: Wen-Bin Cai

Received: 19 July 2022
Accepted: 8 August 2022
Published: 10 August 2022

1. Introduction

Since its discovery, Raman spectroscopy has attracted a lot of attention due to its selective molecular identification [1,2]. A major limitation is the inherently small Raman cross-section, which can be overcome with surface-enhanced Raman spectroscopy (SERS) [3]. On average, the Raman signal can be enhanced by a factor of 10^4–10^6, and sometimes even by a factor of 10^8 by exploiting surface enhancement effects [4–7]. However, the challenge to achieve such high enhancements is strongly dependent on the design and fabrication of the SERS substrates. In many cases, a SERS substrate consists of noble metal nanoparticles (NPs), where the actual shape and distance of the NPs play a crucial role in SERS enhancement. The gap between the NPs has an especially significant impact on the SERS effect, since the electric field can be strongly enhanced in the gap due to confinement by the NPs [8–12]. Hence, the ideal SERS substrate needs to offer high Raman enhancement, which can be altered by manipulating the size, shape, and interparticle distance of

noble metal NPs, and good stability (physically and chemically) to withstand any analyte. Furthermore, the fabrication process should be reproducible, simple, and cost-effective.

There are plenty of SERS substrates available on the market, such as surface-roughened films [13,14], colloidal NPs [15–17], metal/metal island films [18–21], etc. However, most of these substrates lack a certain combination of the aforementioned properties. A preferable substrate would be one that offers resonant excitation of plasmons in NPs and is stable, reproducible in geometry and plasmonic response, easy to prepare, and cost-effective. Plenty of SERS substrates have been fabricated with the aim of an optimal combination of the above-mentioned properties.

Many investigated substrates rely on the uniformity of NP sizes and shapes [22–27]. This uniformity yields a uniform Raman enhancement profile, which allows reproducible SERS results. However, for rapid and extensive screening to find the optimal combination of properties for SERS, it is desirable to have a SERS substrate that offers multiple NP sizes, shapes, and gaps leading to variable resonances.

Gradient assemblies of NPs with gradually changing sizes and densities have attracted interest because of their varied applications [28–36]. These samples fulfill many of the criteria mentioned above. Due to the gradual variation in the size of the NPs, their plasmonic response varies. These assemblies allow manipulation and investigation of their material properties at the micro and nano scales. Several techniques have have been employed to fabricate gradient NP assemblies on various substrates [28,32,36–38]. However, the definite distribution of sizes, shapes, and interparticle distances between NPs can hardly be controlled, especially in micro and nanometer scale gradients.

In this work, we report a facile method of fabricating non-uniform SERS substrates that not only have typical SERS substrate characteristics, but also inhomogeneity in NP sizes and gaps. We show that such a substrate offers multiple plasmonic resonances and that the SERS enhancement varies spatially for different analytes. Additionally, we show that the local surface morphology can be estimated by optical methods. Furthermore, it is easy to prepare, uncomplicated, and comparatively cost-effective. Such a substrate enables fast screening of analytes and is stable, with reproducible trends in the results. This approach shows high controllability for the fabrication of such SERS substrates at the micro and nano scales and increases the potential of practical applications of non-uniform SERS substrates.

2. Results and Discussion

Several non-uniform samples were prepared as described in the Materials and Methods section; one of them has been illustrated in Figure 1. For ease of explanation, we labeled the substrates as S1, S2, and S3. Figure 1a shows a schematic of such non-uniform SERS substrates (S1, S2, S3), where the center of the evaporation source is marked as "C". Figure 1b shows SEM images of the points marked P1 to P9 in Figure 1a. The SEM image at P1 shows that the substrate is covered by relatively spherical NPs. On the contrary, the SEM image at P2 shows the formation of connected Au islands forming percolation paths, which gradually increase in size until P5. This inhomogeneity occurs since points P2 to P5 are closer to the center, such that more metal is deposited in this region, and the thermal annealing of the sample leads to the formation of connected Au islands [39].

Afterwards, SEM images at points P6 and P7 show a slow transition from a connected island-like morphology towards particle-like features. Finally, points P8 and P9 of S3 are further away from the center and are covered by relatively spherical particles. Figure 1c shows the particle size distributions at points P1, P8, and P9, as determined with the image processing software ImageJ. At P1, the average particle size (radius) is 15 ± 10 nm, and moving across the island film to P8 leads to larger particles with 20 ± 13 nm. The largest particle density with the smallest particles is observed at P9, with an average particle size of 10 ± 6 nm. The average particle sizes at points P2 to P7 cannot be easily determined since the substrate is covered with connected Au islands. An important parameter for SERS enhancement is the gap between the particles/islands. Figure 1d shows the average gap size between Au NPs and Au islands at points P1 to P9. The gap sizes were evaluated in

the image processing software Gwydion. At point P1, the average gap size between the Au NPs is 11 ± 4 nm. As can be seen in the SEM images, at P2, the surface morphology changes from NPs to an island film, which leads to an increase in the gap size to 42 ± 6 nm and 52 ± 5 nm at P2/P3, respectively. Moving further towards the center C of the whole sample at P4/P5, the average gap size between islands gradually decreases to 45 ± 3 nm and 32 ± 3 nm. In this area, more metal is deposited, and the thermal annealing of the sample leads to the formation of larger connected islands with smaller gap sizes. Moving further across the substrate, the trend is reverted, and the average gap size increases again at P6 to P8, and decreases when NPs are formed at P8/P9. Finally, at point P9, the average gap size is 11 ± 3 nm, which is similar to P1. This morphology is similar for different fabricated substrates within the limits of the production process of inhomogeneous samples, as can be seen in the supporting information in Figure S1.

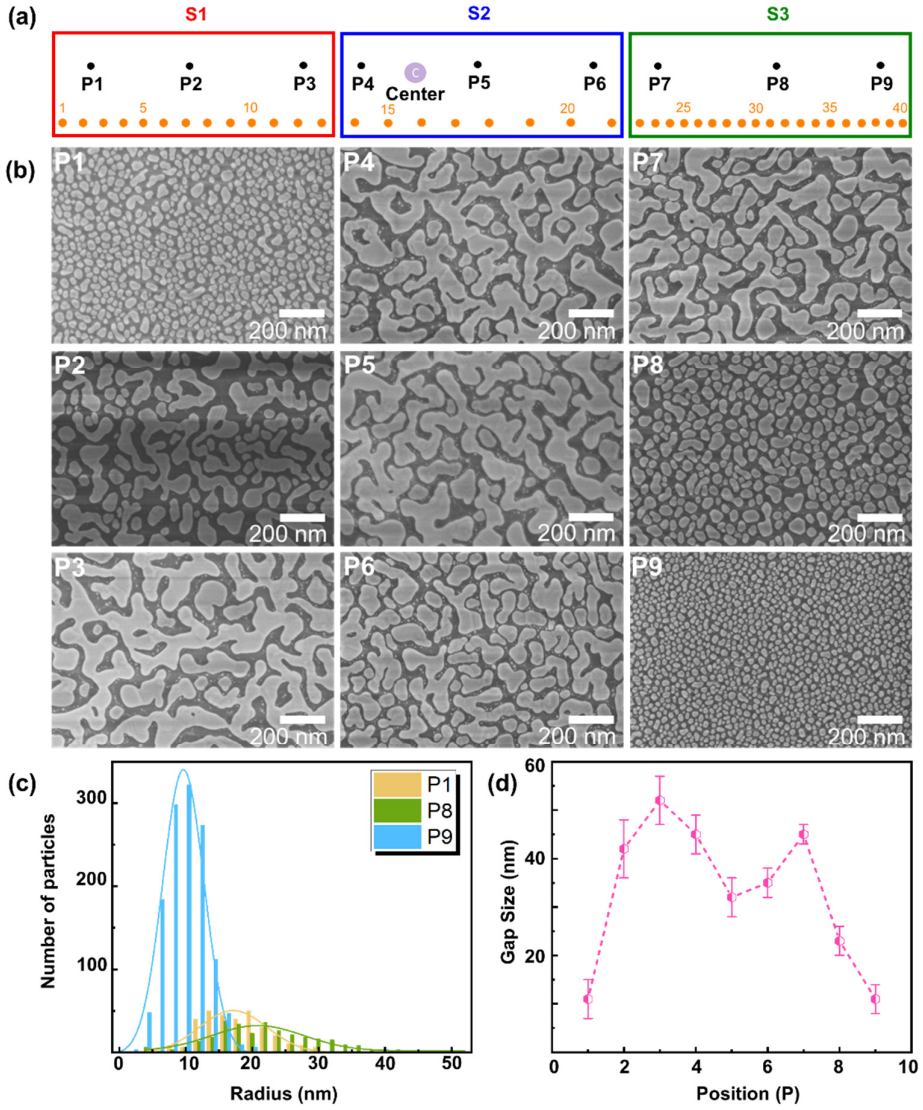

Figure 1. (**a**) Schematic of non-uniform SERS substrates S1, S2, and S3 marked with points P1 to P9 (black, points where SEM images were taken), and with points 1 to 40 (orange, points where extinction spectra were acquired); the length of each substrate is 40 mm. (**b**) SEM images (P1 to P9) at corresponding points marked in (**a**). (**c**) Au particle size distribution at points P1, P8, and P9, and (**d**) average size of gaps between Au NPs/islands at points P1 to P9.

Figure 2a shows a contour plot of extinction spectra acquired across samples S1, S2, and S3 shown in Figure 1. Spectra were recorded at 40 different locations, as shown

schematically in Figure 1a along the substrates (cf. "horizontal position" in Figure 2a,e). The selected extinction spectra in Figure 2b–d correspond to points P1–P9 of the SEM images of S1, S2, and S3 in Figure 1b. The horizontal position locationof P1 to P9 can be seen in Figure 2a.

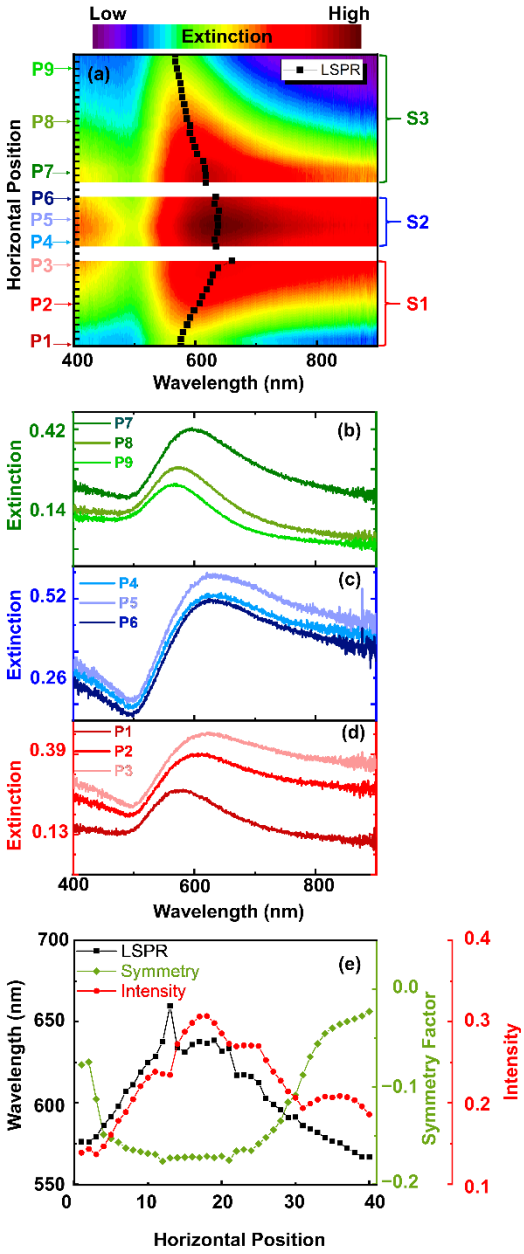

Figure 2. (**a**) Contour of the extinction spectra acquired across substrates S1, S2, and S3, as denoted schematically in orange at 40 locations in Figure 1a. The black markers illustrate the maximum of each spectrum. (**b**) Corresponding extinction spectra of S3 at points P7, P8, and P9, (**c**) corresponding extinction spectra of S2 at positions P4, P5, and P6, (**d**) corresponding extinction spectra of S1 at positions P1, P2, and P3, and (**e**) LSPR, amplitude and symmetry factor of extinction spectra in (**a**).

In general, the extinction maximum of the spectra (illustrated by the black markers in Figure 2a) acquired across the three substrates shifts to longer wavelengths from S1 to S2, and to shorter wavelengths from S2 to S3. Furthermore, the full width at half maximum (FWHM) of the extinction spectra changes from S1 to S3. The extinction spectra of S1 in Figure 2a and the spectra at P1 to P3 in Figure 2d show that the localized surface plasmon resonance (LSPR) is comparably narrow at position P1 and gradually red shifts, broadens,

increases in intensity, and becomes more asymmetric towards position P3. This trend continues until the middle of substrate S2, where the spectra are highly asymmetric and are tailing towards larger wavelengths. Moving further to S3, this trend is reverted and the spectral maximum shifts to the blue. Furthermore, the spectral peak sharpens, decreases in intensity, and becomes more symmetric. On substrate S3 the spectral shape is similar to that on S1, and the spectra exhibit a well-defined maximum, indicating a localized plasmon resonance. This alteration of the spectral shape allows us to draw conclusions on the film morphology at the different positions on the substrate. At the beginning/end of S1/S3, the spectra show a clear LSPR resonance, similar to that of a gold sphere [40–42]. This is also supported by the SEM images in Figure 1b. However, comparing the spectral position of the experimental extinction maxima with simulations based on Mie's theory of spherical gold particles (see supporting information in Figure S2a), it is obvious that the experimental resonances show a large red shift. This indicates a significant contribution of coupling between the NPs, which is favorable for SERS experiments, as it creates intense hotspots in the gaps [43]. Moving towards S2, the spectral maximum shifts further to the red, which suggests that the particle size and/or the coupling between the particles increases. The SEM images in Figure 1b show that the film morphology changes from NPs to a connected Au island film towards the center C. Here, more material is deposited due to the evaporation geometry. This morphology change is also visible in the extinction spectra, since they further red shift, increase in intensity, and become strongly asymmetric in the center of the three substrates. In particular, this asymmetry can be a measure of the film morphology, where a large asymmetry indicates an island-like film, and a small one suggests spherical NPs. These effects are summarized in Figure 2e, where the spectral maximum, the amplitude, and the symmetry factor are shown as a function of the horizontal position. The LSPR spectral position and the intensity of the spectra correlate with each other and show similar trends. Moving across the three substrates, the LSPR (shown in black) red shifts from 580 nm to 660 nm and remains approximately constant at 630 nm on S2. For S3, the LSPR blue shifts from 620 nm to 570 nm. The intensity shows a similar trend, and the maximum extinction is observed at the center C. An increase in intensity indicates an increase in optical cross-section due to more material being deposited in those regions and vice versa. This is supported by SEM images in Figure 1b. Additionally, we characterized the asymmetry of the spectra by a symmetry factor, which is the ratio of the difference of the areas on the right and left sides of the spectral maximum normalized to the full area of the spectrum (see supporting information in Figure S2b). A negative symmetry factor means that the area under the curve on the long-wavelength side of the spectral maximum is larger than the area on the shorter-wavelength side. This symmetry factor is shown by the green markers in Figure 2e. In general, the symmetry factor is anticorrelated with the spectral maximum and the intensity. As the LSPR red shifts, the extinction spectrum is increasingly tailing towards larger wavelengths, and thus, the symmetry factor shifts to increasingly negative values. It remains approximately constant for S2 and gradually decreases in amplitude for S3, indicating that the extinction spectra are becoming more symmetric. Hence, a symmetry factor close to zero indicates a particle-like morphology, and a negative symmetry factor indicates a connected island film.

The potential of such a non-uniform substrate for SERS is shown by using 1,2-bis(4-pyridyl) ethylene (BPE) and methylene blue (MB) as analytes. For this purpose, droplets of suspensions of the respective analyte are positioned on the substrate, as shown in the Materials and Methods section below. The analyte BPE was evaluated at 12 different horizontal positions, whereas 20 horizontal positions for MB were analyzed across the substrate. Note: Due to the symmetry of the substrate, the 12 or 20 droplets were placed at distances of 2–3 mm between positions P1 and P5 by hand. The focus spot sizes for the SERS measurements is in the order of few µm, much larger than the size of the individual nanostructures and much smaller than the droplet size.

The most intense peak of BPE, namely the benzene ring stretching (C-H) at 1608 cm^{-1}, was chosen for analysis. Raman measurements and corresponding extinction spectra

acquired at the same specified points (without analyte) are shown in Figure 3a–c. Please note that different substrates were used for the SEM characterization in Figures 1 and 2 and for the SERS experiments in Figure 3 due to carbon residuals after the SEM measurements.

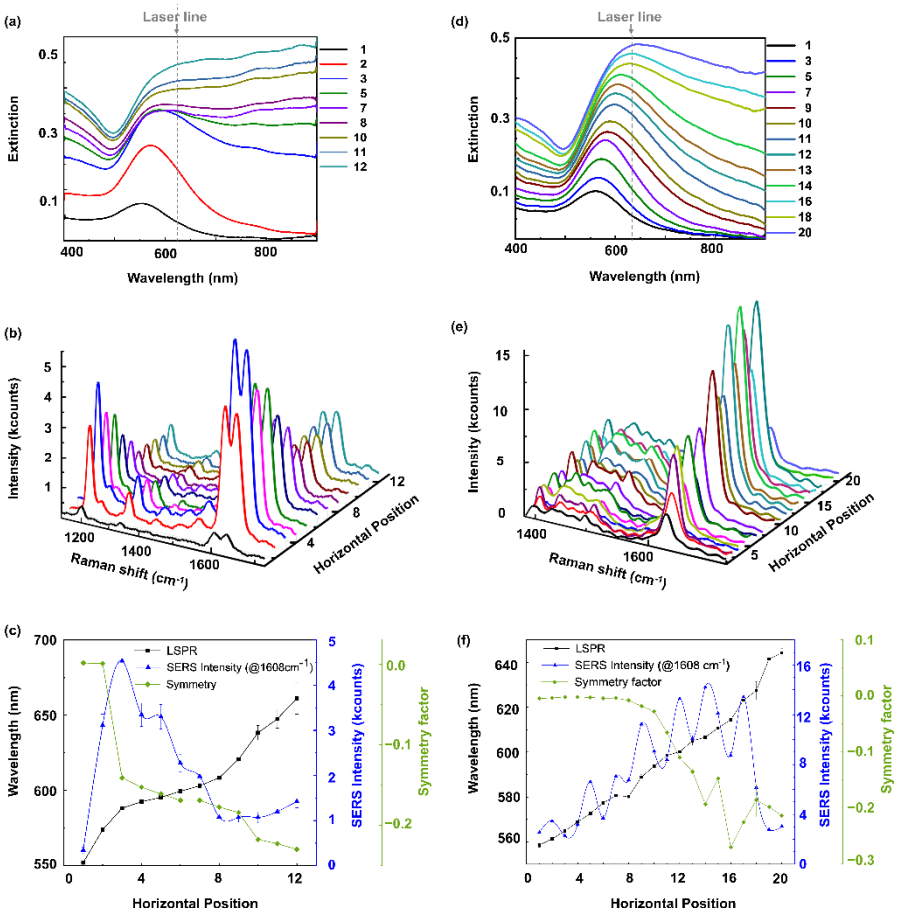

Figure 3. (**a**) Extinction spectra acquired (without analyte) at 12 lateral positions across the substrate used for SERS of BPE. (**b**) Raman spectra of BPE (1 µL—0.25 × 10^{-3} M) acquired at the same 12 positions. (**c**) SERS intensity of BPE (@1608 cm^{-1})—blue curve, spectral maxima of the extinction spectra shown in (**a**)—black curve, symmetry factor of the extinction spectra shown in (**a**)—green curve, (**d**) Extinction spectra acquired (without analyte) at 20 lateral positions across another gradient SERS substrate used for MB. (**e**) Raman spectra of MB (1 µL—0.25 × 10^{-3} M) acquired at the same 20 positions. (**f**) SERS intensity of MB (@1625 cm^{-1})—blue curve, spectral maxima of the extinction spectra shown in (**d**)—black curve, symmetry factor of the extinction spectra shown in (**d**)—green curve.

The extinction spectra in Figure 3a were acquired before deposition of the analytes and show a similar trend as previously observed in Figure 2, suggesting a continuous transition from spherical particles at position 1 to a connected islands film at position 12. The extinction maxima of these spectra are shown in Figure 3c by the black line as a function of the horizontal position. The values are determined using an in-house MATLAB script that also considers the asymmetry of the curve, since in curves 10 to 12, the maxima are no longer discernible. The spectral shape of the extinction spectra suggests that this substrate covers the morphology change between points P1 and P5 of the substrate shown in Figures 1 and 2. For this substrate, there is a red shift from approximately 550 nm at position 1 to 670 nm at position 12. This means that the particle sizes are small at the beginning and gradually increase in size until a connected Au island film is obtained. Note that adding water droplets for the SERS measurements is expected to systematically shift the LSPR resonances to longer wavelengths. The transition from NPs to an island film can

again be seen by the broadening and decreasing symmetry of the extinction spectra. The symmetry factor as a function of the horizontal position is plotted in Figure 3c—green line. The spectrum remains symmetric and only broadens gradually until position 3, indicating that the particles in this region just increase in size, but remain roughly spherical. Moving towards position 12, islands are forming and increasing in size. As a consequence, the gap sizes first increase and then decrease again when the islands become larger. Hence, the morphology at positions 1–12 roughly correlates with the SEM images in Figure 1b of P2–P5. Figure 3b shows a series of Raman spectra of BPE at the 12 positions, and the Raman intensity variation as a function of the horizontal position is summarized in Figure 3c—blue line. The most intense peak of BPE (@1608 cm^{-1}) is chosen to clearly visualize the Raman enhancement along the 12 lateral positions. However, all other peaks of BPE show the same trend, as can be seen in Figure 3b. The Raman intensity of the 1608 cm^{-1} peak increases from position 1 to 3. Here, the red shift of the extinction spectra suggests that the NP size increases. The maximum Raman enhancement is observed at position 3, where the film morphology is still particle-like with comparably small gaps and the extinction maximum in water is presumably spectrally close to the excitation wavelength (633 nm, black dashed line in Figure 3b). Hence, there is a strong absorption of the excitation light and, as a result, the plasmon excitation is very efficient, and the small gaps are creating intense hotspots, further enhancing the Raman intensity. Afterwards, the Raman intensity gradually decreases from position 4 to position 8. The extinction maximum at these lateral positions red shifts from 605 nm to 625 nm, and the symmetry factor gradually decreases from positions 4 to8. This suggests that the film morphology changes from particle-like to connected islands with larger gaps (see Figure 1). These larger gaps lead to a comparably small Raman enhancement. Hence, this film morphology is not favorable to efficiently enhance the Raman signal of BPE, at least compared to the other morphologies. From position 11 to 12, the extinction maximum further red shifts from 630 nm to 650 nm, and the symmetry factor also becomes more negative, suggesting a further growth of the islands. As previously observed in Figure 1, further growth of the islands leads to a reduction in the gap size, resulting in the small increase in the Raman intensity towards position 12.

To demonstrate that such a non-uniform SERS substrate offers fast screening of optimal SERS conditions for different molecules, we compare the results obtained for BPE with those obtained for MB. A fresh non-uniform SERS substrate was fabricated, and MB was about equidistantly deposited at 20 different lateral positions across the substrate. Raman measurements and corresponding extinction spectra (without analyte) acquired at those points are shown in Figure 3d–f. Again, the extinction spectra in Figure 3d show a trend suggesting a gradual transition from spherical particles at position 1 to a connected islands film at position 20. The extinction maxima of these spectra are shown in Figure 3f by the black line as a function of the horizontal position. Similar to Figure 3a, the extinction spectra suggest that the substrate film morphology in the range of points 1 to 20 is comparable to that between points P1 and P5 of the sample shown in Figures 1 and 2. For this substrate, there is a red shift from approximately 560 nm at position 1 to 660 nm at position 20 and a similar evolution of the spectral shape. This means that the morphology of all three substrates shown here changes in a very similar way under identical substrate preparation. The symmetry factor as a function of the horizontal position is plotted in Figure 3f—green line. The spectrum remains symmetric and only broadens gradually until position 10, depicting that the particles in this region just increase in size, but remain roughly spherical. Moving further across the substrate, islands are forming and increasing in size. As a consequence, the gap sizes first increase and then decrease again when the islands become larger. This covers the morphology change observed in the SEM images in Figure 1b of P1–P5. Figure 3e shows a series of Raman spectra of MB at the 20 positions; the most intense peak of MB (@1635 cm^{-1}) is chosen to clearly visualize the Raman enhancement along the 20 lateral positions. However, all other peaks of MB show the same trend, as can be seen in Figure 3e. The Raman intensity variation of the 1635 cm^{-1} peak as a function of the horizontal position is shown in Figure 3f—blue line. The Raman intensity from

position 1 to 20 has a wavy nature, which requires further investigation. The maximum Raman enhancement is observed at position 14, where the Au film consists of connected islands with comparably small gaps with an extinction maximum without analyte (610 nm) spectrally close to the excitation wavelength (633 nm, black dashed line in Figure 3d). Hence, there is a strong absorption of the excitation light and, as a result, the plasmon excitation is very efficient and the small gaps are creating intense hotspots, further enhancing the Raman intensity. Afterwards, the Raman intensity gradually decreases from position 14 onwards to position 20.

Since we have used different substrates for BPE and ME, it is important to compare the results for similar substrate morphologies. This is shown in Figure 4 by plotting the SERS intensity against the extinction maximum of the substrate (without analyte).

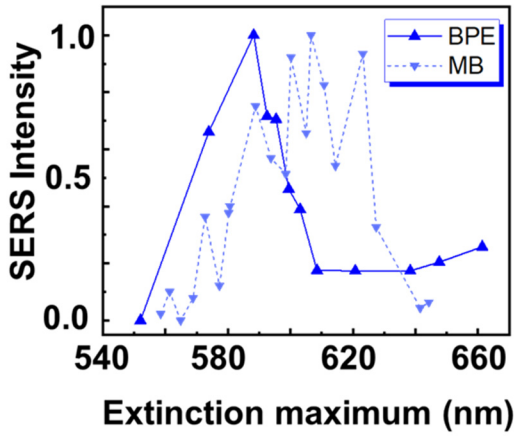

Figure 4. Plot comparing the SERS intensity for the two molecules BPE and MB to the extinction maximum of the LSPR (without analyte).

The highest SERS intensity for BPE (solid blue line in Figure 4) is obtained at position 3, where the maximum extinction of the substrate without analyte is at 585 nm. At this position, the film morphology is particle-like with small gaps. On the other hand, the highest SERS intensity for MB (dashed blue line in Figure 4) is obtained at position 14 with a substrate resonance without analyte at approximately 610 nm. At this position, the film consists of connected islands with small gaps. Hence, these two different molecules show two different laterally separated resonant positions on a non-uniform SERS substrate. This indicates that the type of non-uniform SERS substrate produced for this study offers multiple resonant conditions. Depending on the excitation wavelength and properties of the molecules, the maximum enhancement is observed at different lateral positions on those samples. This is a clear indication that these types of gradient samples can be used to screen for the optimal SERS conditions for different molecules. This also shows that metal islands can be tuned hassle-free and can be used as comparatively low-cost SERS substrates. Furthermore, the parameter range of these substrates can be further expanded by different annealing processes or by patterning of the underlying substrate.

3. Materials and Methods

3.1. Non-Uniform Metallic Au Particles Substrate Fabrication

The SERS substrates were prepared by metal evaporation in a vacuum evaporator (Plassys MEB400, France) using the thermal evaporation mode. The evaporation rate was 0.03 nm/s monitored by a built-in quartz crystal sensor. The working pressure was 1.0×10^{-6} Torr. Prior to metal evaporation, the glass substrates were washed with a mixture of detergent (Decon 90) and ddH_2O (1:9 volume ratio) in an ultrasonic water bath at 50 °C for 20 min, and then dried within an N_2 stream. Figure 5a shows a schematic of a conventional metal evaporation technique to deposit layers of uniform thickness covering the whole substrate. Non-uniform SERS substrates were fabricated by evaporating a thin

layer of gold (Au), followed by thermal annealing, which leads to the formation of Au NPs/islands. To attain non-uniform deposition of metal NPs, the sample holder, containing bare glass substrates, was placed very close to the source. This arrangement is shown in Figure 5b. The distance between source and substrate in this work was 70 mm. Afterwards, the sample is thermally annealed at 250 °C for 30 s on a hot plate. Figure 5c shows an optical image of the resultant non-uniform Au SERS substrates. The sample holder can hold 3 glass substrates of 22 mm × 40 mm each; the non-uniformity is extended over the 3 glass substrates and is even visible by the naked eye (Figure 5c).

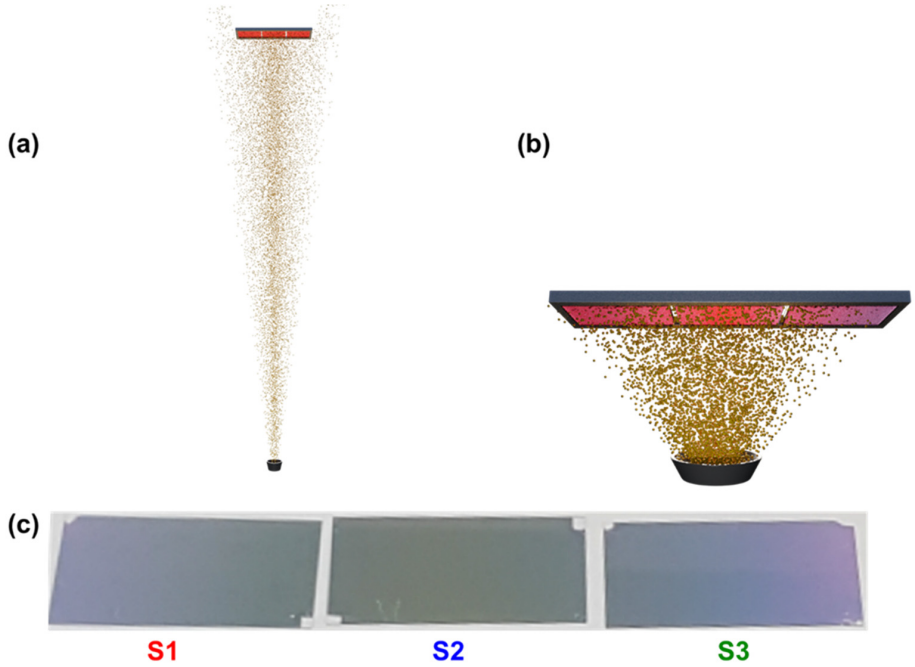

Figure 5. (**a**) Schematic of vacuum evaporator for metal deposition in the conventional method (for approximately uniform thickness of metal deposition), (**b**) schematic of vacuum evaporator for the metal deposition with non-uniform thickness, and (**c**) resulting non-uniform SERS substrates on glass.

3.2. Extinction Spectra

Extinction spectra were recorded in two confocal systems (Setup 1: Figures 2a–c and 3a, Setup 2: Figure 3d). The region of interest in each case is illuminated with a nearly collimated white light source under normal incidence. The transmitted light is collected by an objective, spatially filtered by either an optical fiber or a pinhole, and detected by a spectrometer [44,45]. Due to the spatial filtering, signal from an area of ∼10 µm diameter is recorded. All measurements were conducted at room temperature and ambient conditions.

Setup 1: Illumination takes place with a halogen light bulb in a LabRAM 800HR equipped with an Olympus BX41 microscope. The transmitted light is collected by a 20× objective (NA 0.45) and coupled into an Ocean Optics QE 65,000 spectrometer through a 200 µm fiber.

Setup 2: Illumination takes place with a halogen light bulb in a Nikon Ti-U inverted microscope. The transmitted light is collected by a 20× objective (NA 0.5) and spatially filtered by a 200 µm pinhole in the image plane before entering an Ocean Optics QE 65,000 spectrometer.

Extinction was evaluated in the spectrometer software according to

$$\text{Extinction} = -\log_{10}(\text{Ts}/\text{T}_0),$$

where T_0 represents the light intensity transmitted through a bare glass, and Ts is the intensity transmitted through the fabricated gradient SERS substrates. Both T_0 and Ts were first corrected for the dark current of the spectrometer's CCD detector.

3.3. SERS Experiments

A LabRAM 800HR from Horiba equipped with an Olympus BX41 microscope, a 632.8 nm laser and a 10× (NA = 0.3) objective in a reflection configuration was used for illumination and collection of the Raman signal. SERS experiments were performed with 1,2-bis(4-pyridyl) ethylene (BPE) with a concentration of 0.25×10^{-3} M and methylene blue (MB) with a concentration of 0.25×10^{-3} M in water. The excitation and emission maxima of the fluorescent molecule BPE are located at 388 nm and 456 nm, respectively [46,47], whereas the excitation and emission maxima of MB are located at 400 nm and 686 nm, respectively [48]. For the SERS experiments, droplets of 1 µL each were about equidistantly deposited on the substrate (corresponding to droplets with diameters of several 100 µm at a spacing of ~2–3 mm), and spectra were acquired rapidly before the droplets dried. The location of the droplets is denoted as "horizontal position" in the evaluation of the SERS spectra. Drying of the analyte might cause a non-uniform distribution of the analytes over the substrate surface, resulting in accumulation of the analyte at SERS hotspot regions, eventually hindering a correct characterization of the substrate [49,50]. Furthermore, it is worthwhile to validate the SERS substrate in solution to show its usefulness as a molecular sensor. All the measurements were conducted at room temperature and ambient conditions.

3.4. Scanning Electron Microscopy (SEM)

SEM images were acquired with a Schottky Jeol 6500F at 2 kV, a secondary electron detector, and an accelerating voltage of 0.5 to 30 kV.

4. Conclusions

We have demonstrated a straightforward strategy to design and fabricate non-uniform SERS substrates that offer a wide range of resonance wavelengths for faster screening of analytes. The substrates were fabricated in a metal evaporator by placing the sample holder close to the Au source. The substrate was characterized with SEM and shows a continuous transition from Au NPs to connected Au islands and back at different lateral positions. The intensity maximum of the extinction spectra showed that the resonances of such substrates vary over a wide range from 560 nm to 680 nm. Furthermore, the spectral shape of the extinction spectrum allows us to draw conclusions on the Au film morphology in that region. A comparatively sharp and symmetric spectrum originates from NPs, while a broad and asymmetric spectral shape indicates a connected island morphology. Additionally, the intensity of the spectra increases, since the optical cross-section is increased for islands with a larger area. Hence, acquiring an extinction spectrum can serve as an easy tool to characterize the morphology of an Au film based on the previous knowledge from the SEM images. The SEM images also reveal that the gap size between NPs/islands varies with the amount of material being deposited in that region. Smaller gap sizes between particles and islands create hotspots that increase the Raman enhancement. Such substrates are suitable to finding the optimal surface morphology for SERS. We investigated the SERS efficiency for BPE and MB and found that the maximum SERS enhancement for these molecules occurs at different lateral positions and thus, for different surface morphologies. For the non-resonant molecule BPE, the strongest enhancement was observed when the extinction maximum was close to the excitation laser wavelength, while the film morphology is still particle-like with small gaps was maintained. However, this was not the case for the resonant molecule MB, where it was favorable to have the extinction maximum at an about 20 nm longer resonance wavelength (possibly still closer to the excitation laser wavelength), even though the actual morphology consists of connected islands with larger gaps. (Note that the measured extinction maximawill be shifted to longer wavelengths when the analyte is added.) Hence, such non-uniform SERS substrates provide cost-effective and fast screening of analytes, show reproducible trends, and are reliable and easy to fabricate.

Supplementary Materials: The following supporting information can be downloaded at: https://www.mdpi.com/article/10.3390/molecules27165097/s1, Figure S1: SEM images of different fabricated substrates (substrate 1—red and substrate 2—blue) at the same position P1 and P5 to denote micro and nanoscale reproducibility. Figure S2: (a) Normalized extinction spectra at points P1, P8, and P9 (solid lines—red, blue, black) compared to normalized simulated extinction spectra from Mie theory for spherical gold NPs with radii of 10 nm, 15 nm, and 20 nm (dashed lines—red, blue, black), (b) schematic and equation to determine the symmetry factor of an extinction curve.

Author Contributions: Conceptualization: P.-M.A., A.J.M. and M.B.; data curation: A.M., Q.L. and F.W.; formal analysis: A.M., Q.L. and F.W.; funding acquisition: P.-M.A., A.J.M. and M.B.; investigation: A.M. and Q.L.; methodology: A.M., Q.L. and F.W.; project administration: P.-M.A. and M.B.; resources: F.W., F.D., M.F., P.-M.A., A.J.M. and M.B.; software: Q.L. and F.W.; supervision: M.F., P.-M.A., A.J.M. and M.B.; validation: A.M., Q.L., F.W., P.-M.A. and M.B.; visualization: A.M.; writing—original draft: A.M.; writing—review and editing: A.M., Q.L., F.W., F.D., M.F., P.-M.A., A.J.M. and M.B. All authors have read and agreed to the published version of the manuscript.

Funding: The author(s) disclose receipt of the following financial support for the research, authorship, and publication of this article: The authors would like to acknowledge financial support within the framework IngenieurNachwuchs 2016 (project: CompeTERS) by the German Federal Ministry of Education and Research (BMBF; Grant no.: 13FH596IX6) and gratefully acknowledge the Funding of China Scholarship Council (CSC).

Institutional Review Board Statement: Not applicable.

Informed Consent Statement: Not applicable.

Data Availability Statement: The data sets generated and/or analyzed during the current study are not publicly available since they are part of an ongoing PhD thesis. However, the data sets are available from the corresponding authors on reasonable request.

Conflicts of Interest: The authors declare no conflict of interest.

References

1. Raman, C.V.; Krishnan, K.S. A New Type of Secondary Radiation. *Nature* **1928**, *121*, 501–502. [CrossRef]
2. Liu, Q.; Wackenhut, F.; Hauler, O.; Scholz, M.; Zur Oven-Krockhaus, S.; Ritz, R.; Adam, P.-M.; Brecht, M.; Meixner, A.J. Hypericin: Single Molecule Spectroscopy of an Active Natural Drug. *J. Phys. Chem. A* **2020**, *124*, 2497–2504. [CrossRef] [PubMed]
3. Fleischmann, M.; Hendra, P.J.; McQuillan, A.J. Raman spectra of pyridine adsorbed at a silver electrode. *Chem. Phys. Lett.* **1974**, *26*, 163–166. [CrossRef]
4. Le Ru, E.C.; Blackie, E.; Meyer, M.; Etchegoin, P.G. Surface Enhanced Raman Scattering Enhancement Factors: A Comprehensive Study. *J. Phys. Chem. C* **2007**, *111*, 13794–13803. [CrossRef]
5. Félidj, N.; Aubard, J.; Lévi, G.; Krenn, J.R.; Salerno, M.; Schider, G.; Lamprecht, B.; Leitner, A.; Aussenegg, F.R. Controlling the optical response of regular arrays of gold particles for surface-enhanced Raman scattering. *Phys. Rev. B* **2002**, *65*, 075419. [CrossRef]
6. Félidj, N.; Aubard, J.; Lévi, G.; Krenn, J.R.; Schider, G.; Leitner, A.; Aussenegg, F.R. Enhanced substrate-induced coupling in two-dimensional gold nanoparticle arrays. *Phys. Rev. B* **2002**, *66*, 245407. [CrossRef]
7. Vosgröne, T.; Meixner, A.J. Surface- and resonance-enhanced micro-Raman spectroscopy of xanthene dyes: From the ensemble to single molecules. *Chemphyschem* **2005**, *6*, 154–163. [CrossRef]
8. Milekhin, A.G.; Rahaman, M.; Rodyakina, E.E.; Latyshev, A.V.; Dzhagan, V.M.; Zahn, D.R.T. Giant gap-plasmon tip-enhanced Raman scattering of MoS_2 monolayers on Au nanocluster arrays. *Nanoscale* **2018**, *10*, 2755–2763. [CrossRef]
9. Rahaman, M.; Milekhin, A.G.; Mukherjee, A.; Rodyakina, E.E.; Latyshev, A.V.; Dzhagan, V.M.; Zahn, D.R.T. The role of a plasmonic substrate on the enhancement and spatial resolution of tip-enhanced Raman scattering. *Faraday Discuss.* **2019**, *214*, 309–323. [CrossRef]
10. Rodriguez, R.D.; Sheremet, E.; Deckert-Gaudig, T.; Chaneac, C.; Hietschold, M.; Deckert, V.; Zahn, D.R.T. Surface- and tip-enhanced Raman spectroscopy reveals spin-waves in iron oxide nanoparticles. *Nanoscale* **2015**, *7*, 9545–9551. [CrossRef]
11. Sheremet, E.; Rodriguez, R.D.; Zahn, D.R.T.; Milekhin, A.G.; Rodyakina, E.E.; Latyshev, A.V. Surface-enhanced Raman scattering and gap-mode tip-enhanced Raman scattering investigations of phthalocyanine molecules on gold nanostructured substrates. *J. Vac. Sci. Technol. B Nanotechnol. Microelectron. Mater. Process. Meas. Phenom.* **2014**, *32*, 04E110. [CrossRef]
12. Hauler, O.; Jakob, L.A.; Braun, K.; Laible, F.; Fleischer, M.; Meixner, A.J.; Wackenhut, F. Sensitive Interferometric Plasmon Ruler Based on a Single Nanodimer. *J. Phys. Chem. C* **2021**, *125*, 6486–6493. [CrossRef]
13. Macias, G.; Alba, M.; Marsal, L.F.; Mihi, A. Surface roughness boosts the SERS performance of imprinted plasmonic architectures. *J. Mater. Chem. C* **2016**, *4*, 3970–3975. [CrossRef]

14. Zhao, Y.; Liu, X.; Lei, D.Y.; Chai, Y. Effects of surface roughness of Ag thin films on surface-enhanced Raman spectroscopy of graphene: Spatial nonlocality and physisorption strain. *Nanoscale* **2014**, *6*, 1311–1317. [CrossRef]
15. Muniz-Miranda, M. SERS-active Ag/SiO_2 colloids: Photoreduction mechanism of the silver ions and catalytic activity of the colloidal nanoparticles. *J. Raman Spectrosc.* **2004**, *35*, 839–842. [CrossRef]
16. Qian, X.-M.; Nie, S.M. Single-molecule and single-nanoparticle SERS: From fundamental mechanisms to biomedical applications. *Chem. Soc. Rev.* **2008**, *37*, 912–920. [CrossRef]
17. Ye, Z.; Li, C.; Chen, Q.; Xu, Y.; Bell, S.E.J. Self-assembly of colloidal nanoparticles into 2D arrays at water-oil interfaces: Rational construction of stable SERS substrates with accessible enhancing surfaces and tailored plasmonic response. *Nanoscale* **2021**, *13*, 5937–5953. [CrossRef]
18. Aroca, R.; Martin, F. Tuning metal island films for maximum surface-enhanced Raman scattering. *J. Raman Spectrosc.* **1985**, *16*, 156–162. [CrossRef]
19. Jennings, C.A.; Kovacs, G.J.; Aroca, R. Near-infrared surface-enhanced Raman scattering from metal island films. *J. Phys. Chem.* **1992**, *96*, 1340–1343. [CrossRef]
20. Kovacs, G.J.; Loutfy, R.O.; Vincett, P.S.; Jennings, C.; Aroca, R. Distance dependence of SERS enhancement factor from Langmuir-Blodgett monolayers on metal island films: Evidence for the electromagnetic mechanism. *Langmuir* **1986**, *2*, 689–694. [CrossRef]
21. Rodriguez, R.D.; Sheremet, E.; Nesterov, M.; Moras, S.; Rahaman, M.; Weiss, T.; Hietschold, M.; Zahn, D.R. Aluminum and copper nanostructures for surface-enhanced Raman spectroscopy: A one-to-one comparison to silver and gold. *Sens. Actuators B Chem.* **2018**, *262*, 922–927. [CrossRef]
22. Chen, Y.; Si, K.J.; Sikdar, D.; Tang, Y.; Premaratne, M.; Cheng, W. Ultrathin Plasmene Nanosheets as Soft and Surface-Attachable SERS Substrates with High Signal Uniformity. *Adv. Opt. Mater.* **2015**, *3*, 919–924. [CrossRef]
23. Luo, X.; Liu, W.; Chen, C.; Jiang, G.; Hu, X.; Zhang, H.; Zhong, M. Femtosecond laser micro-nano structured Ag SERS substrates with unique sensitivity, uniformity and stability for food safety evaluation. *Opt. Laser Technol.* **2021**, *139*, 106969. [CrossRef]
24. Wen, P.; Yang, F.; Ge, C.; Li, S.; Xu, Y.; Chen, L. Self-assembled nano-Ag/Au@Au film composite SERS substrates show high uniformity and high enhancement factor for creatinine detection. *Nanotechnology* **2021**, *32*, 395502. [CrossRef]
25. Zheng, Y.; Wang, W.; Fu, Q.; Wu, M.; Shayan, K.; Wong, K.M.; Singh, S.; Schober, A.; Schaaf, P.; Lei, Y. Surface-Enhanced Raman Scattering (SERS) Substrate Based on Large-Area Well-Defined Gold Nanoparticle Arrays with High SERS Uniformity and Stability. *ChemPlusChem* **2014**, *79*, 1622–1630. [CrossRef]
26. Schreiber, B.; Gkogkou, D.; Dedelaite, L.; Kerbusch, J.; Hübner, R.; Sheremet, E.; Zahn, D.R.T.; Ramanavicius, A.; Facsko, S.; Rodriguez, R.D. Large-scale self-organized gold nanostructures with bidirectional plasmon resonances for SERS. *RSC Adv.* **2018**, *8*, 22569–22576. [CrossRef]
27. Milekhin, A.G.; Yeryukov, N.A.; Sveshnikova, L.L.; Duda, T.A.; Rodyakina, E.E.; Sheremet, E.S.; Ludemann, M.; Gordan, O.D.; Latyshev, A.V.; Zahn, D.R. Surface enhanced Raman scattering by organic and inorganic semiconductors formed on laterally ordered arrays of Au nanoclusters. *Thin Solid Film.* **2013**, *543*, 35–40. [CrossRef]
28. Baker, B.E.; Kline, N.J.; Treado, P.J.; Natan, M.J. Solution-Based Assembly of Metal Surfaces by Combinatorial Methods. *J. Am. Chem. Soc.* **1996**, *118*, 8721–8722. [CrossRef]
29. Bhat, R.R.; Genzer, J.; Chaney, B.N.; Sugg, H.W.; Liebmann-Vinson, A. Controlling the assembly of nanoparticles using surface grafted molecular and macromolecular gradients. *Nanotechnology* **2003**, *14*, 1145–1152. [CrossRef]
30. Cao, H.; Tegenfeldt, J.O.; Austin, R.H.; Chou, S.Y. Gradient nanostructures for interfacing microfluidics and nanofluidics. *Appl. Phys. Lett.* **2002**, *81*, 3058–3060. [CrossRef]
31. Gupta, S.; Huda, S.; Kilpatrick, P.K.; Velev, O.D. Characterization and optimization of gold nanoparticle-based silver-enhanced immunoassays. *Anal. Chem.* **2007**, *79*, 3810–3820. [CrossRef] [PubMed]
32. Han, M.; Xu, C.; Zhu, D.; Yang, L.; Zhang, J.; Chen, Y.; Ding, K.; Song, F.; Wang, G. Controllable Synthesis of Two-Dimensional Metal Nanoparticle Arrays with Oriented Size and Number Density Gradients. *Adv. Mater.* **2007**, *19*, 2979–2983. [CrossRef]
33. He, L.; Chen, X.; Mu, Y.; Song, F.; Han, M. Two-dimensional gradient Ag nanoparticle assemblies: Multiscale fabrication and SERS applications. *Nanotechnology* **2010**, *21*, 495601. [CrossRef]
34. Huang, J.; Liu, Y.; He, X.; Tang, C.; Du, K.; He, Z. Gradient nanoporous gold: A novel surface-enhanced Raman scattering substrate. *RSC Adv.* **2017**, *7*, 15747–15753. [CrossRef]
35. Huwiler, C.; Kunzler, T.P.; Textor, M.; Vörös, A.J.; Spencer, N.D. Functionalizable Nanomorphology Gradients via Colloidal Self-Assembly. *Langmuir* **2007**, *23*, 5929–5935. [CrossRef] [PubMed]
36. Song, F.; Cai, Y.; Newby, B.-M.Z. Fabricating tunable nanoparticle density gradients with the contact printing based approach. *Appl. Surf. Sci.* **2006**, *253*, 2393–2398. [CrossRef]
37. Bhat, R.R.; Fischer, A.D.A.; Genzer, J. Fabricating Planar Nanoparticle Assemblies with Number Density Gradients. *Langmuir* **2002**, *18*, 5640–5643. [CrossRef]
38. Oates, T.W.H.; Noda, S. Thickness-gradient dependent Raman enhancement in silver island films. *Appl. Phys. Lett.* **2009**, *94*, 053106. [CrossRef]
39. Pashley, D.W.; Stowell, M.J.; Jacobs, M.H.; Law, T.J. The growth and structure of gold and silver deposits formed by evaporation inside an electron microscope. *Philos. Mag.* **1964**, *10*, 127–158. [CrossRef]
40. Farooq, S.; de Araujo, R.E. Engineering a Localized Surface Plasmon Resonance Platform for Molecular Biosensing. *Open J. Appl. Sci.* **2018**, *8*, 126–139. [CrossRef]

41. Göeken, K.L.; Subramaniam, V.; Gill, R. Enhancing spectral shifts of plasmon-coupled noble metal nanoparticles for sensing applications. *Phys. Chem. Chem. Phys.* **2015**, *17*, 422–427. [CrossRef] [PubMed]
42. Starowicz, Z.; Wojnarowska-Nowak, R.; Ozga, P.; Sheregii, E.M. The tuning of the plasmon resonance of the metal nanoparticles in terms of the SERS effect. *Colloid Polym. Sci.* **2018**, *296*, 1029–1037. [CrossRef] [PubMed]
43. Tabor, C.; van Haute, D.; El-Sayed, M.A. Effect of orientation on plasmonic coupling between gold nanorods. *ACS Nano* **2009**, *3*, 3670–3678. [CrossRef]
44. Khaywah, M.Y.; Jradi, S.; Louarn, G.; Lacroute, Y.; Toufaily, J.; Hamieh, T.; Adam, P.-M. Ultrastable, Uniform, Reproducible, and Highly Sensitive Bimetallic Nanoparticles as Reliable Large Scale SERS Substrates. *J. Phys. Chem. C* **2015**, *119*, 26091–26100. [CrossRef]
45. Dai, F.; Horrer, A.; Adam, P.-M.; Fleischer, M. Accessing the Hotspots of Cavity Plasmon Modes in Vertical Metal–Insulator–Metal Structures for Surface Enhanced Raman Scattering. *Adv. Opt. Mater.* **2020**, *8*, 1901734. [CrossRef]
46. Commission Internationale de L'Eclairag. *Colorimetry*, 3rd ed.; CIE, Central Bureau: Vienna, Austria, 2004; ISBN 3901906339.
47. Guergouri, M.; Bensegueni, R.; Bencharif, L. Synthesis, photophysical properties and electrochemical polymerization of a new blue fluorescent compound based on 3,4-ethylenedioxythiophene moiety. *Mater. Sci. Pol.* **2020**, *38*, 151–158. [CrossRef]
48. Selvam, S.; Sarkar, I. Bile salt induced solubilization of methylene blue: Study on methylene blue fluorescence properties and molecular mechanics calculation. *J. Pharm. Anal.* **2017**, *7*, 71–75. [CrossRef]
49. Kim, A.; Ou, F.S.; Ohlberg, D.A.A.; Hu, M.; Williams, R.S.; Li, Z. Study of molecular trapping inside gold nanofinger arrays on surface-enhanced Raman substrates. *J. Am. Chem. Soc.* **2011**, *133*, 8234–8239. [CrossRef]
50. Altun, A.O.; Youn, S.K.; Yazdani, N.; Bond, T.; Park, H.G. Metal-dielectric-CNT nanowires for femtomolar chemical detection by surface enhanced Raman spectroscopy. *Adv. Mater.* **2013**, *25*, 4431–4436. [CrossRef]

7. Anisotropic and Amphiphilic Mesoporous core-shell silica Microparticles Provide Chemically Selective Environments for Simultaneous Delivery of Curcumin and Quercetin

*Akanksha Dohare[1], Swathi Sudhakar[2], Björn Brodbeck[1,3], Ashutosh Mukherjee[3,4], Marc Brecht[3,4], Andreas Kandelbauer[3], Erik Schäffer[2], and Hermann A. Mayer[1,] *.*

[1]Institute of Inorganic Chemistry, University of Tübingen, Auf der Morgenstelle 18, 72076 Tübingen, Germany

[2]ZMBP, Cellular Nanoscience, University of Tübingen, Auf der Morgenstelle 32, 72076 Tübingen, Germany

[3]Process Analysis and Technology (PA&T), Reutlingen Research Institute, Reutlingen University, Alteburgstrasse 150, 72762 Reutlingen, Germany.

[4]IPTC and LISA+ center, University of Tübingen, Auf der Morgenstelle 18, 72076 Tübingen, Germany

This chapter was originally published in ACS Langmuir as

Akanksha Dohare, Swathi Sudhakar, Björn Brodbeck, Ashutosh Mukherjee, Marc Brecht, Andreas Kandelbauer, Erik Schäffer, and Hermann A. Mayer. Langmuir 2021 37, 45, 13460-13470.

DOI: 10.1021/acs.langmuir.1c02210

Supplementary Material/Supporting Information shown in Appendix 4

LANGMUIR

pubs.acs.org/Langmuir Article

Anisotropic and Amphiphilic Mesoporous Core–Shell Silica Microparticles Provide Chemically Selective Environments for Simultaneous Delivery of Curcumin and Quercetin

Akanksha Dohare, Swathi Sudhakar, Björn Brodbeck, Ashutosh Mukherjee, Marc Brecht, Andreas Kandelbauer, Erik Schäffer, and Hermann A. Mayer*

Cite This: *Langmuir* 2021, 37, 13460–13470

Read Online

ACCESS | Metrics & More | Article Recommendations | Supporting Information

ABSTRACT: Porous silica materials are often used for drug delivery. However, systems for simultaneous delivery of multiple drugs are scarce. Here we show that anisotropic and amphiphilic dumbbell core–shell silica microparticles with chemically selective environments can entrap and release two drugs simultaneously. The dumbbells consist of a large dense lobe and a smaller hollow hemisphere. Electron microscopy images show that the shells of both parts have mesoporous channels. In a simple etching process, the properly adjusted stirring speed and the application of ammonium fluoride as etching agent determine the shape and the surface anisotropy of the particles. The surface of the dense lobe and the small hemisphere differ in their zeta potentials consistent with differences in dye and drug entrapment. Confocal Raman microscopy and spectroscopy show that the two polyphenols curcumin (Cur) and quercetin (QT) accumulate in different compartments of the particles. The overall drug entrapment efficiency of Cur plus QT is high for the amphiphilic particles but differs widely between Cur and QT compared to controls of core–shell silica microspheres and uniformly charged dumbbell microparticles. Furthermore, Cur and QT loaded microparticles show different cancer cell inhibitory activities. The highest activity is detected for the dual drug loaded amphiphilic microparticles in comparison to the controls. In the long term, amphiphilic particles may open up new strategies for drug delivery.

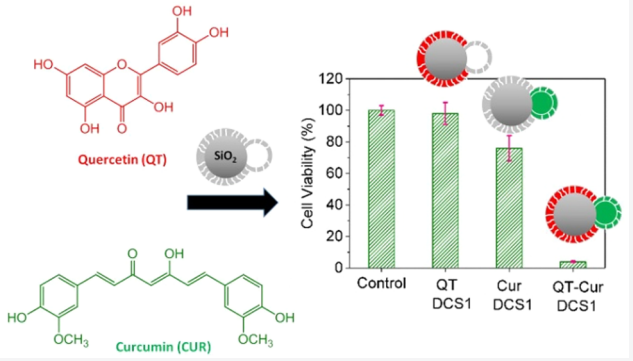

1. INTRODUCTION

Transportation of drugs into cells for medical diagnostics and treatment is of fundamental importance. Many of the present drugs are suffering from stability problems in a biological environment and/or poor water solubility, making the drugs less effective.[1] Thus, drug delivery strategies based on different materials have been developed.[1−6] So far, several types of drug vehicles have been reported which include liposomes,[7] peptides,[8] polymers,[9−11] inorganic nano- and microparticles,[12−17] and organic/inorganic hybrid materials.[18,19] A drawback of many materials is their low drug loading capabilities. To improve their therapeutic efficacy, large amounts of carrier have to be applied. Unfortunately, most of the carriers are accompanied by drawbacks such as poor biocompatibility, the application of large amounts of surfactants, the requirement for chemical modifications, and complex preparation protocols that restrict their access.

The natural, hydrophobic polyphenols curcumin (Cur) and quercetin (QT) affect numerous cellular targets and show activity on the cellular level.[20−25] Both compounds suffer from poor bioavailability because of their low solubility in aqueous solutions and low stability in a biological environment. Consequently, several approaches to deliver both natural polyphenols with different types of drug carriers have been suggested.[26−38]

Mesoporous silica nano- and microparticles are biocompatible and biodegradable and provide networks of pores with a large surface area and high pore volume.[39−42] These properties make them attractive for many applications in different fields[43−45] including drug delivery systems.[15,44,46,47] By trapping the drug in the mesoporous network, drug degradation is reduced and solubility is enhanced.[14] Thus, this enhancement has led to a dramatic increase in the interest of mesoporous silica-based formulations in the past decade.[1,48]

Although several studies have highlighted the controlled release of various therapeutic agents with mesoporous silica

Received: August 18, 2021
Revised: October 19, 2021
Published: November 3, 2021

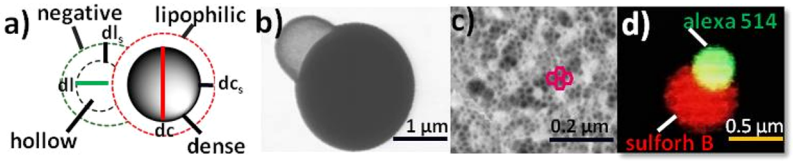

Figure 1. (a) Schematic illustration of the anisotropic, amphiphilic core−shell dumbbell particle (dl, dl_s, dc, and dc_s: diameter and thickness of the hollow cavity and its shell as well as of the dense core and its shell, respectively), (b) STEM micrograph of a representative particle, (c) surface morphology of the shell displaying the hexagonally ordered mesoporous channels, and (d) particle colored with negatively charged Sulforhodamine B (red) and positively charged Alexa Fluor 514 (green).

particles,[49−51] in most of the reported examples only one kind of drug is entrapped.[52] Up to date, the codelivery of multiple drugs with different molecular properties remains difficult.[53] Yet, the possibility to load and release different drugs on the same systems allows to combine therapies and increases the opportunities for treating diseases. This codelivery requires materials with the ability to load and release drugs with different properties and function.

Mesoporous materials with multilevel morphology and hierarchical pore structures have been developed.[54−58] Such particles provide different compartments and phase-separated domains and are thus interesting candidates for multidrug delivery purposes.[59−61] Moreover, the amphiphilic character that multifunctional particles, like Janus particles, often have increases the interfacial activity and improves the particle−cell interaction.[62]

We recently reported on anisotropic dumbbell[63] core−shell silica microparticles, which are composed of two different hemispheres (Figure 1),[64] so that three compartments can be identified: (i) the shell of the large lobe that is partially fluorinated and, therefore, more hydrophobic with a weak surface charge, (ii) the hydrophilic shell of the small lobe that is negatively charged, and (iii) the hollow cage that is covered by the small hemisphere. The diverse hemispheres as well as the different compartments make these amphiphilic particles attractive materials for the codelivery of multiple drugs with different properties and function.

Here we demonstrate that because of the shape, surface anisotropy, and their amphiphilic character, these particles show distinctly different drug loading and release behavior than comparable spherical core−shell silica particles. Moreover, we show that Cur and QT, when loaded on the amphiphilic anisotropic core−shell particles, accumulate in different compartments and lead to an enhanced U2OS human bone osteosarcoma epithelial cancer cell toxicity.

2. MATERIALS AND METHODS

2.1. Materials. Cetyltrimethylammonium bromide (CTAB), *n*-tridecane (99%), ammonium fluoride (98%), and SiO_2 particles (1.5 μm) were purchased from ABCR. Ammonium carbonate (ACS reagent ≥30% NH_3), curcumin, quercetin, dialysis bags (MWCO 10 kDa), dimethyl sulfoxide (DMSO), 3-[4,5-dimethylthiazole-2-yl]-2,5-diphenyltetrazolium bromide (MTT), ammonium hydroxide (28−30%), poly(vinyl alcohol) (PVA), Alexa 514, Sulforhodamine B, Alexa Fluor 514, Atto 488, and Rhodamine 6G were obtained from Sigma-Aldrich. Deionized water and ethanol were used of technical grade.

In all experiments reported below no unexpected or unusual high safety hazards were encountered.

2.2. Synthesis of the Spherical Core−Shell (CS) and the Anisotropic Dumbbell Core−Shell Silica Particles (DCS1 and DCS2). The anisotropic amphiphilic dumbbell core−shell (DCS1) silica particles were synthesized by following a procedure reported earlier[64] with minor variations. Concisely, 2.1 g of CTAB as surfactant and 2.1 g of silica particles of 1.5 μm size were dissolved in 210 mL of water and sonicated for 1 h. Then 11.6 mL of *n*-tridecane was added and sonicated for another hour. To this suspension, 12 mL of an ammonia and ammonium fluoride (1.35 mmol) solution was added and kept stirring at 210−240 rpm at 90 °C for 24 h. The anisotropic dumbbell silica−core−shell particles (DCS1) were collected after centrifugation (2500 rpm for 1 min), washed once with deionized water, twice with ethanol, and once with diethyl ether, and then calcined at 600 °C for 15 h.

The spherical core−shell silica particles (CS) were prepared by following the same procedure with the exception that the stirring speed was kept below 190 rpm.

For the preparation of the uniformly charged DCS2 particles, the ammonium fluoride was replaced by an equimolar amount of ammonium carbonate by otherwise identical reaction conditions.

2.3. Characterization of the CS, DCS1, and DCS2 Particles. Scanning electron microscopy (SEM) and scanning transmission electron microscopy (STEM) images were acquired on a Hitachi SU8030 machine equipped with a triple detector. The particles were suspended in ethanol and kept in an ultrasonic bath for homogenization for 10 min. The samples were spin-coated onto silicon wafers for SEM and spotted on copper grids for STEM analysis. The zeta potential in ethanol was measured at room temperature with a Zetasizer Nano ZS by Malvern. The samples were suspended in ethanol and transferred to a cuvette. For confocal Raman measurements, a WITec alpha300 RA&S microscope was used. This system was equipped with a lens-based UHTS 300 spectrometer connected via a 100 μm (NA = 0.12) multimode optical fiber and thermoelectric cooled CCD and EMCCD (DU970N-BV). All Raman experiments were performed by using a laser of 532 nm with a nominal output power of 60 mW and a grating of 600 lines/mm. For illumination and collection, the laser was focused on the sample through a Zeiss Epiplan-Neofluar objective of magnification 100× (NA = 0.9). Data processing was done by using Control 5.0 software provided by WITec, and all experiments were performed at ambient conditions. We chose sapphire as a substrate because of its low background signal, which does not overshadow the signal intensity from the region of interest. The peak positions of sapphire also do not interfere with the potential peak positions of QT and Cur, thus making sapphire an ideal substrate for Raman analysis of these drug loaded particles. The samples were prepared in the same way as described in the drug loading experiments.

2.4. Dyeing Experiments. Dyeing experiments were performed in ethanol solutions with concentrations between 5×10^{-6} and 5×10^{-4} mol/L of the corresponding dye. The sample preparation was done by mixing 0.2 mg of the sample particles with 50 μL of fluorophore solution (in ethanol) and 50 μL of an aqueous 4% poly(vinyl alcohol) (PVA) solution. This solution was homogenized for 10 min in an ultrasonic bath to allow the diffusion of the dye molecules into the mesopores of the shells of silica particles and into the hollow lobe of the particle. After the sample preparation, just a drop of sample was spotted on a glass slide and kept under the microscope. The thin PVA film prevents movements of the silica particles and provides a random orientation of the small spheres of all dumbbell particles. The image was taken with a Leica TCS SP8 multiphoton confocal microscope. Excitation and emission wavelengths were at 514 and 542 nm (Alexa Fluor 514), 559 and 577 nm (Sulforhodamine B), 500 and 520 nm (Atto 488), and 525 and 548 nm (Rhodamine 6G), respectively.

2.5. Drug Loading of Curcumin (Cur) and Quercetin (QT) in CS, DCS1, and DCS2 Particles. For loading the microparticles CS,

https://doi.org/10.1021/acs.langmuir.1c02210
Langmuir 2021, 37, 13460−13470

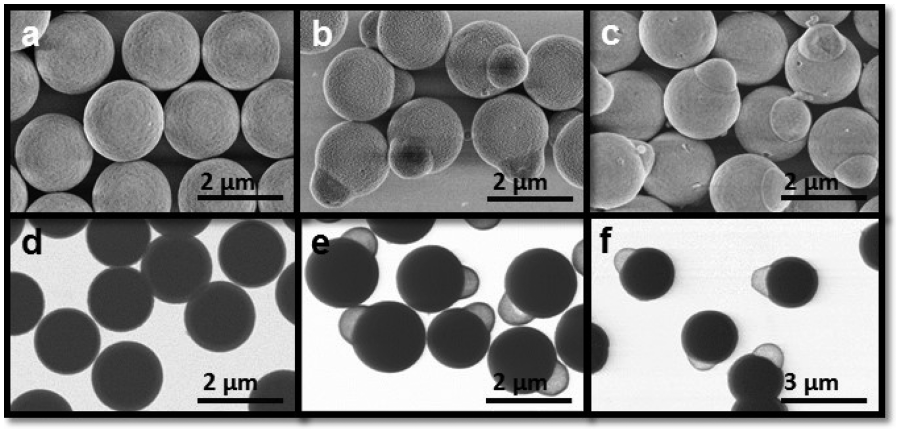

Figure 2. SEM (a–c) and STEM (d–f) images of CS (a, d), DCS1 (b, e), and DCS2 (c, f) silica particles.

DCS1, and DCS2 with drugs, a total volume of 1 mL of 0.75 mM of each drug dissolved in 0.5 mL of ethanol was mixed with 1 mg/mL of the corresponding CS, DCS1, and DCS2 microparticles.[65] The suspensions were shortly ultrasonicated and gently stirred for 4 h. Then, the Cur and QT loaded microparticles were centrifuged at 13000 rpm for 3 min. To determine the drug entrapment efficiency, we measured the UV absorbance (Nanodrop, ND 1000 spectrometer) of Cur and QT at 450 and 270 nm, respectively, in the supernatants of the centrifuged sample and the initial 0.5 mg/mL solution. Subsequently, we used the following equation for both drugs in CS and dumbbell microparticles DCS1 and DCS2.

$$\text{drug entrapment efficiency (\%)} = \frac{\text{theoretical amount of drug loaded} - \text{free drug}}{\text{theoretical amount of drug loaded}} \times 100$$

2.6. *In Vitro* Drug Release Study. *In vitro* drug release studies of Cur and QT from CS, DCS1, and DCS2 were investigated at pH 5.5 (environmental pH for tumors) and at pH 7.4 (physiological pH). The drug loaded CS, DCS1, and DCS2 particles were suspended in 2 mL of phosphate-buffered saline (PBS) and transferred to a dialysis bag (molecular weight cutoff 10 kDa, Sigma). Then they were placed in 25 mL of PBS and incubated at 37 °C while stirring (100 rpm).[66,67] The released drugs were again determined spectrophotometrically by measuring the absorbance at 450 and 270 nm. The concentration of released drug was calculated by using a calibration function derived from reference samples of defined concentrations as described earlier.[66,67] Also, the percentage of released drug was determined as described earlier.[68,69]

2.7. Cell Viability Studies. The cytotoxicity of the cells was studied by performing the 3-(4,5-dimethylthiazol-2-yl)-2,5-diphenyl-tetrazolium bromide (MTT) assay as described.[70] Briefly, the human bone osteosarcoma epithelial cancer cell lines (U2OS; 6 × 103 cells) were seeded in a 96 well culture plate. After 12 h, the cells were treated with 50 μL of CS, DCS1, and DCS2 particles (1 mg/mL) which were loaded with Cur, QT, and both drugs (25 nM) for 24 h. Control cells were treated with 0.1% DMSO in a culture medium. After treatment, the cells were incubated with the MTT solution (5 mg/mL in PBS) at 37 °C for 4 h, and then DMSO was added during shaking at room temperature. The spectrophotometric absorbance was measured at 570 nm on a microplate reader (Biotek, Multiplate reader, USA). Cell viability was expressed as the relative formazan formation in the treated samples compared with control cells after correction for background absorbance. The percentage of cell viability was determined by using the following formula:

$$\text{cell viability (\%)} = \frac{\text{absorbance of the treated sample}}{\text{absorbance of the untreated sample}} \times 100$$

Results were plotted as the mean ± standard deviation (SD) of three separate experiments.

3. RESULTS AND DISCUSSION

3.1. Synthesis of CS, DCS1, and DCS2 Microparticles. The protocol of the recently reported one-pot synthesis was applied to prepare monodisperse core–shell silica particles CS, amphiphilic DCS1, and uniformly charged DCS2 dumbbell core–shell silica particles (Figure 2).[64] To this end, a homogeneous suspension of nonporous dense spherical silica particles (d = 1.5 μm), CTAB, and n-tridecane was treated under stirring with a water solution of ammonia/ammonium fluoride at 90 °C. Stirring below 190 rpm generated the spherical core–shell particles CS (Figure 2a,d), while stirring between 240 and 280 rpm produced the anisotropic and amphiphilic dumbbell particles DCS1 (Figure 2b,e). If the ammonium fluoride is replaced by ammonium carbonate, the anisotropic DCS2 particles (Figure 2c,f) were obtained.

According to the SEM and STEM micrographs, the protocol produced monodisperse spherical CS (Figure 2 a,d) and dumbbell-like anisotropic particles DCS1 and DCS2 (Figure 2b,c,e,f and Figure 1S). The core and the shell as well as the hollow cavity of the small hemispheres in DCS1 and DSC2 can be distinguished in the STEM micrographs (Figure 2e,f and Table 1). The shells that cover all particles consisted of highly

Table 1. Pore Size Distribution, Specific Surface Areas Obtained by Nitrogen Physisorption of CS, DCS1, and DCS2, and Geometrical Parameters dc, dc_s, dl, and dl_s (For Definition See Figure 1)

	specific surf. area [m^2/g]	total pore vol [cm^3/g]	av pore size [nm]	dc [nm]	dc_s [nm]	dl [nm]	dl_s [nm]
CS	239	0.32	4.3, 5.7	1230	176		
DCS1	120	0.17	5.5	1332	118	410	63
DCS2	201	0.30	4.5, 5.9	1220	124	340	47

hexagonally ordered tunnels with uniform pore sizes of approximately 4.3–5.9 nm (Figure 1, Table 1, and Figures 1S and 2S). The thickness of the mesoporous shell of the spherical CS was 176 nm and can be adjusted with the reaction time.[71] During the same reaction time, a shell as thick as 118 and 124 nm around the dense cores of DCS1 and DCS2, respectively, were formed. The shells of the small hemispheres, which cover the hollow cavity, were 63 and 47 nm thick for the two dumbbells, respectively (Table 1).

Reversible nitrogen adsorption and desorption isotherms are found for the core–shell materials CS, DCS1, and DCS2, which

https://doi.org/10.1021/acs.langmuir.1c02210
Langmuir 2021, 37, 13460–13470

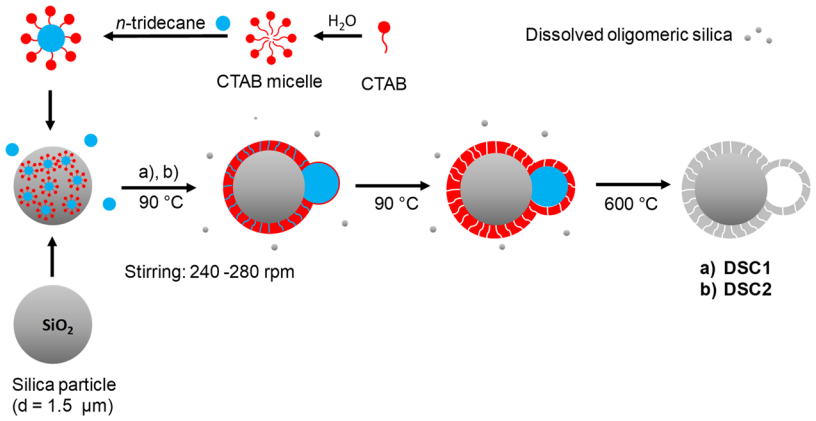

Figure 3. Proposed formation of DCS1 and DCS2: (a) NH_3/NH_4F and (b) $NH_3/(NH_4)_2CO_3$.

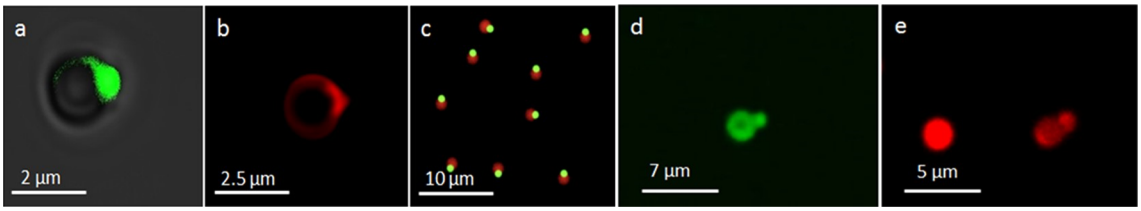

Figure 4. Dying of DCS1 (a–c) and DCS2 (d, e) with (a) positively charged Alexa Fluor 514 (green), (b) negatively charged Sulforhodamine B (red), (c) Alexa Fluor 514 (green) and Sulforhodamine B (red), (d) positively charged Atto 488 (green), and (e) Rhodamine 6G (red).

display a typical Langmuir IV hysteresis (Figure 2S). The H1 loop is characteristic for narrow uniform mesopores as found in template MCM-41 silica.[72] The average pore size calculated from the adsorption branch of the nitrogen isotherms by the BJH method (Table 1) ranged from 4.3 to 5.9 nm. Interestingly, for CS and DCS2 bimodal pore distributions within this range were observed.[71] Compared to the spherical CS and anisotropic DCS2 particles, the amphiphilic dumbbells DCS1 have smaller specific surface areas and smaller pore volumes (Table 1). All physicochemical data of the anisotropic core–shell particles compare well with those reported for dumbbells of this type.[64]

In an etching process,[71,73−75] nucleophilic OH^- ions attack electrophilic silica centers on the surface of the dense spherical silica particles and gradually dissolve small oligomeric silica species (Figure 3). In cooperation with the CTAB micelles which are located on the surface of the silica particles, these silica species recondense close to the site of their dissolution,[43] generating mesoporous shells around the silica particles.[76] Because of the excess of the porogen *n*-tridecane, additional droplets are formed that adsorb on the particle surface and serve as templates for the construction of the second hemispheres in DCS1 and DCS2 (Figure 3). Because of surface tension effects and an overall minimization of interfacial energy, only a single hemisphere forms.[64]

The NH_4F, applied as etching agent in the synthesis of DCS1, is a source of nucleophilic F^- ions that also attack the silica surface producing oligomeric silica species. In contrast to OH^-, which leaves negatively charged SiO^- at the site of attack, F^- generates neutral SiF bonds. Consequently, the negative surface charge of the large hemisphere is reduced, and a lipophilic environment is generated. As the small hemisphere is built with the negatively charged oligomers, the negative charge of the small lobe is higher compared to that of the large lobe. This mechanism results in the amphiphilic character of DCS1 with a lipophilic large lobe and a negatively charged small hemisphere. Introducing ammonium carbonate as etching agent generated the anisotropic dumbbell particles DCS2 with a uniform negative charge distribution across the particle surface.

This finding agrees with an overall smaller zeta potential for DCS2 (−47.4 ± 0.9 mV) compared to that of DCS1 (−25.5 ± 0.6 mV). This difference can also be visualized by dyeing experiments with positively and negatively charged dyes of the rhodamine family (Figure 4). Thus, amphiphilic parts of DCS1 discriminate between positively charged Alexa Fluor 514 (green, Figure 4a,c) and negatively charged Sulforhodamine B (red, Figure 4b,c) when treated with these dyes individually (Figure 4a,b) and with both dyes simultaneously (Figure 4c). Clearly, the positively charged green dye accumulates in the shell of the negatively charged small hemisphere while the negatively charged dye is located on the large lobe (Figure 4a–c). In contrast to the DCS1 particles, the uniformly charged dumbbell particles DCS2 are unable to distinguish between the positively and negatively charged dyes Atto 488 and Rhodamine 6G, respectively. Both dyes are uniformly distributed across the particle surface (Figure 4d,e).

3.2. Drug Entrapment Efficiency. In general, the amount of drug that can be loaded onto mesoporous silica depends on the surface area, the pore volume, the pore geometry, and the number of silanol groups on the surface. Silanol groups, when deprotonated, are responsible for the negative surface charge of the silica material.[1] This above dependency is well reflected in the drug entrapment efficiency of the spherical CS, the anisotropic and amphiphilic DCS1 as well as the anisotropic and nonamphiphilic DCS2 particles when treated with ethanolic solutions of equimolar amounts of both drugs Cur and QT (see Scheme 1S). As summarized in Table 2, the overall entrapment behavior of Cur plus QT is very high for all particles, but the relative amounts vary widely between Cur and QT among these three types of particles.

https://doi.org/10.1021/acs.langmuir.1c02210
Langmuir 2021, 37, 13460−13470

Table 2. Drug Entrapment Efficiency of CS, DCS1, and DCS2

	Cur entrapment efficiency [%]	QT entrapment efficiency [%]	total drug entrapment g [%]
CS	45 ± 5	43 ± 6	88 ± 11
DCS1	58 ± 6	40 ± 7	98 ± 13
DCS2	85 ± 6	10 ± 5	95 ± 11

While comparable entrapped contents were found for Cur (45 ± 5%) and QT (43 ± 6%) in mesoporous CS, the anisotropic and amphiphilic DCS1 entrapped more Cur (58 ± 6%) than QT (40 ± 7%) (Table 2). This difference was even more pronounced in the anisotropic and nonamphiphilic particle DCS2. For these particles, the entrapment efficiency for Cur was 85 ± 6% and only 10 ± 5% for QT. This difference is remarkable since CS and DCS2 provide comparable specific surface areas and total pore volumes (Table 1). Contrary to this finding and although the total pore volume of the dumbbell particle DCS1 was much less compared to that of the CS particle (Table 1), the overall entrapment efficiency of Cur plus QT in DCS1 was even higher than in CS (Table 2).

From a molecular point of view, these results can be explained in terms of the interaction of Cur and QT with the surface Si−OH and Si−F functions, respectively. Both polyphenols can interact with Si−OH groups on silica surfaces. The keto−enol tautomerism of Cur supports donating as well as accepting hydrogen bonds.[21,77] However, under the present reaction conditions, it is assumed that Cur interacts in its enolic form with the nucleophilic Si−OH groups on the silica surface of the particles.[78] Consequently, Cur prefers to accumulate in those areas of the particles with negative zeta potentials. In contrast, QT selects a more lipophilic environment when forming adducts with surface Si−OH groups.[79] Thus, QT is stored in areas with nonpolar Si−F functions. Because the spherical core−shell particles CS contain Si−OH and Si−F functions, which are equally distributed over the whole surface, both polyphenols are loaded in comparable amounts into the mesoporous shell (Table 2). In DSC2, only Si−OH groups are uniformly spread across the anisotropic particle, making it more attractive for Cur than for QT.

Most interestingly, the amphiphilic character of DSC1 allows QT to be loaded into the porous shell of the large lobe and most of Cur into the porous shell of the small hemisphere. Moreover, the hollow cavity of the small hemisphere in DCS1 serves as a compartment for Cur as well. This is deduced from the large amount of Cur loaded in DCS1 compared to the small shell of the small lobe (Tables 1 and 2). Thus, the mesoporous channels in the shell of the small lobe allow the diffusion of Cur into the cavity.[80] The permeability for small molecules of the shell covering the cavity has been demonstrated earlier.[64] This finding indicates that if both Cur and QT are loaded at the same time to DCS1 they encapsulate into different areas of the silica particle. This spatially different entrapment is supported by confocal Raman microscopy (Figure 5).

Figure 5a shows the Raman peak intensity distribution across a silica particle of DCS1 loaded with Cur and QT in the spectral range from 150 to 3500 cm^{-1}. The particle is clearly distinguishable from the background; it shows a medium intensity in the area that can be associated with the core particle and a much higher intensity in the region of its small hemisphere. A principal component analysis (PCA) of all Raman spectra yielded three principal components explaining 93% of the total data. Based on this number of responsible components, the data were further analyzed (see the Methods section). For better visualization, the components were assigned to different colors (blue, red, and green). The result of the deconvolution is shown in Figure 5b. The blue component can be associated with the substrate (sapphire), the red with the core particle, and the green with the lobe of the small hemisphere. The shell of the large lobe is yellow, indicating a coexistence of the two components (green and red). The corresponding spectra are shown in Figure 5c.

The spectrum of the blue component is dominated by the signals from sapphire with prominent peaks at 412, 645, and 312 cm^{-1}; the increasing background starting at 2500 cm^{-1} is also typical for sapphire.[81]

The spectrum of the red component shows a number of peaks. Besides the prominent peaks of sapphire, typical signals from silica and residual template molecules are also present at 969, 1073, 1305, and 1444 cm^{-1} as well as a broad peak at 2893 cm^{-1}. This peak can be assigned to residual template molecules in the pores of DCS1 since a spectrum was measured with and without entrapped drugs (Figure 3S). The remaining peaks at 1550 and 1616 cm^{-1} can be assigned to the entrapped polyphenols. The assignment was not straightforward due to the strong signal overlap in this region. The peaks at 1616 and 1550 cm^{-1} are close to the C═O stretch and O−H bend of QT, respectively.[82] Nevertheless, certain peaks of Cur also appear in the same range, for example, the C═O stretch at 1626 cm^{-1} and the C═C aromatic stretch at 1601 cm^{-1}.[83−86] However, Cur should show a luminescence which was not observed in this contribution. Also, its prominent peak at 1626 cm^{-1} is missing. The green component is dominated by luminescence without additional

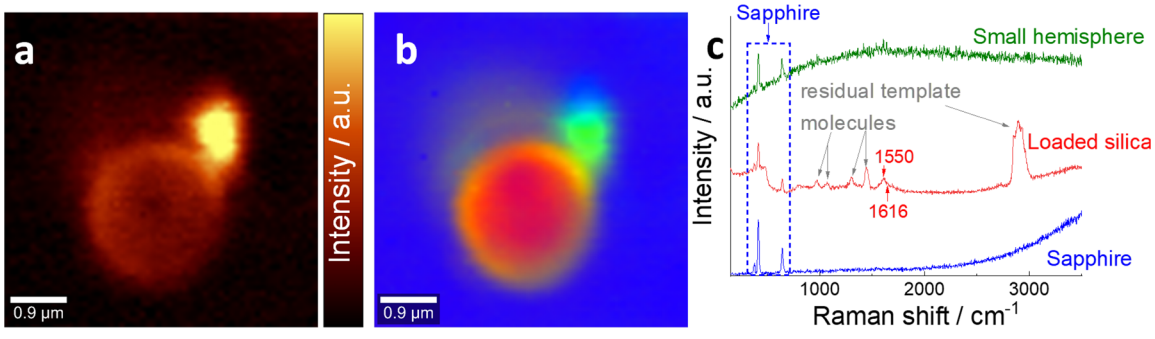

Figure 5. (a) Raman intensity distribution image of Cur-QT-DCS1 in the spectral range 150−3500 cm^{-1}. (b) Intensity distribution of the Cur-QT-DCS1 of three components based on a principal component analysis (PCA). Colors correspond to (c) the corresponding spectra for each component (see also Figure 3S).

https://doi.org/10.1021/acs.langmuir.1c02210
Langmuir 2021, 37, 13460−13470

Raman peaks. This luminescence peak can be attributed to Cur since the fitting results showed a maximum at ~1500 cm^{-1} which corresponds to 578 nm. This wavelength is close to the fluorescence emission of Cur.[87,88] In conclusion, QT prefers to load into the shell of the large lobe while Cur was in the shell and in the cavity of the small hemisphere. Note that accumulation of minor amounts of Cur on the large lobe cannot be excluded.

3.3. *In Vitro* Drug Release Study. The release behavior for Cur and QT loaded CS, DCS1, and DCS2 particles was evaluated at pH 5.5 and 7.4 (Figure 6). As the entrapped Cur content was higher than that of QT in DCS1 and DCS2, the absolute amounts of drug release were also higher, but relative amounts were similar. Also, all particles released all content, overall quicker at acidic pH.[89] Interestingly, in the acidic environment, both drugs were released faster from the dumbbell particles DCS1 (6 h) and DCS2 (7 h) compared to the spherical CS (9 h) mesoporous particles. Generally, Cur was released somewhat faster than QT from all particles except for DCS2 at physiological pH (Figure 6).

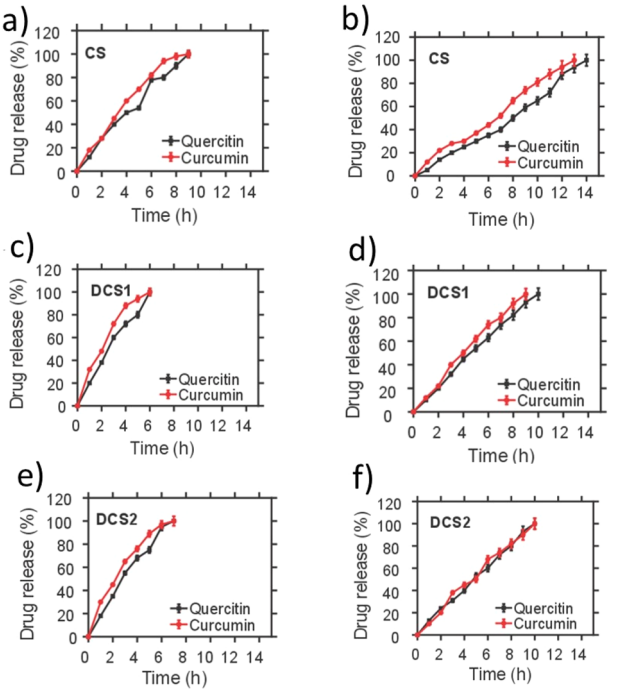

Figure 6. Cumulative percentage of Cur and QT released from CS (a, b), DCS1 (c, d), and DCS2 (e, f) at pH 5.5 (left column) and pH 7.4 (right column). Note that some error bars are smaller than the data symbols.

A crucial requirement for pharmaceutical formulation of poorly water-soluble drugs is the enhancement of their bioavailability via increasing the local concentration of the active ingredient in the vicinity of the target cell. This requires a controlled drug release from microcarrier particles. In good agreement with this precondition, upon formulating the drug as a molecular dispersion adsorbed into the different compartments of our silica microparticles, a rapid release from the DCS1 and DCS2 particles was observed. There are reports that it took 30 h to complete the release of the drug catophril and that it took 19 h for the complete release of 5-fluorouracil from mesoporous silica particles.[90] Even though there are drug release studies on mesoporous silica particles, the time taken for releasing the loaded drug is typically much longer than the time for 100% drug release observed in this study.

3.4. Cell Viability Assay. Typical for cancer cells is the uncontrolled proliferation of the cells. Thus, an ideal treatment results in cell death specific to cancer cells. The nontoxicity of quercetin, curcumin, and mesoporous silica particles on normal cells was reported elsewhere.[48,91,92] The cytotoxicity of Cur and QT loaded on CS, DCS1, and DCS2 individually as well as in combination was examined by performing the 3-(4,5-dimethylthiazol-2-yl)-2,5-diphenyltetrazolium bromide (MTT) assay against human bone osteosarcoma epithelial cell lines (U2OS).[70] The results indicate that Cur and QT loaded particles had significant toxicity toward the U2OS cancer cells. Moreover, the activity strongly depended on the amounts of drugs entrapped and the shape and the amphiphilic character of the silica particles (Figure 7 and Table 2).

The cell viability of QT-CS, Cur-CS, and Cur-QT-CS particles was 97%, 95%, and 92%, respectively, when incubated with 25 nM of drug after 24 h (Figure 7a). The corresponding epifluorescence and phase contrast images (Figure 8) for the QT-CS, Cur-CS, and Cur-QT-CS particles also show that cells did not undergo any morphological changes or cell death after 24 h.

For the QT-DCS2, Cur-DCS2, and Cur-QT-DCS2 particles cell viability was about 97%, 50%, and 30%, respectively (Figure 7c). The higher cell toxicity of Cur-DCS2 compared to Cur-CS is attributed to the higher concentration of Cur delivered by DCS2 (Table 2).

Under the same conditions for QT-DCS1, Cur-DCS1, and Cur-QT-DCS1, the mean cell viability was 85%, 79%, and 4%, respectively (Figure 7b). Note that the drugs Cur and QT have a cell cytotoxicity effect at micromolar concentrations.[93,94] Surprisingly, the DCS1 particles loaded with Cur and QT

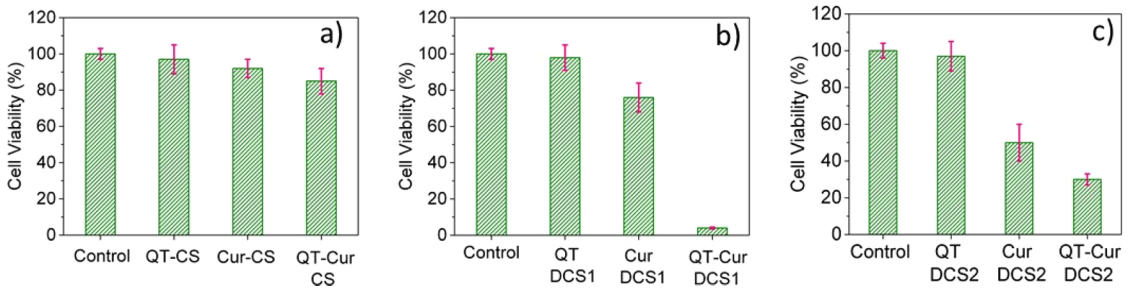

Figure 7. Cell viability assays after 24 h incubation of U2OS cancer cells with (a) CS, (b) DCS1, and (c) DCS2. Control experiments were performed with CS particles without drugs. Each particle is incubated at 25 nM alone, loaded with CS, Cur, or both drugs, and 1 mg/mL of the respective particles was applied. The data represent the average of at least three independent measurements.

https://doi.org/10.1021/acs.langmuir.1c02210
Langmuir 2021, 37, 13460−13470

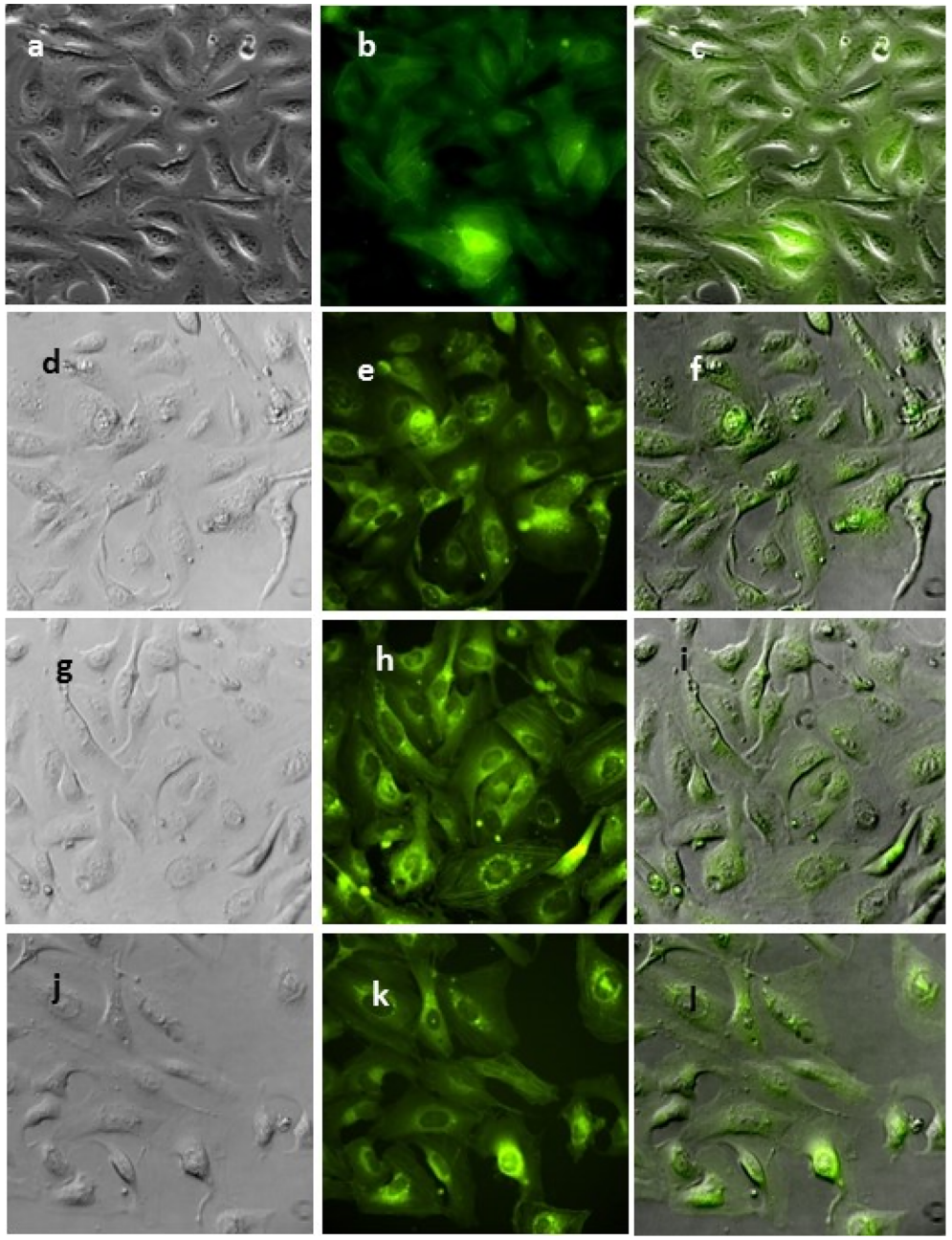

Figure 8. Phase contrast (first column), epifluorescence (second column), and overlaid (third column) images of U2OS cell lines. U2OS cells treated with the following particles for 24 h: (a–c) CS alone, (d–f) Cur-QT-CS, (g–i) Cur-CS, and (j–l) QT-CS.

showed an enhanced effect already at nanomolar concentrations when compared to drug loaded CS and drugs alone.

The corresponding cell images of DCS1 after 24 h are shown in Figure 9. Figures 9a–c show the phase contrast, epifluorescence, and overlay images of the cells, respectively, when treated with DCS1 without drugs. All cells were viable, and no cytotoxicity was observed from DCS1, which agrees with reports that silica particles are nontoxic to cells.[15] When cells were treated with 25 nM of drug loaded Cur-QT-DCS1 particles, changes in the cell morphology were observed. The cells died because of either necrosis or apoptosis as shown in the Figures 9d–f. Figures 9g–i and 9j–l correspond to cells treated with 25 nM of single-drug-loaded Cur-DCS1 and QT-DCS1 particles, respectively. Also in this case, changes in the morphological structure of the cells were observed. In conclusion, the Cur-QT-DCS1 particles had a much larger cytotoxicity than the Cur-QT-CS and Cur-QT-DCS2 particles.

4. CONCLUSION

Varying the stirring speed and the added salts in a simple etching process of micrometer sized silica particles allowed the syntheses of spherical core–shell CS, anisotropic core–shell DCS2 and anisotropic and amphiphilic core–shell DCS1 silica particles. The three types of particles show diverse architectures that provide mesoporous channels, hollow cavities, and anisotropic surface charge distributions. Moreover, the amphiphilic mesoporous core–shell dumbbell particles offer chemically selective environments which show different interactions with complex molecules like dyes and polyphenols. The differential distribution was demonstrated by loading the polyphenols QT

https://doi.org/10.1021/acs.langmuir.1c02210
Langmuir 2021, 37, 13460–13470

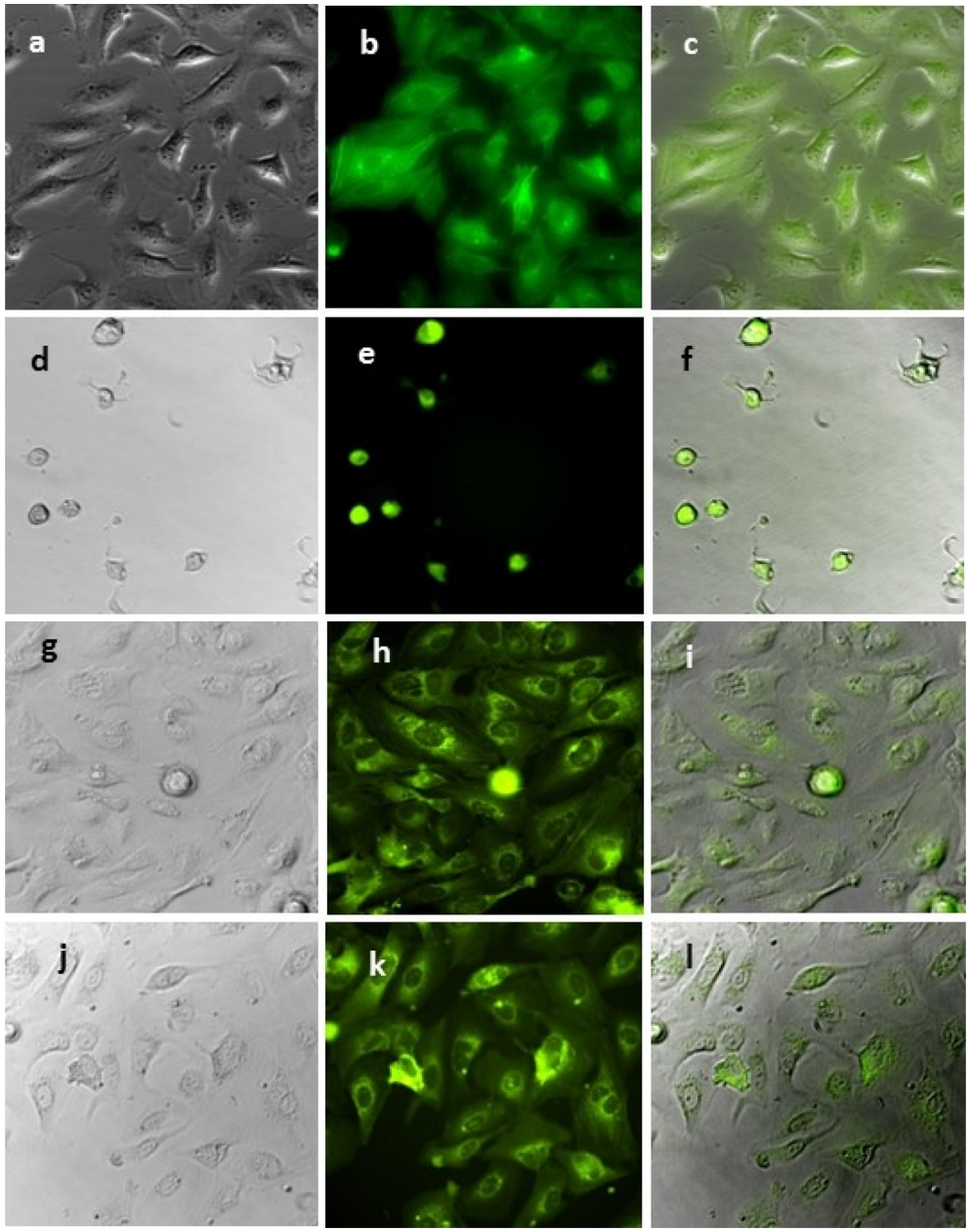

Figure 9. Phase contrast (first column), epifluorescence (second column), and overlaid (third column) images of the U2OS cell lines. U2OS cells treated with 25 nM of the following particles for 24 h: (a–c) DCS1 alone, (d–f) Cur-QT-DCS1, (g–i) Cur-DCS1, and (j–l) QT-DCS1.

and Cur into the mesopores and cavities of the particles. The entrapment of these two drugs varied significantly between the three particles. Moreover, the anisotropic and amphiphilic core–shell DCS1 particle was able to discriminate between Cur and QT by accumulating them in different regions of the particle.

Cell viability studies also showed major differences between the three drug-loaded particles. While the effect of drug loaded CS on cells was moderate, the cell toxicity increased from drug loaded DCS2 to drug loaded DCS1. Intriguingly, although CS and DCS1 delivered comparable amounts of both drugs, the cell toxicity of Cur-QT-DCS1 was dramatically higher compared to Cur-QT-CS. Apparently, the anisotropic character in shape and surface charge of DCS1 allowed for a much better interaction of the drug loaded particle with the cells.[62] In the future, different pairs of drugs can be tested for other treatments.

■ ASSOCIATED CONTENT

Supporting Information

The Supporting Information is available free of charge at https://pubs.acs.org/doi/10.1021/acs.langmuir.1c02210.

SEM (a, b) and STEM (c, d) micrographs of DCS1 particles, nitrogen adsorption and desorption isotherms, comparison between Raman spectra of the DCS1 particles with drugs loaded and without drugs loaded (PDF)

■ AUTHOR INFORMATION

Corresponding Author

Hermann A. Mayer – *Institute of Inorganic Chemistry, University of Tübingen, 72076 Tübingen, Germany;* orcid.org/0000-0002-8263-4255; Email: hermann.mayer@uni-tuebingen.de

https://doi.org/10.1021/acs.langmuir.1c02210
Langmuir 2021, 37, 13460–13470

Authors

Akanksha Dohare − *Institute of Inorganic Chemistry, University of Tübingen, 72076 Tübingen, Germany*

Swathi Sudhakar − *ZMBP, Cellular Nanoscience, University of Tübingen, 72076 Tübingen, Germany*

Björn Brodbeck − *Institute of Inorganic Chemistry, University of Tübingen, 72076 Tübingen, Germany; Process Analysis and Technology (PA&T), Reutlingen Research Institute, Reutlingen University, 72762 Reutlingen, Germany*

Ashutosh Mukherjee − *Process Analysis and Technology (PA&T), Reutlingen Research Institute, Reutlingen University, 72762 Reutlingen, Germany; IPTC and LISA+ Center, University of Tübingen, 72076 Tübingen, Germany*

Marc Brecht − *Process Analysis and Technology (PA&T), Reutlingen Research Institute, Reutlingen University, 72762 Reutlingen, Germany; IPTC and LISA+ Center, University of Tübingen, 72076 Tübingen, Germany*

Andreas Kandelbauer − *Process Analysis and Technology (PA&T), Reutlingen Research Institute, Reutlingen University, 72762 Reutlingen, Germany*

Erik Schäffer − *ZMBP, Cellular Nanoscience, University of Tübingen, 72076 Tübingen, Germany;* orcid.org/0000-0001-7876-085X

Complete contact information is available at: https://pubs.acs.org/10.1021/acs.langmuir.1c02210

Author Contributions

A.D. and S.S. contributed equally to this work.

Notes

The authors declare no competing financial interest.

■ ACKNOWLEDGMENTS

We thank Dr. Johannes Rheinländer and Prof. Dr. Tilman E. Schäffer for providing the U2OS cells. We are grateful to Elke Nadler (University of Tübingen) for SEM and STEM measurements. Lorenz Bock is acknowledged for measuring N_2 adsorption and desorption isotherms. A.D. was supported by a National Overseas Scholarship and is thankful to the Government of India for financial support. B.B. was financially supported by a HAW Prom grant within the "Programm zur Stärkung der Hochschulen für Angewandte Wissenschaften in Promotionsverfahren durch Förderung kooperativer (Einzel-) Promotionen)". We thank the Ministerium für Wissenschaft, Forschung und Kunst Baden-Württemberg for financial support. A.M. acknowledges the financial support within the framework "IngenieurNachwuchs 2016" (project: CompeTERS) by the German Federal Ministry of Education and Research (BMBF). S.S. thanks the PhD Network "Novel Nanoparticles" of the Universität Tübingen for financial support.

■ REFERENCES

(1) Ditzinger, F.; Price, D. J.; Ilie, A.-R.; Köhl, N. J.; Jankovic, S.; Tsakiridou, G.; Aleandri, S.; Kalantzi, L.; Holm, R.; Nair, A.; Saal, C.; Griffin, B.; Kuentz, M. Lipophilicity and Hydrophobicity Considerations in Bio-Enabling Oral Formulations Approaches − a PEARRL Review. *J. Pharm. Pharmacol.* **2019**, *71* (4), 464−482.

(2) Barbé, C.; Bartlett, J.; Kong, L.; Finnie, K.; Lin, H. Q.; Larkin, M.; Calleja, S.; Bush, A.; Calleja, G. Silica Particles: A Novel Drug-Delivery System. *Adv. Mater.* **2004**, *16* (21), 1959−1966.

(3) Biswas, A.; Shukla, A.; Maiti, P. Biomaterials for Interfacing Cell Imaging and Drug Delivery: An Overview. *Langmuir* **2019**, *35* (38), 12285−12305.

(4) Hoffman, A. S. The Origins and Evolution of "Controlled" Drug Delivery Systems. *J. Controlled Release* **2008**, *132* (3), 153−163.

(5) Folkman, J. How the Field of Controlled-Release Technology Began, and Its Central Role in the Development of Angiogenesis Research. *Biomaterials* **1990**, *11* (9), 615−618.

(6) Park, K. Controlled Drug Delivery Systems: Past Forward and Future Back. *J. Controlled Release* **2014**, *190*, 3−8.

(7) Allen, T. M.; Cullis, P. R. Liposomal Drug Delivery Systems: From Concept to Clinical Applications. *Adv. Drug Delivery Rev.* **2013**, *65* (1), 36−48.

(8) Böhme, D.; Beck-Sickinger, A. G. Drug Delivery and Release Systems for Targeted Tumor Therapy. *J. Pept. Sci.* **2015**, *21* (3), 186−200.

(9) Logie, J.; Owen, S. C.; McLaughlin, C. K.; Shoichet, M. S. PEG-Graft Density Controls Polymeric Nanoparticle Micelle Stability. *Chem. Mater.* **2014**, *26* (9), 2847−2855.

(10) Skorb, E. V.; Möhwald, H. "Smart" Surface Capsules for Delivery Devices. *Adv. Mater. Interfaces* **2014**, *1* (6), 1400237.

(11) Gong, M.-Q.; Wu, J.-L.; Chen, B.; Zhuo, R.-X.; Cheng, S.-X. Self-Assembled Polymer/Inorganic Hybrid Nanovesicles for Multiple Drug Delivery To Overcome Drug Resistance in Cancer Chemotherapy. *Langmuir* **2015**, *31* (18), 5115−5122.

(12) Morales, V.; Idso, M. N.; Balabasquer, M.; Chmelka, B.; García-Muñoz, R. A. Correlating Surface-Functionalization of Mesoporous Silica with Adsorption and Release of Pharmaceutical Guest Species. *J. Phys. Chem. C* **2016**, *120* (30), 16887−16898.

(13) Geng, H.; Zhao, Y.; Liu, J.; Cui, Y.; Wang, Y.; Zhao, Q.; Wang, S. Hollow Mesoporous Silica as a High Drug Loading Carrier for Regulation Insoluble Drug Release. *Int. J. Pharm.* **2016**, *510* (1), 184−194.

(14) Lainé, A.-L.; Price, D.; Davis, J.; Roberts, D.; Hudson, R.; Back, K.; Bungay, P.; Flanagan, N. Enhanced Oral Delivery of Celecoxib via the Development of a Supersaturable Amorphous Formulation Utilising Mesoporous Silica and Co-Loaded HPMCAS. *Int. J. Pharm.* **2016**, *512* (1), 118−125.

(15) Tarn, D.; Ashley, C. E.; Xue, M.; Carnes, E. C.; Zink, J. I.; Brinker, C. J. Mesoporous Silica Nanoparticle Nanocarriers: Biofunctionality and Biocompatibility. *Acc. Chem. Res.* **2013**, *46* (3), 792−801.

(16) Joshi, R.; Feldmann, V.; Koestner, W.; Detje, C.; Gottschalk, S.; Mayer, H. A.; Sauer, M. G.; Engelmann, J. Multifunctional Silica Nanoparticles for Optical and Magnetic Resonance Imaging. *Biol. Chem.* **2013**, *394* (1), 125−135.

(17) Heikkilä, T.; Salonen, J.; Tuura, J.; Kumar, N.; Salmi, T.; Murzin, D. Y.; Hamdy, M. S.; Mul, G.; Laitinen, L.; Kaukonen, A. M.; Hirvonen, J.; Lehto, V.-P. Evaluation of Mesoporous TCPSi, MCM-41, SBA-15, and TUD-1 Materials as API Carriers for Oral Drug Delivery. *Drug Delivery* **2007**, *14* (6), 337−347.

(18) Yang, Y.-Y.; Wang, X.; Hu, Y.; Hu, H.; Wu, D.-C.; Xu, F.-J. Bioreducible POSS-Cored Star-Shaped Polycation for Efficient Gene Delivery. *ACS Appl. Mater. Interfaces* **2014**, *6* (2), 1044−1052.

(19) Yang, Y.; Achazi, K.; Jia, Y.; Wei, Q.; Haag, R.; Li, J. Complex Assembly of Polymer Conjugated Mesoporous Silica Nanoparticles for Intracellular PH-Responsive Drug Delivery. *Langmuir* **2016**, *32* (47), 12453−12460.

(20) Hewlings, S. J.; Kalman, D. S. Curcumin: A Review of Its Effects on Human Health. *Foods* **2017**, *6* (10), 92.

(21) Nelson, K. M.; Dahlin, J. L.; Bisson, J.; Graham, J.; Pauli, G. F.; Walters, M. A. The Essential Medicinal Chemistry of Curcumin. *J. Med. Chem.* **2017**, *60* (5), 1620−1637.

(22) Stanić, Z. Curcumin, a Compound from Natural Sources, a True Scientific Challenge − A Review. *Plant Foods Hum. Nutr.* **2017**, *72* (1), 1−12.

(23) Pallauf, K.; Rimbach, G. Autophagy, Polyphenols and Healthy Ageing. *Ageing Res. Rev.* **2013**, *12* (1), 237−252.

(24) Hasima, N.; Ozpolat, B. Regulation of Autophagy by Polyphenolic Compounds as a Potential Therapeutic Strategy for Cancer. *Cell Death Dis.* **2014**, *5* (11), e1509−e1509.

(25) Adiwidjaja, J.; McLachlan, A. J.; Boddy, A. V. Curcumin as a Clinically-Promising Anti-Cancer Agent: Pharmacokinetics and Drug Interactions. *Expert Opin. Drug Metab. Toxicol.* **2017**, *13* (9), 953−972.
(26) Zhao, G.; Dong, X.; Sun, Y. Self-Assembled Curcumin−Poly(Carboxybetaine Methacrylate) Conjugates: Potent Nano-Inhibitors against Amyloid β-Protein Fibrillogenesis and Cytotoxicity. *Langmuir* **2019**, *35* (5), 1846−1857.
(27) Li, Z.; Zhang, L.; Wei, X.; Liu, J.; Wang, Z. Temperature/PH-Responsive Hexagonal Liquid Crystal for Curcumin Release. *Langmuir* **2019**, *35* (2), 453−460.
(28) Nasab, N. A.; Kumleh, H. H.; Beygzadeh, M.; Teimourian, S.; Kazemzad, M. Delivery of Curcumin by a PH-Responsive Chitosan Mesoporous Silica Nanoparticles for Cancer Treatment. *Artif. Cells, Nanomed., Biotechnol.* **2018**, *46* (1), 75−81.
(29) Agrawal, M.; Saraf, S.; Saraf, S.; Antimisiaris, S. G.; Chougule, M. B.; Shoyele, S. A.; Alexander, A. Nose-to-Brain Drug Delivery: An Update on Clinical Challenges and Progress towards Approval of Anti-Alzheimer Drugs. *J. Controlled Release* **2018**, *281*, 139−177.
(30) Shahani, K.; Panyam, J. Highly Loaded, Sustained-Release Microparticles of Curcumin for Chemoprevention. *J. Pharm. Sci.* **2011**, *100* (7), 2599−2609.
(31) Radhakrishnan, K.; Tripathy, J.; Datey, A.; Chakravortty, D.; Raichur, A. M. Mesoporous Silica−Chondroitin Sulphate Hybrid Nanoparticles for Targeted and Bio-Responsive Drug Delivery. *New J. Chem.* **2015**, *39* (3), 1754−1760.
(32) Aras, A.; Khokhar, A. R.; Qureshi, M. Z.; Silva, M. F.; Sobczak-Kupiec, A.; Pineda, E. A. G.; Hechenleitner, A. A. W.; Farooqi, A. A. Targeting Cancer with Nano-Bullets: Curcumin, EGCG, Resveratrol and Quercetin on Flying Carpets. *Asian Pac. J. Cancer Prev.* **2014**, *15* (9), 3865−3871.
(33) Sunoqrot, S.; Al-Debsi, T.; Al-Shalabi, E.; Hasan Ibrahim, L.; Faruqu, F. N.; Walters, A.; Palgrave, R.; Al-Jamal, K. T. Bioinspired Polymerization of Quercetin to Produce a Curcumin-Loaded Nanomedicine with Potent Cytotoxicity and Cancer-Targeting Potential in Vivo. *ACS Biomater. Sci. Eng.* **2019**, *5* (11), 6036−6045.
(34) Sun, X.; Yu, D.; Ying, Z.; Pan, C.; Wang, N.; Huang, F.; Ling, J.; Ouyang, X. Fabrication of Ion-Crosslinking Aminochitosan Nanoparticles for Encapsulation and Slow Release of Curcumin. *Pharmaceutics* **2019**, *11* (11), 584.
(35) Zhang, H.; Jiang, L.; Tong, M.; Lu, Y.; Ouyang, X.-K.; Ling, J. Encapsulation of Curcumin Using Fucoidan Stabilized Zein Nanoparticles: Preparation, Characterization, and in Vitro Release Performance. *J. Mol. Liq.* **2021**, *329*, 115586.
(36) Zhang, D.; Jiang, F.; Ling, J.; Ouyang, X.; Wang, Y.-G. Delivery of Curcumin Using a Zein-Xanthan Gum Nanocomplex: Fabrication, Characterization, and in Vitro Release Properties. *Colloids Surf., B* **2021**, *204*, 111827.
(37) Sun, X.; Pan, C.; Ying, Z.; Yu, D.; Duan, X.; Huang, F.; Ling, J.; Ouyang, X. Stabilization of Zein Nanoparticles with K-Carrageenan and Tween 80 for Encapsulation of Curcumin. *Int. J. Biol. Macromol.* **2020**, *146*, 549−559.
(38) Xue, J.; Li, Z.; Duan, H.; He, J.; Luo, Y. Chemically Modified Phytoglycogen: Physicochemical Characterizations and Applications to Encapsulate Curcumin. *Colloids Surf., B* **2021**, *205*, 111829.
(39) Kresge, C. T.; Leonowicz, M. E.; Roth, W. J.; Vartuli, J. C.; Beck, J. S. Ordered Mesoporous Molecular Sieves Synthesized by a Liquid-Crystal Template Mechanism. *Nature* **1992**, *359* (6397), 710−712.
(40) Brinker, C. J.; Lu, Y.; Sellinger, A.; Fan, H. Evaporation-Induced Self-Assembly: Nanostructures Made Easy. *Adv. Mater.* **1999**, *11* (7), 579−585.
(41) Zhao, D.; Feng, J.; Huo, Q.; Melosh, N.; Fredrickson, G. H.; Chmelka, B. F.; Stucky, G. D. Triblock Copolymer Syntheses of Mesoporous Silica with Periodic 50 to 300 Angstrom Pores. *Science* **1998**, *279* (5350), 548−552.
(42) Wan, Y.; Zhao. On the Controllable Soft-Templating Approach to Mesoporous Silicates. *Chem. Rev.* **2007**, *107* (7), 2821−2860.
(43) Galarneau, A.; Iapichella, J.; Bonhomme, K.; Di Renzo, F.; Kooyman, P.; Terasaki, O.; Fajula, F. Controlling the Morphology of Mesostructured Silicas by Pseudomorphic Transformation: A Route Towards Applications. *Adv. Funct. Mater.* **2006**, *16* (13), 1657−1667.
(44) Huh, S.; Wiench, J. W.; Trewyn, B. G.; Song, S.; Pruski, M.; Lin, V. S.-Y. Tuning of Particle Morphology and Pore Properties in Mesoporous Silicas with Multiple Organic Functional Groups. *Chem. Commun.* **2003**, *0* (18), 2364−2365.
(45) Travaglini, L.; De Cola, L. Morphology Control of Mesoporous Silica Particles Using Bile Acids as Cosurfactants. *Chem. Mater.* **2018**, *30* (12), 4168−4175.
(46) Luo, L.; Liang, Y.; Chassé, T.; Anwander, R. Ultrafast Myoglobin Adsorption into Double-Shelled Hollow Mesoporous Silica Nanospheres. *Part. Part. Sys. Char.* **2018**, *35* (12), 1800312.
(47) Torney, F.; Trewyn, B. G.; Lin, V. S.-Y.; Wang, K. Mesoporous Silica Nanoparticles Deliver DNA and Chemicals into Plants. *Nat. Nanotechnol.* **2007**, *2* (5), 295−300.
(48) Slowing, I. I.; Vivero-Escoto, J. L.; Wu, C.-W.; Lin, V. S.-Y. Mesoporous Silica Nanoparticles as Controlled Release Drug Delivery and Gene Transfection Carriers. *Adv. Drug Delivery Rev.* **2008**, *60* (11), 1278−1288.
(49) Deodhar, G. V.; Adams, M. L.; Trewyn, B. G. Controlled Release and Intracellular Protein Delivery from Mesoporous Silica Nanoparticles. *Biotechnol. J.* **2017**, *12* (1), 1600408.
(50) Yu, M.; Gu, Z.; Ottewell, T.; Yu, C. Silica-Based Nanoparticles for Therapeutic Protein Delivery. *J. Mater. Chem. B* **2017**, *5* (18), 3241−3252.
(51) Dai, L.; Li, J.; Zhang, B.; Liu, J.; Luo, Z.; Cai, K. Redox-Responsive Nanocarrier Based on Heparin End-Capped Mesoporous Silica Nanoparticles for Targeted Tumor Therapy in Vitro and in Vivo. *Langmuir* **2014**, *30* (26), 7867−7877.
(52) Li, R.; Xie, Y. Nanodrug Delivery Systems for Targeting the Endogenous Tumor Microenvironment and Simultaneously Overcoming Multidrug Resistance Properties. *J. Controlled Release* **2017**, *251*, 49−67.
(53) Zhao, Y.; Trewyn, B. G.; Slowing, I. I.; Lin, V. S.-Y. Mesoporous Silica Nanoparticle-Based Double Drug Delivery System for Glucose-Responsive Controlled Release of Insulin and Cyclic AMP. *J. Am. Chem. Soc.* **2009**, *131* (24), 8398−8400.
(54) Motahari, A.; Hu, N.; Vahid, A.; Omrani, A.; Rostami, A. A.; Schaefer, D. W. Multilevel Morphology of Complex Nanoporous Materials. *Langmuir* **2018**, *34* (23), 6719−6726.
(55) Du, J.; O'Reilly, R. K. Anisotropic Particles with Patchy, Multicompartment and Janus Architectures: Preparation and Application. *Chem. Soc. Rev.* **2011**, *40* (5), 2402−2416.
(56) Zhang, A.; Gu, L.; Hou, K.; Dai, C.; Song, C.; Guo, X. Mesostructure-Tunable and Size-Controllable Hierarchical Porous Silica Nanospheres Synthesized by Aldehyde-Modified Stöber Method. *RSC Adv.* **2015**, *5* (72), 58355−58362.
(57) Möller, K.; Bein, T. Talented Mesoporous Silica Nanoparticles. *Chem. Mater.* **2017**, *29* (1), 371−388.
(58) Cauda, V.; Schlossbauer, A.; Kecht, J.; Zürner, A.; Bein, T. Multiple Core−Shell Functionalized Colloidal Mesoporous Silica Nanoparticles. *J. Am. Chem. Soc.* **2009**, *131* (32), 11361−11370.
(59) Tran, L.-T.-C.; Lesieur, S.; Faivre, V. Janus Nanoparticles: Materials, Preparation and Recent Advances in Drug Delivery. *Expert Opin. Drug Delivery* **2014**, *11* (7), 1061−1074.
(60) Luo, L.; Liang, Y.; Erichsen, E. S.; Anwander, R. Hierarchical Mesoporous Organosilica−Silica Core−Shell Nanoparticles Capable of Controlled Fungicide Release. *Chem. - Eur. J.* **2018**, *24* (28), 7200−7209.
(61) Tuncelli, G.; Ay, A. N.; Zümreoglu-Karan, B. 5-Fluorouracil Intercalated Iron Oxide@layered Double Hydroxide Core-Shell Nanocomposites with Isotropic and Anisotropic Architectures for Shape-Selective Drug Delivery Applications. *Mater. Sci. Eng., C* **2015**, *55*, 562−568.
(62) Agrawal, G.; Agrawal, R. Janus Nanoparticles: Recent Advances in Their Interfacial and Biomedical Applications. *ACS Appl. Nano Mater.* **2019**, *2* (4), 1738−1757.

https://doi.org/10.1021/acs.langmuir.1c02210
Langmuir 2021, 37, 13460−13470

(63) Perro, A.; Reculusa, S.; Ravaine, S.; Bourgeat-Lami, E.; Duguet, E. Design and Synthesis of Janus Micro- and Nanoparticles. *J. Mater. Chem.* **2005**, *15* (35−36), 3745−3760.
(64) Maisch, J.; Jafarli, F.; Chassé, T.; Blendinger, F.; Konrad, A.; Metzger, M.; Meixner, A. J.; Brecht, M.; Dähne, L.; Mayer, H. A. One-Pot Synthesis of Micron Partly Hollow Anisotropic Dumbbell Shaped Silica Core−Shell Particles. *Chem. Commun.* **2016**, *52* (100), 14392−14395.
(65) Sudhakar, S. Germanium nanospheres as high precision optical tweezers probes. Doctoral dissertation, Eberhard Karls Universität Tübingen, Tübingen, 2021.
(66) Elbialy, N. S.; Aboushoushah, S. F.; Sofi, B. F.; Noorwali, A. Multifunctional Curcumin-Loaded Mesoporous Silica Nanoparticles for Cancer Chemoprevention and Therapy. *Microporous Mesoporous Mater.* **2020**, *291*, 109540.
(67) Yang, P.; Gai, S.; Lin, J. Functionalized Mesoporous Silica Materials for Controlled Drug Delivery. *Chem. Soc. Rev.* **2012**, *41* (9), 3679−3698.
(68) Islami, F.; Sauer, A. G.; Miller, K. D.; Siegel, R. L.; Fedewa, S. A.; Jacobs, E. J.; McCullough, M. L.; Patel, A. V.; Ma, J.; Soerjomataram, I.; Flanders, W. D.; Brawley, O. W.; Gapstur, S. M.; Jemal, A. Proportion and Number of Cancer Cases and Deaths Attributable to Potentially Modifiable Risk Factors in the United States. *Ca-Cancer J. Clin.* **2018**, *68* (1), 31−54.
(69) Gao, Y.; Ding, S.; Huang, X.; Fan, Z.; Sun, J.; Hai, Y.; Li, K. Development and Evaluation of Hollow Mesoporous Silica Microspheres Bearing on Enhanced Oral Delivery of Curcumin. *Drug Dev. Ind. Pharm.* **2019**, *45* (2), 273−281.
(70) Santhosh, P. B.; Thomas, N.; Sudhakar, S.; Chadha, A.; Mani, E. Phospholipid Stabilized Gold Nanorods: Towards Improved Colloidal Stability and Biocompatibility. *Phys. Chem. Chem. Phys.* **2017**, *19* (28), 18494−18504.
(71) Dong, H.; Brennan, J. D. One-Pot Synthesis of Silica Core−Shell Particles with Double Shells and Different Pore Orientations from Their Nonporous Counterparts. *J. Mater. Chem.* **2012**, *22* (26), 13197−13203.
(72) Thommes, M.; Kaneko, K.; Neimark, A. V.; Olivier, J. P.; Rodriguez-Reinoso, F.; Rouquerol, J.; Sing, K. S. W. Physisorption of Gases, with Special Reference to the Evaluation of Surface Area and Pore Size Distribution (IUPAC Technical Report). *Pure Appl. Chem.* **2015**, *87* (9−10), 1051−1069.
(73) Fang, X.; Chen, C.; Liu, Z.; Liu, P.; Zheng, N. A Cationic Surfactant Assisted Selective Etching Strategy to Hollow Mesoporous Silica Spheres. *Nanoscale* **2011**, *3* (4), 1632−1639.
(74) Zhang, T.; Ge, J.; Hu, Y.; Zhang, Q.; Aloni, S.; Yin, Y. Formation of Hollow Silica Colloids through a Spontaneous Dissolution−Regrowth Process. *Angew. Chem., Int. Ed.* **2008**, *47* (31), 5806−5811.
(75) Chen, Y.; Chen, H.; Guo, L.; He, Q.; Chen, F.; Zhou, J.; Feng, J.; Shi, J. Hollow/Rattle-Type Mesoporous Nanostructures by a Structural Difference-Based Selective Etching Strategy. *ACS Nano* **2010**, *4* (1), 529−539.
(76) Monnier, A.; Schüth, F.; Huo, Q.; Kumar, D.; Margolese, D.; Maxwell, R. S.; Stucky, G. D.; Krishnamurty, M.; Petroff, P.; Firouzi, A.; Janicke, M.; Chmelka, B. F. Cooperative Formation of Inorganic-Organic Interfaces in the Synthesis of Silicate Mesostructures. *Science* **1993**, *261* (5126), 1299−1303.
(77) Jain, B. A Spectroscopic Study on Stability of Curcumin as a Function of PH in Silica Nanoformulations, Liposome and Serum Protein. *J. Mol. Struct.* **2017**, *1130*, 194−198.
(78) Gangwar, R. K.; Tomar, G. B.; Dhumale, V. A.; Zinjarde, S.; Sharma, R. B.; Datar, S. Curcumin Conjugated Silica Nanoparticles for Improving Bioavailability and Its Anticancer Applications. *J. Agric. Food Chem.* **2013**, *61* (40), 9632−9637.
(79) Berlier, G.; Gastaldi, L.; Ugazio, E.; Miletto, I.; Iliade, P.; Sapino, S. Stabilization of Quercetin Flavonoid in MCM-41 Mesoporous Silica: Positive Effect of Surface Functionalization. *J. Colloid Interface Sci.* **2013**, *393*, 109−118.
(80) Jin, D.; Park, K.-W.; Lee, J. H.; Song, K.; Kim, J.-G.; Seo, M. L.; Jung, J. H. The Selective Immobilization of Curcumin onto the Internal Surface of Mesoporous Hollow Silica Particles by Covalent Bonding and Its Controlled Release. *J. Mater. Chem.* **2011**, *21* (11), 3641−3645.
(81) Du, X.; Zhang, M.; Meng, Q.; Song, Y.; He, X.; Yang, Y.; Han, J. Phonon Dynamics in γ-Ray Irradiated Sapphire Crystals Studied by Fs-CARS Technique. *Opt. Express* **2010**, *18* (22), 22937−22943.
(82) Numata, Y.; Tanaka, H. Quantitative Analysis of Quercetin Using Raman Spectroscopy. *Food Chem.* **2011**, *126* (2), 751−755.
(83) Kolev, T. M.; Velcheva, E. A.; Stamboliyska, B. A.; Spiteller, M. DFT and Experimental Studies of the Structure and Vibrational Spectra of Curcumin. *Int. J. Quantum Chem.* **2005**, *102* (6), 1069−1079.
(84) Mohan, P. R. K.; Sreelakshmi, G.; Muraleedharan, C. V.; Joseph, R. Water Soluble Complexes of Curcumin with Cyclodextrins: Characterization by FT-Raman Spectroscopy. *Vib. Spectrosc.* **2012**, *62*, 77−84.
(85) Sanphui, P.; Goud, N. R.; Khandavilli, U. B. R.; Bhanoth, S.; Nangia, A. New Polymorphs of Curcumin. *Chem. Commun.* **2011**, *47* (17), 5013.
(86) Van Nong, H.; Hung, L. X.; Thang, P. N.; Chinh, V. D.; Vu, L. V.; Dung, P. T.; Van Trung, T.; Nga, P. T. Fabrication and Vibration Characterization of Curcumin Extracted from Turmeric (Curcuma Longa) Rhizomes of the Northern Vietnam. *SpringerPlus* **2016**, *5* (1), 1147.
(87) Leung, M. H. M.; Pham, D.-T.; Lincoln, S. F.; Kee, T. W. Femtosecond Transient Absorption Spectroscopy of Copper(II)−Curcumin Complexes. *Phys. Chem. Chem. Phys.* **2012**, *14* (39), 13580−13587.
(88) Singh, P. K.; Wani, K.; Kaul-Ghanekar, R.; Prabhune, A.; Ogale, S. From Micron to Nano-Curcumin by Sophorolipid Co-Processing: Highly Enhanced Bioavailability, Fluorescence, and Anti-Cancer Efficacy. *RSC Adv.* **2014**, *4* (104), 60334−60341.
(89) Sun, X.; Wang, N.; Yang, L. Y.; Ouyang, X. K.; Huang, F. Folic Acid and Pei Modified Mesoporous Silica for Targeted Delivery of Curcumin. *Pharmaceutics* **2019**, *11* (9), 430.
(90) She, X.; Chen, L.; Yi, Z.; Li, C.; He, C.; Feng, C.; Wang, T.; Shigdar, S.; Kong, W. D.; Tailored, L. Mesoporous Silica Nanoparticles for Controlled Drug Delivery: Platform Fabrication, Targeted Delivery, and Computational Design and Analysis http://www.eurekaselect.com/141796/article (accessed 2020-05-15).
(91) Ebrahimifar, M.; Roudsari, M. H.; Kazemi, S. M.; Shahmabadi, H. E.; Kanaani, L.; Alavi, S.; Vasfi, M. I. Enhancing Effects of Curcumin on Cytotoxicity of Paclitaxel, Methotrexate and Vincristine in Gastric Cancer Cells. *Asian Pac. J. Cancer Prev.* **2017**, *18* (1), 65−68.
(92) Hashemzaei, M.; Delarami Far, A.; Yari, A.; Heravi, R. E.; Tabrizian, K.; Taghdisi, S. M.; Sadegh, S. E.; Tsarouhas, K.; Kouretas, D.; Tzanakakis, G.; Nikitovic, D.; Anisimov, N. Y.; Spandidos, D. A.; Tsatsakis, A. M.; Rezaee, R. Anticancer and Apoptosis-inducing Effects of Quercetin in Vitro and in Vivo. *Oncol. Rep.* **2017**, *38* (2), 819−828.
(93) Walters, D. K.; Muff, R.; Langsam, B.; Born, W.; Fuchs, B. Cytotoxic Effects of Curcumin on Osteosarcoma Cell Lines. *Invest. New Drugs* **2008**, *26* (4), 289.
(94) Catanzaro, D.; Ragazzi, E.; Vianello, C.; Caparrotta, L.; Montopoli, M. Effect of Quercetin on Cell Cycle and Cyclin Expression in Ovarian Carcinoma and Osteosarcoma Cell Lines. *Nat. Prod. Commun.* **2015**, *10* (8), 1365.

https://doi.org/10.1021/acs.langmuir.1c02210
Langmuir 2021, 37, 13460−13470

8. Chemical Imaging of Single Anisotropic Polystyrene/Poly (Methacrylate) Microspheres with Complex Hierarchical Architecture

Alexandra Wagner[1], Stefanie Wagner[2], Jan-Erik Bredfeldt[1], Julia C. Steinbach[1], Ashutosh Mukherjee[1,3], Sandra Kronenberger[2], Kai Braun[3], Andreas Kandelbauer[1], Hermann A. Mayer[2] and Marc Brecht[1,]*

[1]Process Analysis and Technology (PA&T), Reutlingen Research Institute, Reutlingen University, Alteburgstrasse 150, 72762 Reutlingen, Germany;

[2]Institute of Inorganic Chemistry, University of Tübingen, Auf der Morgenstelle 18, 72076 Tübingen, Germany;

[3]Institute of Physical Chemistry, University of Tübingen, Auf der Morgenstelle 18, 72076 Tübingen, Germany;

This chapter was originally published in MDPI-Polymers as

Wagner, A.; Wagner, S.; Bredfeldt, J.-E.; Steinbach, J.C.; Mukherjee, A.; Kronenberger, S.; Braun, K.; Kandelbauer, A.; Mayer, H.A.; Brecht, M. Chemical Imaging of Single Anisotropic Polystyrene/Poly (Methacrylate) Microspheres with Complex Hierarchical Architecture. Polymers 2021, 13, 9, 1438.

DOI: https://doi.org/10.3390/polym13091438

polymers

MDPI

Article

Chemical Imaging of Single Anisotropic Polystyrene/Poly (Methacrylate) Microspheres with Complex Hierarchical Architecture

Alexandra Wagner [1], Stefanie Wagner [2], Jan-Erik Bredfeldt [1], Julia C. Steinbach [1], Ashutosh Mukherjee [1,3], Sandra Kronenberger [2], Kai Braun [3], Andreas Kandelbauer [1], Hermann A. Mayer [2] and Marc Brecht [1,*]

[1] Process Analysis and Technology (PA&T), Reutlingen Research Institute, Reutlingen University, Alteburgstrasse 150, 72762 Reutlingen, Germany; Alexandra.Wagner@Reutlingen-University.de (A.W.); janerik.bredfeldt@googlemail.com (J.-E.B.); Julia.Steinbach@Reutlingen-University.de (J.C.S.); Ashutosh.Mukherjee@Reutlingen-University.de (A.M.); Andreas.Kandelbauer@Reutlingen-University.de (A.K.)

[2] Institute of Inorganic Chemistry, University of Tübingen, Auf der Morgenstelle 18, 72076 Tübingen, Germany; stefanie.wagner@uni-tuebingen.de (S.W.); km231@stud.uni-heidelberg.de (S.K.); hermann.mayer@uni-tuebingen.de (H.A.M.)

[3] Institute of Physical Chemistry, University of Tübingen, Auf der Morgenstelle 18, 72076 Tübingen, Germany; Braun.Kai@web.de

* Correspondence: marc.brecht@Reutlingen-University.de

Abstract: Monodisperse polystyrene spheres are functional materials with interesting properties, such as high cohesion strength, strong adsorptivity, and surface reactivity. They have shown a high application value in biomedicine, information engineering, chromatographic fillers, supercapacitor electrode materials, and other fields. To fully understand and tailor particle synthesis, the methods for characterization of their complex 3D morphological features need to be further explored. Here we present a chemical imaging study based on three-dimensional confocal Raman microscopy (3D-CRM), scanning electron microscopy (SEM), focused ion beam (FIB), diffuse reflectance infrared Fourier transform (DRIFT), and nuclear magnetic resonance (NMR) spectroscopy for individual porous swollen polystyrene/poly (glycidyl methacrylate-co-ethylene di-methacrylate) particles. Polystyrene particles were synthesized with different co-existing chemical entities, which could be identified and assigned to distinct regions of the same particle. The porosity was studied by a combination of SEM and FIB. Images of milled particles indicated a comparable porosity on the surface and in the bulk. The combination of standard analytical techniques such as DRIFT and NMR spectroscopies yielded new insights into the inner structure and chemical composition of these particles. This knowledge supports the further development of particle synthesis and the design of new strategies to prepare particles with complex hierarchical architectures.

Keywords: anisotropic polymer particles; hierarchical particles; chemical imaging; correlative microscopy; Raman microscopy

Citation: Wagner, A.; Wagner, S.; Bredfeldt, J.-E.; Steinbach, J.C.; Mukherjee, A.; Kronenberger, S.; Braun, K.; Kandelbauer, A.; Mayer, H.A.; Brecht, M. Chemical Imaging of Single Anisotropic Polystyrene/Poly (Methacrylate) Microspheres with Complex Hierarchical Architecture. *Polymers* **2021**, *13*, 1438. https://doi.org/10.3390/polym13091438

Academic Editor: Andrea Mele

Received: 25 March 2021
Accepted: 26 April 2021
Published: 29 April 2021

1. Introduction

Modified polystyrene particles are versatile and popular in many scientific fields, e.g., in material sciences, engineering, catalysis, nanomedicine, and biotechnology [1–4]. The tailored design of particles enables new approaches for imaging and drug delivery [5]. One of the most important approaches is the tuning of particle morphology and topology as well as their charge distribution [4]. The most prominent examples are Janus particles, which are special types of nanoparticles or microparticles whose surfaces have regions of two or more distinctly different physical properties. This unique surface of Janus particles allows different types of chemistry to co-exist on the same particle [6].

The availability of synthetic procedures leading to polystyrene spheres with narrow size distributions and their ability to swell in different media make them ideal templates for

the generation of more complex isotropic and anisotropic materials [6–15]. For this purpose, it is important to control specific particle properties, such as size and size distribution, shape, surface porosity, and chemical composition during synthesis [11].

SEM and bulk-IR as well as solid-state NMR spectroscopy have proven to be the most efficient characterization methods for these particles [16–25]. The high magnification of SEM images enables precise characterization of their size, shape, and surface properties. Additionally, the combination of SEM and milling with a focused ion beam (FIB) allows insight into their internal structure. However, with these techniques, it is not possible to obtain information about the distribution of chemical components and functionalities across these particles.

The high-resolution imaging technique, 3D confocal Raman microscopy (3D-CRM), is often used in combination with other analytical methods to characterize the chemical and molecular compositions of materials. The correlation of Raman imaging and SEM (RISE), especially, provides information on physical surface properties in combination with molecular compound information of a sample [26,27]. Depth profiles and 3D images can be created with exceptionally good spectral and spatial resolution [28], and the chemical properties can be analyzed with high spatial resolution close to the diffraction limit of light. The 3D-CRM technique is non-invasive, non-destructive, and does not require any complex sample preparation such as staining or labeling [29–34]. Since no interference with vibrational bands from water is observed, the particles can be examined directly from aqueous solution.

Here, we present a micro-spectroscopic analysis for the characterization of anisotropic single polystyrene/poly (glycidyl methacrylate-co-ethylene di-methacrylate) particles. The correlation of the results from DRIFT, NMR, SEM, and 3D-CRM enables us to show that particles with Janus-like properties are formed. Using this combination of methods allowed us to observe changes in the particle properties in response to variations in reaction conditions applied during synthesis.

2. Materials and Methods

2.1. Particle Synthesis

Glycidyl methacrylate (GMA), benzoyl peroxide (BPO), and sodium dodecyl sulfate (SDS) were purchased from abcr GmbH, Karlsruhe, Germany. Ethylene di-methacrylate (EDMA) was obtained from Sigma-Aldrich, Taufkirchen, Germany. Polyvinylpyrrolidone (PVP) and 1-hexanol were supplied from Merck GmbH, Darmstadt, Germany.

We sonicated 1 g of polystyrene and 30 mL of deionized water for 5 min. The suspension was stirred (200 rpm) for 1.5 h at 30 °C and argon was bubbled through the solution. An emulsion of GMA (7 mL), EDMA (7 mL), SDS (0.3 g), PVP (3 g) 25,000 D, 1-hexanol, 0.56 g BPO, and 250 mL of water was prepared by sonicating the mixture (10 min), stirring at RT for 10 min, and bubbling argon through the solution for another 10 min. The emulsion was added to the suspension of the polystyrene particles and stirred for 2 h at 30 °C. The temperature was raised to 70 °C and kept constant for 24 h. The particles were separated and washed with water (3 times) and ethanol (3 times) and dried at 70 °C for 30 min. The volume of 1-hexanol was increased from 7 mL (**S2**) by 14 mL (**S3**) to 21 mL (**S4**).

2.2. Particle Characterization

A Hitachi SU8030 (Hitachi High-Technologies Corporation, Tübingen, Germany) was used to obtain SEM images. FIB cuts were prepared with a dual cross-beam FEI Strata DB235 (FEI, Tübingen, Germany). The primary Ga^+ Ion current was reduced to 50 pA via an aperture. DRIFT spectra were measured with a Bruker Vertex 70 spectrometer (Bruker, Ettlingen, Germany). Solid-state NMR spectra were recorded on a Bruker Avance III-HD spectrometer (Bruker, Ettlingen, Germany) with a wide-bore magnet operating at 300.13 MHz (^{1}H) and 75.46 MHz (^{13}C). The powdered samples of the respective materials were packed in 4 mm o.d. zirconia rotors; the spinning speed was 10 KHz, the relaxation delay 4 s, and the contact time 2 ms.

For Raman measurements, particle samples were dispersed in ethanol and thoroughly mixed. One droplet (10 µL) of the mixed dispersion was placed on a cleansed sapphire microscope slide and evaporated. Raman spectra and Raman images were obtained using a confocal Raman microscope (WiTec alpha300 RA&S, Ulm, Germany) equipped with an air objective (EC Epiplan-Neofluar DIC M27, 100×, NA = 0.9, Carl Zeiss, Oberkochen, Germany) with a lateral resolution of 360 nm. This system was equipped with a lens-based UHTS 300 spectrometer (WiTec, Ulm, Germany) connected via a 100 µm (NA = 0.12) multi-mode optical fiber and thermoelectric cooled CCD and EMCCD (DU970N-BV, WiTec, Ulm, Germany). All Raman experiments were carried out using a laser of 532 nm with a nominal output power of approx. 39 mW and a grating of 600 lines/mm. Data were processed using Control 5.0 software provided by WITec. All experiments were carried out in ambient conditions. We chose sapphire as a substrate due to its low background signal, which does not interfere with the signal intensity from the region of interest. Additionally, the absorbance signals of sapphire do not overlap with those of the sample, making it an ideal substrate for Raman analysis of these particles.

3. Results

Polystyrene particles (**S1**) were synthesized from styrene via a free-radical chain propagation polymerization. Porous poly (glycidyl methacrylate-co-ethylene di-methacrylate) particles **S2**, **S3,** and **S4** were prepared in a seeded swelling polymerization process. In this process, polystyrene particles **S1** were dispersed in water and treated with an emulsion consisting of glycidyl methacrylate (GMA), ethylene di-methacrylate (EDMA), sodium lauryl sulfate (SDS), polyvinyl pyrrolidone (PVP), and 1-hexanol. Benzoyl peroxide was added to start the polymerization. To control the size of the pores, the amount of the porogen (1-hexanol) was gradually increased from 7 mL (**S2**) by 14 mL (**S3**) to 21 mL (**S4**) under otherwise identical reaction conditions.

Figure 1A shows the solid-state ^{13}C CP/MAS NMR spectra of the particles **S1**–**S4**. In the spectra of **S1**, characteristic bands of polystyrene are observed, whereas the spectra of **S2**–**S4** show the characteristic peaks of poly (glycidyl methacrylate-co-ethylene di-methacrylate) polymers as well as those of polystyrene.

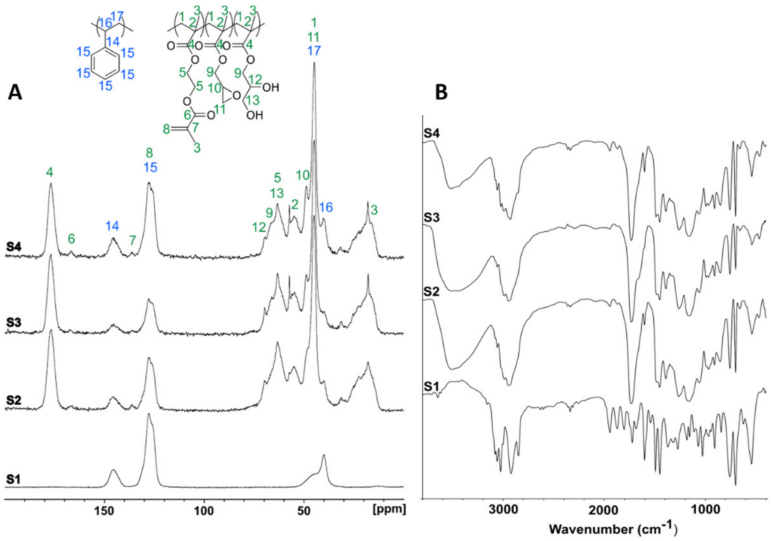

Figure 1. (**A**) Solid-state ^{13}C CP/MAS NMR spectra of particles **S1**–**S4** and (**B**) DRIFT spectra of the particles **S1**–**S4**.

The carbon nuclei forming the polymer backbone resonate at 18, 44, and 54 ppm; the oxygen-containing side chains resonate at 63 and 66 ppm, whereas the carbonyl carbon atoms produce to a broad peak at 176 ppm. All samples still contained a considerable amount of polystyrene as indicated by broad peaks in the aromatic region at 127

and 145 ppm. This finding is supported by the comparison of the DRIFT spectrum of polystyrene (**S1**) with those of the particles **S2**–**S4** shown in Figure 1B. All DRIFT spectra of the materials **S2**–**S4** contain absorption bands that are assigned to aromatic C=C at 1600 cm^{-1}, C=C–H bending at 700 cm^{-1} and 735 cm^{-1}, as well as C=C–H stretching at 3023–3083 cm^{-1}. These vibrations of the polystyrene appear along with the characteristic absorptions of poly (glycidyl methacrylate-co-ethylene di-methacrylate) polymers [35]. Characteristic for that polymer is the ester carbonyl (C=O) stretch at around 1725 cm^{-1} and the aliphatic C–H stretch just around 2980 cm^{-1}.

The surface/bulk porosity, roughness, and chemical distribution were revealed by SEM and 3D-CRM. Figure 2 compares the images of the samples **S1**–**S4** generated by SEM (left column A,C,E,G,I) with those obtained by 3D-CRM (right column B,D,F,H,J). For **S1**, both techniques revealed spherical, highly monodisperse particles. After the swelling of the polystyrene particles **S1** with EDMA, GMA, and 1-hexanol (porogen), larger particles were found with smaller particles attached to them (Figure 2C,E,G,I). The small particles had a more or less spherical shape and a smooth surface; the large particles were dented at one side and are porous. With an increasing amount of porogen, which was in the series **S2** (7 mL), **S3** (14 mL), and **S4** (21 mL), the pore size increased. In the cases of **S2** and **S3**, the small spherical particles were located in the dented area of the large particles (Figure 2C,E,G). Interestingly, the particles **S4** showed non-porous caps in the area of the dent (Figure 2I). To reveal the porosity of the bulk, particles from **S3** were cut through by line milling with a Ga+ FIB (50 pA beam current). The corresponding SEM images (Figure 2K,L) demonstrate that the porosity inside the main particle is comparable to that on its surface.

The 3D-CRM images of the samples **S1**–**S4** shown in Figure 2B,D,F,H,J reproduced the size and the shape of the particles as shown in the corresponding SEM images. Due to the poor resolution of the optical light-microscopy compared with SEM, the porosity and surface morphology can only be assumed. However, the advantage of 3D-CRM is that the chemical composition and distribution of the sample can be deduced by the fingerprint Raman spectrum at different positions on the particles.

The assignment of the Raman peaks to specific vibration bands and the resulting color coding of the images are shown in Figure 3. Figure 3A shows a two-dimensional scan of one particle. Here, the integral intensity of Raman scattering in the range of 350–3200 cm^{-1} is used. The particle is distinguishable from the background. In the region of the attached small particle, the observed intensity is significantly higher compared with the main particle. Figure 3B,C shows Raman spectra recorded at the positions marked by X. The Raman spectrum recorded at the position of the small particle can be assigned to polystyrene due to the characteristic Raman peaks at 1002, 1603, and 1448 cm^{-1} (red arrows) [35–37]. The Raman spectrum recorded at the main particle can be assigned to poly (glycidyl methacrylate-co-ethylene di-methacrylate) polymer due to the Raman peak at 1723 cm^{-1} [35]. The peaks at 1454 and 1259 cm^{-1} (blue arrows) can be assigned to ketones and epoxides from EDMA and GMA, respectively [35,38,39].

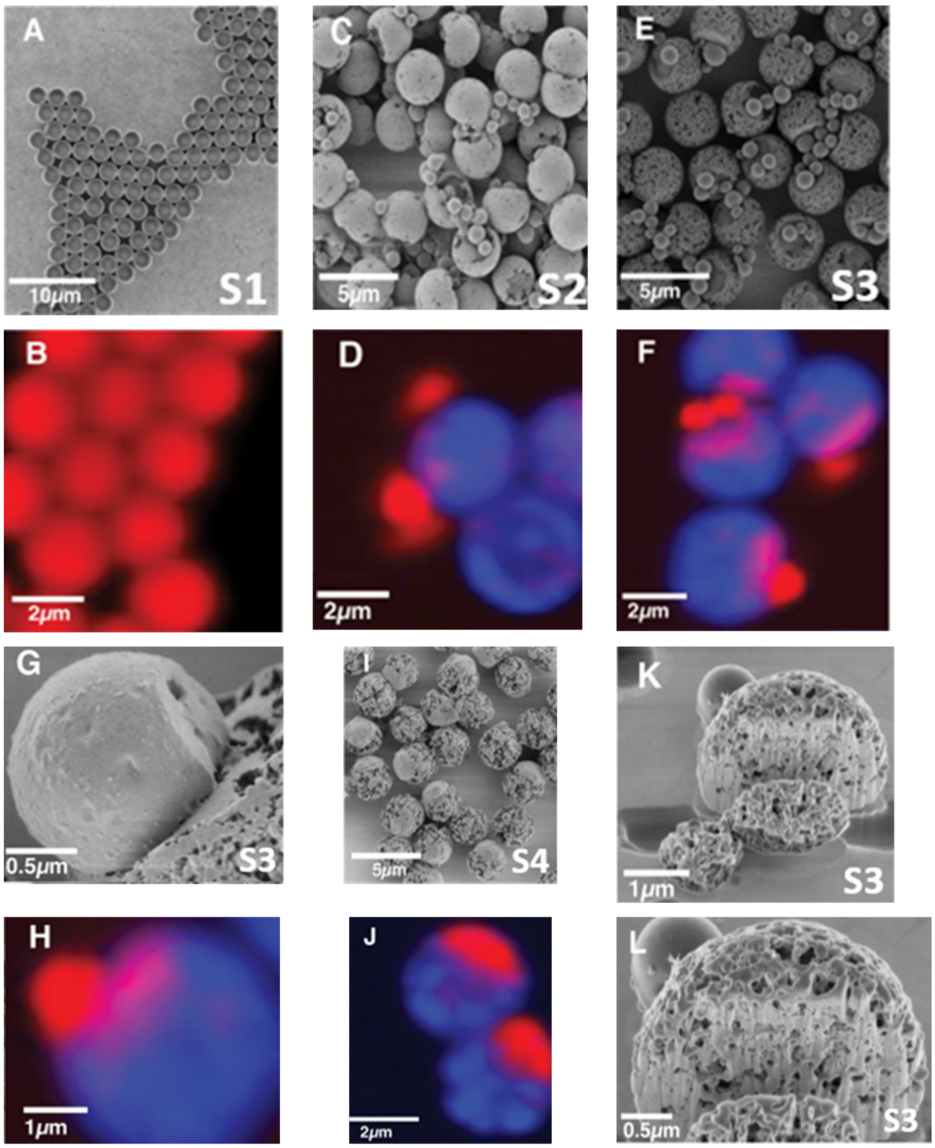

Figure 2. Particles **S1**–**S4** imaged by SEM (**A**,**C**,**E**,**G**,**I**) and the corresponding Raman images (**B**,**D**,**F**,**H**,**J**). A magnified SEM image of **S3** (**G**) and the corresponding Raman image (**H**) are shown. A particle of the sample **S3** milled with Ga^+ FIB (**K**,**L**). Particles **S1** (**A**,**B**) consist of pure polystyrene. Particles **S2**, **S3**, and **S4** consist of poly (glycidyl methacrylate-co-ethylene di-methacrylate) polymer with an increasing concentration of porogen **S2** (**C**,**D**; 7 mL porogen), **S3** (**E**,**F**; 14 mL porogen), and **S**4 (**I**,**J**; 21 mL porogen).

A principal component analysis (PCA) of all Raman spectra yielded two principal components explaining 95% of the total data. Based on this number of relevant components, the data were analyzed with Control 5.0 data processing software provided by WITec using an inbuilt PCA. The components were assigned to colors (blue, red) for better visualization. Regions dominated by the polystyrene were assigned the color red, while those dominated by EDMA/GMA were assigned the color blue; the resulting image is depicted in Figure 3D. Consequently, the small particles attached to the larger particles could be assigned to polystyrene and the large particles to EDMA/GMA. Based on this assignment, all 3D-CRM images in Figure 2 are color-coded following the same procedure.

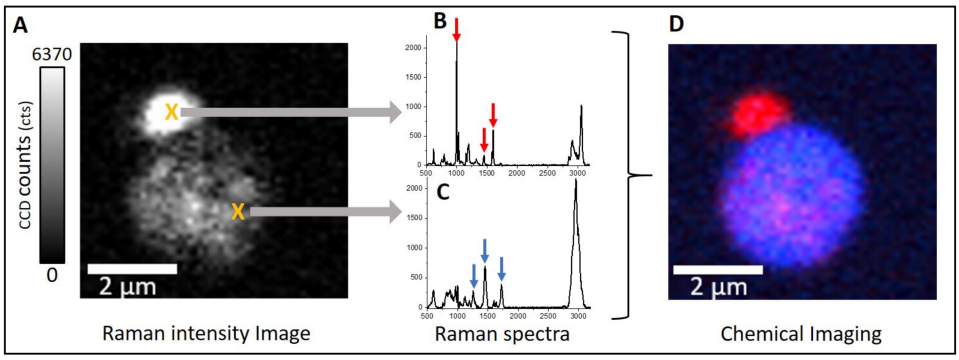

Figure 3. (**A**) Raman intensity image of a particle **S3**. (**B**,**C**) Raman spectra recorded in the range from 500 to 3200 cm^{-1} at the locations marked with X. Characteristic Raman signals are marked with red and blue arrows (see text for details). (**D**) The Raman image is based on the assignment of spectra in each pixel. Pixels dominated by spectrum (**B**,**C**) are color-coded with red and blue, respectively.

4. Discussion

A correlation between NMR, DRIFT, SEM, and 3D-CRM is presented in this study of polystyrene particles. With the combination of these techniques, the swelling of polystyrene/poly (glycidyl methacrylate-co-ethylene di-methacrylate) particles depending on the concentration of the porogen (1-hexanol) was studied. The ^{13}C CP/MAS NMR spectra (Figure 1A) show that, in all swollen particles, polystyrene and poly (glycidyl methacrylate-co-ethylene di-methacrylate) are present. These results are consistent with the results of the DRIFT measurements (Figure 1B).

The first indications of a deviation from uniformity/sphericity of the particles are found in the SEM images (Figure 2). The SEM images of the particles from the synthesis using 7 mL (**S2**) (Figure 2C) and 14 mL (**S3**) (Figure 2E) porogen show different types of particles. They clearly show small- and large-sized particles. The large particles show a dented area where the small particles are attached. The relative amount of small particles in relation to the larger ones varies within the sample. SEM revealed that the surface roughness of the small particles is lower than that of the large particles. When 21 mL (**S4**) (Figure 2I) of porogen was used, no dented areas or small particles were observed. The **S4** particles were almost spherical, with a flat nonporous cap in the region wherein the dented areas in the other particles were observed. This reduced roughness is comparable to the roughness that was found for small particles (**S2** and **S3**) at lower porogen concentrations.

The porosity of the particles on the surface and in the bulk was further investigated. For this, the particles were milled with FIB. SEM images of a milled particle **S3** (14 mL porogen) are shown in Figure 2K,L. The FIB image indicates a comparable porosity throughout the particle. Milling of the smaller particles was unsuccessful.

Next, the chemical composition of individual particles was studied in detail with 3D-CRM. The analysis of the Raman spectra enables an assignment of the observed vibrational bands to molecule specific vibrations. The spectra recorded at the position of the small particles are dominated by vibrations assigned to polystyrene, whereas the spectra recorded at the large particles show bands assigned to poly (glycidyl methacrylate-co-ethylene di-methacrylate). The CRM images suggest that polystyrene is extruded from the forming EDMA/GMA polymer network during polymerization. When the porogen concentration was increased to 21 mL (**S4**) (Figure 2I,J), the extrusion of polystyrene remained incomplete, and the extruded polystyrene formed an adherent cap on the dented areas of the large particles.

A presumed mechanism for the formation of these particles is shown in Scheme 1.

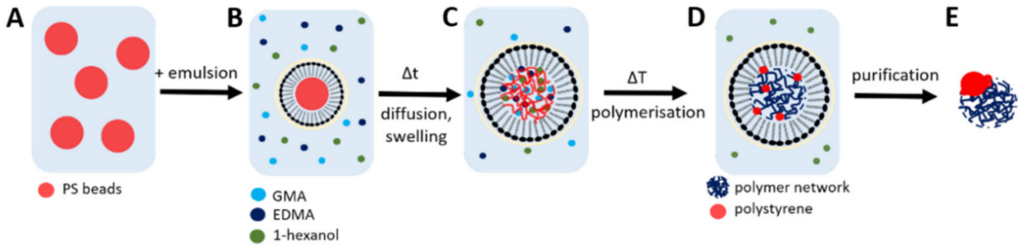

Scheme 1. (**A**,**B**) Suspension of monodisperse micron-sized polystyrene beads in water mixed with an emulsion consisting of GMA, EDMA, SDS, PVP, BPO, and 1-hexanol (in adequate quantities for **S2**, **S3**, and **S4**). For clarity, BPO (radical starter) is not included in the scheme. Hydrophobic attractions between PS and SDS are responsible for the formation of micelles. Water-soluble PVP stabilizes the micelles from the outside. (**C**) The particles swell due to the diffusion of GMA, EDMA, 1-hexanol, and BPO into the bead. (**D**) Upon polymerization, both methacrylates form the porous poly (glycidyl methacrylate-ethylene dimethacrylate) network with 1-hexanol as an inert solvent. (**E**) At a certain point, the micelles rupture and release a porous particle.

Pore formation in particles depends on the solubility of porogen and the seed particle. Materials with similar solubility parameters have a high affinity to each other. Notably, 1-hexanol has a poor theoretical solubility with polystyrene and poly (glycidyl methacrylate-co-ethylene di-methacrylate). As polymerization starts, phase separation occurs due to insufficient solubility and 1-hexanol is displaced as an inert molecule, leaving the pore structure in the particle. In the magnified SEM image (Figure 2G), it appears that polystyrene is squeezed out of the particle. This can be also explained by solubility effects. Due to a rather good solubility in GMA and EDMA, the polystyrene bead is dissolved into individual polymer chains of high mobility and flexibility [40–42]. Upon GMA and EDMA polymerization, phase separation occurs again, and polystyrene becomes insoluble in the three-dimensional network and is squeezed out.

The syntheses described here yield particles with variable size, shape, and porosity. This is achieved by changing only one parameter, which is the amount of porogen added during synthesis. In chemistry, managing critical parameters precisely plays a crucial role in the final properties of the particles [11]. The 3D-CRM results revealed that these particles show a Janus particle behavior not only in terms of their morphology, but also in terms of their chemical composition. Both properties are controllable by the concentration of the porogen. We also showed that 3D-CRM is a useful tool for analyzing and characterizing inhomogeneous particles in a spatially resolved and three-dimensional way. Thus, the synthesis can be adjusted accordingly to achieve particles of defined 3D morphology and controlled chemical composition. Potential applications of these particles include as template molecules for large porous silica microspheres for protein separation, drug delivery systems, microcapsule systems for extrinsic self-healing applications, or, for instance, as templating materials used in energy storage applications [18,43–51].

5. Conclusions

This study shows that the combination of NMR, DRIFT, SEM, and 3D-CRM is well-suited for controlled synthesis of polymer particles. Synthesized particles with varying proportions of porogen were analyzed with the aforementioned methods at each step of synthesis development. This provides direct insight into the development of the synthesis at every step. Both solid-state ^{13}C CP/MAS NMR and DRIFT spectra showed that all particles (**S1**, **S2**, **S3**, and **S4**) contain a significant amount of polystyrene. Swollen particles (**S2**, **S3** and **S4**) showed both polystyrene and other constituent byproducts as a result of synthesis. Interpretation of the morphology and the chemical composition of the particles was facilitated by the combined use of SEM and 3D-CRM. This approach revealed the distribution of the chemical entities across the particles. We found that 3D-CRM is indispensable for the assignment of the different chemical entities to the morphological features on the particles, and distribution of chemical species can be visualized using PCA.

Similar problems are often analyzed with fluorescence microscopy; however, this requires the addition of staining chemicals or labeling steps [29–31]. For the selection of appropriate labels, making assumptions about the resulting particles is necessary. Consequently, the selection of the labels influences the information accessible by the measurement and may bias the result. In contrast, the marker-free approach presented here minimizes sample alteration and eliminates the need for an additional step, since no labeling is necessary for 3D-CRM measurements and the Raman spectra provide a detailed insight into the chemical composition.

Author Contributions: Conceptualization, H.A.M. and M.B.; Data curation, A.W. and J.-E.B.; Formal analysis, A.W., S.W. and J.-E.B.; Funding acquisition, H.A.M. and M.B.; Methodology, A.W., S.W., J.-E.B., K.B. and A.K.; Project administration, S.K., H.A.M. and M.B.; Software, A.W. and J.-E.B.; Supervision, A.K., H.A.M. and M.B.; Visualization, A.W., S.W., J.-E.B. and Kai Braun; Writing—original draft, A.W., A.K., H.A.M. and M.B.; Writing—review & editing, J.C.S., A.M., A.K., H.A.M. and M.B. All authors have read and agreed to the published version of the manuscript.

Funding: This work was supported by the Bundesministerium für Wirtschaft und Energie (AiF/ZIM, ZF4019203SL8). A.M. would like to acknowledge the financial support within the framework IngenieurNachwuchs 2016 (project: CompeTERS) by the German Federal Ministry of Education and Research (BMBF). J.C.S. was funded by German Federal Ministry of Education and Research, funding program Forschung an Fachhochschulen (project 13FH647IX6). SEM/EDX measurements on a Hitachi SU 8030 SEM were supported by the DFG under contract INST 37/829-1 FUGG. The article processing charge was funded by the Baden−Württemberg Ministry of Science, Research and Culture in the funding program Open Access Publishing.

Institutional Review Board Statement: Not applicable.

Informed Consent Statement: Not applicable.

Data Availability Statement: The data presented in this study are available on request from the corresponding author.

Acknowledgments: The authors are grateful to Elke Nadler (University of Tübingen) for performing SEM measurements.

Conflicts of Interest: The authors declare no conflict of interest. The funders had no role in the design of the study; in the collection, analyses, or interpretation of data; in the writing of the manuscript; or in the decision to publish the results.

References

1. Gulka, C.P.; Swartz, J.D.; Trantum, J.R.; Davis, K.M.; Peak, C.M.; Denton, A.J.; Haselton, F.R.; Wright, D.W. Coffee rings as low-resource diagnostics: Detection of the malaria biomarker Plasmodium falciparum histidine-rich protein-II using a surface-coupled ring of Ni(II)NTA gold-plated polystyrene particles. *ACS Appl. Mater. Interfaces* **2014**, *6*, 6257–6263. [CrossRef] [PubMed]
2. Grafmueller, S.; Manser, P.; Diener, L.; Diener, P.-A.; Maeder-Althaus, X.; Maurizi, L.; Jochum, W.; Krug, H.F.; Buerki-Thurnherr, T.; von Mandach, U.; et al. Bidirectional Transfer Study of Polystyrene Nanoparticles across the Placental Barrier in an ex Vivo Human Placental Perfusion Model. *Environ. Health Perspect.* **2015**, *123*, 1280–1286. [CrossRef] [PubMed]
3. Holzapfel, V.; Musyanovych, A.; Landfester, K.; Lorenz, M.R.; Mailänder, V. Preparation of Fluorescent Carboxyl and Amino Functionalized Polystyrene Particles by Miniemulsion Polymerization as Markers for Cells. *Macromol. Chem. Phys.* **2005**, *206*, 2440–2449. [CrossRef]
4. Fröhlich, E. The role of surface charge in cellular uptake and cytotoxicity of medical nanoparticles. *Int. J. Nanomed.* **2012**, *7*, 5577–5591. [CrossRef] [PubMed]
5. Choi, J.; Xue, Y.; Xia, W.; Ray, T.R.; Reeder, J.T.; Bandodkar, A.J.; Kang, D.; Xu, S.; Huang, Y.; Rogers, J.A. Soft, skin-mounted microfluidic systems for measuring secretory fluidic pressures generated at the surface of the skin by eccrine sweat glands. *Lab Chip* **2017**, *17*, 2572–2580. [CrossRef] [PubMed]
6. Fan, J.-B.; Song, Y.; Liu, H.; Lu, Z.; Zhang, F.; Liu, H.; Meng, J.; Gu, L.; Wang, S.; Jiang, L. A general strategy to synthesize chemically and topologically anisotropic Janus particles. *Sci. Adv.* **2017**, *3*, e1603203. [CrossRef] [PubMed]
7. Yang, M.; Cao, L.; Tan, L. Synthesis of sea urchin-like polystyrene/polyaniline microspheres by seeded swelling polymerization and their catalytic application. *Colloids Surf. A Physicochem. Eng. Asp.* **2014**, *441*, 678–684. [CrossRef]
8. Shim, S.-E.; Cha, Y.-J.; Byun, J.-M.; Choe, S. Size control of polystyrene beads by multistage seeded emulsion polymerization. *J. Appl. Polym. Sci.* **1999**, *71*, 2259–2269. [CrossRef]

9. Zhang, Y.; Lu, Y.; Zhong, J.; Li, W.; Wei, Q.; Wang, K. Molecularly imprinted polymer microspheres prepared via the two-step swelling polymerization for the separation of lincomycin. *J. Appl. Polym. Sci.* **2019**, *136*, 47938. [CrossRef]
10. Li, Y.; Wang, Z.; Wang, C.; Zhao, Z.; Xue, G. Controlling the morphology of micrometre-size polystyrene/polyaniline composite particles by Swelling–Diffusion–Interfacial-Polymerization Method. *Polymer* **2011**, *52*, 409–414. [CrossRef]
11. Park, S.H.; Kim, J.; Lee, W.-E.; Byun, D.-J.; Kim, M.H. One-Step Synthesis of Hollow Dimpled Polystyrene Microparticles by Dispersion Polymerization. *Langmuir* **2017**, *33*, 2275–2282. [CrossRef]
12. Omer-Mizrahi, M.; Margel, S. Synthesis and characterization of spherical and hemispherical polyepoxide micrometer-sized particles of narrow size distribution by a single-step swelling of uniform polystyrene template microspheres with glycidyl methacrylate. *J. Polym. Sci. A Polym. Chem.* **2007**, *45*, 4612–4622. [CrossRef]
13. Galperin, A.; Margel, S. Synthesis and characterization of new micrometer-sized radiopaque polymeric particles of narrow size distribution by a single-step swelling of uniform polystyrene template microspheres for X-ray imaging applications. *Biomacromolecules* **2006**, *7*, 2650–2660. [CrossRef]
14. Boguslavsky, L.; Margel, S. Synthesis and characterization of micrometer-sized homo and composite polyacrylonitrile particles of narrow size distribution on the basis of single-step swelling of uniform polystyrene template microspheres. *J. Polym. Sci. A Polym. Chem.* **2004**, *42*, 4847–4861. [CrossRef]
15. Bryce, D.A.; Kitt, J.P.; Harris, J.M. Confocal Raman Microscopy Investigation of Molecular Transport into Individual Chromatographic Silica Particles. *Anal. Chem.* **2017**, *89*, 2755–2763. [CrossRef]
16. Wang, W.-P.; Pan, C.-Y. Preparation and characterization of polystyrene/graphite composite prepared by cationic grafting polymerization. *Polymer* **2004**, *45*, 3987–3995. [CrossRef]
17. Podsiadlo, P.; Stachowiak, G.W. Characterization of surface topography of wear particles by SEM stereoscopy. *Wear* **1997**, *206*, 39–52. [CrossRef]
18. Wang, Q.; Zhang, Y.; Jiang, H.; Li, X.; Cheng, Y.; Meng, C. Designed mesoporous hollow sphere architecture metal (Mn, Co, Ni) silicate: A potential electrode material for flexible all solid-state asymmetric supercapacitor. *Chem. Eng. J.* **2019**, *362*, 818–829. [CrossRef]
19. Chatterjee, J.; Haik, Y.; Chen, C.-J. Modification and characterization of polystyrene-based magnetic microspheres and comparison with albumin-based magnetic microspheres. *J. Magn. Magn. Mater.* **2001**, *225*, 21–29. [CrossRef]
20. Nagy, J.B. Multinuclear NMR characterization of microemulsions: Preparation of monodisperse colloidal metal boride particles. *Colloids Surf.* **1989**, *35*, 201–220. [CrossRef]
21. Leu, G.; Liu, Y.; Werstler, D.D.; Cory, D.G. NMR Characterization of Elastomer−Carbon Black Interactions. *Macromolecules* **2004**, *37*, 6883–6891. [CrossRef]
22. Stinner, C.; Tang, Z.; Haouas, M.; Weber, T.; Prins, R. Preparation and 31P NMR Characterization of Nickel Phosphides on Silica. *J. Catal.* **2002**, *208*, 456–466. [CrossRef]
23. Santamaria, A.; Mondragon, F.; Molina, A.; Marsh, N.; Eddings, E.; Sarforim, A. FT-IR and 1H NMR characterization of the products of an ethylene inverse diffusion flame. *Combust. Flame* **2006**, *146*, 52–62. [CrossRef]
24. Joshi, R.; Feldmann, V.; Koestner, W.; Detje, C.; Gottschalk, S.; Mayer, H.A.; Sauer, M.G.; Engelmann, J. Multifunctional silica nanoparticles for optical and magnetic resonance imaging. *Biol. Chem.* **2013**, *394*, 125–135. [CrossRef]
25. Lica, G.C.; Zelakiewicz, B.S.; Tong, Y.Y. Electrochemical and NMR characterization of octanethiol-protected Au nanoparticles. *J. Electroanal. Chem.* **2003**, *554–555*, 127–132. [CrossRef]
26. Markervich, E.; Salitra, G.; Levi, M.D.; Aurbach, D. Capacity fading of lithiated graphite electrodes studied by a combination of electroanalytical methods, Raman spectroscopy and SEM. *J. Power Sources* **2005**, *146*, 146–150. [CrossRef]
27. Santini, A.; Miletic, V. Comparison of the hybrid layer formed by Silorane adhesive, one-step self-etch and etch and rinse systems using confocal micro-Raman spectroscopy and SEM. *J. Dent.* **2008**, *36*, 683–691. [CrossRef]
28. Jin, Q.; Li, M.; Polat, B.; Paidi, S.K.; Dai, A.; Zhang, A.; Pagaduan, J.V.; Barman, I.; Gracias, D.H. Mechanical Trap Surface-Enhanced Raman Spectroscopy for Three-Dimensional Surface Molecular Imaging of Single Live Cells. *Angew. Chem.* **2017**, *129*, 3880–3884. [CrossRef]
29. Liu, B.; Möhwald, H.; Wang, D. Synthesis of Janus particles via kinetic control of phase separation in emulsion droplets. *Chem. Commun.* **2013**, *49*, 9746–9748. [CrossRef]
30. Chang, F.; Ouhajji, S.; Townsend, A.; Sanogo Lacina, K.; van Ravensteijn, B.G.P.; Kegel, W.K. Controllable synthesis of patchy particles with tunable geometry and orthogonal chemistry. *J. Colloid Interface Sci.* **2021**, *582*, 333–341. [CrossRef]
31. Maisch, J.; Jafarli, F.; Chassé, T.; Blendinger, F.; Konrad, A.; Metzger, M.; Meixner, A.J.; Brecht, M.; Dähne, L.; Mayer, H.A. One-pot synthesis of micron partly hollow anisotropic dumbbell shaped silica core-shell particles. *Chem. Commun.* **2016**, *52*, 14392–14395. [CrossRef] [PubMed]
32. Bhaskar, S.; Gibson, C.T.; Yoshida, M.; Nandivada, H.; Deng, X.; Voelcker, N.H.; Lahann, J. Engineering, characterization and directional self-assembly of anisotropically modified nanocolloids. *Small* **2011**, *7*, 812–819. [CrossRef] [PubMed]
33. Kumamoto, Y.; Harada, Y.; Takamatsu, T.; Tanaka, H. Label-free Molecular Imaging and Analysis by Raman Spectroscopy. *Acta Histochem. Cytochem.* **2018**, *51*, 101–110. [CrossRef] [PubMed]
34. Xie, W.; Walkenfort, B.; Schlücker, S. Label-free SERS monitoring of chemical reactions catalyzed by small gold nanoparticles using 3D plasmonic superstructures. *J. Am. Chem. Soc.* **2013**, *135*, 1657–1660. [CrossRef]

35. Socrates, G. Polymers—Macromolecules. In *Infrared and Raman Characteristic Group Frequencies: Tables and Charts*, 3rd ed.; John Wiley & Sons LTD: Chichester, UK, 2015; ISBN 0470093072.
36. Anema, J.R.; Brolo, A.G.; Felten, A.; Bittencourt, C. Surface-enhanced Raman scattering from polystyrene on gold clusters. *J. Raman Spectrosc.* **2010**, *41*, 745–751. [CrossRef]
37. Palm, A. Raman Spectrum of Polystyrene. *J. Phys. Chem.* **1951**, *55*, 1320–1324. [CrossRef]
38. Filipecka, K.; Miedziński, R.; Sitarz, M.; Filipecki, J.; Makowska-Janusik, M. Optical and vibrational properties of phosphorylcholine-based contact lenses-Experimental and theoretical investigations. *Spectrochim. Acta A Mol. Biomol. Spectrosc.* **2017**, *176*, 83–90. [CrossRef]
39. Boerio, F.J.; Yuann, J.K. Determination of copolymer composition by Raman spectroscopy. *J. Polym. Sci. Polym. Phys. Ed.* **1973**, *11*, 1841–1848. [CrossRef]
40. Gokmen, M.T.; Du Prez, F.E. Porous polymer particles—A comprehensive guide to synthesis, characterization, functionalization and applications. *Prog. Polym. Sci.* **2012**, *37*, 365–405. [CrossRef]
41. Gong, B.-L.; Ke, C.-Y.; Geng, X.-D. Synthesis of Monodisperse Poly(glycidylmethacrylate-co-ethylene dimethacrylate) Beads and Their Application in Separation of Biopolymers. *Chin. J. Chem.* **2004**, *22*, 283–289. [CrossRef]
42. Gong, B.; Ke, C.; Geng, X. Preparation of weak cation exchange packings based on monodisperse poly(glycidyl methacrylate-co-ethylene dimethacrylate) beads and their chromatographic properties. *Anal. Bioanal. Chem.* **2003**, *375*, 769–774. [CrossRef]
43. Kutuzova, L.; Kandelbauer, A. Self-healing thermosets. In *Handbook of Thermoset Plastics*, 4th ed.; Dodiuk, H., Ed.; William Andrew Inc. & Elsevier: Norwich, NY, USA, 2021; ISBN 978-0-12-821632-3.
44. Urdl, K.; Weiss, S.; Karpa, A.; Peric, M.; Zikulnig-Rusch, E.M.; Brecht, M.; Kandelbauer, A.; Müller, U.; Kern, W. Furan-functionalized melamine-formaldehyde particles performing Diels-Alder reactions. *Eur. Polym. J.* **2018**, *108*, 225–234. [CrossRef]
45. Urdl, K.; Weiss, S.; Brodbeck, B.; Kandelbauer, A.; Zikulnig-Rusch, E.M.; Müller, U.; Kern, W. Homogeneous, monodispersed furan-melamine particles performing reversible binding and forming networks. *Eur. Polym. J.* **2019**, *116*, 158–168. [CrossRef]
46. Urdl, K.; Kandelbauer, A.; Kern, W.; Müller, U.; Thebault, M.; Zikulnig-Rusch, E.M. Self-healing of densely crosslinked thermoset polymers—a critical review. *Prog. Org. Coat.* **2017**, *104*, 232–249. [CrossRef]
47. Wang, Q.; Yang, H.; Meng, T.; Yang, J.; Huang, B.; Gu, F.L.; Zhang, S.; Meng, C.; Tong, Y. Boosting Electron Transfer with Heterointerface Effect for High-Performance Lithium-Ion Storage. *Energy Storage Mater.* **2021**, *36*, 365–375. [CrossRef]
48. Wang, Q.; Li, Y.; Meng, T.; Huang, B.; Hu, L.; Su, H.; Meng, C.; Tong, Y. Engineering Heterostructure-Incorporated Metal Silicates Anchored on Carbon Nanotubes for Highly Durable Lithium Storage. *ACS Appl. Energy Mater.* **2021**, *4*, 1548–1559. [CrossRef]
49. Meng, T.; Li, B.; Wang, Q.; Hao, J.; Huang, B.; Gu, F.L.; Xu, H.; Liu, P.; Tong, Y. Large-Scale Electric-Field Confined Silicon with Optimized Charge-Transfer Kinetics and Structural Stability for High-Rate Lithium-Ion Batteries. *ACS Nano* **2020**, *14*, 7066–7076. [CrossRef]
50. Barbé, C.; Bartlett, J.; Kong, L.; Finnie, K.; Lin, H.Q.; Larkin, M.; Calleja, S.; Bush, A.; Calleja, G. Silica Particles: A Novel Drug-Delivery System. *Adv. Mater.* **2004**, *16*, 1959–1966. [CrossRef]
51. Xia, H.; Wan, G.; Yang, F.; Wang, J.; Bai, Q. Preparation of monodisperse large-porous silica microspheres with polymer microspheres as the templates for protein separation. *Mater. Lett.* **2016**, *180*, 19–22. [CrossRef]

9. Three-dimensional (3D) Surface-enhanced Raman Spectroscopy (SERS) Substrates: Fabrication and SERS Applications.

Ashutosh Mukherjee[1,2,3], Frank Wackenhut[1,2,], Akanksha Dohare[4], Anke Horneber[5,6], Anita Lorenz[1,2], Hendrik Müchler[1], Alfred J. Meixner[3,6], Hermann A. Mayer[4] and Marc Brecht[1,2,3,6,*]*

[1] Center for Process Analysis and Technology (PA&T), School of Life Sciences, Reutlingen University, Reutlingen, Germany

[2] Reutlingen Research Institute (RRI), Reutlingen University, Reutlingen, Germany

[3] Institute of Physical and Theoretical Chemistry, Eberhard Karls University of Tübingen, Tübingen, Germany

[4] Institute of Inorganic Chemistry, Eberhard Karls University of Tubingen, Tubingen, Germany.

[5] Institute for Applied Physics, University of Tübingen, Tübingen, Germany

[6] Center for Light-Matter-Interaction, Sensors and Analytics (LISA$^+$), University of Tübingen, Tübingen, Germany

This chapter was originally published in The Journal of Physical Chemistry C as

Ashutosh Mukherjee, Frank Wackenhut, Akanksha Dohare, Anke Horneber, Anita Lorenz, Hendrik Müchler, Alfred J. Meixner, Hermann A. Mayer, and Marc Brecht. The Journal of Physical Chemistry C 2023 127, 28, 13689-13698.

DOI: 10.1021/acs.jpcc.3c02410

Supplementary Material/Supporting Information shown in Appendix 5

THE JOURNAL OF PHYSICAL CHEMISTRY C
A JOURNAL OF THE AMERICAN CHEMICAL SOCIETY

pubs.acs.org/JPCC

Article

Three-Dimensional (3D) Surface-Enhanced Raman Spectroscopy (SERS) Substrates: Fabrication and SERS Applications

Ashutosh Mukherjee, Frank Wackenhut,* Akanksha Dohare, Anke Horneber, Anita Lorenz, Hendrik Müchler, Alfred J. Meixner, Hermann A. Mayer, and Marc Brecht*

Cite This: *J. Phys. Chem. C* 2023, 127, 13689–13698

Read Online

ACCESS | Metrics & More | Article Recommendations | Supporting Information

ABSTRACT: This study introduces a straightforward approach to construct three-dimensional (3D) surface-enhanced Raman spectroscopy (SERS) substrates using chemically modified silica particles as microcarriers and by attaching metal nanoparticles (NPs) onto their surfaces. Tollens' reagent and sputtering techniques are utilized to prepare the SERS substrates from mercapto-functionalized silica particles. Treatment with Tollens' reagent generates a variety of silver NPs, ranging from approximately 10 to 400 nm, while sputtering with gold (Au) yields uniformly distributed NPs with an island-like morphology. Both substrates display wide plasmon resonances in the scattering spectra, making them effective for SERS in the visible spectral range, with enhancement factors (ratio of the analyte's intensity at the hotspot compared to that on the substrate in the absence of metal nanoparticles) of up to 25. These 3D substrates have a significant advantage over traditional SERS substrates because their active surface area is not limited to a 2D surface but offers a much greater active surface due to the 3D arrangement of the NPs. This feature may enable achieving much higher SERS intensity from within streaming liquids or inside cells/tissues.

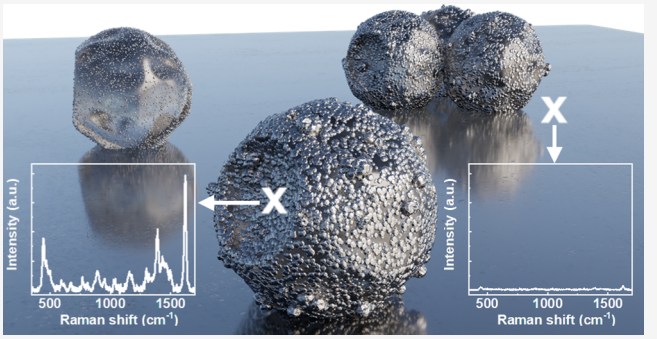

INTRODUCTION

Surface-enhanced Raman spectroscopy (SERS) has received a lot of attention since its discovery in 1974 due to the strong enhancement of the inherently weak Raman signal.[1] In particular, noble metal nanoparticles (NPs) of various sizes and shapes have been used to boost the SERS signal with enhancement factors (EFs) ranging from 10^4 to 10^6, occasionally reaching 10^8.[2,3] In these instances, the EF has been accurately assessed by considering the molecular density and electromagnetic field enhancement associated in both SERS and normal Raman measurements. However, developing a suitable and reliable SERS substrate has always been a difficult task. Several commercial SERS samples have been reported to have significant EFs, high reliability, reproducibility, and long-term stability. Many different substrate geometries, like surface-roughened films, colloidal NPs,[4,5] metal/metal island films,[6,7] metal films with multiple resonances,[8] and nano-cones/nano-rods,[9,10] have been used to achieve the optimal SERS enhancement. All these samples have one thing in common: their SERS effect is based on a basic 2D arrangement of metal NPs. Hence, the detection volume is strongly confined to the surface and the enhanced electric field reaches only a few tens of nanometers (max. 100 nm) into the surrounding medium. This technically renders it obsolete for measurements in liquids, flow measurements, and complex structures such as cells, tissues, or any analyte, which is located inside a material or a medium. This disadvantage can be overcome by using 3D-SERS substrates, which have a carrier particle that can accommodate a high density of metal NPs in 3D.

Silica microspheres (SMPs) are excellent candidates for this purpose and have attracted great attention for their usage in drug delivery,[11] electrochemical sensors,[12,13] and catalysis.[14] The versatile synthesis of SMPs gives the flexibility to tailor their properties like size, shape, and porosity.[13,15,16] The tuning of the porosity allows to control pore size and pore volume, and their surface can be chemically modified by different functional groups.[14,15] This physical and chemical flexibility allows to optimize the properties to immobilize metal NPs on their surface.[17] A combination of SMPs and noble metal NPs, wherein the functionalized SMP can act as a microcarrier for metal NPs, may provide a promising new concept for 3D-SERS substrates.

Received: April 11, 2023
Revised: June 19, 2023
Published: July 6, 2023

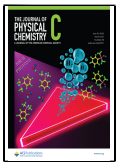

There have been prior reports of functionalized silica and polystyrene particles decorated with silver and Au NPs for SERS measurements.[18−24] Several techniques have been used to immobilize the metal NPs onto these particles, such as in situ chemical reaction/reduction with long and complex fabrication procedures, seeded growth, lab-on-a-bubble, colloidal self-assembly, and colloid synthesis. While these techniques have demonstrated several advantages, it is worth noting that they also come with certain limitations. These may include longer and more intricate fabrication procedures, the formation of larger agglomerates of base particles, challenges in ease of preparation, variable plasmonic responses along the substrate, and potential reproducibility issues.

In this paper, we present a simple technique for covering functionalized SMPs with silver and Au NPs. To deposit metal NPs on bare SMPs, two methods were used: Tollens' reagent for silver and sputtering for Au. The surface morphology of the functionalized SMPs was investigated by electron microscopy, and the elemental composition was determined by energy-dispersive X-ray spectroscopy (EDX). The optical properties were characterized by light scattering, which allows to observe resonances of the bare and functionalized SMPs and enables to draw conclusions about their homogeneity. Finally, the silver- and Au-functionalized SMPs were tested for their SERS activity to provide conclusive results.

Prior research has showcased the fabrication and synthesis of silica or polystyrene spheres functionalized with plasmonic metal NPs for various applications such as electrochemical sensors, SERS substrates, and optical probes.[21,25−28] In contrast, our work distinguishes itself by introducing a simple and straightforward preparation method, where metal NPs are directly grown on silica spheres without the need of any seed particles. This approach leads to different particle and gap sizes, offering the advantage that one SMP exhibits plasmon resonances covering the visible and near-infrared spectral region. Moreover, the research demonstrates the visualization of nanoscale spatial distribution of hotspots on the 3D SERS substrate through SERS imaging, providing valuable insights into the arrangement of metal NPs on SMPs. Such functionalized SMPs can be used as microcarriers and provide a stable substrate where the SERS active metal NPs are attached to the surface. Due to spherical symmetry of the microcarriers, the metal NPs can be excited regardless of the orientation of the microcarriers relative to the excitation focus. Another significant advantage of these metal-carrying microcarriers is that they possess many open gaps between the metal NPs, where analytes can be efficiently detected using gap mode SERS. The main advantage is that they can penetrate or enter a 3D material, e.g., a solution, cells, and tissues, and allow to bring the SERS substrate to the region of interest, and the detection is not limited to the surface. Hence, SERS information can be extracted from within the sample increasing the depth information, which is not accessible in conventional 2D SERS.

MATERIALS AND METHODS

Fabrication of Mercapto-Functionalized SMPs. The SMPs were prepared according to a protocol for previously reported silica particles with similar morphology but different functionalization.[29,30] A solution containing 115 mL of water and 0.266 mL of aqueous ammonium hydroxide (NH_4OH) is stirred continuously for 40 min. A syringe pump is used to add 2.6 mL of a mixture of tetraethoxysilane (TEOS) and mercapto-trimethoxysilane (MerTMS) with a ratio of 22 mmol:88.3 mmol. The amount and composition of this mixture allows to control the shape, size, and morphology of particles. After adding the silane mixture, the solution was stirred at room temperature for 14 h. As the solvent is removed, the particles were washed with water and ethanol and dried in an oven at 70 °C for 16 h.

Synthesizing SMPs with Metal NPs. *Tollens' Reagent (Silver—Ag).* Tollens' reagent precipitates elemental Ag producing a Ag mirror on a surface. Silver nitrate ($AgNO_3$) 53.0 mg−312 μmol, aqueous ammonia solution (NH_3) 25%−380 μL, and saturated aqueous D-(−)-fructose solution (2.0 mL) were dissolved in 3 mL of deionized water. Subsequently, one small pellet of NaOH was added and stirred until all the content was visibly dissolved. 500 μL of this resulting solution was added to an Eppendorf tube containing mercapto-functionalized SMPs and was stirred continuously to allow Tollens' reagent to uniformly react with the complete surface area. The Eppendorf tube containing the freshly synthesized particles was allowed to rest for 1 min at room temperature to avoid agglomerations. Afterwards, the Eppendorf tube was placed in an ice bath to stop the chemistry and the contents were washed with deionized water.

Sputtering (Au). Sputtering deposition is a physical vapor deposition method to create thin films. This involves the ejection of material from a target onto a substrate by ion or atom bombardment. An SCD 030 sputtering system from Balzers (Balzers, Liechtenstein) was used, and the sputtering target was a circular Au disk. The deposited Au atoms form a thin film on the SMPs (substrate). The sputtering rate was 9 Å/s for a sputtering time of 30 s, yielding a nominal film thickness of approximately 25 nm.

SERS Experiments. A commercial microscope from WITec (Oxford Instruments) alpha300RAandS was used. For excitation, a diode laser at 532 nm with a nominal output power of 40 mW and a helium−neon laser at 633 nm with an output power of 25 mW were used. Illumination and collection of the detected signal were both carried out from the top by an objective lens (Carl Zeiss; EC Epiplan-Neofluar DIC M27, 100×, NA = 0.9). The detected signal is guided by multi-mode fibers with different diameters to the spectrometer. The diameter (10, 25, 50, and 100 μm all with an NA = 0.12) of these fibers determines the confocal pinhole size. For detection, the microscope is equipped with a lens-based ultra-high-throughput spectrometer (UHTS 300) with a thermoelectrically cooled (down to −60°C) back-illuminated CCD and an EMCCD (Andor DU970N-BV).[31] All SERS experiments were performed using a 600 L/mm grating since it offers a wide spectral range. Data processing for all the above measurements was done using Control 5.0 software provided by WITec, and all experiments were carried out under ambient conditions.

SERS experiments were performed with methylene blue (MB) with a concentration of 3.5×10^{-4} M. MB exhibits an absorption peak at 665 nm along with a smaller peak at 610 nm and an additional peak at 293 nm, respectively.[32] For the SERS experiments, droplets of 40 μL were drop cast on the glass substrate containing the SMPs covered with metal NPs and the sample was measured immediately.

Temperature-Dependent Measurements. A THMS600 heating and freezing stage from Linkam Scientific Instruments was coupled with the WITec alpha300RAandS upright microscope. A photograph of the temperature stage integrated

https://doi.org/10.1021/acs.jpcc.3c02410
J. Phys. Chem. C 2023, 127, 13689−13698

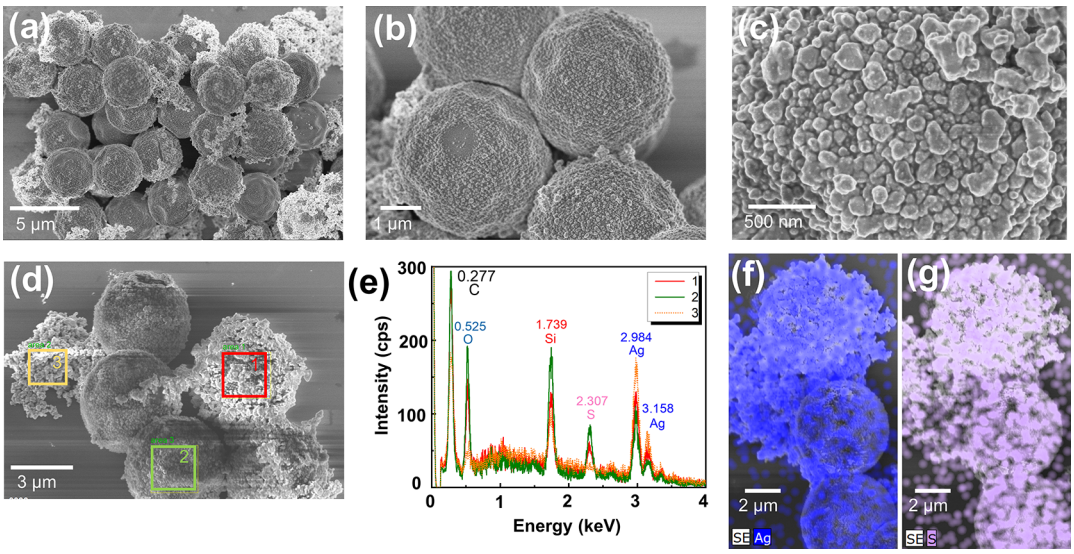

Figure 1. (a, b) SEM images of SMPs treated with Tollens' reagent. (c) Close-up view SEM image of the surface of a SMP. (d) SEM image of SMPs with marked areas 1 (red), 2 (green), and 3 (orange) for EDX measurements. (e) EDX spectra of areas 1 (red), 2 (green), and 3 (orange) marked in (d). (f) EDX elemental distribution image of silver (at silver (Ag) 2.934 keV) superimposed with the corresponding SEM image, and (g) EDX elemental distribution image of sulfur (at S 2.307 keV) superimposed with SEM image.

in the setup of the microscope is included in the supporting information in Figure S1. The THMS600 offers a wide temperature range from −196 to 600 °C with a temperature rate of up to 150 °C/min heating and temperature stability of 0.1 °C. Furthermore, it includes a 16 mm XY manipulation stage with a sample area of 22 mm diameter. Samples were loaded onto a 0.17 mm-thick cover slip glass and placed on a highly polished pure Ag heating element to ensure heat transfer and sensitive temperature measurements. In this case, spectra were collected using a Carl Zeiss objective EC Epiplan-Neofluar 5x NA = 0.15, with a long working distance to be isolated from the sample stage lid window, which is at a fixed distance from the heating/cooling element.

Scattering Spectroscopy. Scattering spectra were recorded with a Nikon Eclipse Ti-U inverted confocal microscope. The illumination was achieved with a 100 W halogen light bulb. A dark-field condenser (NA 0.85−0.95) directs the light with an angle of 58−72° on the sample. The scattered light is collected by a 60× objective with a NA of 0.7. The collected light was detected by a spectrometer (LOT SR-303i-B) with an Andor iDus CCD camera. All measurements were conducted at room temperature and ambient conditions.

The raw dark-field scattering spectra were corrected using the following equation:

$$\text{scattering} = \frac{T_i - T_0}{T_L - T_D}$$

where T_0 represents the scattered light intensity through a bare glass slide, T_i is the signal intensity of SMPs, T_L is the intensity of the halogen lamp, and T_D is the dark intensity of the spectrometer.

Scanning Electron Microscopy (SEM)−EDX. SEM images were acquired with a HITACHI SU8030 at 2 kV, a secondary electron detector, and an accelerating voltage of 0.5 to 30 kV. EDX was measured by a Bruker detector QUANTAX 6G − Typ 200 attached to the SEM.

RESULTS AND DISCUSSION

Prior to NP deposition, the freshly prepared SMPs were characterized using SEM and EDX to visualize the structural modifications and the elemental distribution as a result of the particle synthesis (data not shown). Then, Ag NPs were deposited on these SMPs with Tollens' reagent. Figure 1 shows the SEM and EDX characterization of these SMPs.

Figure 1a shows a SEM image of a large area containing SMPs covered by NPs deposited with Tollens' reagent. The deposition of Ag NPs on SMPs is very heterogeneous, and the NP density varies for different particles within the same sample. In some SMPs, the density of Ag NPs is high and hence they appear brighter, whereas SMPs with lower density appear darker. The close-up view in Figure 1b shows that the surface of the SMPs is densely covered by NPs. Figure 1c shows a detailed view of the surface of one SMP. The sizes of the Ag NPs vary from 10 to 400 nm, with different shapes for each individual particle. This also leads to a high variability of gap sizes between Ag NPs, which are able to create intense hot spots leading to strong enhancement of the SERS signal. This variety of sizes, shapes, and gaps is beneficial, since it results in different plasmon resonances and allows to efficiently excite different molecules.[8]

The elemental distribution is determined by EDX elemental analysis of the SMPs. Figure 1d shows a SEM image of particles with strongly differing NP distribution. The marked areas 1 (red), 2 (green), and 3 (orange) denote the positions where the EDX spectra in Figure 1e were acquired. It can be seen in Figure 1d that areas 1 (red) and 2 (green) show quite different Ag NP densities whereas area 3 (orange) shows a large agglomeration of Ag NPs. In Figure 1e, the respective EDX spectra are shown. The carbon (C) peak at 0.277 keV is common for all areas, which occurs due to C residuals by the SEM and EDX measurements. Hence, the C peak cannot be avoided and is present in all EDX measurements. The silicon (Si) peak at 1.739 keV originates from the SMPs, as well as from the substrate (a Si wafer used to avoid any charging effects). The peaks at 2.984 and 3.158 keV are caused by Ag

https://doi.org/10.1021/acs.jpcc.3c02410
J. Phys. Chem. C 2023, 127, 13689−13698

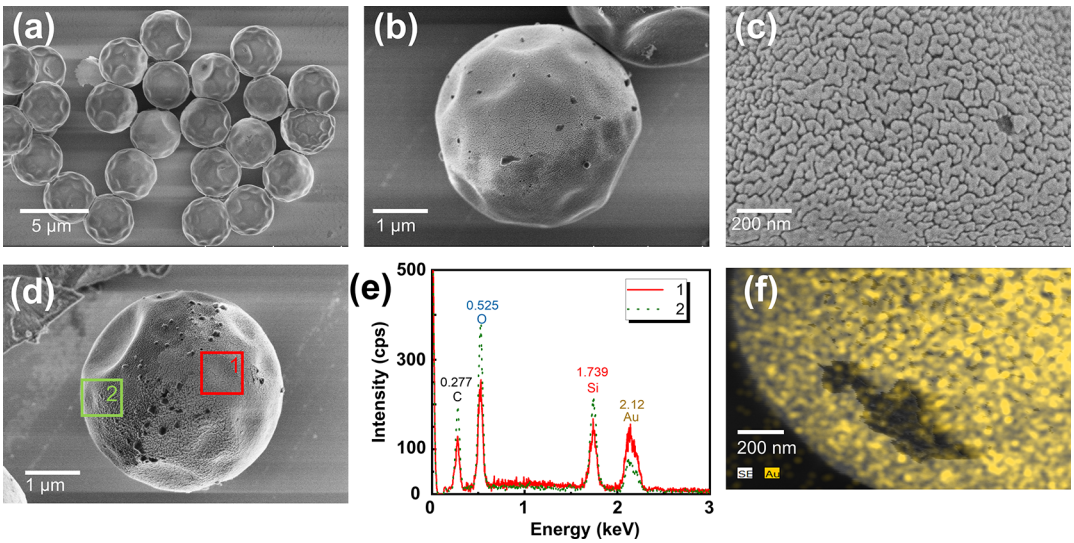

Figure 2. (a, b) SEM images of SMPs sputtered with gold. (c) Close-up view SEM image of the surface of one SMP. (d) SEM image marked with areas 1 (red) and 2 (green) denoting the areas where EDX spectra were acquired. (e) EDX spectra of areas 1 (red) and 2 (green) marked in (d), and (f) EDX elemental distribution image of gold (at gold (Au) 2.12 keV) superimposed with the SEM image.

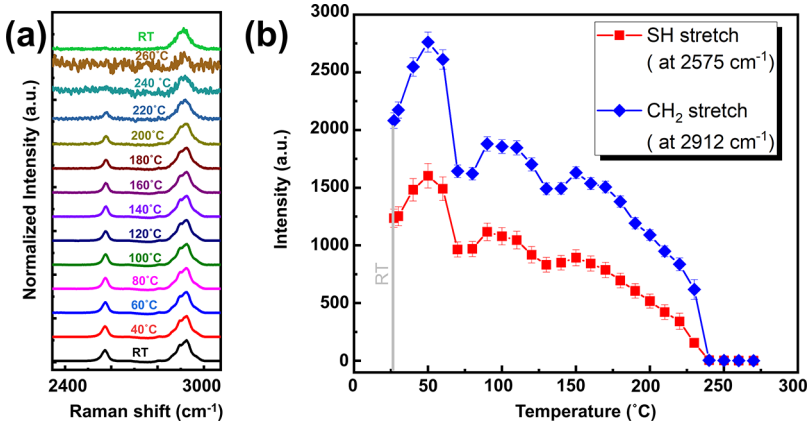

Figure 3. (a) Temperature-dependent Raman spectra of mercapto-functionalized SMPs ranging from room temperature (RT) at 27 to 260 °C normalized to the intensity of the 2912 cm^{-1} peak. (b) Integrated peak intensity of SH stretch (at 2566 cm^{-1})—red graph, and CH_2 stretch (at 2912 cm^{-1})—blue graph as a function of the temperature.

and can be observed in all areas with varying intensities. The highest Ag intensity is found in area 3, because this area consists of an agglomeration of NPs. The intensity of the Ag peak is higher in area 1 than in area 2 because of the larger density of NPs in area 1. The oxygen (O) peak at 0.525 keV and the sulfur (S) peak at 2.307 keV are the main signatures of the SMPs; they are only visible in areas 1 and 2 and absent in area 3. S can be observed in the EDX spectra, since the SMPs are functionalized with mercapto groups to immobilize the NPs. The intensities of the O and S peaks are higher in area 2 than in area 1, because the higher density of NPs in area 1 leads to a stronger shielding of the signal of the substrate SMP, which agrees with the SEM image in Figure 1d. Apart from the abovementioned elements, no other elements were detected in the EDX measurements. Figure 1f and g show superpositions of SEM images and the elemental distribution mapped with EDX for Ag (blue) and S (pink), respectively. These superpositions show that the Ag and S peaks are highly correlated and originate mainly from the SMPs.

Next, NPs were deposited on the SMPs by sputtering with Au. The results are shown in Figure 2.

Figure 2a shows a SEM image of a large area containing SMPs covered by NP sputtered with Au. The close-up view in Figure 2b shows a single SMP sputtered with Au. The brighter areas in the images are covered by Au, and the darker areas are bare SMPs. Sputtering with Au does not uniformly cover the whole surface of SMPs, since Au is only deposited on the side of SMPs exposed to the Au target (shadowing effect). Figure 2c shows a detailed view of the surface of one SMP sputtered with Au. The surface morphology consists of several connected metal islands with small gaps between them. This surface morphology is observed in all SEM images and SMPs alike. The Au deposition is very homogeneous within SMPs. In other words, the morphology of the Au surface of different SMPs is rather similar, unlike depositing Ag by Tollens' reagent where the Ag layer is heterogeneous. Figure 2d shows a SEM image of a single SMP, where the marked areas 1 (red) and 2 (green) denote the positions where the EDX spectra shown in Figure 2e were acquired. The C peak (at 0.227 keV) is a result of residuals from SEM and EDX measurements, and the Si peak (at 1.739 keV) originates from the SMPs and the substrate. The intensity of the O peak (at 0.525 keV) is larger in area 2

https://doi.org/10.1021/acs.jpcc.3c02410
J. Phys. Chem. C 2023, 127, 13689−13698

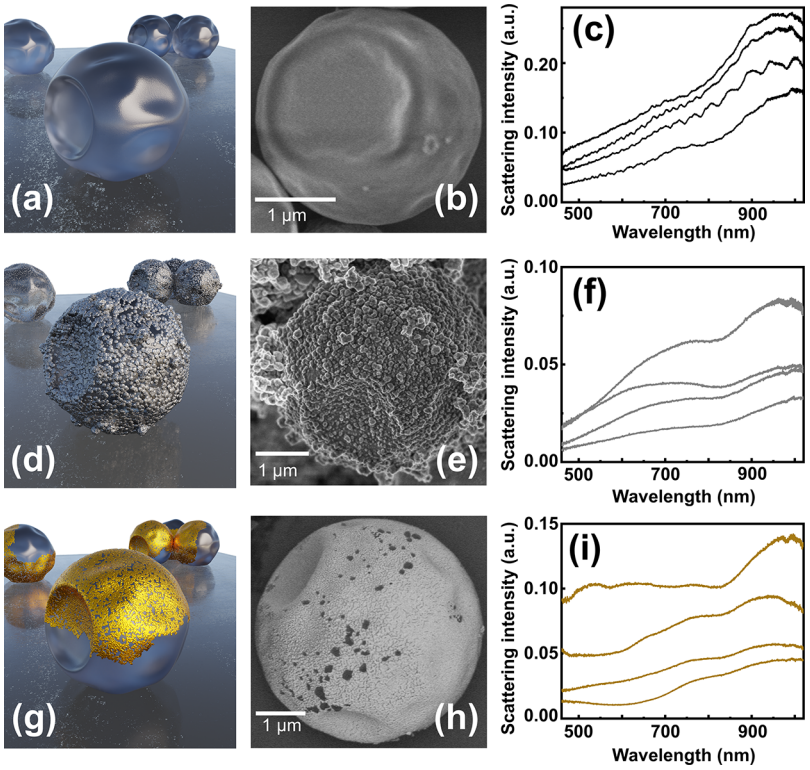

Figure 4. (a) Schematics (not to scale) of mercapto-functionalized bare SMPs. (b) SEM image of a mercapto-functionalized bare SMP. (c) Scattering resonances of several mercapto-functionalized bare SMPs. (d) Schematics (not to scale) of SMPs with silver NPs. (e) SEM image of a SMP with silver NPs. (f) Exemplary scattering spectra of SMPs with silver NPs exhibiting plasmon resonances. (g) Schematics (not to scale) of SMPs with gold NPs. (h) SEM image of a SMP with gold NPs. (i) Some exemplary scattering spectra of SMPs with gold NPs exhibiting plasmon resonances.

compared to area 1, because the density of Au in area 1 is larger, masking the signal of the underlying SMP. The inverse behavior is evident for the Au peak (Au) at 2.12 keV, where its intensity is higher in area 1. Figure 2f shows superimposed images of SEM and elemental distribution mapped by EDX for Au in the same area. Here, it can be seen that Au is uniformly spread across the region and no other elements have been detected. It should be noted that S has not been observed in these measurements, although the same basic mercapto-functionalized SMPs were used. The S peak at 2.307 keV can be observed neither in the shadowed nor in the exposed regions. This suggests that the S bond is breaking during the sputtering process, where the temperatures can rise up to 300 °C. Figure 3 shows temperature-dependent Raman measurements of several bare mercapto-functionalized SMPs.

The temperature was increased from RT at 27 to 270 °C, and Raman spectra were acquired every 10 °C interval. After every 10 °C increase, the temperature was kept constant for a few minutes to reach thermal equilibrium throughout the sample. Figure 3a shows Raman spectra in the spectral range from 2350 to 3050 cm^{-1} at different temperatures with 20 °C intervals. Both visible peaks at 2566 cm^{-1} (SH stretching) and at 2912 cm^{-1} (CH_2 stretch, band of four overlapping peaks) decrease in intensity for increasing temperatures. Since the spectra are normalized to the intensity of the 2912 cm^{-1} peak, this fact becomes apparent from the increasing background noise. The variation of the integrated intensity as a function of temperature for the peak at 2566 cm^{-1} is shown in Figure 2b (red graph). From RT (27 °C) to 50 °C, the intensity of the SH peak increases; this behavior needs further investigation. Afterwards, the intensity steadily decreases for increasing temperatures until reaching a temperature of 220 °C. Above 230 °C, the SH Raman peak is not detectable anymore. The green spectrum in Figure 3a is acquired from the same sample after cooling down back to RT, and the SH Raman peak is not visible anymore. This proves that at high temperatures, the SH bond breaks and the intensity of the SH peak decreases completely. This also explains why no S is detected in the EDX spectra for SMPs sputtered with Au. A similar behavior is observed for the CH_2 stretch peak at 2912 cm^{-1} in the spectra in Figure 3a and the integrated intensity in Figure 3b (blue graph). It has the same trend as that of the SH peak. After cooling down, the CH_2 stretch however can be seen again, but the spectral shape and peak position are altered, indicating that also this bond was chemically altered.

An important parameter for the SERS enhancement is the optical properties of the substrate, since the excitation light needs to efficiently couple to the NPs. The dark-field scattering spectra of bare SMPs as well as SMPs covered with Ag and Au are shown in Figure 4.

Figure 4a shows a schematic representation (not to scale) of bare SMPs with a large dent and several smaller dents on their surface. These dents are common for all the particles that have been fabricated with the method described in the Materials and Methods section. Figure 4b shows a SEM image of a single SMP, and Figure 4c shows the scattering resonances with a maximum at approximately 950 nm for four bare SMPs along with a significantly small shoulder at approx. 720 nm. Since the bare SMPs do not absorb light in this spectral region, the observed signal can mostly be assigned to Mie scattering.[33,34]

https://doi.org/10.1021/acs.jpcc.3c02410
J. Phys. Chem. C 2023, 127, 13689−13698

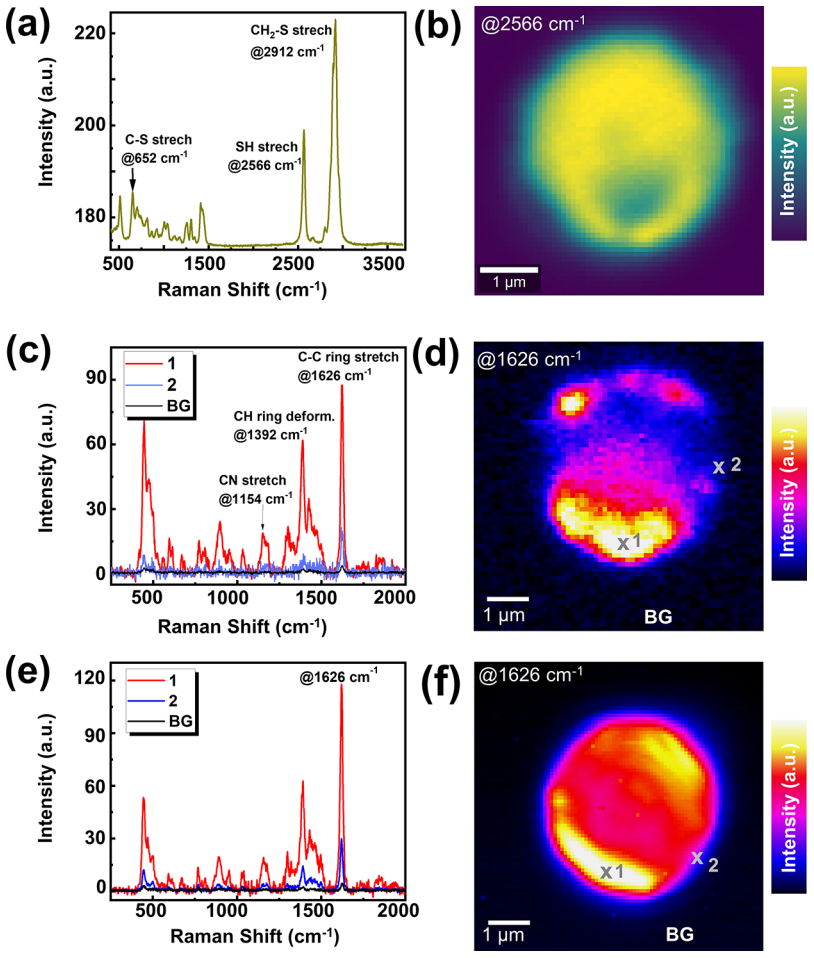

Figure 5. (a) Raman spectrum of mercapto-functionalized SMPs. (b) Confocal Raman imaging of bare SMPs functionalized with mercapto groups for the SH peak (at 2566 cm^{-1}). (c) SERS spectra of MB for the positions marked in (d) for hotspot (1—bright regions), hotspot (2—low-intensity regions), and glass substrate (BG—absence of any metal NPs). (d) SERS imaging of SMPs with silver NPs (excitation laser: 633 nm) of MB analytes (at 1626 cm^{-1}: C−C ring stretch) marked with areas 1 and 2, and glass substrate (BG). (e) SERS spectra of MB for the positions marked in (f) for hotspot (1—bright regions), hotspot (2—low-intensity regions), and glass substrate (BG—absence of any metal NPs) (excitation laser: 633 nm). (f) SERS imaging of SMPs with Au NPs (excitation laser: 633 nm) of MB analyte (at 1626 cm^{-1}: C−C ring stretch) marked with areas 1, 2, and substrate.

Figure 4d and e show a schematic representation and a SEM image of SMPs covered with Ag NPs, respectively. The particles display a diverse range of surface morphologies, which is evident from the SEM images shown in Figure 1. This heterogeneity will lead to different plasmon resonances at different spatial locations on the SMP. Figure 4f shows that the particles exhibit multiple broad plasmon resonances that span a wavelength range of 600 to 750 nm. In all spectra, the underlying SMP displays a scattering maximum at approx. 950 nm, which is consistent. However, several additional resonances at around 620, 660, 700, and 750 nm can also be observed. This resonance can be assigned to the plasmon resonance of the Ag NPs. Typically, the plasmon resonance of a Ag sphere with a size of 10 nm (diameter) is spectrally located around 392 nm.[35] The presence of multiple plasmon resonances across a spectral range of 600 to 750 nm indicates that there are tiny gaps between adjacent Ag NPs or variations in the size/shape of the NPs themselves. However, such an extensive spectral redshift of the plasmon resonance suggests that there is significant coupling between the NPs.[36,37] Previous studies have documented the presence of plasmon resonances of Ag NPs in similar systems, with peak wavelengths ranging from 420 to 530 nm and occasionally up to 800 nm. This has been attributed to a strong coupling between NPs, resulting in a red-shifted peak wavelength.[38] This coupling is very beneficial for SERS, since it creates strong electromagnetic fields in the gaps leading to intense hot spots. Since the NPs exhibit a broad range of plasmon resonance wavelengths, this allows for the enhanced detection of multiple molecules on a single substrate.[8] This attribute makes these particles particularly useful for fast screening of molecules within a single sample, as it is to be expected that multiple analytes can be detected simultaneously. Such an ability could significantly enhance the efficiency of sample analysis and make it a valuable tool in various fields such as biomedical research and environmental monitoring. Figure 4g and h show a schematic representation and a SEM image of SMPs sputtered with Au, respectively. The scattering resonance of the particles is displayed in Figure 4i, and in contrast to Ag, these particles exhibit a regular plasmon resonance at approximately 760 nm, which is visible in all spectra. The peak at 760 nm can be attributed to the plasmon resonance of the Au film, and interestingly, it is consistent across all the particles despite the observed intra-particle heterogeneity in

https://doi.org/10.1021/acs.jpcc.3c02410
J. Phys. Chem. C 2023, 127, 13689−13698

the SEM images. The detection of few other resonances at higher energies around 530/630/650 nm is apparent in certain spectra. Typically, the plasmon resonance of a Au sphere with a size of 10 nm (diameter) is spectrally located at 520 nm.[39] The plasmon resonance detected at 530 nm suggests the existence of isolated spherical Au particles on the SMP that are relatively small. Similarly to SMPs covered with Ag NPs, the redshift of the plasmon resonance to 760 nm suggests that there are several small gaps between the Au islands leading to coupling between them.[36,37] Furthermore, the scattering resonance of the uncoated SMPs is also visible at 950 nm and it remains consistent across all spectra.

The bare SMPs were further characterized with confocal Raman imaging and spectroscopy. The results are summarized in Figure 5. Figure 5a shows a typical Raman spectrum of mercapto-functionalized SMPs. The strong band at 2566 cm^{-1} is assigned to the SH stretching mode of the mercaptopropyl group of the SMP.[40] The C−S stretching mode is found at 652 cm^{-1} in SMPs. The CH_2 wagging modes for the propylene bridge between the silicate and the S, CH_2−Si, and CH_2−S are observed in the SMPs at 1305 and 1264 cm^{-1}. The peak at 2912 cm^{-1} is assigned to the CH_2 stretch.[41,42] Figure 5b shows the spatially resolved intensity of the SH stretch at 2566 cm^{-1} of the functionalized SMP. The intensity varies across the whole SMP, suggesting that the density of SH groups is lower in some regions that might be associated with the dented regions of those particles.

For SERS analysis, the analyte used here was MB. Figure 5c shows the SERS spectra of MB at three different spatial positions on the SMP covered with Ag NPs measured with a 633 nm excitation laser. The fluorescence background of MB has been removed from all spectra. The most intense Raman peaks for MB are the C−C ring stretch at 1626 cm^{-1}, the C−H in-plane ring deformation at 1388 cm^{-1}, and the C−N asymmetric and symmetric stretching at 1441 and 1154 cm^{-1}, respectively. It should be noted that the SERS spectra are dominated by MB and no evident signals from the SMP are visible. For SERS imaging, the most intense Raman peak of MB, which is the C−C ring stretch at 1626 cm^{-1}, is considered. Spectrum 1 (red) is from a hotspot (position × 1), while spectrum 2 (blue) is from the low-intensity region (position × 2). The black spectrum is an average spectrum acquired from the glass substrate (BG), which is also covered with MB. The most intense MB peak at 1626 cm^{-1} was significantly enhanced at the hotspot, compared to the glass substrate (BG). Besides the SERS effect, the Raman signal is enhanced by the resonance Raman effect, since MB has an absorption maximum at 665 nm, which is spectrally close to the 633 nm excitation laser wavelength.[43] Figure 5d shows the spatial distribution of the integrated signal of the most intense peak at 1626 cm^{-1} (C−C ring stretch). Here, it can be seen that the edges of the SMP show enhancement of the MB peak, because the plane of excitation is set to be in the center of the SMP and Ag is only deposited on its surface. Furthermore, the intensity is not homogenous and shows certain bright regions at the edges. The ratio between the spectral intensity of the 1626 cm^{-1} peak at the bright region and on the glass substrate can be termed EF:

$$\mathrm{EF} = \frac{I_{\mathrm{Hotspot}}}{I_{\mathrm{Substrate}}},$$

where I_{Hotspot} is the spectral intensity of a certain peak at the bright regions and $I_{\mathrm{Substrate}}$ is the spectral intensity of the same peak on the substrate (glass slide) in the absence of any metal NPs. The reason behind deliberately employing the aforementioned method to calculate the SERS EF, as shown above, stems from the inherent difficulties in accurately estimating the number of molecules present within a given spot, which can be influenced by factors such as molecule accumulation. This approach aligns with previous publications that have also utilized similar SERS EF calculations.[44−47] The EF for SERS on SMPs with Ag NPs with MB as analyte and 633 nm excitation laser was calculated to reach up to 24. The second SMP type is sputtered with Au NPs, and the results of SERS with these particles are summarized in Figure 5e,f. Figure 5e shows the SERS spectra of MB at three different positions. Spectrum 1 (red) is from the region with highest intensity (position 1), spectrum 2 (blue) is from the lower-intensity region (position 2), and the black spectrum is the average signal from the glass substrate (BG), which is glass covered with MB. All the abovementioned positions are marked in Figure 5f. When comparing the spectrum at the most intense region to that on the glass substrate, it can be seen that all peaks of MB are significantly enhanced. Figure 5f shows the spatial intensity distribution of the MB peak at 1626 cm^{-1} (C−C ring stretch). Here, it can be seen that the edges of the SMP show enhancement of the MB peak, since the surface of the SMP is covered with Au and the plane of excitation is set to the center of the SMP. Furthermore, the strongest intensity can be observed when the electric field of the excitation beam is parallel to the surface of the Au film, leading to the double-lobed shape of the image. This distinction in the intensity can also be seen in their corresponding spectra acquired at the most intense region (1, red) and the less intense region (2, blue) in Figure 5e. The EF for SERS with SMPs covered with Au NPs, MB as an analyte, and 633 nm excitation laser was calculated to be up to 26.

The application of the 3D SERS substrates, specifically in solution, will be reported in an upcoming publication.

CONCLUSIONS

The manuscript details the successful fabrication of three-dimensional (3D) SERS substrates based on SMPs using a two-step fabrication process. In the first step, base particles or SMPs were synthesized using sol−gel synthesis and functionalized with mercapto groups. In the second step, noble metal NPs were synthesized and deposited on the SMP surface. Confocal Raman imaging was used to confirm the uniform distribution of mercapto groups on the surface of the SMPs and in the bulk, with the exception of areas with deformations or dents. Temperature-dependent Raman measurements showed that mercapto groups are unstable at temperatures above 220 °C, as the mercapto bonds break, and the Raman signal of the mercapto groups becomes undetectable.

To deposit Ag NPs, Tollens' reagent was used in the first approach. SEM images revealed that the deposition of Ag NPs was random and the size the of NPs ranged from 10 to 400 nm. We observed inter-particle heterogeneity, meaning the deposition of Ag varied for different SMPs within the same batch. The scattering spectra of these particles indicated the presence of multiple, broad plasmon resonance peaks spanning a wavelength range from 550 to 800 nm.

In the second approach, sputtering was used to deposit Au NPs. SEM images revealed that the surface consisting of

https://doi.org/10.1021/acs.jpcc.3c02410
J. Phys. Chem. C 2023, 127, 13689−13698

connected Au islands with small gaps between them. We observed intra-particle heterogeneity, meaning that the deposition of Au varied within the SMP. Analysis of the particles' scattering spectra indicated that they possessed a uniform distribution of Au within the sample, as evidenced by a consistent comparably narrow plasmon resonance peak at 730 nm.

For SERS, MB was used as an analyte, and both types of SMPs showed enhancement of the MB Raman signal. It was noted that the EF, which is the intensity ratio of the MB signal in bright regions and on the substrate, showed an enhancement of the Raman signal by a factor up to 25.

The spherical shape of the 3D-SERS substrates offers advantages over classical 2D surface-based SERS substrates. Due to their spherical geometry, they can be excited regardless of their orientation relative to the excitation laser. Additionally, they open up many new possibilities to apply SERS for various new types of samples, as SERS with SMPs is not limited to a surface. For example, they can be used floating in solution or can be incorporated into a cell or tissue. The ability to use the SMPs in a variety of sample types, including cells and tissues, allows for further exploration of SERS in biological and medical applications.

■ ASSOCIATED CONTENT

Supporting Information

The Supporting Information is available free of charge at https://pubs.acs.org/doi/10.1021/acs.jpcc.3c02410.

Photograph of the WITec alpha300RAandS upright microscope fitted with Linkam Scientific instruments' THMS600 heating and freezing stage and schematic of the optical path of the WITec alpha300RAandS upright microscope fitted with Linkam Scientific instruments' THMS600 heating and freezing stage with all the labeled parts, path, and components (PDF)

■ AUTHOR INFORMATION

Corresponding Authors

Frank Wackenhut − *Center for Process Analysis and Technology (PA&T), School of Life Sciences and Reutlingen Research Institute (RRI), Reutlingen University, Reutlingen 72762, Germany;* orcid.org/0000-0001-6554-6600; Email: Frank.Wackenhut@reutlingen-university.de

Marc Brecht − *Center for Process Analysis and Technology (PA&T), School of Life Sciences and Reutlingen Research Institute (RRI), Reutlingen University, Reutlingen 72762, Germany; Institute of Physical and Theoretical Chemistry, Eberhard Karls University of Tübingen, Tübingen 72076, Germany; Center for Light-Matter Interaction, Sensors and Analytics (LISA$^+$), University of Tübingen, Tübingen 72076, Germany*; Email: Marc.Brecht@reutlingen-university.de

Authors

Ashutosh Mukherjee − *Center for Process Analysis and Technology (PA&T), School of Life Sciences and Reutlingen Research Institute (RRI), Reutlingen University, Reutlingen 72762, Germany; Institute of Physical and Theoretical Chemistry, Eberhard Karls University of Tübingen, Tübingen 72076, Germany;* orcid.org/0000-0002-8162-598X

Akanksha Dohare − *Institute of Inorganic Chemistry, Eberhard Karls University of Tubingen, Tübingen 72076, Germany;* orcid.org/0000-0003-2996-7410

Anke Horneber − *Institute for Applied Physics and Center for Light-Matter Interaction, Sensors and Analytics (LISA$^+$), University of Tübingen, Tübingen 72076, Germany*

Anita Lorenz − *Center for Process Analysis and Technology (PA&T), School of Life Sciences and Reutlingen Research Institute (RRI), Reutlingen University, Reutlingen 72762, Germany;* orcid.org/0000-0003-4658-9036

Hendrik Müchler − *Center for Process Analysis and Technology (PA&T), School of Life Sciences, Reutlingen University, Reutlingen 72762, Germany*

Alfred J. Meixner − *Institute of Physical and Theoretical Chemistry, Eberhard Karls University of Tübingen, Tübingen 72076, Germany; Center for Light-Matter Interaction, Sensors and Analytics (LISA$^+$), University of Tübingen, Tübingen 72076, Germany;* orcid.org/0000-0002-0187-2906

Hermann A. Mayer − *Institute of Inorganic Chemistry, Eberhard Karls University of Tubingen, Tübingen 72076, Germany;* orcid.org/0000-0002-8263-4255

Complete contact information is available at: https://pubs.acs.org/10.1021/acs.jpcc.3c02410

Notes

The authors declare no competing financial interest.

■ ACKNOWLEDGMENTS

The authors disclose receipt of the following financial support for the research, authorship, and publication of this article: A.M., A.L., and M.B. would like to acknowledge financial support within the framework IngenieurNachwuchs 2016 (project: CompeTERS) by the German Federal Ministry of Education and Research (BMBF; Grant no. 13FH596IX6). A.D. was supported by a National Overseas Scholarship and is thankful to the Government of India for financial support. The authors would like to thank Elke Nadler of the Eberhard Karls University in Tübingen for her assistance in obtaining SEM images and EDX measurements. The authors would also like to thank Prof. Dr. Monika Fleischer, Institute for Applied Physics, Eberhard Karls University of Tübingen, for fruitful discussions and valuable inputs to this manuscript and for access to the dark-field scattering spectroscopy setup.

■ REFERENCES

(1) Fleischmann, M.; Hendra, P. J.; McQuillan, A. J. Raman spectra of pyridine adsorbed at a silver electrode. *Chem. Phys. Lett.* **1974**, *26*, 163−166.

(2) Lassiter, J. B.; Aizpurua, J.; Hernandez, L. I.; Brandl, D. W.; Romero, I.; Lal, S.; Hafner, J. H.; Nordlander, P.; Halas, N. J. Close encounters between two nanoshells. *Nano Lett.* **2008**, *8*, 1212−1218.

(3) Félidj, N.; Aubard, J.; Lévi, G.; Krenn, J. R.; Schider, G.; Leitner, A.; Aussenegg, F. R. Enhanced substrate-induced coupling in two-dimensional gold nanoparticle arrays. *Phys. Rev. B* **2002**, *66*, 51.

(4) Baia, M.; Toderas, F.; Baia, L.; Popp, J.; Astilean, S. Probing the enhancement mechanisms of SERS with p-aminothiophenol molecules adsorbed on self-assembled gold colloidal nanoparticles. *Chem. Phys. Lett.* **2006**, *422*, 127−132.

(5) Macias, G.; Alba, M.; Marsal, L. F.; Mihi, A. Surface roughness boosts the SERS performance of imprinted plasmonic architectures. *J. Mater. Chem. C* **2016**, *4*, 3970−3975.

(6) Aroca, R.; Martin, F. Tuning metal island films for maximum surface-enhanced Raman scattering. *J. Raman Spectrosc.* **1985**, *16*, 156−162.

(7) Royer, P.; Goudonnet, J. P.; Warmack, R. J.; Ferrell, T. L. Substrate effects on surface-plasmon spectra in metal-island films. *Phys. Rev. B* **1987**, *35*, 3753−3759.
(8) Mukherjee, A.; Liu, Q.; Wackenhut, F.; Dai, F.; Fleischer, M.; Adam, P.-M.; Meixner, A. J.; Brecht, M. Gradient SERS Substrates with Multiple Resonances for Analyte Screening: Fabrication and SERS Applications. *Molecules* **2022**, *27*, 5097.
(9) Novák, J.; Laurenčíková, A.; Eliáš, P.; Hasenöhrl, S.; Sojková, M.; Dobrocka, E.; Kováč, J.; Ďurišová, J.; Pudiš, D. Nanorods and nanocones for advanced sensor applications. *Appl. Surf. Sci.* **2018**, *461*, 61−65.
(10) Skwierczyńska, M.; Woźny, P.; Runowski, M.; Kulpiński, P.; Lis, S. Optically active plasmonic cellulose fibers based on Au nanorods for SERS applications. *Carbohydr. Polym.* **2022**, *279*, No. 119010.
(11) Dohare, A.; Sudhakar, S.; Brodbeck, B.; Mukherjee, A.; Brecht, M.; Kandelbauer, A.; Schäffer, E.; Mayer, H. A. Anisotropic and Amphiphilic Mesoporous Core-Shell Silica Microparticles Provide Chemically Selective Environments for Simultaneous Delivery of Curcumin and Quercetin. *Langmuir* **2021**, *37*, 13460−13470.
(12) Gupta, R.; Rastogi, P. K.; Ganesan, V.; Yadav, D. K.; Sonkar, P. K. Gold nanoparticles decorated mesoporous silica microspheres: A proficient electrochemical sensing scaffold for hydrazine and nitrobenzene. *Sens. Actuators, B* **2017**, *239*, 970−978.
(13) Walcarius, A. Mesoporous Materials-Based Electrochemical Sensors. *Electroanalysis* **2015**, *27*, 1303−1340.
(14) Dai, X.; Qiu, F.; Zhou, X.; Long, Y.; Li, W.; Tu, Y. Amino-functionalized MCM-41 for the simultaneous electrochemical determination of trace lead and cadmium. *Electrochim. Acta* **2014**, *144*, 161−167.
(15) Kobler, J.; Möller, K.; Bein, T. Colloidal suspensions of functionalized mesoporous silica nanoparticles. *ACS Nano* **2008**, *2*, 791−799.
(16) Pal, M.; Ganesan, V. Electrocatalytic activity of cobalt Schiff base complex immobilized silica materials towards oxygen reduction and hydrazine oxidation. *Catal. Sci. Technol.* **2012**, *2*, 2383.
(17) Gupta, R.; Ganesan, V. Gold Nanoparticles Immobilized Mesoporous Silica Material as Cathodic Electrocatalyst in Fuel Cells. *Energy Environ.* **2015**, *4*, 209−213.
(18) Cai, W.; Wang, W.; Lu, L.; Chen, T. Coating sulfonated polystyrene microspheres with highly dense gold nanoparticle shell for SERS application. *Colloid Polym. Sci.* **2013**, *291*, 2023−2029.
(19) Lupa, D.; Oćwieja, M.; Piergies, N.; Baliś, A.; Paluszkiewicz, C.; Adamczyk, Z. Gold nanoparticles deposited on silica microparticles - Electrokinetic characteristics and application in SERS. *Colloid Interface Sci. Commun.* **2019**, *33*, No. 100219.
(20) Schmit, V. L.; Martoglio, R.; Scott, B.; Strickland, A. D.; Carron, K. T. Lab-on-a-bubble: synthesis, characterization, and evaluation of buoyant gold nanoparticle-coated silica spheres. *J. Am. Chem. Soc.* **2012**, *134*, 59−62.
(21) Wu, J.; Chen, S.; Jia, W. Robust phase transfer, 3D-assembly and SERS application of multi-shaped gold nanoparticles. *J. Dispersion Sci. Technol.* **2021**, *42*, 824−834.
(22) Wang, W.; Ruan, C.; Gu, B. Development of gold-silica composite nanoparticle substrates for perchlorate detection by surface-enhanced Raman spectroscopy. *Anal. Chim. Acta* **2006**, *567*, 121−126.
(23) Zhao, W.; Xiao, S.; Zhang, Y.; Pan, D.; Wen, J.; Qian, X.; Wang, D.; Cao, H.; He, W.; Quan, M.; et al. Binary "island" shaped arrays with high-density hot spots for surface-enhanced Raman scattering substrates. *Nanoscale* **2018**, *10*, 14220−14229.
(24) Zhu, W.; Wu, Y.; Yan, C.; Wang, C.; Zhang, M.; Wu, Z. Facile Synthesis of Mono-Dispersed Polystyrene (PS)/Ag Composite Microspheres via Modified Chemical Reduction. *Materials* **2013**, *6*, 5625−5638.
(25) Li, J.-M.; Ma, W.-F.; Wei, C.; Guo, J.; Hu, J.; Wang, C.-C. Poly(styrene-co-acrylic acid) core and silver nanoparticle/silica shell composite microspheres as high performance surface-enhanced Raman spectroscopy (SERS) substrate and molecular barcode label. *J. Mater. Chem.* **2011**, *21*, 5992.
(26) Li, J.-M.; Ma, W.-F.; Wei, C.; You, L.-J.; Guo, J.; Hu, J.; Wang, C.-C. Detecting trace melamine in solution by SERS using Ag nanoparticle coated poly(styrene-co-acrylic acid) nanospheres as novel active substrates. *Langmuir* **2011**, *27*, 14539−14544.
(27) Zhao, Y.; Liu, X.; Lei, D. Y.; Chai, Y. Effects of surface roughness of Ag thin films on surface-enhanced Raman spectroscopy of graphene: spatial nonlocality and physisorption strain. *Nanoscale* **2014**, *6*, 1311−1317.
(28) Jensen, R. A.; Sherin, J.; Emory, S. R. Single nanoparticle based optical pH probe. *Appl. Spectrosc.* **2007**, *61*, 832−838.
(29) Yang, H.; Lu, X.; Xin, Z. One-Step Synthesis of Nonspherical Organosilica Particles with Tunable Morphology. *Langmuir* **2018**, *34*, 11723−11728.
(30) Zhou, Q.; Xiang, H.; Fan, H.; Yang, X.; Zhao, N.; Xu, J. Facile fabrication of golf ball-like hollow microspheres of organic-inorganic silica. *J. Mater. Chem.* **2011**, *21*, 13056.
(31) Mukherjee, A.; Lorenz, A.; Brecht, M. Determination and Monitoring of Quality Parameters: A Detailed Study of Optical Elements of a Lens-Based Raman Spectrometer. *Appl. Spectrosc.* **2021**, *76*, 199−206.
(32) Selvam, S.; Sarkar, I. Bile salt induced solubilization of methylene blue: Study on methylene blue fluorescence properties and molecular mechanics calculation. *J. Pharm. Anal.* **2017**, *7*, 71−75.
(33) Heinisch, R. L.; Bronold, F. X.; Fehske, H. Mie scattering by a charged dielectric particle. *Phys. Rev. Lett.* **2012**, *109*, No. 243903.
(34) Sudiarta, I. W.; Chylek, P. Mie-scattering formalism for spherical particles embedded in an absorbing medium. *J. Geophys. Res. Atmos.* **2001**, *18*, 1275−1278.
(35) Paramelle, D.; Sadovoy, A.; Gorelik, S.; Free, P.; Hobley, J.; Fernig, D. G. A rapid method to estimate the concentration of citrate capped silver nanoparticles from UV-visible light spectra. *Analyst* **2014**, *139*, 4855−4861.
(36) Batson, P. E. Surface Plasmon Coupling in Clusters of Small Spheres. *Phys. Rev. Lett.* **1982**, *49*, 936−940.
(37) Funston, A. M.; Novo, C.; Davis, T. J.; Mulvaney, P. Plasmon coupling of gold nanorods at short distances and in different geometries. *Nano Lett.* **2009**, *9*, 1651−1658.
(38) Liu, T.; Li, D.; Yang, D.; Jiang, M. An improved seed-mediated growth method to coat complete silver shells onto silica spheres for surface-enhanced Raman scattering. *Colloids Surf.* **2011**, *387*, 17−22.
(39) Link, S.; El-Sayed, M. A. Size and Temperature Dependence of the Plasmon Absorption of Colloidal Gold Nanoparticles. *J. Phys. Chem. B* **1999**, *103*, 4212−4217.
(40) Okabayashi, H.; Izawa, K.; Yamamoto, T.; Masuda, H.; Nishio, E.; O'Connor, C. J. Surface structure of silica gel reacted with 3-mercaptopropyltriethoxysilane and 3-aminopropyltriethoxysilane: formation of the S-S bridge structure and its characterization by Raman scattering and diffuse reflectance Fourier transform spectroscopic studies. *Colloid Polym. Sci.* **2002**, *280*, 135−145.
(41) Möller, K.; Kobler, J.; Bein, T. Colloidal suspensions of mercapto-functionalized nanosized mesoporous silica. *J. Mater. Chem.* **2007**, *17*, 624−631.
(42) Socrates, G. *Infrared and Raman characteristic group frequencies:Tables and charts*, 3rd ed.; John Wiley & Sons LTD, 2015.
(43) Fernández-Pérez, A.; Marbán, G. Visible Light Spectroscopic Analysis of Methylene Blue in Water; What Comes after Dimer? *ACS Omega* **2020**, *5*, 29801−29815.
(44) Ansar, S. M.; Li, X.; Zou, S.; Zhang, D. Quantitative Comparison of Raman Activities, SERS Activities, and SERS Enhancement Factors of Organothiols: Implication to Chemical Enhancement. *J. Phys. Chem. Lett.* **2012**, *3*, 560−565.
(45) Etchegoin, P. G.; Meyer, M.; Blackie, E.; Le Ru, E. C. Statistics of single-molecule surface enhanced Raman scattering signals: fluctuation analysis with multiple analyte techniques. *Anal. Chem.* **2007**, *79*, 8411−8415.

https://doi.org/10.1021/acs.jpcc.3c02410
J. Phys. Chem. C 2023, 127, 13689−13698

10. Three-Dimensional (3D) Surface-Enhanced Raman Spectroscopy (SERS) Substrates for Sensing Low Concentration Molecules in Solution

Ashutosh Mukherjee[1,2,3], Frank Wackenhut[1,2,], Alfred J. Meixner[3,4], Hermann A. Mayer[5] and Marc Brecht[1,2,3,4,*]*

[1] Center for Process Analysis and Technology (PA&T), School of Life Sciences, Reutlingen University, Reutlingen, Germany

[2] Reutlingen Research Institute (RRI), Reutlingen University, Reutlingen, Germany

[3] Institute of Physical and Theoretical Chemistry, Eberhard Karls University of Tübingen, Tübingen, Germany

[4] Center for Light-Matter-Interaction, Sensors and Analytics (LISA$^+$), University of Tübingen, Tübingen, Germany

[5] Institute of Inorganic Chemistry, Eberhard Karls University of Tubingen, Tubingen, Germany.

This chapter was originally published in MDPI Nanomaterials as.

Mukherjee, A.; Wackenhut, F.; Meixner, A.J.; Mayer, H.A.; Brecht, M. Three-Dimensional (3D) Surface-Enhanced Raman Spectroscopy (SERS) Substrates for Sensing Low-Concentration Molecules in Solution. Nanomaterials 2024, 14, 21, 1728.

DOI: https://doi.org/10.3390/nano14211728

Supplementary Material/Supporting Information shown in Appendix 6

nanomaterials

MDPI

Article

Three-Dimensional (3D) Surface-Enhanced Raman Spectroscopy (SERS) Substrates for Sensing Low-Concentration Molecules in Solution

Ashutosh Mukherjee [1,2,3], Frank Wackenhut [1,2,*], Alfred J. Meixner [3,4], Hermann A. Mayer [5] and Marc Brecht [1,2,3,4,*]

[1] Center for Process Analysis and Technology (PA&T), School of Life Sciences, Reutlingen University, Alteburgstraße 150, 72762 Reutlingen, Germany; ashutosh.mukherjee@reutlingen-university.de
[2] Reutlingen Research Institute (RRI), Reutlingen University, Alteburgstraße 150, 72762 Reutlingen, Germany
[3] Institute of Physical and Theoretical Chemistry, Eberhard Karls University of Tübingen, Auf der Morgenstelle 18, 72076 Tübingen, Germany; alfred.meixner@uni-tuebingen.de
[4] Center for Light-Matter-Interaction, Sensors and Analytics (LISA+), Eberhard Karls University of Tübingen, Auf der Morgenstelle 15, 72076 Tübingen, Germany
[5] Institute of Inorganic Chemistry, Eberhard Karls University of Tubingen, Auf der Morgenstelle 18, 72076 Tübingen, Germany; hermann.mayer@uni-tuebingen.de
* Correspondence: frank.wackenhut@reutlingen-university.de (F.W.); marc.brecht@reutlingen-university.de (M.B.)

Abstract: The use of surface-enhanced Raman spectroscopy (SERS) in liquid solutions has always been challenging due to signal fluctuations, inconsistent data, and difficulties in obtaining reliable results, especially at very low analyte concentrations. In our study, we introduce a new method using a three-dimensional (3D) SERS substrate made of silica microparticles (SMPs) with attached plasmonic nanoparticles (NPs). These SMPs were placed in low-concentration analyte solutions for SERS analysis. In the first approach to perform SERS in a 3D environment, glycerin was used to immobilize the particles, which enabled high-resolution SERS imaging. Additionally, we conducted time-dependent SERS measurements in an aqueous solution, where freely suspended SMPs passed through the laser focus. In both scenarios, EFs larger than 200 were achieved, which enabled the detection of low-abundance analytes. Our study demonstrates a reliable and reproducible method for performing SERS in liquid environments, offering significant advantages for the real-time analysis of dynamic processes, sensitive detection of low-concentration molecules, and potential applications in biomolecular interaction studies, environmental monitoring, and biomedical diagnostics.

Keywords: surface-enhanced Raman spectroscopy; silica microparticles; SERS substrates; three-dimensional SERS substrates; plasmonics; SERS in solution

Citation: Mukherjee, A.; Wackenhut, F.; Meixner, A.J.; Mayer, H.A.; Brecht, M. Three-Dimensional (3D) Surface-Enhanced Raman Spectroscopy (SERS) Substrates for Sensing Low-Concentration Molecules in Solution. *Nanomaterials* **2024**, *14*, 1728. https://doi.org/10.3390/nano14211728

Academic Editor: Sabina Botti

Received: 29 September 2024
Revised: 22 October 2024
Accepted: 24 October 2024
Published: 29 October 2024

1. Introduction

Raman spectroscopy is highly valued for its specificity, but small Raman scattering cross-sections often limit its applicability. One approach to significantly increase sensitivity is surface-enhanced Raman scattering (SERS), where a suitable surface enhances the Raman signal [1,2]. With enhancement factors (EFs) ranging from 10^2 to 10^8, SERS allows for the detection of low-abundance species even in complex mixtures.

In solution, SERS enables the real-time analysis of dynamic processes and the detection of low-concentration molecules with good sensitivity and specificity [3–8]. However, SERS in solution poses several challenges due to its three-dimensional (3D) geometry. The enhancement of the Raman signal in conventional two-dimensional (2D) SERS substrates is limited to a few tens of nanometers above the surface [9–11]. Dynamic and complex solutions, particularly biological fluids and environmental samples, require SERS substrates

to perform reliably in these 3D environments. Hence, there is a growing need for effective SERS platforms that operate in solution [12,13].

Silica microspheres functionalized with silver (Ag) nanoparticles (SMP@Ag) have emerged as promising candidates for such applications. These substrates combine the high surface area and ease of modification of silica microspheres with the plasmonic properties of Ag NPs, offering an effective 3D SERS platform [14,15]. The fabrication and characterization of mercapto-functionalized silica microspheres (SMPs), subsequently decorated with silver (Ag) nanoparticles using Tollens' reagent (SMP@Ag), has already been described [15]. Three-dimensional (3D) substrates demonstrate excellent performance in complex matrices and have the potential for multiplexed detection, thus broadening their application in diagnostics, environmental monitoring, and chemical sensing. Additionally, they can be suspended in a solution or any biological environment and distributed across different spatial locations.

In comparison to similar SERS platforms reported in the literature, a few studies have employed different strategies to achieve SERS in solution or on dried samples, resulting in notable variations in EFs, sensitivity, and detection limits. For instance, Li et al. developed poly(styrene-co-acrylic acid) core-silver nanoparticle/silica shell microspheres, demonstrating high sensitivity [16,17]. In contrast, Liu et al. presented SiO_2@Ag core–shell particles that exhibited strong SERS enhancement [18]. Similarly, Jensen et al. focused on single-molecule detection using highly sensitive pH-responsive substrates, achieving single-molecule sensitivity [19]. Kim et al. described a CRISPR-mediated SERS assay that achieved remarkable femtomolar sensitivity for bacterial DNA detection [20]. Chen et al. investigated silver nanoparticle-decorated carbon nanospheres for melamine detection, demonstrating strong SERS activity in solution [21]. Cai et al. developed gold-coated sulfonated polystyrene microspheres, enabling nanomolar sensitivity for 4-aminothiophenol (4-ATP) [22]. Trinh et al. uniquely combined solar-to-steam generation with SERS detection, achieving nanomolar sensitivity without quantifying the EF, offering a dual-functional platform that sets it apart from traditional SERS substrates [23]. Lastly, Lupa et al. reported relatively low EFs (ranging from 2.75 to 5.75) for Au NPs-coated SMPs [24]. This diversity in substrates emphasizes the difficulties in directly comparing EFs and detection capabilities due to differing methodologies and measurement conditions, especially when contrasting solution-based and dried-sample environments.

This study investigates two distinct scenarios for 3D-SERS, each contributing novel insights to the field.

In the first, stationary scenario, SMP@Ag particles were dispersed in a highly viscous solution of methylene blue (MB) and glycerin. In this case, glycerin served as a medium to immobilize the SMP@Ag particles. This use of glycerin enabled high-resolution SERS imaging within a 3D matrix, allowing for the acquisition of spatially resolved SERS spectra of analytes across the substrate. This technique provides a unique method for mapping analyte distribution in solution, thereby enhancing the utility of SERS substrates in complex environments.

In the second scenario, referred to as the dynamic scenario, SMP@Ag particles were freely floating in a water–MB solution, simulating real-world conditions where substrates were suspended in fluidic environments. Here, we introduced time-dependent SERS measurements to capture the temporal fluctuations in the SERS signal as the particles moved through the laser focus. This capability enables the real-time detection of low-concentration analytes, which is essential for continuous monitoring in environments such as biological fluids and environmental samples. Additionally, we employed mercapto-functionalized silica spheres for immobilizing metal NPs, marking a novel fabrication strategy. Combined with the straightforward fabrication of these SMP@Ag substrates using Tollens' reagent, this study presents a versatile and innovative approach to the development of 3D SERS substrates.

This method's excellent, reproducible, and reliable performance, coupled with its simple fabrication, means it can be produced at a low cost. It is helpful for real-time, on-site SERS detection in fields like analytical chemistry, biomedical research, environmental

research, and forensic science. Three-dimensional (3D) SERS substrates provide valuable depth information, advancing SERS-based sensing and enabling new scientific insights.

2. Materials and Methods

2.1. Fabrication of Mercapto-Functionalized SMPs

The functionalized SMPs were prepared according to a previously published protocol regarding silica particles with similar morphology but different functionalization [25,26]. A solution containing 115 mL of water and 0.266 mL of aqueous ammonium hydroxide (NH_4OH) was stirred continuously for 40 min. A syringe pump added 2.6 mL of a mixture of tetraethoxysilane (TEOS) and mercapto-trimethoxysilane (MerTMS) with a ratio of 22 mmol:88.3 mmol. The amount and composition of this mixture allowed for the control of the particles' shape, size, and morphology. After adding the silane mixture, the solution was stirred at room temperature for 14 h. The solvent was removed by washing with water and ethanol, and the SMPs were dried in an oven at 70 °C for 16 h. The resultant SMPs were non-porous, monodispersed, approx. 3 µm sized mercapto-functionalized spherical silica particles. The details can be found in reference [15].

2.2. Synthesizing SMPs with Metal Nanoparticles

Tollens' Reagent (Ag)

Tollens' reagent was used to precipitate elemental Ag, producing a Ag mirror on the surface of the SMP. For this, Ag nitrate ($AgNO_3$) 53.0 mg—312 µmol, aqueous ammonia solution (NH_3) 25%—380 µL, and saturated aqueous D-(−)-Fructose solution (2.0 mL) were dissolved in 3 mL of deionized water. Subsequently, one small pellet of NaOH was added and stirred until visibly dissolved. A total of 500 µL of this resulting solution was added to an Eppendorf tube containing mercapto-functionalized SMPs and was stirred continuously to allow Tollens' reagent to react uniformly with the complete surface area, generating SMP@Ag particles. Then, the mixture in the Eppendorf tube was allowed to rest for 1 min at room temperature. Afterward, the Eppendorf tube was placed in an ice bath to stop the chemical reaction, and the contents were washed with deionized water.

2.3. SERS Experiments

A commercial microscope from WITec (Oxford Instruments, Ulm, Germany) alpha300RAandS was used for the SERS experiments. A 532 nm diode laser with a nominal output power of 40 mW was used for excitation. The illumination and collection of the detected signal were carried out using two configurations illustrated in Supplementary Materials in Figure S1. Figure S1a illustrates the top excitation/detection configuration using an objective lens (Carl Zeiss, Jena, Germany; EC Epiplan, 20×, NA = 0.4). This configuration was suitable for dynamic experiments, as the 3D SERS substrates were suspended in the solution. Figure S2b shows bottom excitation/detection by an objective lens (NIKON 60×, NA = 0.55, Tokyo, Japan). In static/stationary experiments, high-resolution spatial images of the substrate within the solution were possible due to the nature of the solution. To achieve this, a bottom illumination/detection configuration was used. Multi-mode fibers with different diameters guide the detected signal to the spectrometer. The diameter (10 µm, 25 µm, 50 µm, and 100 µm, all with an NA = 0.12) of these fibers determines the confocal pinhole size [27]. For detection, the microscope is equipped with a lens-based ultra-high-throughput spectrometer (UHTS 300) with a thermoelectrically cooled (down to −60 °C) back-illuminated CCD and an EMCCD (Andor DU970N-BV, Belfast, UK). All SERS experiments were performed using a 600 L/mm grating, which offers an extensive spectral range. Data processing for all the above measurements was performed using Control 5.0 software provided by WITec (Ulm, Germany). All experiments were carried out under ambient conditions.

2.4. Preparation of Solution

SERS experiments were performed with methylene blue (MB) as an analyte (purchased from Carl Roth Gmbh & Co. Kg, Karlsruhe, Germany). MB exhibits an absorption peak at 665 nm, a smaller peak at 610 nm, and an additional peak at 293 nm [28].

2.4.1. Glycerin–MB Solution

Glycerin (99% pure) was put into a glass beaker, and a few milligrams of MB was added to achieve a concentration of MB of 3×10^{-5} M. After adding MB, the solution was vigorously stirred for an extended period inside the glass beaker using a spatula. The SMP@Ags were then added to this mixture and blended well. The mixture was sonicated for 5 min to prevent the aggregation of the SMP@Ag particles inside the solution. With significantly extended sonication times, there is a chance that Ag NPs might separate from the SMP@Ags.

2.4.2. Water–MB Solution

Distilled water was poured into a beaker with a few milligrams of MB to obtain an MB concentration of 3×10^{-5} M. The solution was mixed briefly before being placed in a small ceramic Petri dish to be tested for SERS. After that, SMPs treated with Tollens' reagent were added to the solution and left to float for a while before the SERS measurements.

2.5. Scanning Electron Microscopy (SEM)

SEM images were acquired with a HITACHI SU8030 (Tokyo, Japan) at 2 kV, a secondary electron detector, and an accelerating voltage of 0.5 to 30 kV.

A detailed characterization of such SMP@Ags using SEM, energy dispersive X-ray (EDX), and dark field scattering are shown in our previous publication [15].

3. Results and Discussion

The preparation of SMPs functionalized with Ag nanoparticles (SMP@Ag) was already discussed in a previous publication. The SMP@Ags were characterized by scanning electron microscopy (SEM), energy dispersive X-ray (EDX), and dark-field scattering, and their SERS activity was investigated in a stationary 2D environment [15]. These particles provide multiple resonances throughout the visible and near-infrared spectral region within the same SMP, thus enabling multi-analyte screening [9,15].

The SMP@Ags were immobilized by glycerin for the first experiments. The immobilization enables the acquisition of SERS spectra at specific points on the SMP@Ag particle and SERS imaging. Apart from MB, glycerin serves as a second analyte. A sizable drop of the glycerin–MB solution containing SMP@Ags was deposited onto a glass slide, according to the scheme in Figure 1a. A microscopic image of the SMP@Ags immersed in this solution is shown in Figure 1b. The SMP@Ags in the center of Figure 1b are within the microscope's focal plane, while the others are out of focus. The SEM picture in the inset of Figure 1b depicts the morphology of the SMP@Ags and shows Ag particles with sizes ranging from 10 nm to 400 nm on the SMP surface. Due to the high viscosity of glycerin, the position of the SMP@Ags remains stationary within the timescale of the subsequent experiments, enabling extended optical measurements. Raman imaging in a bottom excitation/detection configuration was optimal for conducting SERS experiments and high-resolution imaging within the solution; the results are shown in Figure 2.

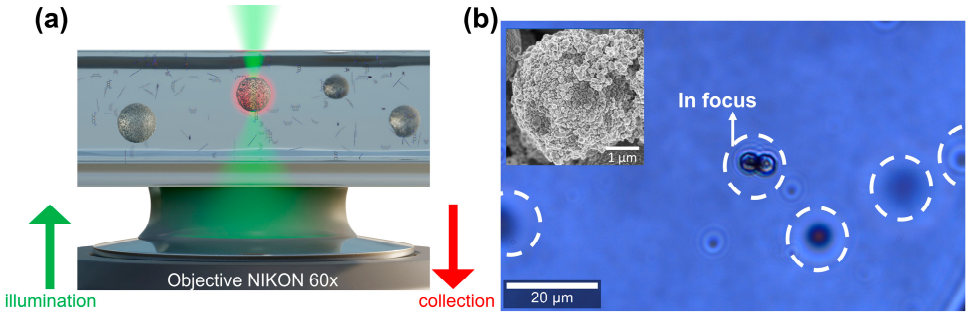

Figure 1. (**a**) Schematics (not to scale) of bottom illumination/collection configuration for SMPs@Ags immersed in a solution of glycerin and MB, and (**b**) microscopic (bright-field) image of SMP@Ags mixed in glycerin–MB. The image shows that the SMP@Ags are localized in different planes in the solution. Inset: SEM image of an SMP@Ag.

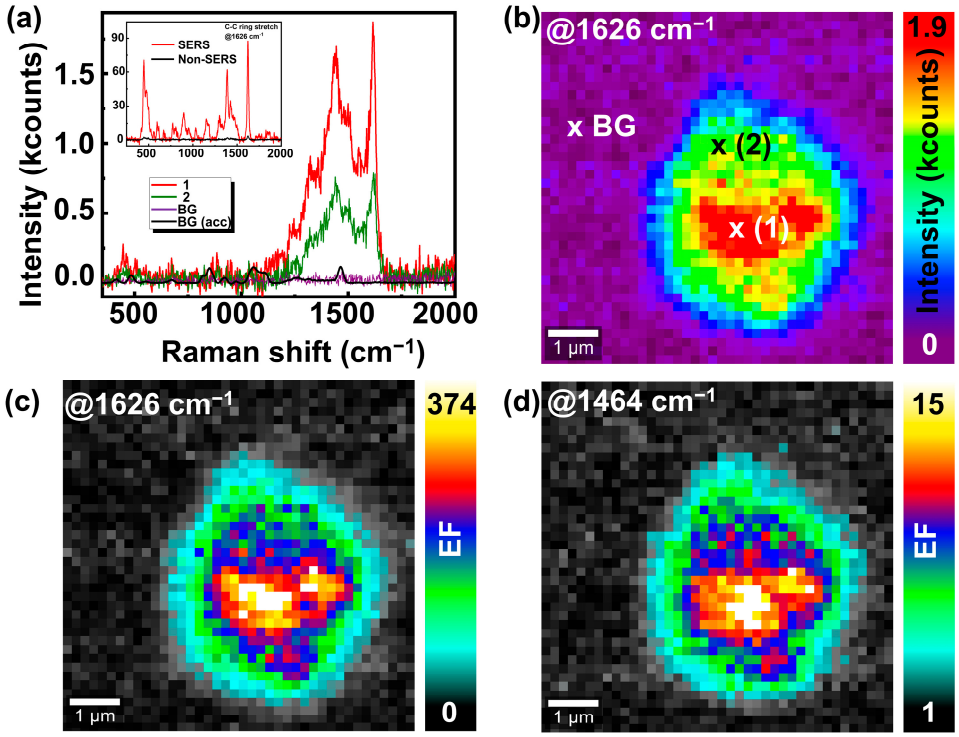

Figure 2. (**a**) SERS spectra of glycerin and MB at different spatial positions on SMP@Ags, position 1 (bright region), position 2 (low-intensity region), background (BG), and BG accumulated (BG acc), acquired separately from the same solution with 500 accumulations. Inset: SERS spectra and non-SERS spectra of MB in water (measured separately only for reference). (**b**) SERS image of an SMP@Ag immersed in glycerin–MB solution at 1626 cm^{-1}. The marks show the positions where the spectra in (**a**) are acquired. (**c**) Spatial distribution of EF for the MB peak at 1626 cm^{-1} and (**d**) spatial distribution of EF for the glycerin peak at 1464 cm^{-1}.

Figure 2a depicts the SERS spectra acquired at the different spatial positions on a single SMP@Ag (as marked in Figure 2b) in a glycerin–MB solution. The spectrum at position 1 (red in Figure 2a) is obtained from a bright region on the SMP@Ag particle, and the green spectrum in Figure 2a is acquired at position 2 with lower intensity. The background (BG, purple in Figure 2a) spectrum is recorded beside the SMP@Ag. The SERS spectrum of glycerin–MB deviates significantly from the MB spectra (shown in the inset). This can be ascribed to the additional presence of glycerin. For example, the most intense peak of MB is at 1626 cm^{-1}, corresponding with the C-C ring stretch [28], while the signal at 1464 cm^{-1} is due to the CH_2 vibration of glycerin [29]. No Raman signal from MB or glycerin can be

observed in the BG spectrum in Figure 2a. Hence, it was necessary to significantly increase the acquisition time to obtain any observable signal from the BG. The black spectrum shows the accumulated BG spectrum (BG acc) for 500 accumulations. Without SERS enhancement, glycerin dominates the spectrum, and only a weak MB Raman signal is visible in the close-up view of the spectrum, as shown in the Supplementary Materials in Figure S2. The SERS image in Figure 2b was based on the integrated intensity of the most intense MB peak (1626 cm^{-1}) with a spectral width of 20 cm^{-1}. The small region shown in red exhibits the strongest SERS enhancement. Additional SERS images of single SMP@Ags immersed in a solution of glycerin–MB are presented in Figure S3 of the Supplementary Materials. The EF was determined using the Raman signals in the accumulated BG (BG acc) spectrum. The EF is calculated as the intensity ratio of the most intense peak of MB (at 1626 cm^{-1}) on the SMP and the substrate:

$$EF = \frac{I_{Hotspot}}{I_{Substrate}} \quad (1)$$

$I_{Hotspot}$ is the intensity of a specific Raman peak at the bright regions and $I_{Substrate}$ is the intensity of the same peak on the substrate (glass slide) without any metal NPs. The reason behind deliberately employing this method to calculate the SERS EF stems from the inherent difficulties to accurately estimate the number of molecules present within a given spot, their exact location in the hot spot, and their distance from the surface [30–32]. It is important to note that the method used to calculate EF in this study results in lower EF values compared to those reported in other SERS research, which typically range from 10^2 to 10^{10} [5,33,34]. Figure 2c,d show the spatial distribution of EFs at the characteristic Raman frequencies of MB (at 1626 cm^{-1}) and glycerin (at 1464 cm^{-1}), respectively, derived from the identical dataset as presented in Figure 2b. The spatial EF distributions for MB and glycerin are quite similar. Strong differences are observed for the maximum EFs of glycerin (EF_{max} = 15) and MB (EF_{max} = 374). This could be due to MB accumulating on the SMP@Ag due to the electrochemical properties of MB containing a sulfur atom within its structure. Additionally, the large surface area of SMP@Ag provides numerous adsorption sites, facilitating the accumulation of MB molecules. This combined effect leads to a higher effective concentration of MB on SMP@Ags, contributing to the enhanced signal and larger EF of MB compared to glycerin. The maximum (EF_{max}) and minimum (EF_{min}) EF calculations for Figure 2c,d are shown in Supplementary Materials.

The results shown in Figure 2 were obtained for immobilized SMP@Ags. However, in less viscous solutions, the SMP@Ags will not remain stationary. Consequently, freely floating SMP@Ags are investigated in a water–MB solution. The results are shown in Figure 3.

Next, the laser was focused in the water–MB solution in a beaker, and the detection was in a top excitation/detection configuration (back-scattering detection geometry) for easier alignment with the sample and to ensure efficient capture of scattered light from the solution. Several videos were recorded in the bright-field mode of the microscope, showing the movement of SMP@Ags in solution. Figure 3a presents snapshots from one of these videos, illustrating an SMP@Ag (located out of the focal plane) moving through a much smaller laser spot (approx. 700 nm) than the size of the particles (approx. 3 µm). The images suggest that the laser focus widens as the SMP@Ag passes through it. This is attributed to the increased signal intensity resulting from the scattering of the Ag nanoparticles on the SMP, which in turn causes the camera to reach saturation.

Additionally, a SERS spectrum was acquired every second with an integration time of 500 ms. Figure 3b displays the temporally resolved SERS intensity of MB at 1626 cm^{-1}. In Figure 3b, intensity spikes are observable, for instance, around the 15 s mark, indicating the passage of SMP@Ags through the laser focus volume, resulting in a noticeable enhancement of the MB SERS signal. At approximately 175 s and 315 s, extended periods with high SERS intensity suggest a passage of multiple SMP@Ags or a single slowly moving SMP@Ag. However, there are several intensity spikes with durations shorter than 3 s, e.g., at 200 s, 210 s, and 225 s, where a single SMP@Ag swiftly passes the excitation focus.

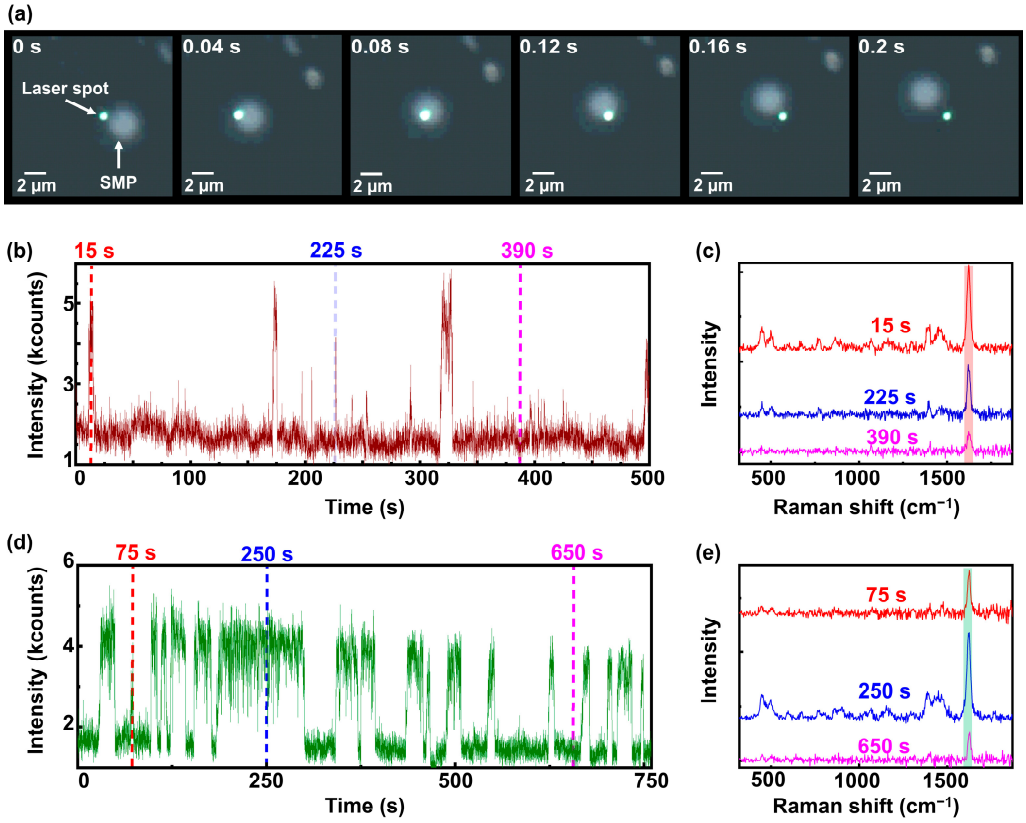

Figure 3. (**a**) Video snapshots of SMP@Ags immersed in a water–MB solution passing through a laser spot at different time frames. (**b**) SERS intensity of MB (at 1626 cm^{-1}) measured as a function of time (for a preset duration of 500 s) for SMP@Ags passing through the laser focus spot in a water–MB solution. (**c**) SERS spectra of MB for the corresponding time frames shown in (**b**). (**d**) SERS intensity of MB (at 1626 cm^{-1}) acquired after a resting time, also measured as a function of time (for a preset duration of 750 s) for SMP@Ags passing through the laser focus spot in a water–MB solution. (**e**) SERS spectra of MB for the corresponding time frames shown in (**d**).

Figure 3c shows Raman spectra at three distinct time points, i.e., 15 s, 225 s, and 390 s, indicated by the dashed lines in Figure 3b. The spectrum at 390 s resembles the BG level. Here, only the most intense MB peak at 1626 cm^{-1} is visible. The spectrum at 225 s shows a clear MB SERS signal when the SMP passes the laser focus. However, the enhancement strongly depends on the actual position of the SMP@Ag to the excitation focus, the number of Ag nanoparticles on the SMP, and their distribution on the surface, which can vary between different SMP@Ags [15].

After a resting period of 10 min, the experiment was repeated, as shown in Figure 3d. At first glance, the dwell time of SMP@Ags in the laser focus is increased compared to Figure 3b. In Figure 3d, high-intensity periods are observed for extended periods of several seconds, and only one very short intensity increase is visible at around 75 s. Figure 3e shows Raman spectra at three distinct time points, i.e., 75 s, 250 s, and 650 s, indicated by the dashed lines in Figure 3d. The spectrum at 650 s resembles the BG level. Here, only the most intense MB peak at 1626 cm^{-1} is visible. The spectrum at 250 s shows a clear MB SERS signal when the SMP passes the laser focus. This observation suggests that the SMP@Ag movement is slowing down or that the SMP@Ags have clustered. However, this situation is advantageous for sensing applications due to the prolonged high-intensity phases.

Figure 4a shows a 2D surface plot of the Raman spectra (shown in Figure 3d,e) in the range from 1200 cm^{-1} to 1700 cm^{-1}. The simultaneous fluctuation of all significant lines indicates an enhancement of all Raman lines of MB. In the next step, the time-dependent EF is calculated. First, the dataset is subdivided into 18 high-intensity periods, and then

the maximum and average EF is calculated for each period according to Equation (1). A non-SERS spectrum was acquired separately from a solution of the same concentration and under the same experimental conditions without the addition of SMP@Ags.

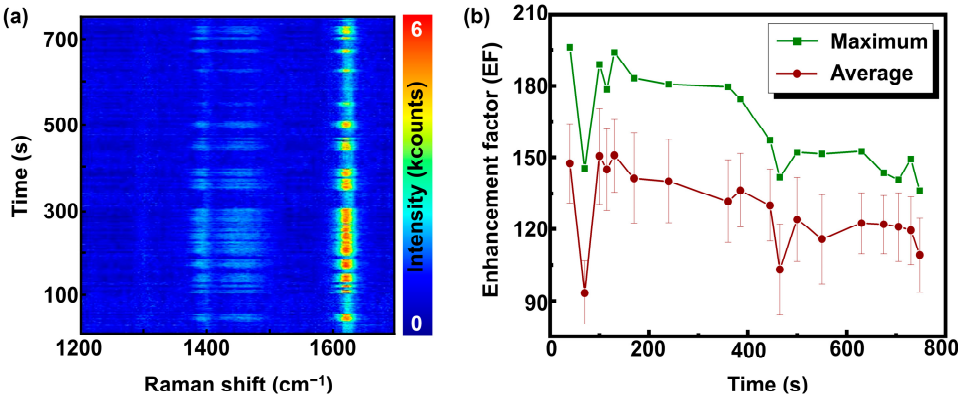

Figure 4. (**a**) Surface plot of MB spectra spanning 750 s ranging from 1200 cm^{-1} to 1700 cm^{-1} and (**b**) maximum and average EFs for the SMPs in water–MB solution.

The result is given in Figure 4b. The maximum EF using Equation (1) is calculated using the maximum intensity within a certain high-intensity period, whereas the average EF is based on the average intensity over the whole period. The maximum and average EF vary depending on the precise location of the SMP@Ag in the laser focus. The largest maximum EF observed in this dataset is approx. 200, whereas the average EF can reach up to 150 $\pm$ 20. As previously mentioned, the EF values obtained in this study are lower due to the specific method of calculation employed, as outlined in Equation (1). The EF for the water–MB solution is lower than the glycerin–MB solution, likely due to the rapid movement of SMP@Ag particles through the laser focus in the water–MB experiments. This reduces measurement time, which may be less than intended. Additionally, in the water–MB solution, SMP@Ag particles constantly move across different planes, leading to instances where particles detected at the laser focus may not be fully in focus. These factors contribute to the differences in EF observed between the glycerin–MB and water–MB solutions. The maximum and average EF graphs exhibit a declining trend; this might result from gradual changes in the focus position in the solution.

4. Conclusions

This study examined SMPs functionalized with Ag nanoparticles in two different 3D environments: a stationary and a dynamic scenario.

In the stationary scenario, glycerin was used to immobilize the SMP@Ags, making SERS imaging within the solution possible. Furthermore, this scenario mimics a situation where the SMP@Ags are immobilized in, e.g., specific cell compartments or tissue. Along with MB, glycerin can function as an analyte to further investigate the use of enhancing multiple analytes within the same sample. Glycerin and MB both showed good enhancement, although their EFs differed significantly. The EF can reach up to 374 for MB, whereas for glycerin, it can reach up to 15. This indicates that multiple analytes are enhanced on the same SMP.

In the dynamic scenario, MB solution in water was used. Here, the SMP@Ags were mobile and randomly floating. Time-dependent experiments were performed, where the MB's SERS signal was detected when an SMP@Ag passed through the laser focus. An SMP@Ag traveled across the laser EF in video snapshots at different time frames. The results indicate that single and clustered SMP@Ags pass the laser focus. SERS enhancement can be achieved with the SMPs functionalized with Ag nanoparticles and EFs up to 200.

The novel use of mercapto-functionalized silica spheres as a natural 'glue' for immobilizing metal NPs in 3D SERS substrates, along with the easy fabrication using Tollens'

reagent, represents an important advancement. Furthermore, the glycerin-immobilized system allowed for detailed spatial SERS imaging within a 3D matrix, while the dynamic system enabled real-time detection of low-concentration analytes in solution. In the long term, these findings could pave the way for innovative applications in biomedicine and environmental science, particularly in developing more effective 3D SERS substrates. These might detect and identify a broader range of analytes in complex 3D environments, such as cells, tissues, pollutants, and trace elements in water or other solutions.

Supplementary Materials: The following supporting information can be downloaded at https://www.mdpi.com/article/10.3390/nano14211728/s1, Figure S1: Schematics of experimental details that illustrate top and bottom excitation and detection configurations of WITec alpha 300RA&S Raman microscope; Figure S2: Raman spectrum of glycerin–MB solution (with 500 accumulations) with most intense peaks marked; Figure S3: Additional examples of SERS imaging of SMP@Ags in glycerin–MB solution.

Author Contributions: Conceptualization, F.W., A.J.M., H.A.M. and M.B.; Data curation, A.M., F.W. and M.B.; Formal analysis, A.M., F.W. and M.B.; Funding acquisition, A.J.M., H.A.M. and M.B.; Investigation, A.M. and F.W.; Methodology, A.M., F.W. and M.B.; Project administration, A.J.M., H.A.M. and M.B.; Resources, F.W., A.J.M., H.A.M. and M.B.; Software, F.W.; Supervision, A.J.M., H.A.M. and M.B.; Validation, A.M., F.W., A.J.M., H.A.M. and M.B.; Visualization, A.M.; Writing—original draft, A.M.; Writing—review and editing, A.M., F.W., A.J.M., H.A.M. and M.B. All authors have read and agreed to the published version of the manuscript.

Funding: The author(s) disclose receipt of the following financial support for the research, authorship, and publication of this article: The authors would like to acknowledge financial support within the framework of IngenieurNachwuchs 2016 (project: CompeTERS) by the German Federal Ministry of Education and Research (BMBF; Grant no.: 13FH596IX6).

Data Availability Statement: The datasets generated and analyzed during the current study are not publicly available since they are part of an ongoing PhD thesis. However, they are available from the corresponding authors upon reasonable request.

Acknowledgments: The authors would like to thank Elke Nadler of Eberhard Karls University in Tübingen for her assistance in obtaining SEM images. The authors would like to express their gratitude to Tobias Drieschner from the Process, Analysis, and Technology group at Hochschule Reutlingen for his valuable insights and engaging discussions regarding this manuscript. The authors would also like to thank Akanksha Dohare from the Institute of Inorganic Chemistry at Eberhard Karls University of Tübingen for her assistance in fabricating mercapto-functionalized SMPs.

Conflicts of Interest: The authors declare no conflicts of interest.

References

1. Fleischmann, M.; Hendra, P.J.; McQuillan, A.J. Raman spectra of pyridine adsorbed at a silver electrode. *Chem. Phys. Lett.* **1974**, *26*, 163–166. [CrossRef]
2. Pettinger, B.; Wenning, U.; Wetzel, H. Surface plasmon enhanced Raman scattering frequency and angular resonance of Raman scattered light from pyridine on Au, Ag and Cu electrodes. *Surf. Sci.* **1980**, *101*, 409–416. [CrossRef]
3. Zhang, J.; Chen, S.; Gong, T.; Zhang, X.; Zhu, Y. Tapered Fiber Probe Modified by Ag Nanoparticles for SERS Detection. *Plasmonics* **2016**, *11*, 743–751. [CrossRef]
4. Guo, Y.; Zhang, L.; You, H.; Fang, J. A solution-based SERS sensing protocol via the ultra-rapid and highly efficient molecule enrichment strategy. *Sens. Actuators B Chem.* **2022**, *367*, 132064. [CrossRef]
5. Mosier-Boss, P.A. Review of SERS Substrates for Chemical Sensing. *Nanomaterials* **2017**, *7*, 142. [CrossRef]
6. Laurence, T.A.; Braun, G.; Talley, C.; Schwartzberg, A.; Moskovits, M.; Reich, N.; Huser, T. Rapid, solution-based characterization of optimized SERS nanoparticle substrates. *J. Am. Chem. Soc.* **2009**, *131*, 162–169. [CrossRef]
7. Amin, M.U.; Zhang, R.; Li, L.; You, H.; Fang, J. Solution-Based SERS Detection of Weak Surficial Affinity Molecules Using Cysteamine-Modified Au Bipyramids. *Anal. Chem.* **2021**, *93*, 7657–7664. [CrossRef] [PubMed]
8. Wang, H.; Fang, J.; Xu, J.; Wang, F.; Sun, B.; He, S.; Sun, G.; Liu, H. A hanging plasmonic droplet: Three-dimensional SERS hotspots for a highly sensitive multiplex detection of amino acids. *Analyst* **2015**, *140*, 2973–2978. [CrossRef]
9. Mukherjee, A.; Liu, Q.; Wackenhut, F.; Dai, F.; Fleischer, M.; Adam, P.-M.; Meixner, A.J.; Brecht, M. Gradient SERS Substrates with Multiple Resonances for Analyte Screening: Fabrication and SERS Applications. *Molecules* **2022**, *27*, 5097. [CrossRef]

10. Liu, Q.; Wackenhut, F.; Wang, L.; Hauler, O.; Roldao, J.C.; Adam, P.-M.; Brecht, M.; Gierschner, J.; Meixner, A.J. Direct Observation of Structural Heterogeneity and Tautomerization of Single Hypericin Molecules. *J. Phys. Chem. Lett.* **2021**, *12*, 1025–1031. [CrossRef]
11. Geladari, O.; Haizmann, P.; Maier, A.; Strienz, M.; Eberle, M.; Scheele, M.; Peisert, H.; Schnepf, A.; Chassé, T.; Braun, K.; et al. Direct laser induced writing of high precision gold nanosphere SERS patterns. *Nanoscale Adv.* **2024**, *6*, 1213–1217. [CrossRef] [PubMed]
12. Wu, L.-A.; Li, W.-E.; Lin, D.-Z.; Chen, Y.-F. Three-Dimensional SERS Substrates Formed with Plasmonic Core-Satellite Nanostructures. *Sci. Rep.* **2017**, *7*, 13066. [CrossRef] [PubMed]
13. Lee, H.K.; Lee, Y.H.; Phang, I.Y.; Wei, J.; Miao, Y.-E.; Liu, T.; Ling, X.Y. Plasmonic liquid marbles: A miniature substrate-less SERS platform for quantitative and multiplex ultratrace molecular detection. *Angew. Chem. Int. Ed. Engl.* **2014**, *53*, 5054–5058. [CrossRef] [PubMed]
14. Gupta, R.; Rastogi, P.K.; Ganesan, V.; Yadav, D.K.; Sonkar, P.K. Gold nanoparticles decorated mesoporous silica microspheres: A proficient electrochemical sensing scaffold for hydrazine and nitrobenzene. *Sens. Actuators B Chem.* **2017**, *239*, 970–978. [CrossRef]
15. Mukherjee, A.; Wackenhut, F.; Dohare, A.; Horneber, A.; Lorenz, A.; Müchler, H.; Meixner, A.J.; Mayer, H.A.; Brecht, M. Three-Dimensional (3D) Surface-Enhanced Raman Spectroscopy (SERS) Substrates: Fabrication and SERS Applications. *J. Phys. Chem. C* **2023**, *127*, 13689–13698. [CrossRef]
16. Li, J.-M.; Ma, W.-F.; Wei, C.; Guo, J.; Hu, J.; Wang, C.-C. Poly(styrene-co-acrylic acid) core and silver nanoparticle/silica shell composite microspheres as high performance surface-enhanced Raman spectroscopy (SERS) substrate and molecular barcode label. *J. Mater. Chem.* **2011**, *21*, 5992. [CrossRef]
17. Li, J.-M.; Ma, W.-F.; Wei, C.; You, L.-J.; Guo, J.; Hu, J.; Wang, C.-C. Detecting trace melamine in solution by SERS using Ag nanoparticle coated poly(styrene-co-acrylic acid) nanospheres as novel active substrates. *Langmuir* **2011**, *27*, 14539–14544. [CrossRef]
18. Liu, T.; Li, D.; Yang, D.; Jiang, M. An improved seed-mediated growth method to coat complete silver shells onto silica spheres for surface-enhanced Raman scattering. *Colloids Surf. A Physicochem. Eng. Asp.* **2011**, *387*, 17–22. [CrossRef]
19. Jensen, R.A.; Sherin, J.; Emory, S.R. Single nanoparticle based optical pH probe. *Appl. Spectrosc.* **2007**, *61*, 832–838. [CrossRef]
20. Kim, H.; Lee, S.; Seo, H.W.; Kang, B.; Moon, J.; Lee, K.G.; Yong, D.; Kang, H.; Jung, J.; Lim, E.-K.; et al. Clustered Regularly Interspaced Short Palindromic Repeats-Mediated Surface-Enhanced Raman Scattering Assay for Multidrug-Resistant Bacteria. *ACS Nano* **2020**, *14*, 17241–17253. [CrossRef]
21. Chen, L.-M.; Liu, Y.-N. Surface-enhanced Raman detection of melamine on silver-nanoparticle-decorated silver/carbon nanospheres: Effect of metal ions. *ACS Appl. Mater. Interfaces* **2011**, *3*, 3091–3096. [CrossRef] [PubMed]
22. Cai, W.; Wang, W.; Lu, L.; Chen, T. Coating sulfonated polystyrene microspheres with highly dense gold nanoparticle shell for SERS application. *Colloid Polym. Sci.* **2013**, *291*, 2023–2029. [CrossRef]
23. Trinh, B.T.; Cho, H.; Lee, D.; Omelianovych, O.; Kim, T.; Nguyen, S.K.; Choi, H.-S.; Kim, H.; Yoon, I. Dual-Functional Solar-to-Steam Generation and SERS Detection Substrate Based on Plasmonic Nanostructure. *Nanomaterials* **2023**, *13*, 1003. [CrossRef] [PubMed]
24. Lupa, D.; Oćwieja, M.; Piergies, N.; Baliś, A.; Paluszkiewicz, C.; Adamczyk, Z. Gold nanoparticles deposited on silica microparticles—Electrokinetic characteristics and application in SERS. *Colloid Interface Sci. Commun.* **2019**, *33*, 100219. [CrossRef]
25. Yang, H.; Lu, X.; Xin, Z. One-Step Synthesis of Nonspherical Organosilica Particles with Tunable Morphology. *Langmuir* **2018**, *34*, 11723–11728. [CrossRef]
26. Zhou, Q.; Xiang, H.; Fan, H.; Yang, X.; Zhao, N.; Xu, J. Facile fabrication of golf ball-like hollow microspheres of organic-inorganic silica. *J. Mater. Chem.* **2011**, *21*, 13056. [CrossRef]
27. Mukherjee, A.; Lorenz, A.; Brecht, M. Determination and Monitoring of Quality Parameters: A Detailed Study of Optical Elements of a Lens-Based Raman Spectrometer. *Appl. Spectrosc.* **2022**, *76*, 199–206. [CrossRef]
28. Tu, K.T.; Chung, C.K. Enhancement of Surface Raman Spectroscopy Performance by Silver Nanoparticles on Resin Nanorods Arrays from Anodic Aluminum Oxide Template. *J. Electrochem. Soc.* **2017**, *164*, B3081–B3086. [CrossRef]
29. Mudalige, A.; Pemberton, J.E. Raman spectroscopy of glycerol/D2O solutions. *Vib. Spectrosc.* **2007**, *45*, 27–35. [CrossRef]
30. Le Ru, E.C.; Meyer, M.; Etchegoin, P.G. Proof of single-molecule sensitivity in surface enhanced Raman scattering (SERS) by means of a two-analyte technique. *J. Phys. Chem. B* **2006**, *110*, 1944–1948. [CrossRef]
31. Etchegoin, P.G.; Meyer, M.; Blackie, E.; Le Ru, E.C. Statistics of single-molecule surface enhanced Raman scattering signals: Fluctuation analysis with multiple analyte techniques. *Anal. Chem.* **2007**, *79*, 8411–8415. [CrossRef] [PubMed]
32. Ansar, S.M.; Li, X.; Zou, S.; Zhang, D. Quantitative Comparison of Raman Activities, SERS Activities, and SERS Enhancement Factors of Organothiols: Implication to Chemical Enhancement. *J. Phys. Chem. Lett.* **2012**, *3*, 560–565. [CrossRef] [PubMed]
33. Félidj, N.; Aubard, J.; Lévi, G.; Krenn, J.R.; Schider, G.; Leitner, A.; Aussenegg, F.R. Enhanced substrate-induced coupling in two-dimensional gold nanoparticle arrays. *Phys. Rev. B* **2002**, *66*, 245407. [CrossRef]
34. Lassiter, J.B.; Aizpurua, J.; Hernandez, L.I.; Brandl, D.W.; Romero, I.; Lal, S.; Hafner, J.H.; Nordlander, P.; Halas, N.J. Close encounters between two nanoshells. *Nano Lett.* **2008**, *8*, 1212–1218. [CrossRef]

Conclusion and Outlook

The studies on improving the practicality of instrumentations in Raman spectroscopy and chemical imaging combined with advanced data processing techniques and improving the applicability of SERS have provided valuable insights into the field.

The investigation into SR parameters has highlighted crucial instrument, experiment, and sample-specific factors that influence Raman spectroscopy outcomes. Key parameters, such as pinhole widths and quality factors, have emerged as critical determinants of SR performance. This has emphasized the importance of optimizing instrument-specific settings to achieve SR close to the natural bandwidth of the sample. These findings confirm the high quality of the spectrometer and its potential for significant precision when certain parameter combinations are applied.

In clinical applications, Raman spectroscopy, combined with MVA, has proven effective in accurately classifying SGT. Distinctive spectral patterns associated with RNA, DNA/RNA, proteins, lipids, and collagen content allow for differentiation between non-tumor salivary gland tissues, Warthin tumors, and pleomorphic adenomas. The PCA-DA model has exhibited high predictive accuracy, demonstrating its potential for clinical diagnostics. However, the study acknowledges the need for automation to increase throughput. It highlights the necessity of further validation across diverse tumor types, particularly in addressing the challenges of tissue heterogeneity.

Exploring non-uniform SERS substrates revealed diverse morphological variations and gap sizes, allowing for tailored enhancements and flexible SERS conditions. Resonance shifts in extinction spectra provided insights into plasmonic behavior, guiding optimal conditions for specific analytes. Comparing different substrates and analytes highlighted the need for customized conditions and positioning non-uniform substrates as practical tools for molecular screening.

Additionally, the deposition of Ag and Au NPs on SMPs has demonstrated the potential of 3D SERS substrates for diverse analytical purposes. Mercapto-functionalized SMPs have been identified as particularly effective for trapping metal NPs. Temperature-dependent Raman analysis has further deepened the understanding of mercapto bond breaking, which is crucial for optimizing substrate performance. The efficient SERS performance detecting analytes such as MB highlights the substrate’s effectiveness.

This study examined SMPs functionalized with Ag nanoparticles in stationary and dynamic 3D environments. In the stationary setup, glycerin was used to immobilize the SMP@Ags, facilitating SERS imaging within the solution. Multiple analytes demonstrated significant differences in their EFs. Time-dependent experiments were conducted in the dynamic scenario, with mobile SMP@Ags floating in an MB solution. The SERS signal is detected as the SMP@Ags pass through the laser focus, highlighting their applicability in real-time detection.

The collective outlook from this research underscores the significant advancements in the practicality and effectiveness of Raman spectroscopy and SERS technologies. The research presented in this thesis advances the field in several key areas, including optimizing SR parameters for Raman spectroscopy, developing novel 3D SERS substrates, and integrating advanced data processing techniques. These contributions represent significant strides in improving the precision, sensitivity, and applicability of Raman-based techniques in real-world settings.

The vision involves pushing the boundaries in fabrication techniques for non-uniform SERS substrates, focusing on tailoring resonance conditions, integrating multimodal analysis, and designing dynamic substrates. The goal is to enhance substrate functionality through in-situ characterization methods, diverse analyte testing, and optimization algorithms. Collaborative interdisciplinary research and integration into portable devices aim to bridge the gap between theoretical advancements and practical applications, addressing scalability and commercialization challenges for broader adoption.

3D SERS substrates on SMPs showcase tunable and versatile SERS performance. This highlights the potential for responsive substrates for molecular sensing, spatial resolution improvements, and adaptability for dynamic environments. Future research involves optimizing the fabrication process for better control and reproducibility, exploring a broader range of analytes, and expanding applications in various fields. Real-time monitoring capabilities in dynamic environments open avenues for on-the-fly sensing and diagnostics, encouraging further refinement and exploration of the SMP@Ag SERS platform.

Refining Raman spectroscopy techniques and instruments emphasizes the need to understand instrument-specific parameters, mitigate deviations, and optimize spectrometer designs for higher SR. Future work is suggested to explore innovative methodologies, improve pixel technology, and precisely control quality factors for enhanced

spectral precision. The outlook underscores the study's contribution to advancing theoretical models and practical applications in Raman spectroscopy.

A Raman spectroscopic imaging diagnostic model envisions a future with increased efficiency and larger sample sizes through automation. The potential clinical utility prompts for prospective clinical trials, especially with a more diverse set of tumor entities, addressing tissue heterogeneity and continuous optimization of the diagnostic model. Collaboration across disciplines and exploration of extended tissue sets are emphasized to gain a comprehensive understanding of spectroscopic variations and refine diagnostic capabilities. The combined knowledge paves the way for continued progress in developing and applying these techniques in various scientific and clinical domains.

These findings enhance the understanding of instrument-specific parameters and SERS substrate optimization and lay the groundwork for future innovations in biomedical diagnostics, environmental monitoring, and chemical sensing. The versatility of these techniques opens avenues for expanding their use in other analytical fields. This research bridges the gap between theoretical advancements in Raman spectroscopy and their practical applications, contributing valuable insights that will support future innovations in academic research and industry.

References

1. C.V. RAMAN, K.S. KRISHNAN, Nature **121**, 501 (1928)
2. E. Papadopoulou, S.E.J. Bell, Chemistry (Weinheim an der Bergstrasse, Germany) **18**, 5394 (2012)
3. M. Li, J. Xu, M. Romero-Gonzalez, S.A. Banwart, W.E. Huang, Current opinion in biotechnology **23**, 56 (2012)
4. J.A. Stammeier, B. Purgstaller, D. Hippler, V. Mavromatis, M. Dietzel, MethodsX **5**, 1241 (2018)
5. G. Févotte, Chemical Engineering Research and Design **85**, 906 (2007)
6. T.M. Devine, F. Adar, in *Characterization of Materials*, ed. by E.N. Kaufmann (Wiley, 2002), p. 1
7. C.J. Strachan, T. Rades, K.C. Gordon, J. Rantanen, The Journal of pharmacy and pharmacology **59**, 179 (2007)
8. N. Zotov, H. Keppler, American Mineralogist **85**, 600 (2000)
9. J.T. Frith, A.E. Russell, N. Garcia-Araez, J.R. Owen, Electrochemistry Communications **46**, 33 (2014)
10. E. Markevich, V. Baranchugov, G. Salitra, D. Aurbach, M.A. Schmidt, J. Electrochem. Soc. **155**, A132 (2008)
11. G.A.N. Connell, R.J. Nemanich, C.C. Tsai, Applied Physics Letters **36**, 31 (1980)
12. M. Hippler, Analytical chemistry **87**, 7803 (2015)
13. M. Kerker, D.S. Wang, H. Chew, Applied optics **19**, 3373 (1980)
14. A. Knebl, Di Yan, J. Popp, T. Frosch, TrAC Trends in Analytical Chemistry **103**, 230 (2018)
15. B. Robert, Photosynthesis research **101**, 147 (2009)
16. R.M. Stöckle, Y.D. Suh, V. Deckert, R. Zenobi, Chemical Physics Letters **318**, 131 (2000)
17. S.L. McCall, P.M. Platzman, P.A. Wolff, Physics Letters A **77**, 381 (1980)
18. M. Fleischmann, P.J. Hendra, A.J. McQuillan, Chemical Physics Letters **26**, 163 (1974)
19. C.S. Allen, G.C. Schatz, R.P. van Duyne, Chemical Physics Letters **75**, 201 (1980)
20. N. Félidj, J. Aubard, G. Lévi, J.R. Krenn, M. Salerno, G. Schider, B. Lamprecht, A. Leitner, F.R. Aussenegg, Phys. Rev. B **65** (2002)
21. E.C. Le Ru, E. Blackie, M. Meyer, P.G. Etchegoin, J. Phys. Chem. C **111**, 13794 (2007)
22. J.A. Dieringer, R.B. Lettan, K.A. Scheidt, R.P. van Duyne, Journal of the American Chemical Society **129**, 16249 (2007)
23. K. Kneipp, Y. Wang, H. Kneipp, L.T. Perelman, I. Itzkan, R.R. Dasari, M.S. Feld, Phys. Rev. Lett. **78**, 1667 (1997)
24. S. Nie, Emory, SR, Science (New York, N.Y.) **275**, 1102 (1997)
25. A. Weiss, G. Haran, J. Phys. Chem. B **105**, 12348 (2001)
26. H. Xu, E.J. Bjerneld, M. Käll, L. Börjesson, Phys. Rev. Lett. **83**, 4357 (1999)
27. S. Yang, D. Slotcavage, J.D. Mai, F. Guo, S. Li, Y. Zhao, Y. Lei, C.E. Cameron, T.J. Huang, J. Mater. Chem. C **2**, 8350 (2014)
28. G. Macias, M. Alba, L.F. Marsal, A. Mihi, J. Mater. Chem. C **4**, 3970 (2016)
29. J.C. Fraire, V.N. Sueldo Ocello, L.G. Allende, A.V. Veglia, E.A. Coronado, J. Phys. Chem. C **119**, 8876 (2015)

30. A.Y.F. Mahmoud, C.J. Rusin, M.T. McDermott, The Analyst **145**, 1396 (2020)
31. X. Li, W. Xu, J. Zhang, H. Jia, B. Yang, B. Zhao, B. Li, Y. Ozaki, Langmuir **20**, 1298 (2004)
32. M.K. Tatmyshevskiy, D.I. Yakubovsky, O.O. Kapitanova, V.R. Solovey, A.A. Vyshnevyy, G.A. Ermolaev, Y.A. Klishin, M.S. Mironov, A.A. Voronov, A.V. Arsenin, V.S. Volkov, S.M. Novikov, Nanomaterials (Basel, Switzerland) **11** (2021)
33. Z. Fusco, R. Bo, Y. Wang, N. Motta, H. Chen, A. Tricoli, J. Mater. Chem. C **7**, 6308 (2019)
34. P. Royer, J.P. Goudonnet, R.J. Warmack, T.L. Ferrell, Phys. Rev. B **35**, 3753 (1987)
35. Y. Chen, K.J. Si, D. Sikdar, Y. Tang, M. Premaratne, W. Cheng, Advanced Optical Materials **3**, 919 (2015)
36. X. Luo, W. Liu, C. Chen, G. Jiang, X. Hu, H. Zhang, M. Zhong, Optics & Laser Technology **139**, 106969 (2021)
37. P. Wen, F. Yang, C. Ge, S. Li, Y. Xu, L. Chen, Nanotechnology **32** (2021)
38. R.J. Thibeau, C.W. Brown, R.H. Heidersbach, Appl Spectrosc **32**, 532 (1978)
39. F.J. Owens, J. Phys. C: Solid State Phys. **12**, 2255 (1979)
40. R.L. Farrow, P.L. Mattern, A.S. Nagelberg, Applied Physics Letters **36**, 212 (1980)
41. B.P. Gaber, W.L. Peticolas, Biochimica et biophysica acta **465**, 260 (1977)
42. S.A. Brawer, W.B. White, The Journal of Chemical Physics **63**, 2421 (1975)
43. M.M. Coleman, P.C. Painter, J.L. Koenig, J. Raman Spectrosc. **5**, 417 (1976)
44. D. Bloor, R.J. Kennedy, D.N. Batchelder, J. Polym. Sci. Polym. Phys. Ed. **17**, 1355 (1979)
45. J.-M. Delabar, W. Guschlbauer, Biopolymers **18**, 2073 (1979)
46. L.S. Lichtmann, D.B. Fitchen, H. Temkin, Synthetic Metals **1**, 139 (1980)
47. S.R. Nivaz, R. Geethalakshmi, G.S. Lekshmi, D. Surendhiran, C. Mustansar Hussain, A.R. Sirajunnisa, in *Handbook of Microbial Nanotechnology* (Elsevier, 2022), p. 145
48. C.S.S.R. Kumar, *Raman Spectroscopy for Nanomaterials Characterization* (Springer Berlin Heidelberg, Berlin, Heidelberg, 2012)
49. G. Gouadec, P. Colomban, Progress in Crystal Growth and Characterization of Materials **53**, 1 (2007)
50. K. Boldt, Nano Futures **6**, 12003 (2022)
51. S. Wood, J.R. Hollis, J.-S. Kim, J. Phys. D: Appl. Phys. **50**, 73001 (2017)
52. K.K. Nanda, S.N. Sarangi, S.N. Sahu, S.K. Deb, S.N. Behera, Physica B: Condensed Matter **262**, 31 (1999)
53. P.M. Fauchet, I.H. Campbell, Critical Reviews in Solid State and Materials Sciences **14**, s79-s101 (1988)
54. S. Loridant, Catalysis Today **373**, 98 (2021)
55. C. Hess, Chemical Society reviews **50**, 3519 (2021)
56. P.C. Stair, Current Opinion in Solid State and Materials Science **5**, 365 (2001)
57. T. Runka, Physical Sciences Reviews **2** (2017)
58. Z. Li, L. Deng, I.A. Kinloch, R.J. Young, Progress in Materials Science **135**, 101089 (2023)
59. L. Bokobza, J. Zhang, Express Polym. Lett. **6**, 601 (2012)
60. Y. Li, S. Ji, Y. Gao, H. Luo, M. Kanehira, Scientific reports **3**, 1370 (2013)
61. G.R. Ramos, J.E. Zorzi, R.C.D. Cruz, C.A. Perottoni, J. Raman Spectrosc. **49**, 1782 (2018)

62. S. Zhang, Y. Li, L. Huang, L. Huang, X. Luo, RSC advances **11**, 23550 (2021)
63. Y. Wang, C. Cong, C. Qiu, T. Yu, Small (Weinheim an der Bergstrasse, Germany) **9**, 2857 (2013)
64. Y. Lan, M. Zondode, H. Deng, J.-A. Yan, M. Ndaw, A. Lisfi, C. Wang, Y.-L. Pan, Crystals **8**, 375 (2018)
65. A. Krylov, Crystals **10**, 981 (2020)
66. B. Zou, D. Xu, X. Lai, Crystal Growth & Design **23**, 6263 (2023)
67. T.P. Devereaux, Phys. Rev. B **45**, 12965 (1992)
68. S.N. Moraes, D.L. Morgado, M. Nalin, Vibrational Spectroscopy **100**, 57 (2019)
69. T.H. Nguyen, T.M.H. Nguyen, B. Kang, B. Cho, M. Han, H.J. Choi, M. Kong, Y. Lee, I.-S. Yang, J. Raman Spectrosc. **50**, 1661 (2019)
70. P. Wang, W. Chen, J. Wang, Y. Lu, Z. Tang, Y. Tan, Analytical chemistry **95**, 6894 (2023)
71. M.S. Dresselhaus, A. Jorio, A.G. Souza Filho, R. Saito, Philosophical transactions. Series A, Mathematical, physical, and engineering sciences **368**, 5355 (2010)
72. L.G. Cançado, A. Jorio, E.H.M. Ferreira, F. Stavale, C.A. Achete, R.B. Capaz, M.V.O. Moutinho, A. Lombardo, T.S. Kulmala, A.C. Ferrari, Nano letters **11**, 3190 (2011)
73. A. Eckmann, A. Felten, A. Mishchenko, L. Britnell, R. Krupke, K.S. Novoselov, C. Casiraghi, Nano letters **12**, 3925 (2012)
74. N. Kuhar, S. Sil, S. Umapathy, Spectrochimica acta. Part A, Molecular and biomolecular spectroscopy **258**, 119712 (2021)
75. W.L. Peticolas, Methods in enzymology **246**, 389 (1995)
76. Y. Yin, B. Wang, Y. E, J. Yao, L. Wang, X. Bai, W. Liu, Commun Phys **3** (2020)
77. X. Zhang, X.-F. Qiao, W. Shi, J.-B. Wu, D.-S. Jiang, P.-H. Tan, Chemical Society reviews **44**, 2757 (2015)
78. R. Merlin, A. Pinczuk, W.H. Weber, in *Raman Scattering in Materials Science*, ed. by A. Zunger, R.M. Osgood, R. Hull, H. Sakaki, W.H. Weber, R. Merlin (Springer Berlin Heidelberg Berlin, Heidelberg, 2000), p. 1
79. G.C.K. Roberts (ed), *Encyclopedia of Biophysics* (Springer Berlin Heidelberg, Berlin, Heidelberg, 2013)
80. C. Krafft, in *Encyclopedia of Biophysics*, ed. by G.C.K. Roberts (Springer Berlin Heidelberg Berlin, Heidelberg, 2013), p. 2178
81. T. Huser, J. Chan, Advanced drug delivery reviews **89**, 57 (2015)
82. H. Sato, M. Ishigaki, A. Taketani, B.B. Andriana, BSI **7**, 97 (2019)
83. A.A. Fung, L. Shi, Wiley interdisciplinary reviews. Systems biology and medicine **12**, e1501 (2020)
84. A. Rygula, K. Majzner, K.M. Marzec, A. Kaczor, M. Pilarczyk, M. Baranska, J. Raman Spectrosc. **44**, 1061 (2013)
85. J.M. Benevides, S.A. Overman, G.J. Thomas, Current protocols in protein science **Chapter 17**, 17.8.1-17.8.35 (2004)
86. G.J. Thomas, Annual review of biophysics and biomolecular structure **28**, 1 (1999)
87. F. Ripanti, C. Fasolato, F. Mazzarda, S. Palleschi, M. Ceccarini, C. Li, M. Bignami, E. Bodo, S.E.J. Bell, F. Mazzei, P. Postorino, Analytical chemistry **93**, 10825 (2021)
88. K. Czamara, K. Majzner, M.Z. Pacia, K. Kochan, A. Kaczor, M. Baranska, J. Raman Spectrosc. **46**, 4 (2015)

89. H. Rosales-Solano, V. Galievsky, K. Murtada, P.V. Radovanovic, J. Pawliszyn, Analytical chemistry **94**, 606 (2022)
90. M. Uematsu, T. Shimizu, Communications biology **4**, 1176 (2021)
91. M. Dudek, G. Zajac, E. Szafraniec, E. Wiercigroch, S. Tott, K. Malek, A. Kaczor, M. Baranska, Spectrochimica acta. Part A, Molecular and biomolecular spectroscopy **206**, 597 (2019)
92. E. Wiercigroch, E. Szafraniec, K. Czamara, M.Z. Pacia, K. Majzner, K. Kochan, A. Kaczor, M. Baranska, K. Malek, Spectrochimica acta. Part A, Molecular and biomolecular spectroscopy **185**, 317 (2017)
93. Z. Farhane, F. Bonnier, A. Casey, H.J. Byrne, The Analyst **140**, 4212 (2015)
94. M. Li, H.-X. Liao, K. Bando, Y. Nawa, S. Fujita, K. Fujita, Analytical chemistry **94**, 10019 (2022)
95. K. Hanna, E. Krzoska, A.M. Shaaban, D. Muirhead, R. Abu-Eid, V. Speirs, British journal of cancer **126**, 1125 (2022)
96. S. Cui, S. Zhang, S. Yue, Journal of healthcare engineering **2018**, 8619342 (2018)
97. G.W. Auner, S.K. Koya, C. Huang, B. Broadbent, M. Trexler, Z. Auner, A. Elias, K.C. Mehne, M.A. Brusatori, Cancer metastasis reviews **37**, 691 (2018)
98. K. Dodo, K. Fujita, M. Sodeoka, Journal of the American Chemical Society **144**, 19651 (2022)
99. M. Wächtler, J. Guthmuller, L. González, B. Dietzek, Coordination Chemistry Reviews **256**, 1479 (2012)
100. K.N. Heck, B.G. Janesko, G.E. Scuseria, N.J. Halas, M.S. Wong, Journal of the American Chemical Society **130**, 16592 (2008)
101. Y.-H. Wang, J. Wei, P. Radjenovic, Z.-Q. Tian, J.-F. Li, Analytical chemistry **91**, 1675 (2019)
102. S. Lukin, K. Užarević, I. Halasz, Nature protocols **16**, 3492 (2021)
103. J. Dong, Z. Qian, P. Xu, M.-F. Yue, R.-Y. Zhou, Y. Wang, Z.-A. Nan, S. Huang, Q. Dong, J.-F. Li, F.R. Fan, Z.-Q. Tian, Chemical science **13**, 5639 (2022)
104. B. Zhou, J. Zhong, X. Tang, J. Liu, J. Shen, C. Wang, W. Ou, H. Wang, L. Liu, J. Pan, J. Lu, Y. Yang Li, Journal of Catalysis **413**, 527 (2022)
105. A. Tokmakoff, M.J. Lang, D.S. Larsen, G.R. Fleming, V. Chernyak, S. Mukamel, Phys. Rev. Lett. **79**, 2702 (1997)
106. V. Balos, N.K. Kaliannan, H. Elgabarty, M. Wolf, T.D. Kühne, M. Sajadi, Nature chemistry **14**, 1031 (2022)
107. W.-T. Wang, H. Zhang, Y. Yuan, Y. Guo, S.-X. He, AAPS PharmSciTech **19**, 2921 (2018)
108. N. Jung, M. Windbergs, Physical Sciences Reviews **3** (2018)
109. W.J. Tipping, M. Lee, A. Serrels, V.G. Brunton, A.N. Hulme, Chemical Society reviews **45**, 2075 (2016)
110. U. Gala, H. Chauhan, Expert opinion on drug discovery **10**, 187 (2015)
111. M. Gao, S. Liu, J. Chen, K.C. Gordon, F. Tian, C.M. McGoverin, International journal of pharmaceutics **597**, 120334 (2021)
112. D.-D. Chen, X.-F. Xie, H. Ao, J.-L. Liu, C. Peng, Journal of the Chinese Medical Association : JCMA **80**, 288 (2017)
113. J. Omar, A. Boix, F. Ulberth, Vibrational Spectroscopy **111**, 103147 (2020)
114. A. Silge, K. Weber, D. Cialla-May, L. Müller-Bötticher, D. Fischer, J. Popp, TrAC Trends in Analytical Chemistry **153**, 116623 (2022)

115. K. Buckley, P. Matousek, Journal of pharmaceutical and biomedical analysis **55**, 645 (2011)
116. Y. Liu, J. Doddi, Y. Zheng, V. Ho, M. Pheil, Y. Shi, Appl Spectrosc **74**, 108 (2020)
117. P.J. Larkin, M. Dabros, B. Sarsfield, E. Chan, J.T. Carriere, B.C. Smith, Appl Spectrosc **68**, 758 (2014)
118. L. Saerens, L. Dierickx, B. Lenain, C. Vervaet, J.P. Remon, T. de Beer, European journal of pharmaceutics and biopharmaceutics : official journal of Arbeitsgemeinschaft fur Pharmazeutische Verfahrenstechnik e.V **77**, 158 (2011)
119. A. Pugliese, M. Tobyn, L.E. Hawarden, A. Abraham, F. Blanc, Molecular pharmaceutics **19**, 3685 (2022)
120. N. Altangerel, B.W. Neuman, P.R. Hemmer, V.V. Yakovlev, N. Rajil, Z. Yi, A.V. Sokolov, M.O. Scully, Proceedings of the National Academy of Sciences of the United States of America **120**, e2218826120 (2023)
121. D. Di Mascolo, A. Coclite, F. Gentile, M. Francardi, Nanoscale advances **1**, 1541 (2019)
122. H. Du Choi, K.H. Kim, J.S. Park, S.H. Jeong, K. Park, Journal of controlled release : official journal of the Controlled Release Society **172**, 763 (2013)
123. Z. Li, M.J. Deen, S. Kumar, P.R. Selvaganapathy, Sensors (Basel, Switzerland) **14**, 17275 (2014)
124. Z. Li, J. Wang, D. Li, Applied Spectroscopy Reviews **51**, 333 (2016)
125. L. Chang, S. Jiang, J. Luo, J. Zhang, X. Liu, C.-Y. Lee, W. Zhang, Environ. Sci.: Nano **9**, 542 (2022)
126. Y. Yang, H. Guo, Environmental pollution (Barking, Essex : 1987) **329**, 121712 (2023)
127. S. Sze, Atmospheric Environment **35**, 561 (2001)
128. D.C. Doughty, S.C. Hill, Journal of Quantitative Spectroscopy and Radiative Transfer **248**, 106907 (2020)
129. C. Estefany, Z. Sun, Z. Hong, J. Du, Ecotoxicology and environmental safety **249**, 114405 (2023)
130. W.P. GRIFFITH, in *The Infrared Spectra of Minerals*, ed. by V.C. Farmer (Mineralogical Society of Great Britain and Ireland Londan, 1974), p. 119
131. V.C. Farmer (ed), *The Infrared Spectra of Minerals* (Mineralogical Society of Great Britain and Ireland, Londan, 1974)
132. D. Bersani, P.P. Lottici, J. Raman Spectrosc. **47**, 499 (2016)
133. A. Tournié, L.C. Prinsloo, C. Paris, P. Colomban, B. Smith, J. Raman Spectrosc. **42**, 399 (2011)
134. S. JORGEVILLAR, H. EDWARDS, L. BENNING, Icarus **184**, 158 (2006)
135. J. Jehlicka, O. Urban, J. Pokorný, Spectrochimica acta. Part A, Molecular and biomolecular spectroscopy **59**, 2341 (2003)
136. J. Jehlička, H. Edwards, Organic Geochemistry **39**, 371 (2008)
137. D.G. Henry, I. Jarvis, G. Gillmore, M. Stephenson, Earth-Science Reviews **198**, 102936 (2019)
138. A. Wang, K. Kuebler, B. Jolliff, L.A. Haskin, J. Raman Spectrosc. **35**, 504 (2004)
139. A. Wesełucha-Birczyńska, M. Żmudzka, Journal of Molecular Structure **887**, 253 (2008)
140. M. Musa, R. Rossini, D. Di Martino, M.P. Riccardi, M. Clemenza, G. Gorini, Materials (Basel, Switzerland) **14** (2021)

141. H. Cao, C. Wang, J. Chen, X. Che, X. Fu, Y. Shi, D. Liu, Z. Ling, Le Qiao, X. Lu, X. Qi, C. Yin, P. Liu, C. Liu, Y. Xin, J. Liu, Geophysical Research Letters **49** (2022)
142. E.A. Cloutis, C. Caudill, E.A. Lalla, J. Newman, M. Daly, E. Lymer, J. Freemantle, R. Kruzelecky, D. Applin, H. Chen, S. Connell, D. Fernandes, F. Giusto, J. Hawke, J. Lamamry, P. Murzionak, A. Parkinson, Q.-Y. Peng, N. Turenne, Z.U. Wolf, Front. Astron. Space Sci. **9** (2022)
143. S.M. Angel, N.R. Gomer, S.K. Sharma, C. McKay, Appl Spectrosc **66**, 137 (2012)
144. N. Tarcea, T. Frosch, P. Rösch, M. Hilchenbach, T. Stuffler, S. Hofer, H. Thiele, R. Hochleitner, J. Popp, Space Sci Rev **135**, 281 (2008)
145. R.V. Morris, D.C. Golden, J.F. Bell, T.D. Shelfer, A.C. Scheinost, N.W. Hinman, G. Furniss, S.A. Mertzman, J.L. Bishop, D.W. Ming, C.C. Allen, D.T. Britt, J. Geophys. Res. **105**, 1757 (2000)
146. S.W. Squyres, J.P. Grotzinger, R.E. Arvidson, J.F. Bell, W. Calvin, P.R. Christensen, B.C. Clark, J.A. Crisp, W.H. Farrand, K.E. Herkenhoff, J.R. Johnson, G. Klingelhöfer, A.H. Knoll, S.M. McLennan, H.Y. McSween, R.V. Morris, J.W. Rice, R. Rieder, L.A. Soderblom, Science (New York, N.Y.) **306**, 1709 (2004)
147. M.H. Hecht, S.P. Kounaves, R.C. Quinn, S.J. West, S.M.M. Young, D.W. Ming, D.C. Catling, B.C. Clark, W.V. Boynton, J. Hoffman, L.P. Deflores, K. Gospodinova, J. Kapit, P.H. Smith, Science (New York, N.Y.) **325**, 64 (2009)
148. D.F. Blake, R.V. Morris, G. Kocurek, S.M. Morrison, R.T. Downs, D. Bish, D.W. Ming, K.S. Edgett, D. Rubin, W. Goetz, M.B. Madsen, R. Sullivan, R. Gellert, I. Campbell, A.H. Treiman, S.M. McLennan, A.S. Yen, J. Grotzinger, D.T. Vaniman, S.J. Chipera, C.N. Achilles, E.B. Rampe, D. Sumner, P.-Y. Meslin, S. Maurice, O. Forni, O. Gasnault, M. Fisk, M. Schmidt, P. Mahaffy, L.A. Leshin, D. Glavin, A. Steele, C. Freissinet, R. Navarro-González, R.A. Yingst, L.C. Kah, N. Bridges, K.W. Lewis, T.F. Bristow, J.D. Farmer, J.A. Crisp, E.M. Stolper, D.J. Des Marais, P. Sarrazin, Science (New York, N.Y.) **341**, 1239505 (2013)
149. S.M. McLennan, R.B. Anderson, J.F. Bell, J.C. Bridges, F. Calef, J.L. Campbell, B.C. Clark, S. Clegg, P. Conrad, A. Cousin, D.J. Des Marais, G. Dromart, M.D. Dyar, L.A. Edgar, B.L. Ehlmann, C. Fabre, O. Forni, O. Gasnault, R. Gellert, S. Gordon, J.A. Grant, J.P. Grotzinger, S. Gupta, K.E. Herkenhoff, J.A. Hurowitz, P.L. King, S. Le Mouélic, L.A. Leshin, R. Léveillé, K.W. Lewis, N. Mangold, S. Maurice, D.W. Ming, R.V. Morris, M. Nachon, H.E. Newsom, A.M. Ollila, G.M. Perrett, M.S. Rice, M.E. Schmidt, S.P. Schwenzer, K. Stack, E.M. Stolper, D.Y. Sumner, A.H. Treiman, S. VanBommel, D.T. Vaniman, A. Vasavada, R.C. Wiens, R.A. Yingst, Science (New York, N.Y.) **343**, 1244734 (2014)
150. D.M. Hassler, C. Zeitlin, R.F. Wimmer-Schweingruber, B. Ehresmann, S. Rafkin, J.L. Eigenbrode, D.E. Brinza, G. Weigle, S. Böttcher, E. Böhm, S. Burmeister, J. Guo, J. Köhler, C. Martin, G. Reitz, F.A. Cucinotta, M.-H. Kim, D. Grinspoon, M.A. Bullock, A. Posner, J. Gómez-Elvira, A. Vasavada, J.P. Grotzinger, Science (New York, N.Y.) **343**, 1244797 (2014)
151. I.B. Hutchinson, R. Ingley, H.G.M. Edwards, L. Harris, M. McHugh, C. Malherbe, J. Parnell, Philosophical transactions. Series A, Mathematical, physical, and engineering sciences **372** (2014)
152. B. Leimer, R. Garbutt, F. Weesner, J. Hodkiewicz, Microsc Microanal **9**, 1124 (2003)

153. N. George, H. Singh, R. Jotaniya, S.R. Pandya, Forensic science international **340**, 111441 (2022)
154. Y.V. Kistenev, A.V. Borisov, A.A. Samarinova, S. Colón-Rodríguez, I.K. Lednev, Scientific reports **13**, 5384 (2023)
155. K.X.E. Kay, A.H. Atabaki, W.B. Ng, Z. Li, G.P. Singh, S.W.L. Tan, R.J. Ram, J. Raman Spectrosc. **53**, 1321 (2022)
156. S. Azimi, A. Docoslis, Sensors (Basel, Switzerland) **22** (2022)
157. S. Neuberger, C. Neusüß, Journal of pharmaceutical and biomedical analysis **112**, 70 (2015)
158. K. Dégardin, A. Guillemain, Y. Roggo, Journal of Spectroscopy **2017**, 1 (2017)
159. J.M. Chalmers, H.G.M. Edwards, M.D. Hargreaves, *Infrared and Raman Spectroscopy in Forensic Science* (Wiley, 2012)
160. S.R. Khandasammy, M.A. Fikiet, E. Mistek, Y. Ahmed, L. Halámková, J. Bueno, I.K. Lednev, Forensic Chemistry **8**, 111 (2018)
161. M.A. Fikiet, S.R. Khandasammy, E. Mistek, Y. Ahmed, L. Halámková, J. Bueno, I.K. Lednev, Spectrochimica acta. Part A, Molecular and biomolecular spectroscopy **197**, 255 (2018)
162. E.-R. Mojica, Z. Dai, Talanta Open **6**, 100124 (2022)
163. H.G.M. Edwards, P. Vandenabeele, P. Colomban, *Raman Spectroscopy in Cultural Heritage Preservation* (Springer International Publishing, Cham, 2023)
164. M.C.A.N. Analytical, Analytical methods : advancing methods and applications **7**, 4844 (2015)
165. P. Ropret, J.M. Madariaga, J. Raman Spectrosc. **45**, 985 (2014)
166. J. Stenger, K. Eremin, N. Khandekar, P.M. Champion, L.D. Ziegler, in (AIP, 2010), p. 233
167. C.-H. Lin, Y.-F. Chang, Analytical sciences : the international journal of the Japan Society for Analytical Chemistry **38**, 483 (2022)
168. K.L. Wustholz, C.L. Brosseau, F. Casadio, R.P. van Duyne, Physical chemistry chemical physics : PCCP **11**, 7350 (2009)
169. C. Muehlethaler, K. Ng, L. Gueissaz, M. Leona, J.R. Lombardi, Dyes and Pigments **137**, 539 (2017)
170. P. Vandenabeele, B. Wehling, L. Moens, H. EDWARDS, M. de Reu, G. van Hooydonk, Analytica Chimica Acta **407**, 261 (2000)
171. K. Sugawa, T. Akiyama, Y. Tanoue, T. Harumoto, S. Yanagida, A. Yasumori, S. Tomita, J. Otsuki, Physical chemistry chemical physics : PCCP **17**, 21182 (2015)
172. K.-K. Liu, S. Tadepalli, L. Tian, S. Singamaneni, Chem. Mater. **27**, 5261 (2015)
173. B. Han, N. Ma, S. Guo, J. Yu, L. Xiao, Y. Park, E. Park, S. Jin, L. Chen, Y.M. Jung, J. Phys. Chem. C **124**, 16616 (2020)
174. A.I. Pérez-Jiménez, D. Lyu, Z. Lu, G. Liu, B. Ren, Chemical science **11**, 4563 (2020)
175. J. Langer, D. Jimenez de Aberasturi, J. Aizpurua, R.A. Alvarez-Puebla, B. Auguié, J.J. Baumberg, G.C. Bazan, S.E.J. Bell, A. Boisen, A.G. Brolo, J. Choo, D. Cialla-May, V. Deckert, L. Fabris, K. Faulds, F.J. García de Abajo, R. Goodacre, D. Graham, A.J. Haes, C.L. Haynes, C. Huck, T. Itoh, M. Käll, J. Kneipp, N.A. Kotov, H. Kuang, E.C. Le Ru, H.K. Lee, J.-F. Li, X.Y. Ling, S.A. Maier, T. Mayerhöfer, M. Moskovits, K. Murakoshi, J.-M. Nam, S. Nie, Y. Ozaki, I. Pastoriza-Santos, J. Perez-Juste, J. Popp, A. Pucci, S. Reich, B. Ren, G.C. Schatz, T. Shegai, S. Schlücker, L.-L. Tay, K.G. Thomas, Z.-Q. Tian, R.P. van Duyne, T. Vo-Dinh,

Y. Wang, K.A. Willets, C. Xu, H. Xu, Y. Xu, Y.S. Yamamoto, B. Zhao, L.M. Liz-Marzán, ACS nano **14**, 28 (2020)
176. X.X. Han, R.S. Rodriguez, C.L. Haynes, Y. Ozaki, B. Zhao, Nat Rev Methods Primers **1** (2021)
177. X. Xiu, L. Hou, J. Yu, S. Jiang, C. Li, X. Zhao, Q. Peng, S. Qiu, C. Zhang, B. Man, Z. Li, Nanophotonics **10**, 1529 (2021)
178. C. Zhang, T. Zhang, Z. Zhang, H. Zheng, Frontiers in chemistry **7**, 647 (2019)
179. M.S. Dresselhaus, G. Dresselhaus, R. Saito, A. Jorio, Physics Reports **409**, 47 (2005)
180. M.S. Dresselhaus, A. Jorio, M. Hofmann, G. Dresselhaus, R. Saito, Nano letters **10**, 751 (2010)
181. L.M. Malard, M.A. Pimenta, G. Dresselhaus, M.S. Dresselhaus, Physics Reports **473**, 51 (2009)
182. K. Gołasa, M. Grzeszczyk, R. Bożek, P. Leszczyński, A. Wysmołek, M. Potemski, A. Babiński, Solid State Communications **197**, 53 (2014)
183. G. Kukucska, V. Zólyomi, J. Koltai, J. Phys. Chem. C **123**, 1995 (2019)
184. B. Zhang, K. Wang, R. Chang, X. Yi, Y. Zhang, S. Wang, J. Phys. Chem. C **123**, 24943 (2019)
185. C. Schüller, in *Advances in Solid State Physics 38*, ed. by B. Kramer (Springer Berlin Heidelberg Berlin, Heidelberg, 1999), p. 167
186. V.G. Yakunin, R.B. Asilbaeva, S.P. Rodichkina, A.F. Alykova, A.Z. Turmukhambetov, V.Y. Timoshenko, J. Phys.: Conf. Ser. **1348**, 12025 (2019)
187. N. Chen, T.-H. Xiao, Z. Luo, Y. Kitahama, K. Hiramatsu, N. Kishimoto, T. Itoh, Z. Cheng, K. Goda, Nature communications **11**, 4772 (2020)
188. V.K. Aggarwal, S. Sett, J. Sau, A. Ghatak, M. Kumar, A. Singha, A.K. Raychaudhuri, J. Phys. Chem. C **126**, 15046 (2022)
189. Y. Sun, H. Tang, X. Zou, G. Meng, N. Wu, Current Opinion in Food Science **47**, 100910 (2022)
190. M. Petersen, Z. Yu, X. Lu, Biosensors **11** (2021)
191. I.H. Boyaci, H.T. Temiz, H.E. Geniş, E. Acar Soykut, N.N. Yazgan, B. Güven, R.S. Uysal, A.G. Bozkurt, K. İlaslan, O. Torun, F.C. Dudak Şeker, RSC Adv. **5**, 56606 (2015)
192. A. Nilghaz, S. Mahdi Mousavi, A. Amiri, J. Tian, R. Cao, X. Wang, Journal of agricultural and food chemistry **70**, 5463 (2022)
193. Y.-S. Li, J.S. Church, Journal of food and drug analysis **22**, 29 (2014)
194. D. Yang, Y. Ying, Applied Spectroscopy Reviews **46**, 539 (2011)
195. D.A. Long, *The Raman Effect* (Wiley, 2002)
196. T. Dieing, O. Hollricher, J. Toporski, *Confocal Raman Microscopy* (Scholars Portal, Berlin, Heidelberg, 2011)
197. M. Liao, Y.-W. Kuo, J. Howard, Molecular biology of the cell **33**, ar48 (2022)
198. M.R. Hanson, A. Sattarzadeh, Methods in molecular biology (Clifton, N.J.) **1132**, 125 (2014)
199. I.P. Coyle, Methods in molecular biology (Clifton, N.J.) **1075**, 201 (2014)
200. S. Stehbens, H. Pemble, L. Murrow, T. Wittmann, Methods in enzymology **504**, 293 (2012)
201. M.B. Kennedy, Cold Spring Harbor perspectives in biology **8**, a016824 (2013)
202. C. Grienberger, X. Chen, A. Konnerth, Trends in neurosciences **38**, 45 (2015)

203. E. Lopez-Ortega, J.Y. Choi, I. Hong, R.H. Roth, R.H. Cudmore, R.L. Huganir, Cell reports **43**, 113966 (2024)
204. W. Chen, R.G. Natan, Y. Yang, S.-W. Chou, Q. Zhang, E.Y. Isacoff, N. Ji, Nature communications **12**, 6630 (2021)
205. P. Verstraelen, M. van Dyck, M. Verschuuren, N.D. Kashikar, R. Nuydens, J.-P. Timmermans, W.H. de Vos, Frontiers in neuroscience **12**, 389 (2018)
206. E. Sezgin, P. Schwille, Cold Spring Harbor perspectives in biology **3**, a009803 (2011)
207. C.A. Day, L.J. Kraft, M. Kang, A.K. Kenworthy, Current protocols in cytometry **Chapter 2**, Unit2.19 (2012)
208. K. Zhanghao, W. Liu, M. Li, Z. Wu, X. Wang, X. Chen, C. Shan, H. Wang, X. Chen, Q. Dai, P. Xi, D. Jin, Nature communications **11**, 5890 (2020)
209. S. Daemen, M.A.M.J. van Zandvoort, S.H. Parekh, M.K.C. Hesselink, Molecular metabolism **5**, 153 (2016)
210. A.P. Young, D.J. Jackson, R.C. Wyeth, PeerJ **8**, e8806 (2020)
211. A.R. Shakoori, in *Chromosome Structure and Aberrations*, ed. by T.A. Bhat, A.A. Wani (Springer India New Delhi, 2017), p. 343
212. A. Pramanik, Current pharmaceutical biotechnology **5**, 205 (2004)
213. A. Pramanik, R. Rigler, in *Fluorescence Correlation Spectroscopy*, ed. by F.P. Schäfer, J.P. Toennies, W. Zinth, R. Rigler, E.S. Elson (Springer Berlin Heidelberg Berlin, Heidelberg, 2001), p. 101
214. F.P. Schäfer, J.P. Toennies, W. Zinth, R. Rigler, E.S. Elson (eds), *Fluorescence Correlation Spectroscopy* (Springer Berlin Heidelberg, Berlin, Heidelberg, 2001)
215. P. Lengsfeld, N.H. Nickel, Journal of Non-Crystalline Solids **299-302**, 778 (2002)
216. V. Scuderi, M. Zielinski, F. La Via, Materials (Basel, Switzerland) **16** (2023)
217. N.H. Nickel, P. Lengsfeld, I. Sieber, Phys. Rev. B **61**, 15558 (2000)
218. L. Ma, W. Qiu, X. Fan, Microelectronics Reliability **118**, 114045 (2021)
219. A.Z. Samuel, Spectrochimica acta. Part A, Molecular and biomolecular spectroscopy **224**, 117431 (2020)
220. G.S. Papanai, I. Sharma, B.K. Gupta, Materials Today Communications **22**, 100795 (2020)
221. Y. Hagiwara, L. Yokokura, J. Yamamoto, J. Raman Spectrosc. **54**, 1440 (2023)
222. A. Perro, S. Reculusa, S. Ravaine, E. Bourgeat-Lami, E. Duguet, J. Mater. Chem. **15**, 3745 (2005)
223. J. Maisch, F. Jafarli, T. Chassé, F. Blendinger, A. Konrad, M. Metzger, A.J. Meixner, M. Brecht, L. Dähne, H.A. Mayer, Chemical communications (Cambridge, England) **52**, 14392 (2016)
224. K. Pearson, The London, Edinburgh, and Dublin Philosophical Magazine and Journal of Science **2**, 559 (1901)
225. Q. Zhang, Y. Yuan, C. Wang, Z. Zhou, L. Li, S. Zhang, J. Xu, J. Raman Spectrosc. **47**, 395 (2016)
226. C. Brackmann, J. Bood, M. Afzelius, P.-E. Bengtsson, Meas. Sci. Technol. **15**, R13-R25 (2004)
227. S. Roy, J.R. Gord, A.K. Patnaik, Progress in Energy and Combustion Science **36**, 280 (2010)
228. G.O. Ariunbold, N. Altangerel, Coherent Phenomena **3** (2016)

229. A. Virga, C. Ferrante, G. Batignani, D. de Fazio, A.D.G. Nunn, A.C. Ferrari, G. Cerullo, T. Scopigno, Nature communications **10**, 3658 (2019)
230. B. Pettinger, B. Ren, G. Picardi, R. Schuster, G. Ertl, J. Raman Spectrosc. **36**, 541 (2005)
231. R. Zhang, Y. Zhang, Z.C. Dong, S. Jiang, C. Zhang, L.G. Chen, L. Zhang, Y. Liao, J. Aizpurua, Y. Luo, J.L. Yang, J.G. Hou, Nature **498**, 82 (2013)
232. M.D. Sonntag, J.M. Klingsporn, A.B. Zrimsek, B. Sharma, L.K. Ruvuna, R.P. van Duyne, Chemical Society reviews **43**, 1230 (2014)
233. H. Cui, W. Zhao, Y. Wang, Y. Fan, L. Qiu, K. Zhu, Optics express **24**, 10767 (2016)
234. H. Xiong, N. Qian, Y. Miao, Z. Zhao, C. Chen, W. Min, Light, science & applications **10**, 87 (2021)
235. M. Wang, C. Zhang, S. Yan, T. Chen, H. Fang, X. Yuan, ACS Photonics **8**, 1801 (2021)
236. J. Shou, A. Komazawa, Y. Wachi, M. Kawatani, H. Fujioka, S.J. Spratt, T. Mizuguchi, K. Oguchi, H. Akaboshi, F. Obata, R. Tachibana, S. Yasunaga, Y. Mita, Y. Misawa, R. Kojima, Y. Urano, M. Kamiya, Y. Ozeki, Science advances **9**, eade9118 (2023)
237. L. Shi, A. Klimas, B. Gallagher, Z. Cheng, F. Fu, P. Wijesekara, Y. Miao, X. Ren, Y. Zhao, W. Min, Advanced science (Weinheim, Baden-Wurttemberg, Germany) **9**, e2200315 (2022)
238. R.J.H. Clark, T.J. Dines, Angew. Chem. Int. Ed. Engl. **25**, 131 (1986)
239. A.C. Ferrari, J. Robertson, Phys. Rev. B **64** (2001)
240. C. Thomsen, S. Reich, J. Maultzsch, Philosophical transactions. Series A, Mathematical, physical, and engineering sciences **362**, 2337 (2004)
241. E.V. Efremov, F. Ariese, C. Gooijer, Analytica Chimica Acta **606**, 119 (2008)
242. Stefan A. Maier, *Plasmonics: Fundamentals and Applications* (Scholars Portal)
243. J.D. Jackson, *Classical electrodynamics* (John Wiley, Hoboken, NJ, 1998)
244. J. Gersten, A. Nitzan, The Journal of Chemical Physics **73**, 3023 (1980)
245. D.A. Weitz, S. Garoff, J.I. Gersten, A. Nitzan, The Journal of Chemical Physics **78**, 5324 (1983)
246. P.F. Liao, A. Wokaun, The Journal of Chemical Physics **76**, 751 (1982)
247. K. Kneipp, H. Kneipp, I. Itzkan, R.R. Dasari, M.S. Feld, J. Phys.: Condens. Matter **14**, R597-R624 (2002)
248. M. Moskovits, Rev. Mod. Phys. **57**, 783 (1985)
249. M. Moskovits, Physical chemistry chemical physics : PCCP **15**, 5301 (2013)
250. E. Burstein, Y.J. Chen, C.Y. Chen, S. Lundquist, E. Tosatti, Solid State Communications **29**, 567 (1979)
251. E.C. Le Ru, P.G. Etchegoin, *Principles of surface-enhanced raman spectroscopy: And related plasmonic effects: And related plasmonic effects* (Elsevier, Amsterdam, Heidelberg, 2011)
252. Y. Kitahama, P.M. Pancorbo, H. Segawa, M. Marumi, T.-H. Xiao, K. Hiramatsu, W. Yang, K. Goda, Analytical methods : advancing methods and applications **15**, 1028 (2023)
253. T. Vo-Dinh, Sensors and Actuators B: Chemical **29**, 183 (1995)
254. R. Kunihisa, A. Iwata, M. Gen, C.K. Chan, A. Matsuki, Aerosol Science and Technology **54**, 826 (2020)

255. S. Fornasaro, F. Alsamad, M. Baia, L.A.E. Batista de Carvalho, C. Beleites, H.J. Byrne, A. Chiadò, M. Chis, M. Chisanga, A. Daniel, J. Dybas, G. Eppe, G. Falgayrac, K. Faulds, H. Gebavi, F. Giorgis, R. Goodacre, D. Graham, P. La Manna, S. Laing, L. Litti, F.M. Lyng, K. Malek, C. Malherbe, M.P.M. Marques, M. Meneghetti, E. Mitri, V. Mohaček-Grošev, C. Morasso, H. Muhamadali, P. Musto, C. Novara, M. Pannico, G. Penel, O. Piot, T. Rindzevicius, E.A. Rusu, M.S. Schmidt, V. Sergo, G.D. Sockalingum, V. Untereiner, R. Vanna, E. Wiercigroch, A. Bonifacio, Analytical chemistry **92**, 4053 (2020)
256. M. Kahraman, E.R. Mullen, A. Korkmaz, S. Wachsmann-Hogiu, Nanophotonics **6**, 831 (2017)
257. G.M. Das, S. Managò, M. Mangini, A.C. de Luca, Nanomaterials (Basel, Switzerland) **11** (2021)
258. X. Liang, N. Li, R. Zhang, P. Yin, C. Zhang, N. Yang, K. Liang, B. Kong, NPG Asia Mater **13** (2021)
259. Z. Cai, Y. Hu, Y. Sun, Q. Gu, P. Wu, C. Cai, Z. Yan, Analytical chemistry **93**, 1025 (2021)
260. C. Lin, Y. Li, Y. Peng, S. Zhao, M. Xu, L. Zhang, Z. Huang, J. Shi, Y. Yang, Journal of nanobiotechnology **21**, 149 (2023)
261. L. Jiang, M.M. Hassan, S. Ali, H. Li, R. Sheng, Q. Chen, Trends in Food Science & Technology **112**, 225 (2021)
262. J. Perumal, Y. Wang, A.B.E. Attia, U.S. Dinish, M. Olivo, Nanoscale **13**, 553 (2021)
263. M.-L. Xu, Y. Gao, X.-X. Han, B. Zhao, Foods (Basel, Switzerland) **11** (2022)
264. H. Li, E. Dumont, R. Slipets, T. Thersleff, A. Boisen, G.A. Sotiriou, Chemical Engineering Journal **470**, 144023 (2023)
265. D.-Y. Lin, C.-Y. Yu, C.-A. Ku, C.-K. Chung, Micromachines **14** (2023)
266. B. Sharma, R.R. Frontiera, A.-I. Henry, E. Ringe, R.P. van Duyne, Materials Today **15**, 16 (2012)
267. Y. Liu, Z. Qin, J. Deng, J. Zhou, X. Jia, G. Wang, F. Luo, Chemosensors **10**, 455 (2022)
268. B. Yang, S. Jin, S. Guo, Y. Park, L. Chen, B. Zhao, Y.M. Jung, ACS omega **4**, 20101 (2019)
269. M. Baia, S. Astilean, T. Iliescu, *Raman and SERS Investigations of Pharmaceuticals* (Springer Berlin Heidelberg, Berlin, Heidelberg, 2008)
270. R.A. Lodder, J. Am. Chem. Soc. **131**, 4168 (2009)
271. B. Fortuni, M. Ricci, R. Vitale, T. Inose, Q. Zhang, J.A. Hutchison, K. Hirai, Y. Fujita, S. Toyouchi, S. Krzyzowska, I. van Zundert, S. Rocha, H. Uji-I, ACS sensors **8**, 2340 (2023)
272. R.A. Halvorson, P.J. Vikesland, Environmental science & technology **44**, 7749 (2010)
273. G. Bodelón, I. Pastoriza-Santos, Frontiers in chemistry **8**, 478 (2020)
274. T.T.X. Ong, E.W. Blanch, O.A.H. Jones, The Science of the total environment **720**, 137601 (2020)
275. L.R. Terry, S. Sanders, R.H. Potoff, J.W. Kruel, M. Jain, H. Guo, Analytical Science Advances **3**, 113 (2022)
276. J.B.M. Parambath, G. Kim, C. Han, A.A. Mohamed, Res Chem Intermed **49**, 1259 (2023)

277. X. Zhang, K. Zhao, X. Wang, H. Wang, W. Yang, J. Liu, Da Li, The Science of the total environment **856**, 158879 (2023)
278. L. Guerrini, R.A. Alvarez-Puebla, Cancers **11** (2019)
279. M. Blanco-Formoso, R.A. Alvarez-Puebla, International journal of molecular sciences **21** (2020)
280. C. Qiu, W. Zhang, Y. Zhou, H. Cui, Y. Xing, F. Yu, R. Wang, Chemical Engineering Journal **459**, 141502 (2023)
281. C.-C. Xiong, S.-S. Zhu, D.-H. Yan, Y.-D. Yao, Z. Zhang, G.-J. Zhang, S. Chen, Analytical and bioanalytical chemistry **415**, 3449 (2023)
282. J. Song, B. Duan, C. Wang, J. Zhou, L. Pu, Z. Fang, P. Wang, T.T. Lim, H. Duan, J. Am. Chem. Soc. **136**, 6838 (2014)
283. A.L. Chun, Nature Nanotech (2015)
284. I. Calderon, L. Guerrini, R.A. Alvarez-Puebla, Biosensors **11** (2021)
285. F. Pozzi, M. Leona, J. Raman Spectrosc. **47**, 67 (2016)
286. M.C.A.N.B.P. Analytical, Analytical methods : advancing methods and applications **9**, 4338 (2017)
287. M.S. Zalaffi, I. Agostinelli, N. Karimian, P. Ugo, Heritage **3**, 1344 (2020)
288. Y. He, M. Wen, X. Zhou, F. Gao, H. Lu, Analytical Letters **55**, 555 (2022)
289. C.E. Ott, L.E. Arroyo, WIREs Forensic Science **5** (2023)
290. T. Reese, C. Suarez, W.R. Premasiri, M.L. Shaine, H. Ingraham, A.N. Brodeur, L.D. Ziegler, Forensic science international **328**, 111000 (2021)
291. A. Hakonen, K. Wu, M. Stenbæk Schmidt, P.O. Andersson, A. Boisen, T. Rindzevicius, Talanta **189**, 649 (2018)
292. R.S. Golightly, W.E. Doering, M.J. Natan, ACS nano **3**, 2859 (2009)
293. S.I. Rae, I. Khan, The Analyst **135**, 1365 (2010)
294. K. Yang, S. Zong, Y. Zhang, Z. Qian, Y. Liu, K. Zhu, L. Li, N. Li, Z. Wang, Y. Cui, ACS applied materials & interfaces **12**, 1395 (2020)
295. L. Chen, H. Guo, F. Sassa, B. Chen, K. Hayashi, Sensors (Basel, Switzerland) **21** (2021)
296. J. Prakash, P.R. de Oliveira, H.C. Swart, M. Rumyantseva, M. Packirisamy, B.C. Janegitz, X. Li, Sens. Diagn. **1**, 1143 (2022)
297. S. Hy, Felix, Y.-H. Chen, J. Liu, J. Rick, B.-J. Hwang, Journal of Power Sources **256**, 324 (2014)
298. X.-B. Han, K. Kannari, S. Ye, Current Opinion in Electrochemistry **17**, 174 (2019)
299. C. Zhu, C. Fan, E. Cortés, W. Xie, Journal of materials chemistry. A **9**, 20024 (2021)
300. E.G. Loewen, E. Popov, *Diffraction Gratings and Applications* (CRC Press, 2018)
301. S. Brunauer, P.H. Emmett, E. Teller, J. Am. Chem. Soc. **60**, 309 (1938)
302. E.P. Barrett, L.G. Joyner, P.P. Halenda, J. Am. Chem. Soc. **73**, 373 (1951)

Appendix 1

S1. Calculation of incident + diffraction angle

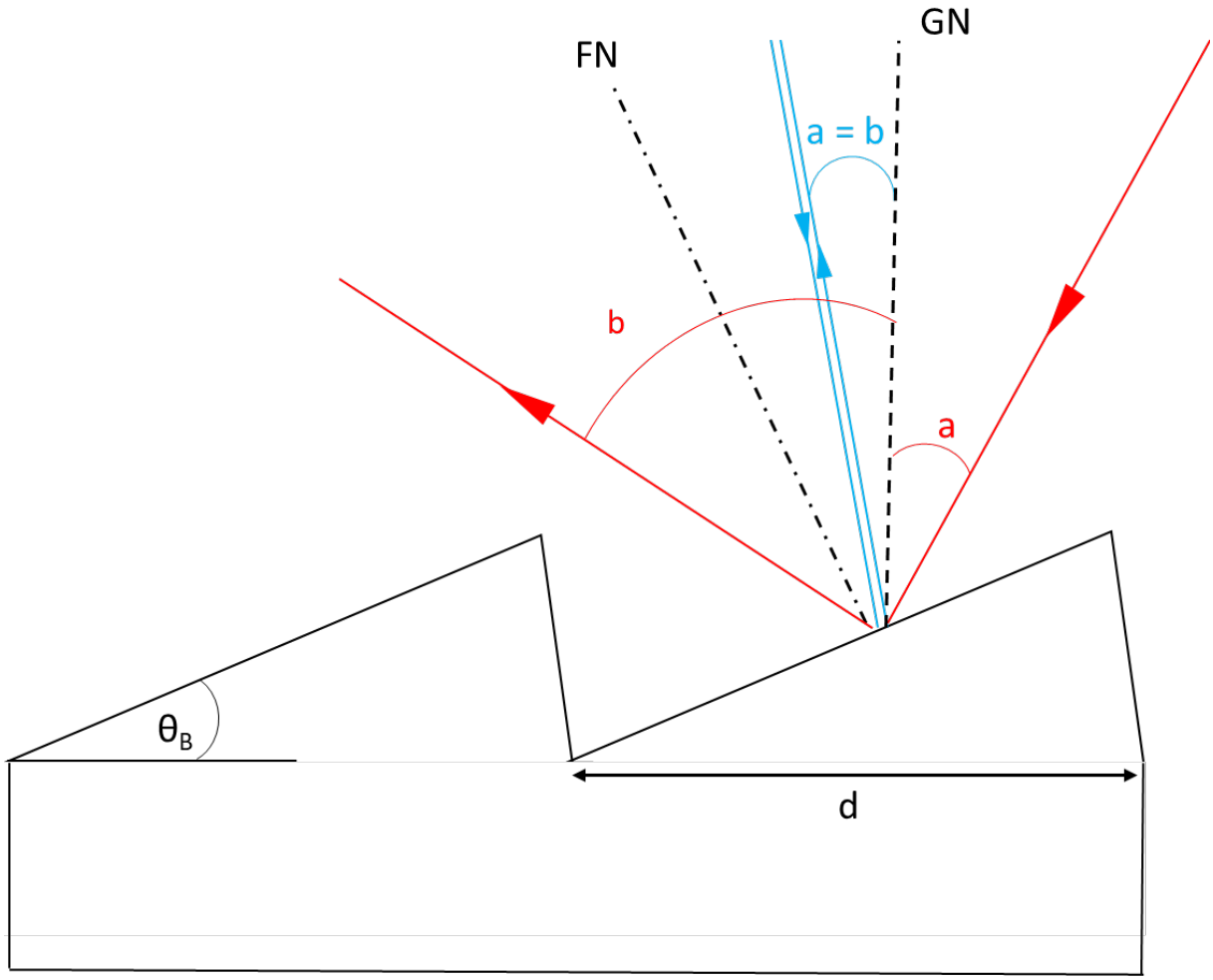

Figure S 1: Schematics of blazed grating: The general case is shown with red rays, and the Littrow configuration is shown with blue rays. GN is grating normal, the normal drawn to the plane of grating, and FN is facet normal: the normal drawn to the facet of the grating.

The grating equation is given by,[300]

$$m\lambda = d(sina + sinb) \qquad \textit{Eqn. 38}$$

The manufacturing specification states that the two gratings (1800 l/mm and 600 l/mm) are configured at a Blaze wavelength of 500 nm. Blaze wavelength λ_B is given by,[300]

$$\lambda_B = \frac{2d}{m} sin\theta_B \qquad \textit{Eqn. 39}$$

At Blaze configuration,

$$\theta_B = \frac{a+b}{2} \qquad \textit{Eqn. 40}$$

Where a is the incident angle to GN and b is the diffracted angle to GN, θ_B is the Blaze angle, is the angle between the face of the groove and the plane of the grating, m is the diffraction order, and d is the grating groove density.

Solving for θ_B from equation Eqn. 40 for both gratings,

$$\theta_B \; for \; 1800\frac{l}{mm} = 27.03° \qquad \textit{Eqn. 41}$$

$$\theta_B \; for \; 600\frac{l}{mm} = 8.66° \qquad \textit{Eqn. 42}$$

Now assume the Blaze condition for maximum efficiency, the Littrow configuration. In this configuration, the incident and the diffracted angle are in the same plane, that is, $a = b$. At Littrow configuration,

$$\theta_B = \frac{a+\beta}{2} = \frac{2a}{2} = a = b \qquad \textit{Eqn. 43}$$

This suggests that the incident or diffracted angle has to be $27.03°$ for 1800 l/mm or $8.66°$ for 600 l/mm. Substituting $a \; or \; b$ in the grating Eqn. 38 and solving for the remaining angle gives for, say, $\lambda = 633$ nm.

$$b \; for \; 1800\frac{l}{mm} = 44.14° \qquad \textit{Eqn. 44}$$

$$b \; for \; 600\frac{l}{mm} = 13.34° \qquad \textit{Eqn. 45}$$

Now, at 633 nm,

$$\alpha \; at \; 1800\frac{l}{mm} = 90 - (a+b) = 90 - (27.03° + 44.14°) = 71.17°$$

$$\alpha \; at \; 600\frac{l}{mm} = 90 - (a+b) = 90 - (8.66° + 13.34°) = 22.00°$$

Similarly, it can be calculated for 442 nm and 532 nm excitation sources.

S2. SR as a function of wavelength and Raman shift

Figure S 2(a) presents the crucial dependence of SR on wavelength for both gratings. This result can be easily derived from the equation by varying the wavelength (ω_L) over the desired range. It is important to note that Q was kept constant (Q = 10 for 1800 l/mm and Q = 50 for 600 l/mm) based on initial experimental results, as depicted in Figure 2 of Chapter 4. Figure S 2(b) further demonstrates the dependence of SR on Raman shift for the two available gratings and three different excitation wavelengths (442 nm, 532 nm, and 633 nm).

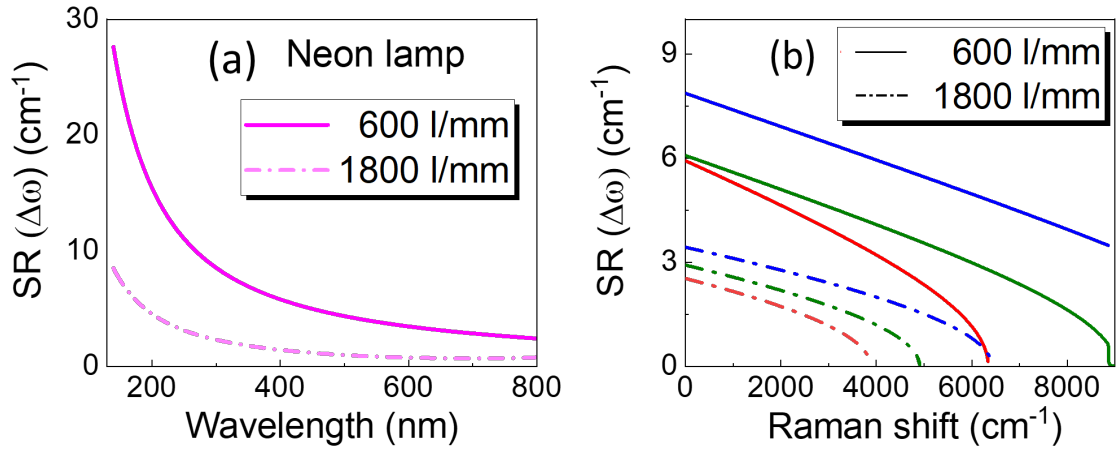

Figure S 2: (a) SR as a function of wavelength for two available gratings 600 lines/mm and 1800 lines/mm and (b) SR as a function of Raman shift for two available gratings and three different excitation sources (442 nm, 532 nm, and 633 nm).

Appendix 2

Figure S 3 provides a comprehensive view of the Raman mean spectra of normal salivary gland (green), warthin tumor (blue), and pleomorphic adenoma (red) within 900 – 1700 cm^{-1}. The superposition of all three spectra reveals striking similarities, with many identical Raman bands. However, it also highlights the subtle differences between the tissue types, which are crucial for their identification.

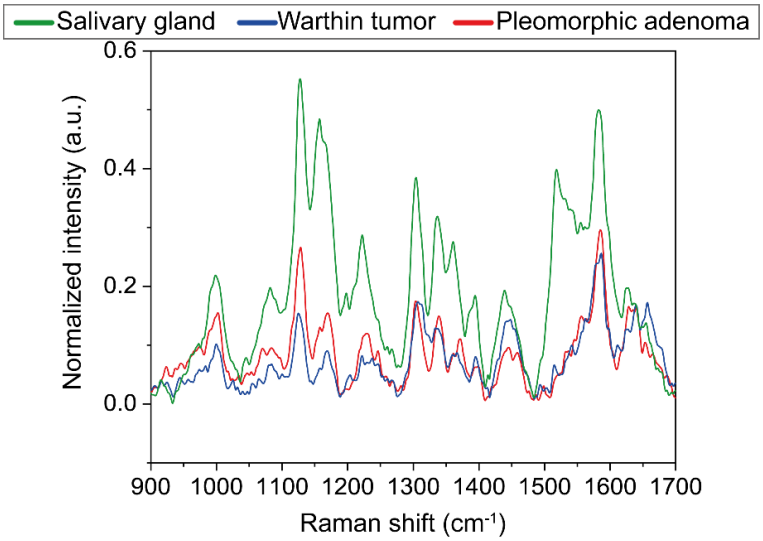

Figure S 3: Superimposed Raman mean spectra of normal salivary gland (green), Warthin tumor (blue), and pleomorphic adenoma (red) within 900 – 1700 cm^{-1}. The spectral pattern of all three tissue types is very similar. Only minor changes in band relations or manifestations are noticeable.

Figure S 3 illustrates the complete PCA evaluation with all used PCs (PC1 – PC5). It displays the respective 2D score plots (a, c, e, g) and corresponding loadings (b, d, f, h) of PC1 – PC5. The requirement of five PCs corroborates the complexity of the spectral data and the significant information content obtained by Raman imaging.

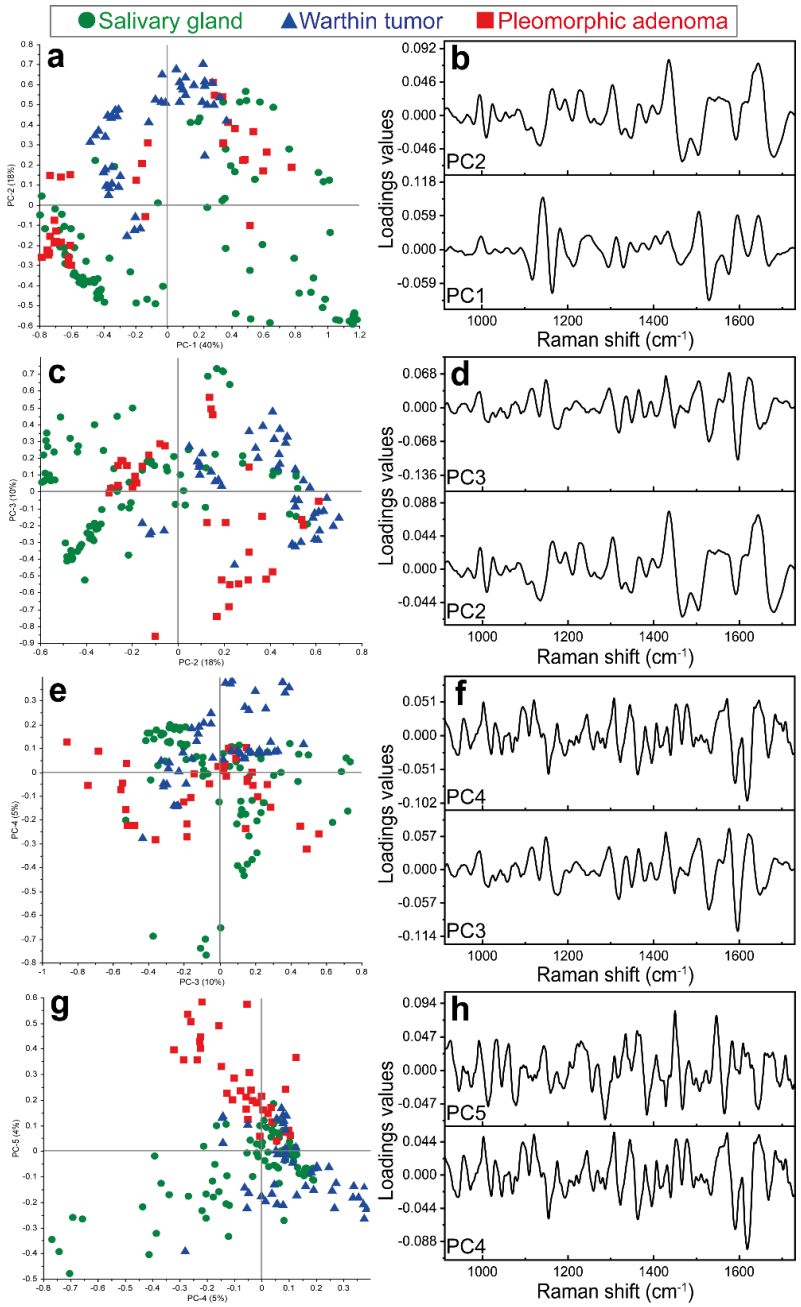

Figure S 4: 2D score plots and corresponding loading plots of the PCA model (a-h). Five PCs (PC1-PC5) are required to enable a complete differentiation of normal salivary gland (green circles), Warthin tumor (blue triangles), and pleomorphic adenoma (red squares). PC1 describes 40 % of the total model variance, whereas PC2, PC3, PC4, and PC5 account for 18 %, 10 %, 5 %, and 4 %, respectively. Two consecutive PCs are always plotted against one another in the 2D score plots, which are PC2 vs. PC1 (a) with related loading plot (b), PC3 vs. PC2 (c) with related loading plot (d), PC4 vs. PC3 (e) with related loading plot (f) and PC5 vs. PC4 (g) with related loading plot (h)

Figure S 4. 2D score plots and corresponding loading plots of the PCA model (**a-h**). Five PCs (PC1-PC5) are required to enable a complete differentiation of normal salivary gland (green circles), Warthin tumor (blue triangles), and pleomorphic adenoma (red squares). PC1 describes 40 % of the total model variance, whereas PC2, PC3, PC4, and PC5 account for 18 %, 10 %, 5 %, and 4 %, respectively. Two consecutive PCs are always plotted against one another in the 2D score plots, which are PC2 vs. PC1 (**a**) with related loading plot (**b**), PC3 vs. PC2 (**c**) with related loading plot (**d**), PC4 vs. PC3 (**e**) with related loading plot (**f**) and PC5 vs. PC4 (**g**) with related loading plot (**h**).

The DA was computed using the PCA score values and the Mahalanobis distance algorithm with five PCs. As a result, the confusion matrix of the PCA-DA is obtained and presented in Table S 1. Raman mean spectra assignments, summarized in the confusion matrix, represent an internal model validation in which each model spectrum is allocated to one tissue cluster as if it was not included in the model. Based on this outcome, performance parameters can be calculated.

Confusion matrix of the parotid tissue PCA-DA		**Actual**		
		Salivary gland tissue	Pleomorphic adenoma	Warthin tumor
Predicted	Salivary gland tissue	91	3	3
	Pleomorphic adenoma	3	31	1
	Warthin tumor	0	1	43

Table S 1: Confusion matrix of the final PCA-DA model. An overall model accuracy of 94 % was achieved, represented by the high number of correctly assigned models, including Raman mean spectra for all tissue types.

Appendix 3

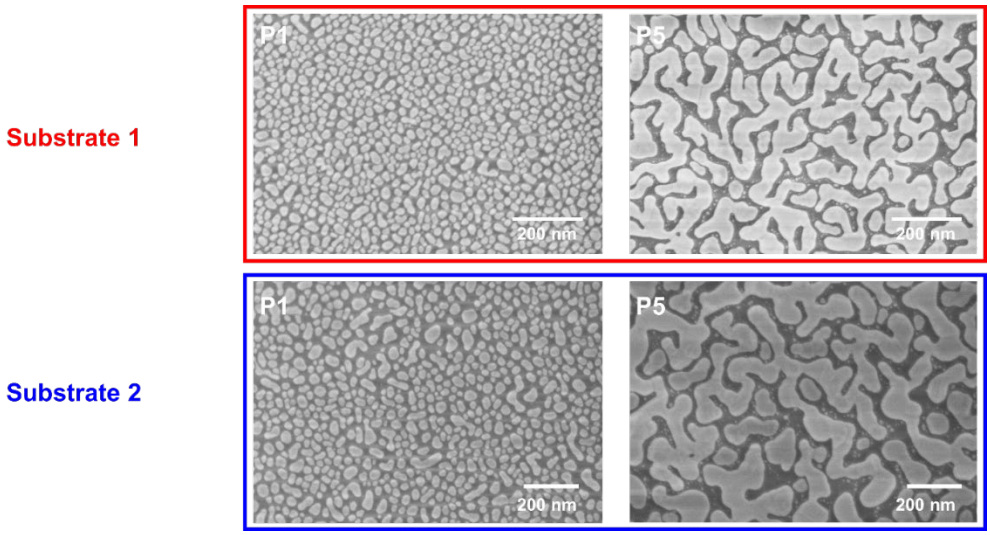

Figure S 5: SEM images of different fabricated substrates (substrate 1 - red and substrate 2 - blue) at the same positions P1 and P5 to denote micro- and nano-scale reproducibility.

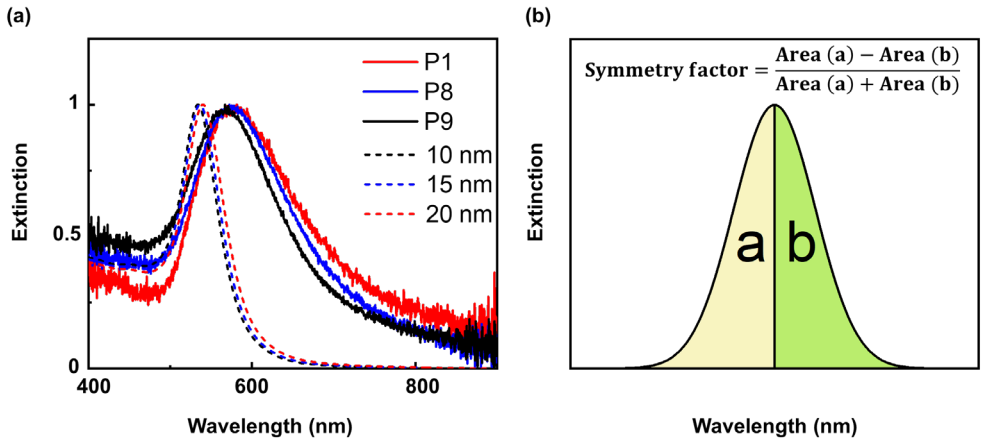

Figure S 6: (a) Normalized extinction spectra at points P1, P8, and P9 (solid lines – red, blue, black) compared to normalized simulated extinction spectra from Mie theory for spherical Au NPs with radii of 10 nm, 15 nm, and 20 nm (dashed lines – red, blue, black), and (b) schematic and equation to determine the symmetry factor of an extinction curve.

Appendix 4

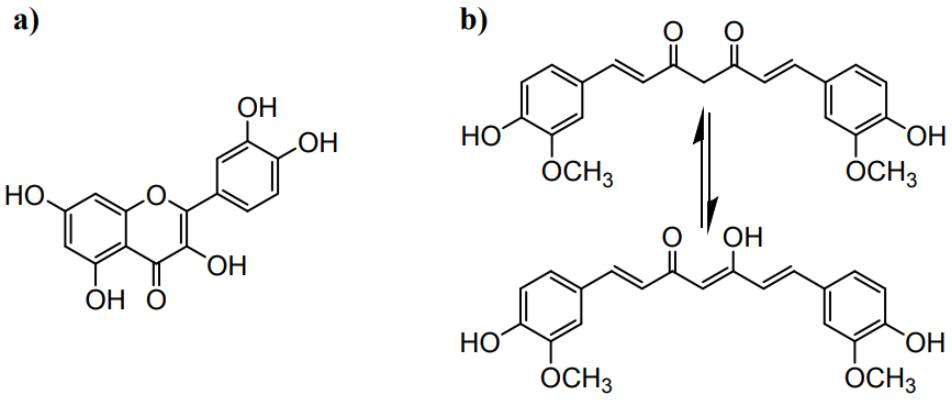

Figure S 7: (a) Chemical structure of quercetin, (b) Keto/enol tautomerism of curcumin.

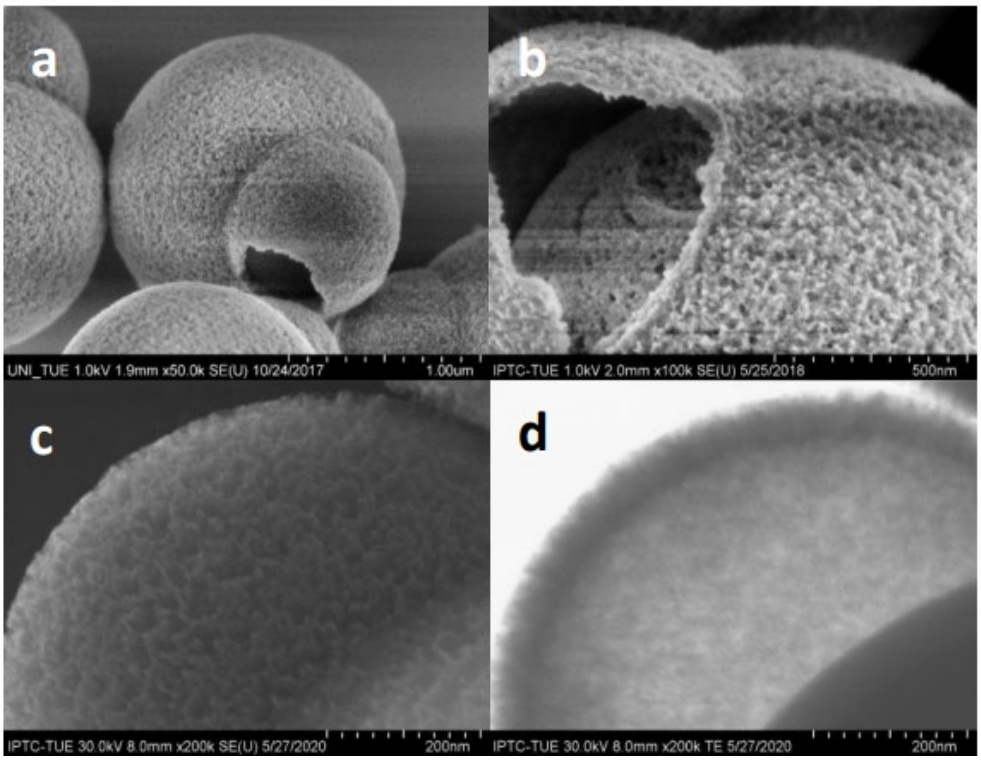

Figure S 8: SEM (a,b) and STEM (c,d) micrographs of DCS1 particles.

Figure S 8 displays SEM (a,b) micrographs of a selected broken dumbbell particle of DCS1.The images demonstrate the mesoporous shell's high porosity covering the large lobe and the small hemisphere. Moreover, the images also give insight into the hollow cavity covered by the small lobe. The STEM (c,d) images show an intact particle in agreement with the broken one.

Physisorption measurements

N_2-physisorption measurements were performed on an ASAP2020 volumetric adsorption apparatus (Micromeritics Instrument Corp.) at 77 K (am (N2, 77 K) = 0.162 nm^2.). The samples were degassed at 250 °C for four hours before analysis. The Brunauer–Emmett–Teller (BET),[301] specific surface area was calculated from the nitrogen adsorption branch of the isotherm in the relative pressure range of 0.07–0.15 for the pure SiO_2 and the hybrid materials. Pore size distributions (dV/dD) were calculated using the Barrett–Joyner–Halenda (BJH) method from the nitrogen desorption branch.[302]

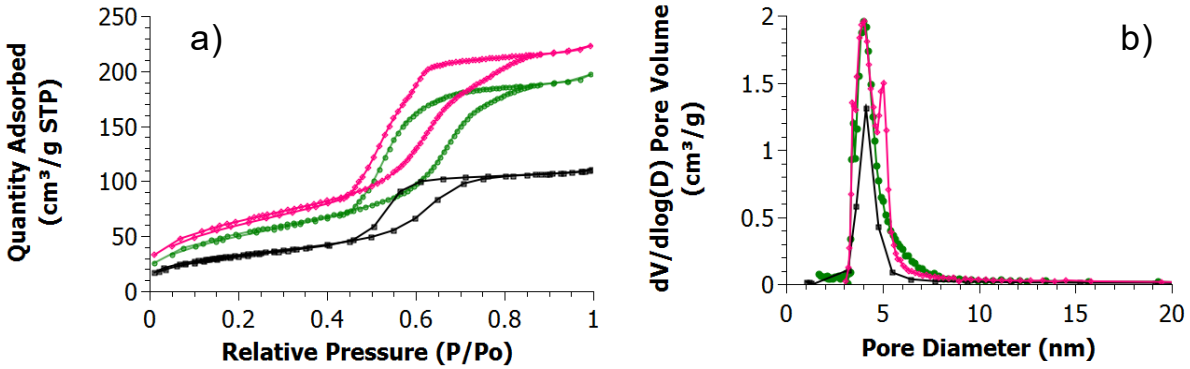

Figure S 9: Nitrogen Adsorption and Desorption Isotherms and b) BJH Pore volume and pore diameter for CS (◆), DCS1 (■), and DCS2 (●).

Confocal Raman measurements

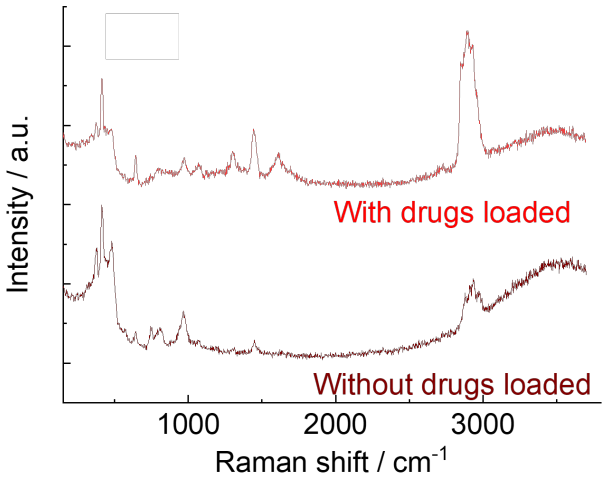

Figure S 10: Comparison between Raman spectra of the DCS1 particles with and without drugs loaded.

Appendix 5

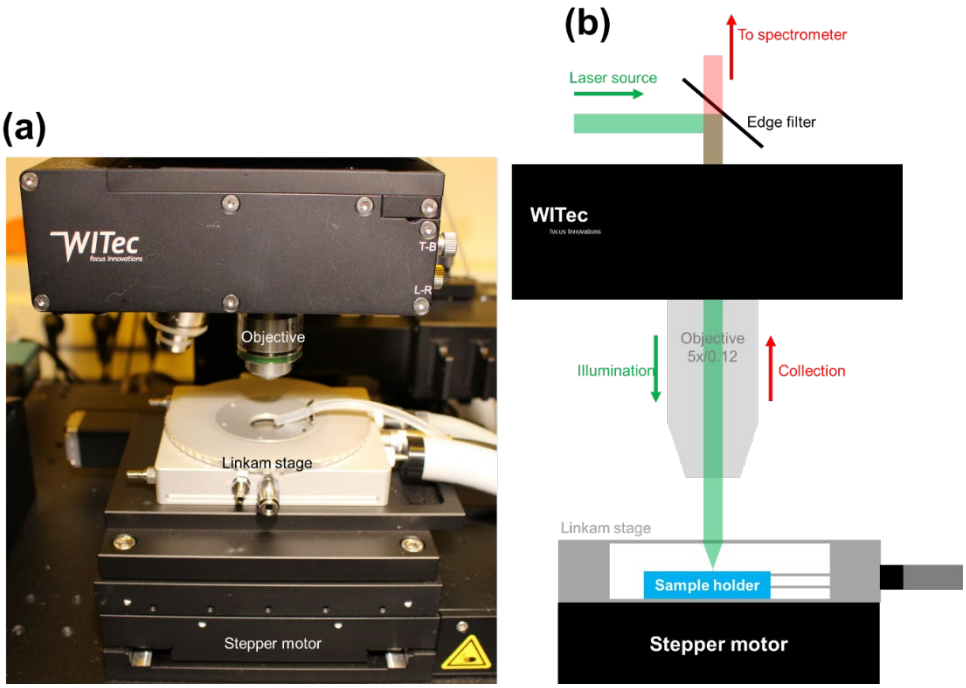

Figure S 11: Photograph of WITec alpha300RAandS upright microscope fitted with LINKAM Scientific instruments' THMS600 heating and freezing stage, and (b) Schematic of the optical path of WITec alpha300RAandS upright microscope equipped with LINKAM Scientific instruments' THMS600 heating and freezing stage with all the labeled parts, optical path, and components.

Appendix 6

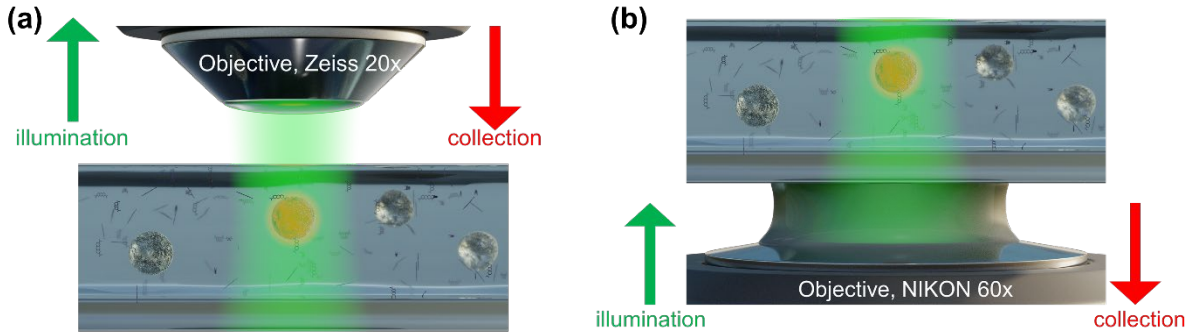

Figure S 12: (a) Schematics of top-excitation and detection configuration through an objective lens (Carl Zeiss; EC Epiplan-Neofluar DIC M27, 100x, N.A.=0.9) at WITec alpha300RA&S, and (b) Schematics of bottom- excitation and detection configuration through an objective lens (NIKON 60x, N.A.=0.55) at WITec alpha300RA&S.

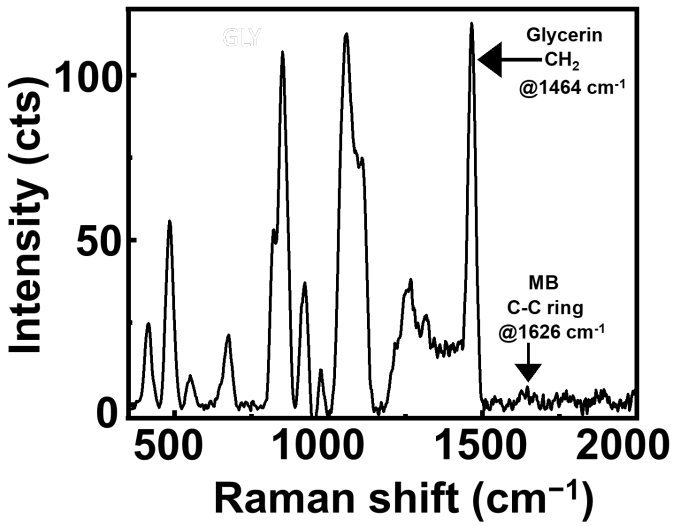

Figure S 13: The Raman spectrum of glycerin -MB solution is marked with its most intense peaks.

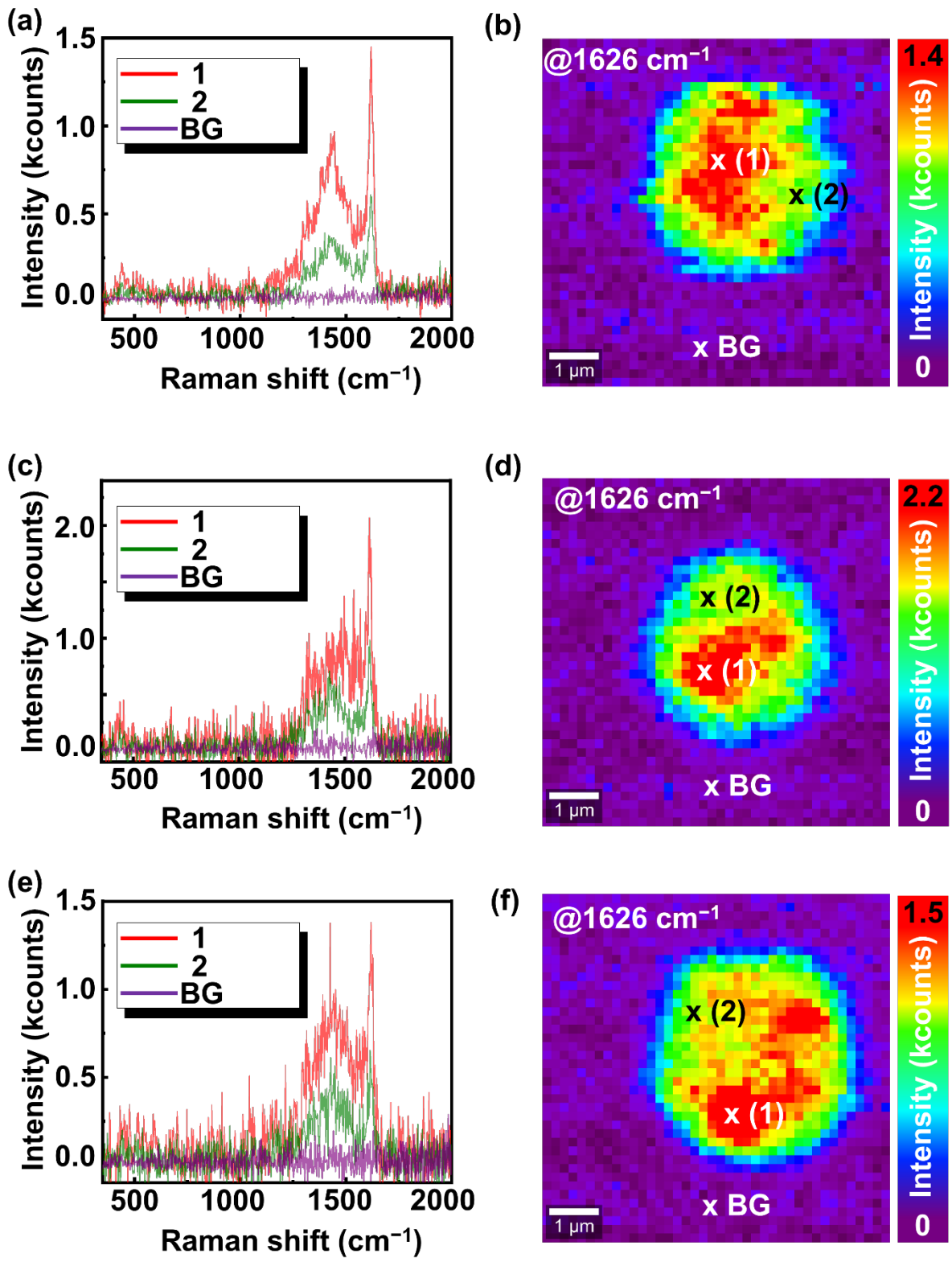

Figure S 14: Example 1 - (a) SERS spectra of glycerin and MB at different spatial positions on SMP, position 1 (bright region), position 2 (low-intensity region), background (BG), (b) SERS image of a SMP immersed in glycerin-MB solution at 1626 cm^{-1}. The marks show the positions where the

spectra in (a) are acquired, Example 2 - (c) SERS spectra of glycerin and MB at different spatial positions on SMP, position 1 (bright region), position 2 (low-intensity region), background (BG), (d) SERS image of a SMP immersed in glycerin-MB solution at 1626 cm^{-1}. The marks show the positions where the spectra in (c) are acquired, and Example 3 - (e) SERS spectra of glycerin and MB at different spatial positions on SMP, position 1 (bright region), position 2 (low-intensity region), background (BG), (e) SERS image of a SMP immersed in glycerin-MB solution at 1626 cm^{-1}. The marks show the positions where the spectra in (e) are acquired.

EF calculations

The calculated EF values for Figures 2(c) and 2(d) of chapter 10 are as follows:

Please note that the same data set shown in Figure 2(b) was used to calculate the EF in Figures 2(c) and 2(d) of Chapter 10. Since the background (BG (acc)) was used to calculate the EF:

For MB:

$$EF\ (for\ MB) = \frac{I_{Hotspot}}{I_{Substrate}} = \frac{I_{Hotspot\ MB}}{I_{BG\ (acc)}} = \frac{1900}{5} = 374$$

Therefore, 374 is the highest value on the z-color scale bar of Figure 2(c) of chapter 10

For the lowest EF value on the z-color scale of Figure 2(c) of chapter 10:

Since the intensity of MB is obscured by noise and not visible, the intensity is considered to be 0

$$EF\ (for\ MB) = \frac{I_{Substrate}}{I_{Substrate}} = \frac{I_{Substrate\ MB}}{I_{BG\ (acc)}} = \frac{0}{5} = 0$$

Thus, 0 is the lowest value on the z-color scale of Figure 2(c) of chapter 10.

Similarly, for glycerin:

$$EF\ (for\ Glycerin) = \frac{I_{Hotspot}}{I_{Substrate}} = \frac{I_{Hotspot\ Glycerin}}{I_{BG\ (acc)}} = \frac{1700}{115} = 14.79 \approx 15$$

Hence, 15 is the highest value on the z-color scale bar of Figure 2(d) of chapter 10.

For the substrate:

$$EF\ (for\ Glycerin) = \frac{I_{Substrate}}{I_{Substrate}} = \frac{I_{Substrate\ Glycerin}}{I_{BG\ (acc)}} = \frac{85}{115} = 0.73 \approx 1$$

Acknowledgment

I want to express my profound gratitude to Prof. Marc Brecht and Prof. Alfred J. Meixner for their invaluable support, unwavering guidance, and scholarly insights throughout my doctoral research. Their dedication to fostering academic excellence and commitment to mentoring have been instrumental in shaping my educational journey. I appreciate their expertise and encouragement, which have greatly enriched my work. I am privileged to have had the opportunity to learn under their mentorship, and I sincerely thank them for their profound impact on my academic development.

I am deeply thankful to Prof. Andreas Schnepf for accepting and agreeing to be a re-viewer for my PhD thesis. His expertise and support will help me improve my work, and I am sincerely grateful for his time and commitment. I am also immensely thankful to Prof. Hermann Mayer for accepting the role of examiner for my PhD thesis; our productive collaboration has been invaluable, and I am grateful for his support and expertise throughout this journey. I also want to acknowledge Prof. Karsten Rebner, Prof. Monika Fleischer, Prof. Erik Schäffer, Prof. Andreas Kandelbauer, and Prof. Pierre-Michel Adam for their support and successful collaborations with them and their department.

I am grateful to Dr. Frank Wackenhut for his valuable contributions to my doctoral journey. His unparalleled support and guidance in various aspects of my research, including organizing results, enriching scientific arguments, planning experiments, scientific writing, and publications, have been instrumental in navigating the complexities of doctoral study. I sincerely appreciate his generosity, time, expertise, and encouragement.

I want to acknowledge the Federal Ministry of Education and Research (Bundesministerium für Bildung and Forschung-BMBF) for their financial support within the framework of IngenieurNachwuchs 2016, with specific reference to the "CompeTERS" project and grant number 13FH596IX6. Under the CompeTERS project, I would like to express my gratitude to our project partners: Dr. Miriam Böhmler, Dr. Jan Englert, Dr. Stefan Gomez da Costa, Dr. Thomas Dieng, Oxford Instruments Witec GmbH, Ulm; Dr. Marc Richter, Renishaw GmbH, Pliezhausen; Prof. Dai Zhang and Prof. Alfred J. Meixner, Institute of Physical and Theoretical Chemistry, University of Tübingen; Dr. Claus Burkhardt, Natural and Medical Science Institute (NMI), Reutlingen.

I extend my appreciation to my colleagues, Dr. Edwin Ostertag, Dr. Miriam Bassler, Dr. Julia Steinbach, Mona Stefanakis, Barbara Boldrini, Alexander Stuhl, Tobias Drieischner, Tim Bäuerle, Mohammad Al Ktash, Robin Böhr, Josune Jeminez, Dmytro Golovko, Anita Lorenz, and Alexandra Wagner. Their contribution to fostering a friendly environment, fostering camaraderie, engaging in enriching scientific discussions, and offering assistance has been constructive throughout my research journey.

I want to express my deepest gratitude to my parents, Ratna and Ashish Mukherjee, and my sister, Anushree Mukherjee, my grandparents, Shreemati Diptima Shree Shyam Sundar Halder, Shreemati Kamala Mukherjee, and Shree Mohinimohan Mukherjee for their unwavering love, encouragement, and support throughout every success and challenge I faced on this journey to achieving a Ph.D. I am equally grateful to my aunt, uncle, Manjoori and Santanu Ganguly, and my cousin Rishabh Ganguly for their constant encouragement and care, which have contributed significantly to my perseverance and success. Their wisdom, blessings, and enduring love have always inspired me. Their belief in me has been a constant source of strength.

Finally, I express my profound gratitude to my wife, Gahana Mukherjee, for her unwavering support in my professional and personal endeavors and her exceptional patience in dealing with my moments of challenge. This accomplishment is as much theirs as it is mine.

Affirmation in Lieu of an Oath

I solemnly affirm that the information, data, and research presented in this thesis result from my work and effort, conducted with integrity and adherence to the ethical standards of scientific research. I further affirm that all sources of information, assistance, and collaboration have been appropriately acknowledged and that no part of this work has been plagiarized or otherwise misrepresented.

I understand and accept the responsibilities inherent in completing and submitting this thesis and affirm that it represents my genuine contributions to the field of study.

Tübingen

_____

Ashutosh Mukherjee

Eidesstaatliche Erklärung

Ich versichere feierlich, dass die in dieser Dissertation vorgestellten Informationen, Daten und Forschungsergebnisse das Ergebnis meiner eigenen Arbeit und Bemühungen sind, die mit Integrität und unter Einhaltung der ethischen Standards wissenschaftlicher Forschung durchgeführt wurden. Ich bestätige ferner, dass alle Informationsquellen, Hilfestellungen und Kooperationen angemessen anerkannt wurden und dass kein Teil dieser Arbeit plagiiert oder anderweitig falsch dargestellt wurde.

Ich verstehe und akzeptiere die Verantwortung, die mit der Fertigstellung und Einreichung dieser Dissertation einhergeht, und erkläre, dass sie meine authentischen Beiträge zum Fachgebiet darstellt.

Tübingen

_____

Ashutosh Mukherjee